Modelling the localized corrosion effects experienced by electroplated zinc and zinc - 4.5 wt.% aluminium steel coatings.

Barnard, Nicholas

Modelling the Localized Corrosion Effects Experienced by Electroplated Zinc and Zinc – 4.5 wt.% Aluminium Steel Coatings

Nicholas Barnard

EPSRC Engineering Doctorate Centre for Steel Technology
University of Wales Swansea
Department of Materials Engineering

Declaration

This work has not previously been accepted in substance for any degree and is not being concurrently submitted in candidature for any degree.

Signed ..... (candidate)

Date ...5th May 2006.....

Statement 1

This thesis is the result of my own investigations, except where otherwise stated. Other sources are acknowledged by footnotes giving explicit references. A bibliography is appended.

Signed .. .. (candidate)

Date ...5th May 2006.....

Statement 2

I hereby give consent for my thesis, if accepted, to be available for photocopying and for inter–library loan, and for the title and summary to be made available to outside organizations.

Signed .. .. (candidate)

Date ...5th May 2006.....

Acknowledgements

This thesis documents the results of four years research on the Engineering Doctorate In Steel Technology at the University of Wales Swansea. Completion of this investigation is testament to the support that I have received over these very enjoyable years. I am grateful for the contributions from the sponsors of this project; Engineering and Physical Sciences Research Council (EPSRC), Corus Colors and Corus Strip Products, UK. In particular, I would like to extend my gratitude to Vernon John and Paul Jones from Corus, both of whom have helped in the industrial and processing aspects of this investigation. The information provided to aid this investigation from Jon Elvins (Corus) and staff at the University of Wales, Swansea is also greatly appreciated.

I am indebted to my academic supervisor Steve Brown for his encouragement, huge support and maintained enthusiasm, especially during the arduous times. A special thanks to Neil McMurray for his discussions and ideas, which were greatly appreciated.

Finally, I would like to thank all fellow EngD researchers, especially those that have participated in the organized events and courses that I have attended for making them very enjoyable affairs. My family have, as always, given me valued advice, unconditional support and love throughout these happy four years. Thank–you all.

Abstract

A general modelling approach is described for the numerical simulation of localized corrosion phenomena. The model is demonstrated using several simple cases and compared both to analytical solutions and experimental measurements. The model is intended to operate at the microscopic–mesoscopic length scales and involves two– or three–dimensional field calculations performed in a finite difference computational framework. Limitations and possible extensions to the algorithm are discussed.

Experimental work has been reported that demonstrates the effects of microstructural variations within Zn–Al Galfan type coatings on the corrosion behaviour of cut-edge material, i.e. those cases where both the underlying steel and the organic coated Galfan layer are simultaneously exposed to a corrosive environment. An attempt to model the localized corrosion effects in electroplated zinc and hot–dip Galfan coatings has been made. The model combines both diffusive and electrochemical phenomena and describes corrosion effects on micro scale coating layers in NaCl electrolyte. The model predicts the 3D form of electrical potential, localized current densities and concentrations and also the time–dependent degradation of the micro scale coating layer. Results of the prototype model are quantitatively compared with measured current densities obtained from Scanning Vibrating Electrode Technique (SVET) studies.

Simulations have been performed to predict the microstructural influence on the corrosion of Galfan coatings cooled at different rates. The model is in good agreement with experimental findings with respect to the cut–edge behaviour of these coatings, although contradicts those SVET measurements made in respect of the surface corrosion performance.

Table of Contents

List of Figures

List of Tables

Chapter 1

Introduction

Corrosion has a far reaching impact on the environment and economy. It is a formidable enemy to the performance of the world's durable goods and infrastructure, since it is the environmental degradation of materials. A measure of the economic implications of corrosion has often been attempted by those working in the field of corrosion science in relation to the gross national product (GNP) of first world nations with vast consumer economies, e.g. United States and United Kingdom. Estimates place the value of corrosion at 3.5% of the GNP, of which it is assumed that a third could be avoided by the application of present knowledge. (Schuze, 2000) First estimated in the United States by Uhlig at 2.1% of the GNP in 1949, later in-depth studies in the United Kingdom saw this figure rise to 3.5% in 1971, excluding the contribution expected from the agricultural industry. By 1975, estimations to the cost of corrosion in the United states stood at $70 billion, equating to 4.2% of GNP. (Trethewey and Chamberlain, 1995)

Corus, as a leading manufacturer of steel products supplies competitive markets from a number of industrial sectors. In terms of the company's turnover, the construction industry represents a major share at approximately 30%, followed by the autmotive and packaging industries with 16% and 15% respectively. With this vast contribution made by the construction sector it is imperative that Corus seeks to maintain or increase its market share by the development of superior products; offering innovative solutions to customers so that the materials used offer greater longevity and flexibility in use. Colorcoat HPS200® and Celestia® are both organically coated steel products (OCS) recommended widely by architects for use in cladding and roofing of modern buildings. These products are beneficial

for ease of on-site fabrication. The delivery of up to 30 years assurance is offered by the Confidex® guarantee which assures customers of the performance and reliability of the OCS product.

In manufacturing products for use as construction materials it is important to note that corrosion can have a considerable detrimental effect. This occurs when insufficient precaution is taken to prevent corrosion or where there is a lack knowledge present about the behaviour of specific materials in the service environment. If a greater understanding is achieved then there is more opportunity to design against the detrimental effects of corrosion. More visible forms of corrosion, such as the general degradation of metals in the ambient atmosphere, are more easily dealt with than those which occur in hidden recesses and in environments far removed from those which we perceive as 'normal'. These more unpredictable cases of corrosion often degrade only small amounts of material critical to the performance of a component. This can cause much inconvenience and destruction to the community. The adverse features of corrosion can include the operational reliability of structures being jeopardised, the loss of natural resources and damage to the environment. (Mattsson, 1996)

The significance of zinc in the attempt to minimize the effects of corrosion is great, especially when considering its low abundance in the earth's crust amounting to only 0.013%. Despite this, zinc production is on a large scale, behind only iron, aluminium and copper. Zinc has been used for over a century to protect metallic products and components from the detrimental effects of corrosion. Of the zinc produced, much is used as protection for metals as coatings, in particular steel coatings.

This investigation attempts to model the localized corrosion effects experienced by zinc and zinc alloy coatings in contact with conductive electrolytes, namely the effect of contact with 0.1% and 5% NaCl solutions on the corrosion performance. Micro-scale modelling of the corrosion performance of zinc and zinc alloy coatings can only serve to increase the understanding of the relationship between the microstructure and corrosion performance. Comparison of predictions from a fundamentally derived model, to both experimental results and weathering data would serve to strengthen the validity of any guarantee offered; both for current products and future ones.

Chapter 2

Review of Literature

This chapter considers the following topics integral to this investigation:

- The importance of metallic coatings in the protection of steel.
- Fundamentals of corrosion and associated phenomena are introduced.
- Relevant modelling techniques are described.
- Approaches taken for modelling microstructure and corrosion are considered.

There are many driving factors that contribute to the need to develop a computer model. The purpose of scientific inquiry has always been to gain understanding and control of some part of the universe. Unfortunately, as is the case with the corrosion of metals, real world situations are highly complex. Appreciation and control can be gained via abstraction, replacing the real world with a model (be it physical or mathematical). Knowledge and understanding are prerequisites for the effective implementation of any tool. In order for an abstract physical model to be produced, understanding of the processes gained by empirical means must be combined effectively with known fundamental laws. In order that the relationship between microstructure and corrosion performance of materials be successfully captured by a computer model, properties and exhibited behaviours must be approximated by suitable fundamental laws. (Chapra and Canale, 2002)

Modelling the corrosion processes occuring on a zinc alloy coated steel product, as with any electrochemical process, is motivated by the desire to reduce the experimental effort to design or optimize a product/process. (Prentice, 1991) In order to produce a cost-effective

predictive tool it is important to evaluate the complexity of the situation from which the need arose. Attempting to model the evolution of a complex system through abstraction requires that only the dominant physical and chemical processes are captured within a suitable modelling framework. This ensures that the essential features of the system are retained whilst avoiding unnecessary mathematical complexity. To this end, the problem is considered in terms of three main areas:

1. Zinc and zinc – aluminium steel coatings.
2. Corrosion as an electrochemical process.
3. Modelling and simulation in computational materials science.

2.1 Steel Coatings

When left unprotected, steel will corrode in almost any environment. The corrosion process is a form of oxidation in which the iron within the steel combines with oxygen and reverts to one of its many oxide forms. This process, commonly called "rusting", varies with the alloy content of the steel, its temperature, the presence of moisture and the specific environment. There are many approaches to prevent corrosion and they fall into three categories:

- Increase the percentage of metallic alloys so that the steel is inherently resistant to most corrosion (stainless steel).
- Coat the steel with a barrier sufficient to protect it from oxygen (air), moisture and corrosive atmospheric environments.
- Coat the steel with a material that sacrifices itself preferentially to corrosion until it is consumed, before the iron corrodes.

2.1.1 Organically Coated Steels (OCS)

As described in chapter 1, there exists a great deal of interest in the performance of organically coated steels (OCS) due to their frequent use in wide ranging applications. An OCS product is built up in layers around a steel substrate, as shown in figure 2.1. The

Figure 2.1: Schematic representation of an organically coated steel product.

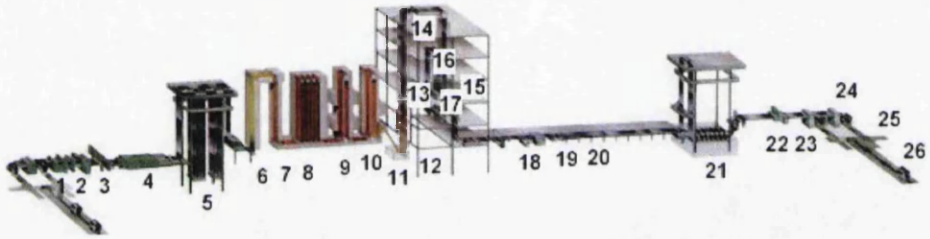

Key: 1. Entry Gauge - 2. Double Cut Shear - 3. Welder - 4. Cleaning - 5. Entry Looping Tower
6. Preheat Furnace - 7. Direct Fired Furnace - 8. Radiant Tube Furnace
9. Gas Jet Cooling - 10. Controlled Cooling - 11. Zinc Pot - 12. Air/Nitrogen Wiping
13. Galvannealing Furnace - 14. Tower Roll Clean - 15. - Quench Tank
16. Water Cooling Dryer - 17. Coating Weight Gauge - 18. Temper Rolling
19. Tension Leveller - 20. Skinpass Mill Dryer
21. Delivery Looping Tower - 21. Electrostatic Oiler - 23. Flying Shear
24. Tension Reel - 25. Coil Cars - 26. Scale and Automatic Shipping

Figure 2.2: Continuous galvanizing line.

thickness of this mild steel is typically between 0.5mm (light gauge) and 0.7mm (heavy gauge) for use in the Colorcoat HPS200® and Celestia® products. The substrate is typically coated first with a zinc or zinc–aluminium coating layer, usually via the hot-dip method. The steel strip is prepared, dipped into a molten bath and finished on a galvanizing line like that shown in 2.2. A chromate based pre-treatment is applied to the zinc–aluminium coating layer which serves to improve adherence for the following layer and also as a corrosion inhibitor. Following the pre-treatment a primer layer is applied, once again adding protection due to it containing corrosion inhibiting pigments. Finally, the organic coating is applied to front and back simultaneously. The top coat is typically 200μm to further increase the barrier

Figure 2.3: Applications of galvanized products.

protection afforded to the substrate but also allows for increased aesthetics due to the custom pigments contained in these layers. The organic coating is a PVC plastisol based paint system in the case of the Colorcoat HPS200® product. The organic coating on the reverse of the OCS is approximately 15μm in thickness and is polyester based. This again acts as a barrier and provides the basis for adhesion to insulation.

2.1.2 Zinc Coatings

For over a century, zinc has enhanced the longevity and performance of steel. Zinc coatings provide the most effective and economical way of protecting steel against corrosion. Zinc coated (galvanized) steel offers a unique combination of positive features including formability, corrosion resistance and recyclability. (Hada, 1998; Trethewey and Chamberlain, 1995; Zhang, 1996) For these reasons, galvanized steel is an ideal material for a multitude of building applications. In the residential market, galvanized steel has particular and cost-effective applications in framing, roofing, rainware (gutters and downspouts), ductwork (heating/cooling and ventilation) and household appliances, as is seen in figure 2.3.

Traditionally zinc coatings are applied to steel via hot dipping, which is the deposition of a hot, liquid metallic coating. Continuous galvanizing is used for the coating of sheet steel, which is subsequently used as the substrate for OCS products. During this process coils of steel are welded end-to-end and fed continuously through a coating facility like that shown in figure 2.2. During the continuous hot-dip process, coils of steel are unwound, joined and fed through cleaning and annealing sections before entering a molten zinc bath at approximately 470°C and at speeds up to 200m/min. As the steel exits the molten zinc

bath, gas jets ("knives") control the coating thickness by "wiping" excess zinc from the steel surface. Once cooled, the zinc surface undergoes a series of mechanical and chemical treatments to satisfy individual customer requirements. These include; surface passivation, oil coatings, corrosion inhibitors, slitting, cutting to length and packaging. The result of coating steel using this process is that there is large scale intermetallic formation at the steel surface, which acts to aid adherence of the coating layer. (Abreu et al., 1999). Unfortunately, a pure zinc coating applied by hot-dipping has low formability due to the formation of a range of iron–zinc intermetallics. These arise from reaction/diffusion occurring at the interface of the molten metal and heated strip.

Improvements in the formability of galvanized coatings can be made via the addition of aluminium to the hot-dip bath. The addition of aluminium serves to regulate the amount and variety of intermetallics. Even at very low levels $\sim$0.15%, the formability of these galvanized steels can be seen to increase. (Gray et al., 1989; Karlson, 1989) This is achieved since the presence of a low amount of aluminium produces a thinner layer of more formable intermetallics ($Fe_2(Al,Zn)_5$).

2.1.3 Galfan Coatings

Galfan is a zinc–aluminium alloy coating with a typical aluminium content 4–5 wt.%. Aluminium additions at these levels have the effect of supressing the development of large-scale intermetallic formation. From the zinc–aluminium equilibrium phase diagram, figure 2.4, it can be seen that this Zn–4.5wt.%Al alloy corresponds to the eutectic composition at 382^{o}C. Under equilibrium conditions the constituents of this alloy may solidify isothermally giving rise to a totally eutectic microstructure. In reality, under non-equilibrium conditions it is the case that the solidification of this alloy will occur below this temperature due to undercooling.

Microstructures of this composition (4.5% Al) solidified on steel substrates can be seen in figure 2.5 where the microstructure is shown through the thickness of the coating layer. From figure 2.5 it can be seen that the microstructure of the Galfan coating observed is dependent upon the cooling rates used during fabrication. The microstructural form most frequently encountered it that shown to the right in figure 2.5. The primary zinc dendrites

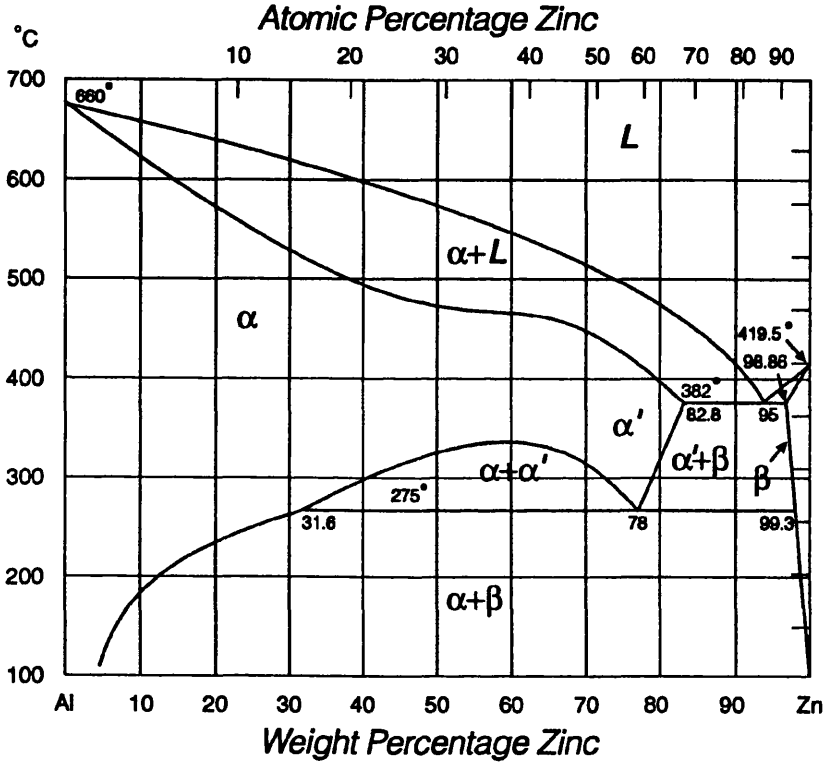

Figure 2.4: Zinc–Aluminium equilibrium phase diagram. (ILZRO, 1993)

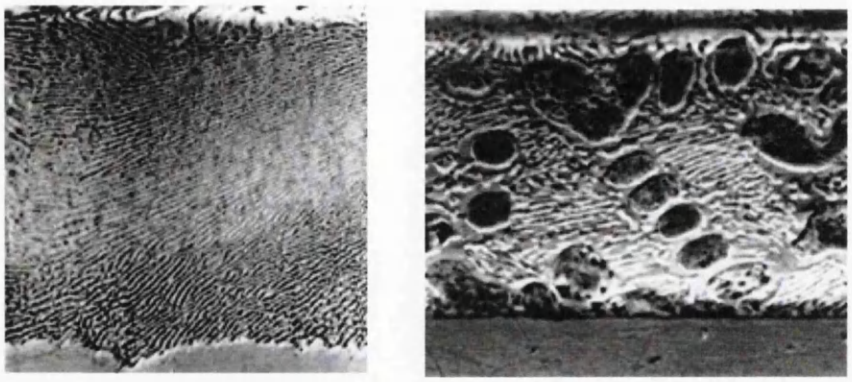

Figure 2.5: (left) Galfan microstructure after minimizing treatment; and, (right) a two-phase, slow-cooled structure. (ILZRO, 1988)

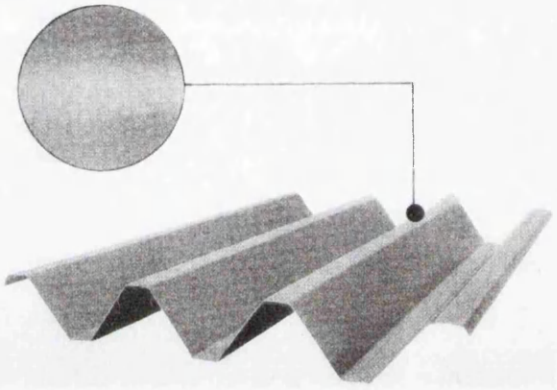

Figure 2.6: Severely profiled Galfan coated sheet typical for construction products. (ILZRO, 1993)

within a Zn–Al eutectic differs greatly to those of predominantly eutectic microstructures, observed at high cooling rates.

The Galfan coating owes its corrosion resistance to its microstructure. It has been shown that Galfan coated steels exhibit a greater corrosion performance that traditional galvanized steels. (Lamberights et al., 1991) The Zn–Al eutectic present in the microstructure of Galfan retains the cathodic properties of zinc, in addition to the formation of a tenacious, adherent passivating aluminium oxide layer, which serves to drive down the rate of corrosion. (Goodwin et al., 1986)

In addition to the increased corrosion protection, also influenced by the eutectic dominated microstructure, is the greater formability and ductility of the Galfan coating than those of traditional galvanizing coatings. (Christian, 1986) This allows for a high degree of

Table 2.1: Composition of the hot–dip zinc bath in the production of Galfan steel coatings. Recommended levels are given.

Element		Composition (wt.%)
Aluminium	Min - Max	4.2 - 7.2
Misch Metals	Min - Max	0.03 - 0.1
Iron	Min - Max	0.005 - 0.075
Silicon	Max	0.015
Lead	Max	0.005
Cadmium	Max	0.005
Tin	Max	0.002
Others, Total	Max	0.04
Zinc	Max	Remainder

profiling similar to that shown in figure 2.6.

2.1.4 Additions to the Hot–Dip Bath

Aside from aluminium, several additions can be added to the hot–dip bath in order to alter the microstructure of the Galfan coating produced. The main addition to the bath could be magnesium, although others can be added at lower volumes, typical compositions are shown in table 2.1.

Effect of Magnesium Additions

The magnesium is added to the zinc bath to increase adhesion by decreasing the fluidity of the molten metal. It has also been seen to reduce the number of areas where the steel is not coated by the alloy, called bare spots, which obviously have an impact on the corrosion protection offered by the coating. Small additions (<0.05 wt.%) reduce the grain boundary irregularities and give a smooth silver–white surface. Larger additions (>0.5 wt.%) lead to eutectic cell coarsening, in addition to the coarsening of other areas of the microstructure due to aluminum–magnesium interactions leading to a poor surface finish of the coating. This will also increase the volume fraction of primary zinc and form a rod eutectic.

Effect of Lead Additions

Additions of lead leads to the formation of spangles, originating from the eutectic lamellar structure. At high production line speeds, lead maintains a continuous coating that has a smooth surface finish. Aside from the environmental considerations, lead has been found to increase inter–granular corrosion.

Effect of Tin Additions

On the whole the addition of tin has been found to be detrimental to the performance of the Galfan coating with regard to inter–granular corrosion. It is also the case that tin is known to cause the delamination of the organic coating applied to the coated steel substrate.

Effect of Silicon Additions

Silicon is added to the hot–dip bath to suppress the reactions between the steel substrate and the zinc coating. This has the effect of minimizing the levels of intermetallics formed, ultimately increasing the ductility and formability of the coated steel produced, since the intermetallics layer is brittle.

Effect of Cadmium Additions

Similarly to lead, cadmium acts as a grain refiner resulting in the formation of spangle structures. Again, a smooth, continuous coating is achieved even at higher production speeds. At levels <0.05 wt.% no significant adverse effects of cadmium are known to affect the microstructure.

2.1.5 Electroplated Zinc Coatings

Another method of applying a zinc coating to steel is through electrodeposition. The process generally comprises three stages, cleaning and degreasing, electroplating and post–treatment. The coating baths used can be acid (chloride) or alkaline (cyanide). Again this can be continuous when dealing with strip steel. The steel coating produced is one of pure zinc without the intermetallic formation that is associated with hot-dip

methods. Benefits of these coatings include; the elimination of pre-finishing processes, good under-paint protection and excellent surface characteristics.

2.2 Corrosion

Originating from the Latin word 'corrodere', which means 'gnaw away', corrosion according to its definition describes a process. (Mattsson, 1996) This process takes place by way of a physiochemical reaction between the material and its environment, which ultimately leads to alterations in the properties of the material. The corrosion of materials is a ubiquitous problem that taxes engineers and scientists alike. The most widely known form of this type of chemical degradation is that of rusting. Rusting is the name given to the atmospheric corrosion of iron (unlike the other transition metals in its group, iron corrodes readily in the presence of oxygen and water) and steel in moist air. Corrosion may assume forms of uniform attack over the whole surface or highly localized attack. The result of the corrosion process is a corrosion effect, which is generally detrimental but can sometimes be useful. Detrimental corrosion effects include; unwanted attacks on a material that produces deleterious consequences for the material's properties, contamination of the environment with corrosion products and functional impairment of the system. The economic impact of this to the community was discussed in chapter 1. An example of useful corrosion effects is the reaction between steel and phosphoric acid to produce a phosphated surface suitable for painting. The processes involved with corrosion are to a large extent electrochemical in nature leading to the deterioration of materials by chemical interaction with their environment.

2.2.1 Classification of Corrosion

The metals used in the construction industry are typical, in that they are thermodynamically unstable in air, since they have previously been extracted from their corresponding thermodynamically stable ores. This is done using energy intensive extraction processes, such as the blast furnace for iron and in the case of aluminium the highly expensive electrolysis process (extraction by passing electricity through cryolite containing alumina). Ores are often oxides, occurring naturally in a chemically combined state. Figure 2.7

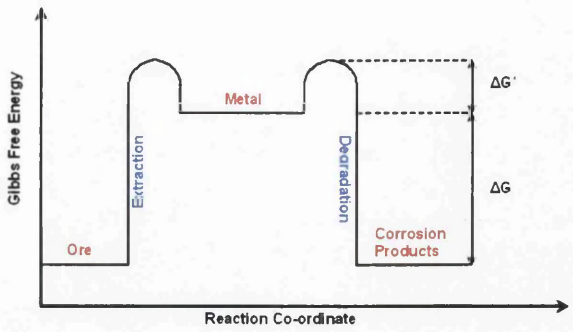

Figure 2.7: Energy profile of the corrosion process.

illustrates the differences in Gibbs free energies between the ore, metallic element and its corrosion products.

From figure 2.7, it is clear that metals in the uncombined state exist at higher energy states than the corresponding ores, denoted by ΔG (kJ mol^{-1}), and the small energy barrier which prevents the thermodynamically favourable reaction proceeding to the corrosion products (similar to the ore, i.e. metallic oxide), denoted by ΔG^*. A result of this is that the surfaces of all metals (with the exception of gold) in air are covered with films.

When such a metal is immersed in an aqueous solution, the oxide film tends to dissolve. Should the solution be sufficiently acidic, the film is totally removed leaving the surface in an 'active' state. The presence of this electrolyte means that the transition in figure 2.7, from the elementary state to a combined condition is lower and this is referred to as 'wet' corrosion. Without the presence of the aqueous solution a large amount of energy is needed for this transformation, which would need to be supplied in the form of heat, and this is referred to as 'hot' corrosion.

2.2.2 Aqueous Metallic Corrosion

'Aqueous' or 'wet' corrosion, is the degradation of a metal in the presence of water and an ionic salt, which combined constitutes an electrolyte. Wet corrosion is the most important issue associated with coated steel products. Wet corrosion provides a lower activation energy, ΔG^*, to proceed to the corrosion products, making the transition shown in figure 2.8 more favourable.

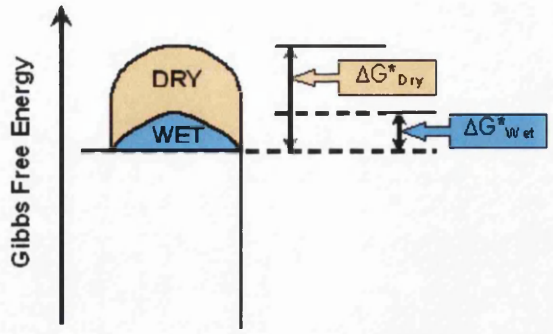

Figure 2.8: Effect of an electrolyte on the activation energy of corrosion.

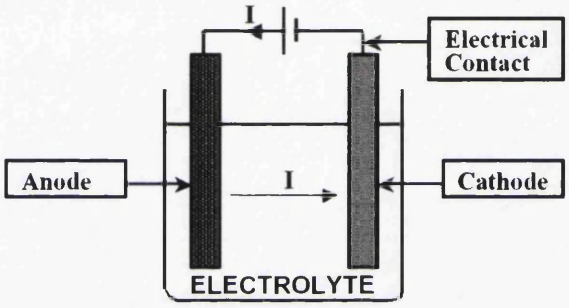

Figure 2.9: Electrochemical cell; the arrows show the direction of the electric current.

An electrochemical reaction is characterized by the fact that it takes place via interfacial electron transfer. This transfer of electrons between species to accomplish change requires the establishment of an electrochemical cell. This cell consists of four constituents:

- Anode, where oxidation occurs, e.g. metal dissolution.
- Cathode, where reduction occurs, e.g. oxygen reduction or hydrogen evolution.
- Electrical Contact, necessary for electron flow between anode and cathode.
- Electrolyte or Aqueous medium (in which anode and cathode are immersed).

If any one of the four components listed is eliminated then corrosion ceases, whereas if the anode or cathode is inhibited then corrosion becomes retarded to an extent. A simple schematic representation of an electrochemical cell set-up is shown in figure 2.9.

When an electrochemical reaction takes place whereby electrons are lost, this is referred to as oxidation. Conversely, when an electrochemical reaction occurs and electrons are gained, this is referred to as reduction. In the case of corrosion, anodic activity involves the oxidation of the metal, therefore the metal atoms lose electrons to form higher oxidation state ions or compounds. Electrons cannot exist freely in a solution in any significant concentration. The electrons emitted in an oxidation reaction must therefore be used up in a simultaneous reduction reaction. In wet corrosion this occurs through oxygen reduction or hydrogen evolution. This kind of process of electron emission and consumption is known as REDOX (REDuction - OXidation) reaction. In corrosion the anodic and cathodic reactions typically occur simultaneously on the same metal surface, where the metal is in contact with the electrolyte. Consequently, the metal surface is the site of both anodic and cathodic activity. In wet corrosion the general anodic reaction to describe metal oxidation and consequent dissolution as aqueous metal ions is,

$$M_{(s)} \rightarrow M^{n+}_{(aq)} + ne^- \tag{2.1}$$

Where M represents a metal atom and n denotes the stoichiometric number of electrons transferred. Cathodic reactions are dependent upon the conditions under which they occur. Under aerobic conditions at near neutral to high pH, oxygen reduction usually occurs,

$$2H_2O + O_{2(g)} + 4e^- \rightarrow 4OH^-_{(aq)} \tag{2.2}$$

The metal ions and hydroxide ions formed through reactions 2.1 and 2.2 tend to inter-diffuse and combine to form visible corrosion product. At very low pH ($<< 7$) the cathodic reaction becomes hydrogen evolution,

$$2H^+_{(aq)} + 2e^- \rightarrow H_{2(g)} \tag{2.3}$$

Anodic and cathodic sites may be physically inseparable on the same surface. However, they may also be spatially distinct provided electrical contact is maintained. The separation of anodes and cathodes on the same metal surface may arise due to:

- Local differences in metal composition.
- Local differences in O_2 concentration.

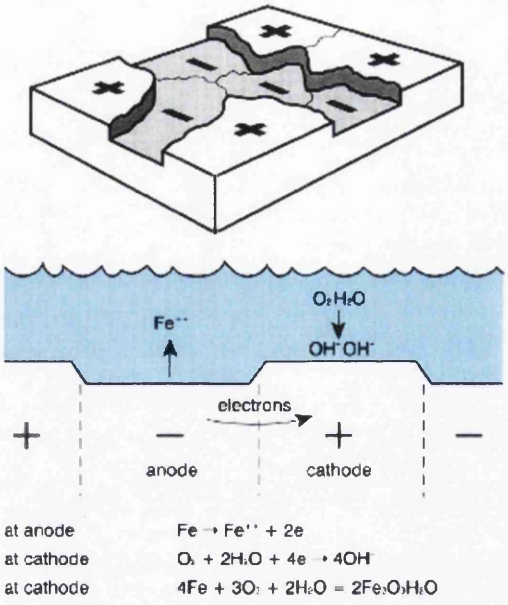

Figure 2.10: Anodic activity and cathodic activity occurring on a single surface.

- Local differences in pH.
- Local differences in permeability of a passive layer.

This is shown in figure 2.10. It is the distance between the anodic and cathodic sites, which determines whether wet corrosion is localized or general corrosion. If the anode and cathode sites are spatially inseparable, then this phenomenon is described as general corrosion. Alternatively, if the anode and cathode sites are spatially distinct then this phenomenon is described as localized corrosion. (Trethewey and Chamberlain, 1995)

2.2.3 Thermodynamics of Corrosion

Electrochemistry has evolved from several disciplines and accordingly conventions relating to electrochemical cells have, historically, reflected this diversity. Electrode reactions are by convention written as reduction reactions regardless of whether they are oxidation or reduction. Another convention is that in conventional current (shown in figure 2.9) the electrons flow in the opposite way to the current experienced in real situations. (Prentice, 1991) As mentioned previously, for corrosion to occur, there must be a negative change in the Gibbs free energy ($-\Delta G$) for the overall reaction. During the corrosion process,

whether on the same surface or not, electrons will flow between the anode to the cathode. This electron flow between anode and cathode leads to a potential difference established between electrodes. When this is the case, each is said to have an electrode potential. This potential difference is that which drives the electrochemical reaction. With this said, it must be the case that the potential difference and Gibbs free energy are related, where each half reaction (as reductions) will have its own electrode potential related by Faraday's Law,

$$\Delta G = -nFE \tag{2.4}$$

Where n is the number of electrons transferred, F is Faradays constant (charge on one mole of electrons = 96,487 C mol^{-1}) and E is the electrode potential (V). The overall Gibbs free energy change would therefore be,

$$\Delta G = \Delta G_1 - \Delta G_2 \tag{2.5}$$

Metals have different electrode potentials, which are a thermodynamic measure of how easy a metal is to extract and also consequently how easily it will corrode. Standard electrochemical series have been measured and documented, again as reduction reactions, which show the electrode potential of metals against a standard hydrogen electrode (S.H.E.). In the case of the S.H.E., the potential of the reduction of protons to hydrogen is set at zero, and so the electrode potentials are arranged around this value as can be seen in table 2.2. Test conditions are standardized, implying a pressure of one atmosphere (atm), a concentration 1M (mol dm^{-3}) and room temperature (298K).

The more positive the reduction electrode potential in table 2.2, the more stable the metal. Conversely, the more negative relative to the S.H.E. potential, the less stable the metal indicating a greater likelihood of corrosion.

In conditions other than those outlined above (standard temperature, pressure and concentration) it is likely that the electrode potentials measured will deviate to some extent from their standard values. A greater understanding of this arose from several key contributions from Walter Nernst at the turn of the twentieth century, which provided the relationship relating non-standard conditions,

$$E_{eq} = E_0 + \frac{RT}{nF} \ln \left(\frac{[products]}{[reactants]} \right) \tag{2.6}$$

Table 2.2: An Electrochemical Series.

Electrode Reaction	Electrode Potential vs SHE $(V)^0/V$
$Au^+ + e^- = Au$	+1.68
$Pt^{2+} + 2e^- = Pt$	+1.20
$Hg^{2+} + 2e^- = Hg$	+0.85
$Ag^+ + e^- = Ag$	+0.80
$Cu^{2+} + 2e^- = Cu$	+1.68
$2H^+ + 2e^- = H_2$	0.00
$Pb^{2+} + 2e^- = Pb$	-1.13
$Sn^{2+} + 2e^- = Sn$	-0.14
$Ni^{2+} + 2e^- = Ni$	-0.25
$Cd^{2+} + 2e^- = Cd$	-0.40
$Fe^{2+} + 2e^- = Fe$	-0.44
$Cr^{3+} + 3e^- = Cr$	-0.71
$Zn^{2+} + 2e^- = Zn$	-0.77
$Al^{3+} + 3e^- = Al$	-1.67
$Mg^{2+} + 2e^- = Mg$	+2.34
$Na^+ + e^- = Na$	+2.71
$Ca^{2+} + 2e^- = Ca$	+2.87
$K^+ + e^- = K$	+2.87

Termed the Nernst equation. E_0 (V) is the standard condition electrode potential, E_{eq} (V) is the electrode potential in non-standard conditions, T is the non-standard temperature (K) and R is the molar gas constant. $[products]$ and $[reactants]$ are concentrations in the aqueous medium. For a RedOx couple ($Ox + ne^- \rightleftharpoons Red$) the equation is,

$$E_{eq} = E_0 + \frac{RT}{nF} \ln\left(\frac{[Ox]}{[Red]}\right) \tag{2.7}$$

Where $[Ox]$ and $[Red]$ are concentrations of the oxidized and reduced forms of a RedOx couple.

2.2.4 Kinetics of Corrosion

If a thermodynamic driving force exists for a corrosion process, then it will take place. However, the rate of corrosion can vary within wide limits. Assessment as to the extent of corrosion can be expressed as the change in mass of the material, the depth of the corrosion effect or the number of oxidation sites. Also changes in the materials properties may be influenced by corrosion products, which can be used to describe the corrosion rate. As corrosion is a process involving electron transfer, (equations 2.1, 2.2 and 2.3) the rate of corrosion can be determined by the quantity of electrons transferred in a period of time. Since current, i, is a measure of electron flow between anode and cathode, the corrosion rate, expresses as the rate of change in metal mass $\left(\frac{dM}{dt}\right)$, is given by,

$$\frac{dM}{dt} = \frac{i}{nF} \tag{2.8}$$

Where i is the current flow (A). During corrosion the Gibbs free energy (ΔG) of the material corroding is reduced, whilst the products are formed. In addition, the rate of corrosion is governed by the Gibbs free energy of activation, ΔG^*. This is represented by the following Arrhenius relationship,

$$k = A \exp\left(\frac{\Delta G^*}{RT}\right) \tag{2.9}$$

Thus the corrosion rate is related to the current, which in turn is related to ΔG^* by an exponential relationship with lower ΔG^* of activation resulting in faster rates of corrosion.

2.2.5 Electrode kinetics

Proportionality exists between the net rate of an electrode reaction, v, and the current, i and thereby the current density, j,

$$v = \frac{dM}{dt} = \frac{i}{nFA} = \frac{j}{nF} \tag{2.10}$$

Where $\frac{dM}{dt}$ describes the reaction rate (mol $s^{-1}m^{-2}$), i is the current (A), A is the area (m^2) and j is the current density (Am^{-2}).

It is also known that for a given electrode process, current does not flow in some potential regions, yet it flows to variable degrees in others. (Bard and Faulkner, 1980) The reaction rate is a strong function of potential, and thus potential–dependent rate constants are required for an accurate description of interfacial charge transfer dynamics. For a reversible reaction at equilibrium, the net conversion rate is zero. In the limit of equilibrium the kinetic relationships must collapse to relations of the thermodynamic form, otherwise the kinetic picture cannot be accurate. Most rate constants observed in experimentation of solution-phase reactions vary with temperature in a common fashion; nearly always, $\ln k$ is linear with $1/T$. This behaviour leads to rate constants being expressed as an Arrhenius form,

$$k = A \exp\left[\frac{-\Delta H^*}{RT}\right] \tag{2.11}$$

Where ΔH^* is the activation enthalpy (kJ mol^{-1}) and here A is a pre–exponential factor. In an electron transfer reaction, the rearrangement of the ionic atmosphere is a fundamental step, and thus it is useful to include the activation entropy ΔS^*. (Brett and Brett, 1993) The reorientation and rearrangement causes the separation between the energy levels to be different than in the initial state. If the pre-exponential factor, A, is written as,

$$A = A' \exp\left[\Delta S^*/R\right] \tag{2.12}$$

Then,

$$k = k' \exp\left[\frac{-(\Delta H^* - T\Delta S^*)}{RT}\right] = k' \exp\left[\frac{-\Delta G^*}{RT}\right] \tag{2.13}$$

Where enthalpy, H, has the units kJ mol^{-1} and entropy, S, has the units J K^{-1}. From thermodynamics $\Delta H - T\Delta S = \Delta G$ (kJ mol^{-1}), the standard free energy of activation, and k' is a constant. Therefore the kinetic theory holds in this case.

2.2.6 Potential and the Phenomena of Polarization

When corroding freely in contact with an electrolyte, a metal will adopt a "free corrosion potential" which is a mixed potential, at which the rate of anodic dissolution of the electrode is equal to the rate of the cathodic reactions taking place, resulting in no net current flow. A corrosion current is the metal dissolution current at the free corrosion potential. Corrosion potential and corrosion current are two important parameters that connect the fundamental electrochemistry and the practical corrosion behaviour of metals. The value of the corrosion potential indicates the state of a corroding metal while the current reflects the instantaneous corrosion rate at the time of measurement. The basic theory of the relationship between corrosion rate and electrochemical polarization resistance was formulated in the 1950s. According to the theory, for a corroding metal there are two coexisting electrochemical reactions: the dissolution–deposition of the metal, $M^{n+} + ne \rightarrow M$, and a reduction–oxidation of a species in the electrolyte, Z^{n+}. (Zhang, 1996)

When a metal is exposed to an aqueous solution containing ions of that metal, at the surface of the metal, both oxidation of the metal (equation 2.1), and a reverse reduction of metal ions as in equation 2.14 occurs,

$$M^{n+}_{(aq)} + ne^- \rightarrow M_{(s)} \tag{2.14}$$

Because an exchange of electrons takes place the rate of the two reactions can be given by two different current densities. i_a and i_c. At equilibrium (E_0),

$$i_a = i_c = i_0 \tag{2.15}$$

And,

$$i_a - i_c = 0 \tag{2.16}$$

Where i_0 is called the exchange current density (Am^{-2}). This assumes that no other electrode reactions take place at the electrode surface. In this case no overall corrosion is taking place. The electrode potential, the so-called equilibrium potential, can thus be calculated according to the Nernst equation (equation 2.6). Applying a net current i, to the surface means that $i_a \neq i_c$. The applied net current density will in actual fact be the difference between i_a and

i_c. When current is applied to the electrode surface the electrode potential is changed and takes on the value E_i. In this instance the electrode is said to be *polarized.* The change in electrode potential is called polarization (or overpotential) and is usually designated by the Greek letter eta, η:

$$\eta = E_i - E_0 \tag{2.17}$$

The polarization (corrected for possible errors in measurement) can be divided into two main components:

- Concentration polarization, caused by the difference in concentration between the layer of electrolyte nearest the electrode surface (the diffusion boundary layer), and the bulk of electrolyte.
- Activation polarization, caused by a retardation of the electrode reaction.

The polarization of an anode is always positive, and that of a cathode always negative, illustrated in figure 2.11.

Polarization thus reduces the terminal voltage of a electrochemical cell, as the current drawn from the cell increases. In a case where polarization can be assigned to a definite electrode reaction, then one can refer to it as overpotential. As can be seen from figure 2.11, the anodic and cathodic currents vary exponentially with this polarization potential, η, termed overpotential, due to the relationship between corrosion rate/current and energy/potential (sections 2.2.3 and 2.2.4). This can be expressed thus:
For the anodic reaction, $M_{(s)} \rightarrow M^{n+}_{(aq)} + ne^-$,

$$i_a = i_0 \exp\left[\frac{(1-\alpha)nF}{RT}(E_i - E_0)\right] \tag{2.18}$$

For the cathodic reaction, $M^{n+}_{(aq)} + ne^- \rightarrow M_{(s)}$,

$$i_c = i_0 \exp\left[\frac{(-\alpha)nF}{RT}(E_i - E_0)\right] \tag{2.19}$$

Where i_0 is the current at equilibrium and α is the asymmetry factor. The relationships shown by equations 2.18 and 2.19 can be seen in figure 2.12. As the overpotential is increased the anodic current increases exponentially the cathodic current decreases exponentially.

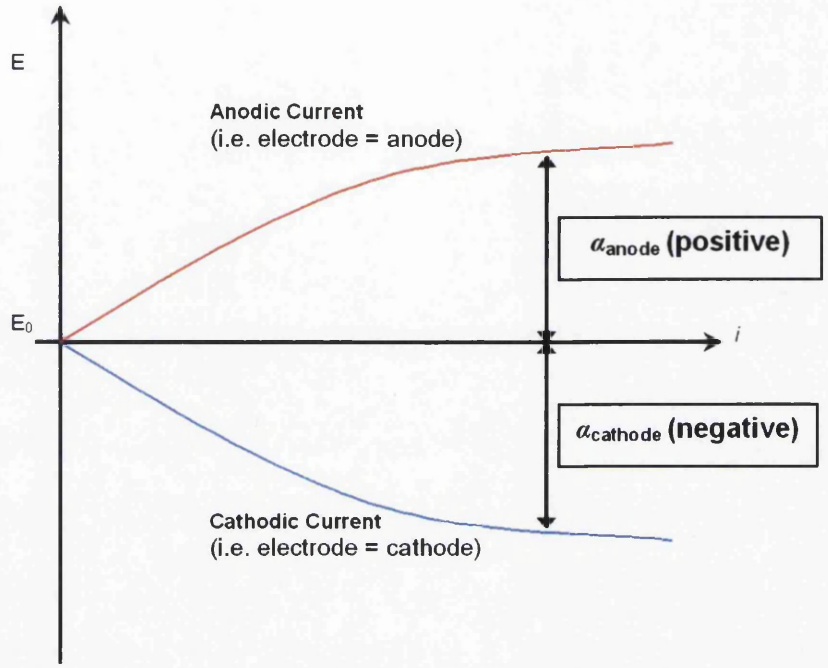

Figure 2.11: Phenomena of polarization.

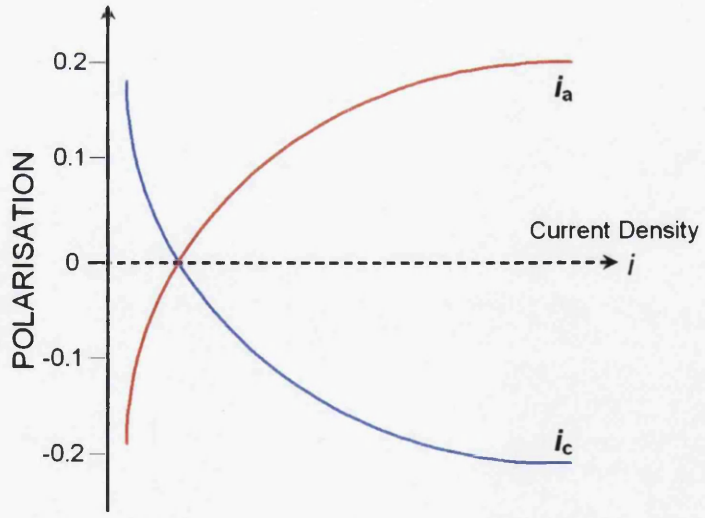

Figure 2.12: Plot of corrosion current vs. potential for the anode reaction of metal dissolution.

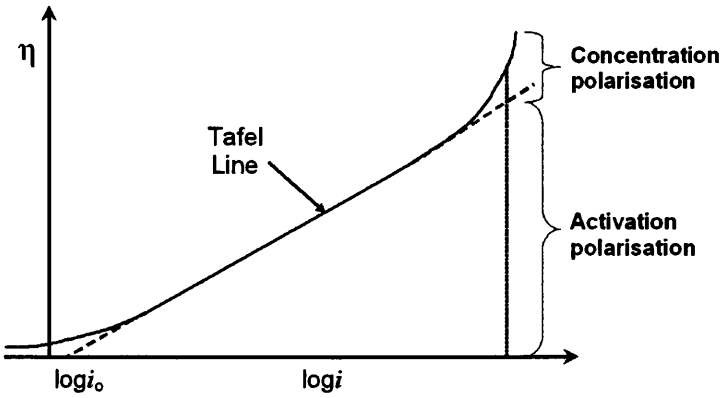

Figure 2.13: Polarization (η) as a function of logarithm of current density (i); the continuous line indicates the total polarization, i_0= exchange current density.

Activation polarization at low polarization values is directly proportional to the current density. At higher polarization values ($>$ *circa* 30-50mV) there is, on the other hand, a linear relationship between activation polarization and the logarithm of the current density.

Current is often limited wholly or partially by the rate at which the electro–reactants are transported to the electrode surface. In the case of low currents and efficient stirring, mass transport is not a factor in determining the current. Instead it is controlled strictly by the interfacial dynamics. The current is often related exponentially to the overpotential, η. That is,

$$i = a' e^{\frac{\eta}{b'}} \tag{2.20}$$

Or, as given by Tafel in 1905,

$$|\eta| = a + b \log_{10} i \tag{2.21}$$

Where a and b are the Tafel parameters and b is the 'Tafel slope'.

Due to this relationship, the polarization curves are represented as a logarithmic function ($\log_{10} i$). These linear representations are referred to as Tafel lines. Concentration polarization is negligible at low current densities, but can be dominating at high current densities, as is shown in figure 2.13.

The combination of the Tafel lines for both the oxidation and reduction of a metal occurring at an electrode is shown in figure 2.14. This simple representation is referred to as

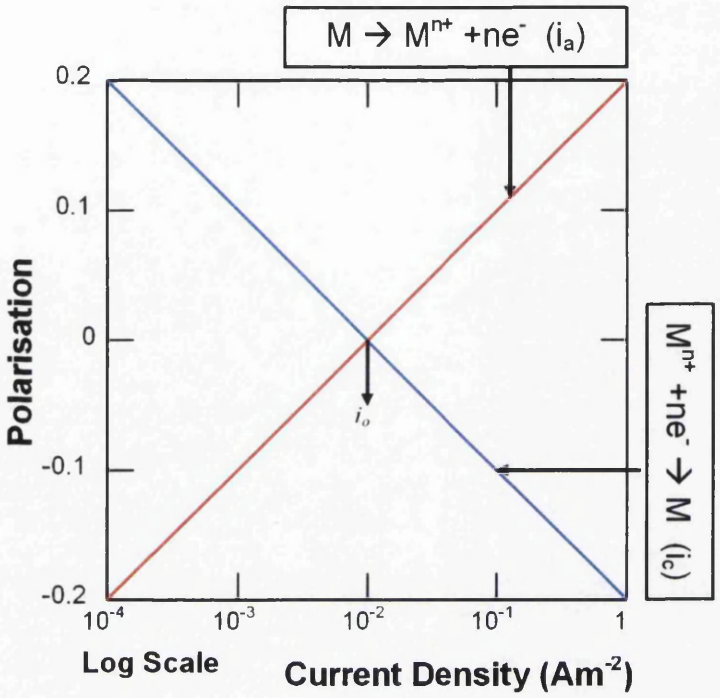

Figure 2.14: Tafel plot for the metal oxidation and reduction reaction equations.

a Tafel plot and presents important information about the rates of electrochemical corrosion. The point of intersection, labelled i_0 in figure 2.14, is the exchange current density. At this point no overall corrosion is taking place and this occurs at the equilibrium potential as predicted by equation 2.6.

The corrosion process in this situation is reversible since there is a forward path and a corresponding backward path. The forward component proceeds at a rate v_f that must be proportional to the surface concentration of the oxidized species. The concentration is expressed, at a distance x from the surface and at a time t, as $C_O(x,t)$; hence the surface concentration ($C_O(0,t)$) is the rate constant k_f.

$$v_f = k_f C_O(0,t) = \frac{i_c}{nFA} \tag{2.22}$$

Since the forward reaction is a reduction, there is a cathodic current i_c proportional to v_f. Similarly, there is a backward reaction,

$$v_b = k_b C_R(0,t) = \frac{i_a}{nFA} \tag{2.23}$$

Where i_a is the anodic component to the total current. Thus the net reaction rate is

$$v_{net} = v_f - v_b = [k_f C_O(0,t)] - [k_b C_R(0,t)] = \frac{i_c}{nFA} \tag{2.24}$$

And the exchange current,

$$i - i_c - i_a = nFA\,[k_f C_O(0,t) - k_b C_R(0,t)] \tag{2.25}$$

Heterogeneous reactions are described differently to homogeneous reactions. An example of this is that the reaction rates in heterogeneous systems refer to unit interfacial area, and hence they have dimensions of mol $s^{-1}m^{-2}$. Since the interface can respond to only its immediate surroundings, the concentrations entering rate expressions are always surface concentrations, which may differ from those of the bulk of the solution phase. It is also clear that any species participating in a heterogeneous redox reaction will have kinetic behaviour that is strongly influenced by the interfacial potential difference.

For electrode reactions where potential differences can be controlled, the way in which the k_f and k_b depend upon potential is given by,

$$k_f = k_0 \exp\left[-\alpha n f(E - E_0)\right] \tag{2.26}$$

And,

$$k_b = k_0 \exp\left[(1-\alpha) n f(E - E_0)\right] \tag{2.27}$$

Where $f = F/RT$, and k_0 and α are adjustable parameters called the standard rate constant and the transfer coefficient respectively. This result is known generally as the Butler–Volmer formulation of electrode kinetics in honour of the pioneers in this area. (Butler, 1924; Gruz and Volmer, 1930)

2.2.7 Pourbaix Diagrams

Marcel Pourbaix identified three states of corrosion. A metal is deemed to be in a corroding condition when the concentration of its ions is 10^{-6}mol dm^{-3}. If the concentration of the metal ions in solution is below this value, then the metal is in a condition of immunity. A state of passivity exists for a metal once an insoluble layer of corrosion products removes contact

between the metal surface and the electrolyte, thus preventing further corrosion. Pourbaix diagrams plot potential versus pH, a parameter also of great importance to corrosion processes. The Pourbaix diagram enables the determination by means of potential and pH measurements as to whether a metal surface is in a region of immunity (where the tendency for corrosion is nil) or not. Therefore a metal may be in a region where the tendency for corrosion is high, or in a region where the tendency for corrosion may exist, but where there is also a tendency to form a protective covering to practically stop corrosion (passivity). A pertinent example of multiple reactions for the corrosion of a metal is zinc. The corrosion of zinc is characterized by five important reactions.

Usual anodic reaction,

$$Zn_{(s)} \rightarrow Zn^{2+}_{(aq)} + 2e^- \tag{2.28}$$

The formation of zinc hydroxide that is insoluble,

$$Zn_{(s)} + 2H_2O_{(l)} \rightarrow Zn(OH)_{2(s)} + 2H^+ + 2e^- \tag{2.29}$$

The formation of a soluble zincate from zinc metal,

$$Zn_{(s)} + 2H_2O_{(l)} \rightarrow ZnO^{2-}_{2(aq)} + 4H^+ + 2e^- \tag{2.30}$$

Which all involve electron transfer. In addition; The dissolution of zinc hydroxide by acid,

$$Zn(OH)_{2(s)} + 2H^+ \rightarrow Zn^{2+}_{(aq)} + 2H_2O_{(l)} \tag{2.31}$$

And dissolution of the zinc hydroxide by alkali,

$$Zn(OH)_{2(s)} \rightarrow ZnO^{2-}_{2(aq)} + 2H^+ \tag{2.32}$$

Both of which involve protons and the position on the Pourbaix diagram will obviously be influenced by the pH of the system. The lines on the Pourbaix diagram are calculated using the Nernst equation, for the reactions outlined. The correlation of the dependence of pH and the potential of each electrode versus a standard hydrogen reference electrode can be seen in the resultant Pourbaix diagram in figure 2.15, with the index of the reactions labelled on their corresponding lines.

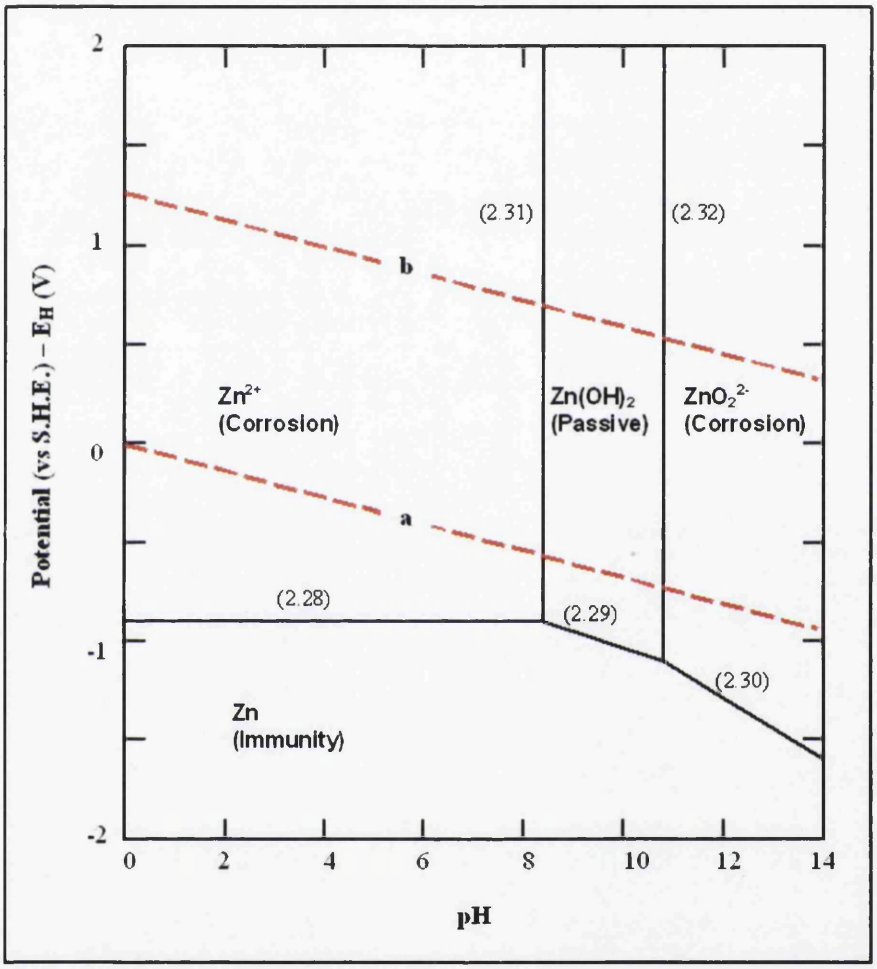

Figure 2.15: The Pourbaix Diagram for Zinc; the band between the dashed lines *a* and *b* is the stability domain of water.

It must be noted that Pourbaix diagrams are constructed (calculated) from thermochemical data for the pure metals, oxides, hydroxides and metal ions. (Pourbaix, 1995) They do not take into account complexation reactions involving electrolyte derived species, e.g. Cl^-, SO_4^{2-} etc. Consequently, Pourbaix diagrams are only completely accurate for "non-complexing" electrolytes. Regions of passivity may be significantly reduced in the presence of 'aggressive' anions such as Cl^-. It is important to note that the major cause of corrosion of passive metals is the failure of the passivating layer to reform following its breakdown. (Isaacs, 1989)

2.2.8 Evans Diagrams

In a corrosion cell, both anodic metal dissolution and cathodic oxygen reduction occur simultaneously. The potential and current of the resulting system can be displayed in one diagram incorporating the relevant Tafel data for the individual electrode reactions. Figure 2.16 shows the anodic reaction of metal dissolution reaction, and completing the corrosion cell is the cathodic reaction of the oxygen reduction reaction.

The diagonal dashed lines shown in figure 2.16 are usually omitted since these play no part in the corrosion process, and represent the metal reduction and hydroxide oxidation. During the early stages of corrosion, the system will rapidly balance itself so that the rates of metal oxidation (dissolution) and oxygen reduction balance one another and the potential adjusts accordingly. At the point of intersection in figure 2.16, the anodic and cathodic processes are occurring at equal rates. If this were not the case, a build up of electrons would result in the alteration of the overpotential until such a situation described previously was to be reached. Also shown in figure 2.16, is the extraction of i_{corr} and E_{corr} values. As discussed previously the corrosion rate can be described as the corrosion current, i_{corr}. The potential adopted by the corroding system, E_{corr}, differs from those equilibrium potentials predicted from the Nernst equation.

2.2.9 Passivity and the Breakdown of Passivity

Passivation is a process in which the metal surface transforms from an active state to an inactive state owing to the formation of a barrier layer. Passivation can be simplistically

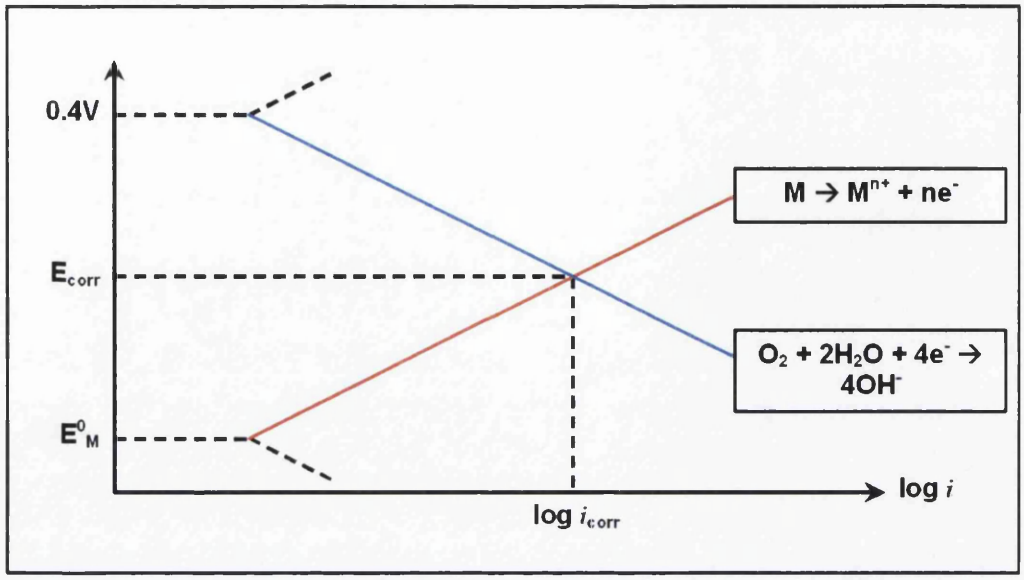

Figure 2.16: Generic Evans Diagram.

characterized by an anodic polarisation curve, as shown in figure 2.17. Whilst in the active state, the metal electrode dissolves according to the reaction $M \rightarrow M^{n+} + ne^-$, and the dissolution current increases sharply with increasing potential.

At a certain potential value, denoted by the passivation potential E_p in figure 2.17, the current stops increasing and starts decreasing rapidly to much lower values, marking the onset of passivity. The current on the passivated surface, called the passivation current, i_p in figure 2.17, can be several orders of magnitude smaller than that on an active surface at the same potential. With further increase of the potential beyond a certain value, E_b, the current may start to sharply increase, and the electrode is said to be in a transpassive state. This sharp increase in current is either associated with the breakdown of the passive film, leading to severe dissolution of the electrode, usually localized, or with the onset of another reaction such as oxygen evolution. (Zhang, 1996) This sequence of changing states of the surface of the metal are represented graphically in figure 2.18, with the resulting state being pitting at the surface, a highly localized form of corrosion. When this transition is associated with the breakdown of the passive film, E_b is called the breakdown potential. This critical potential can also be termed the pitting potential since localized corrosion, such as pitting, generally occurs above the breakdown potential.

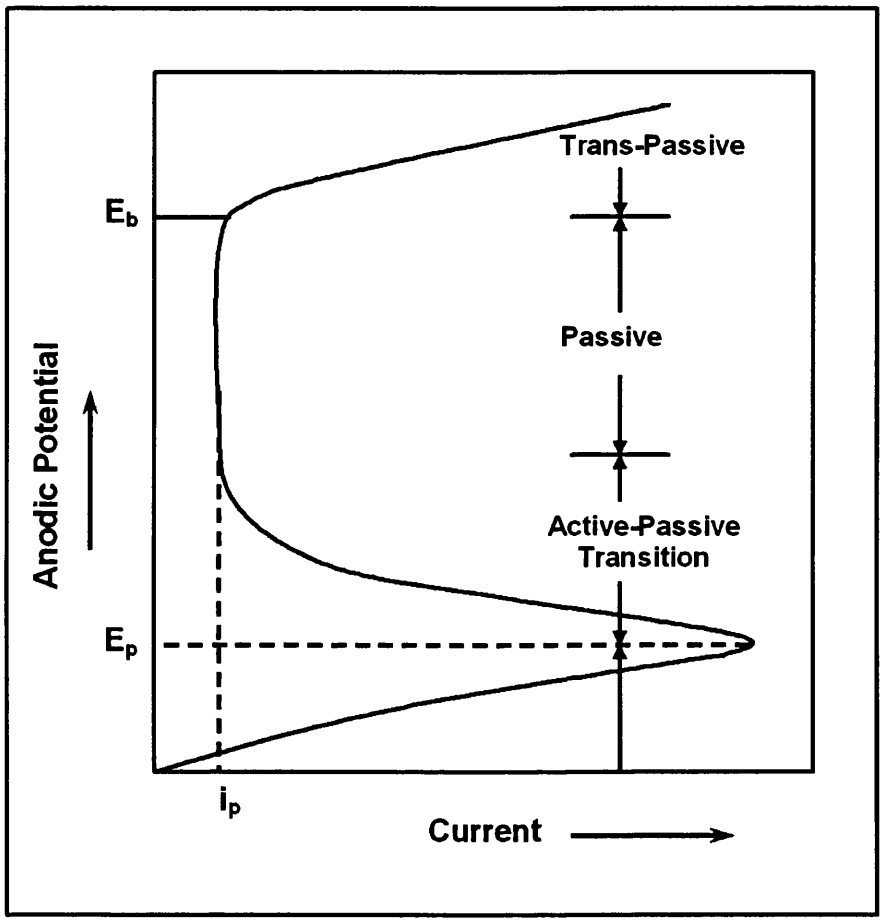

Figure 2.17: Schematic plot of a typical current–potential curve showing the transition from the active to the passive state of a metal.

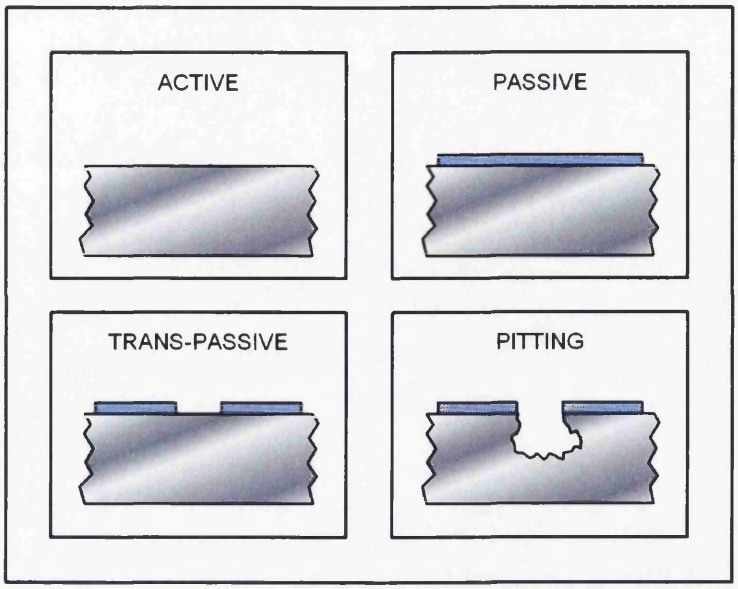

Figure 2.18: Stages in the breakdown of passivity. (Worsley, 2001)

Generally, passivation occurs when the dissolution of a metal produces a situation in which the solubility of a salt, or hydroxide in the electrolyte near the electrode surface is exceeded and a compact solid film is formed. As a result of the film formation, ions must move from the metal phase into the surface film in order for further dissolution of the metal to take place. At least three processes are involved in the dissolution on the passivated electrode:

- Transfer of metal ions from the metal phase into the surface film.
- Transfer of ionic species from the solution phase into the surface film.
- Transfer and hydration of metal ions across the film/solution interface.

The last process is the dissolution of the film and determines, in general, the passivation current, i_p, which equals the net corrosion rate of the metal in the passive state.

2.3 Localized Corrosion

Existing in many forms, often difficult to detect practically, localized areas of corrosion are often detrimental to component performance in service, since prediction of, and prevention

against this type of corrosion is extremely difficult. Localized forms of corrosion are a particular problem for coated steels since compositional differences and physical aspects of the hot dipping procedure can precede the onset of localized corrosion. The occurrence of localized corrosion is manifest proof that anodic surface area can be much smaller than the corresponding cathodic site. The S_a/S_c ratio, or degree of localization can be an important driving force of all localized corrosion problems since this corresponds to equal anodic and cathodic absolute currents, and therefore activities.

In localized corrosion the corrosive micro-environments encountered can be very different from that experienced in the bulk environment (aqueous metallic corrosion). It is these differences in the process of localized corrosion (the initiation, propagation and ultimately the termination of, for example, pits) that complicate the prediction process. In general, small anodic areas lead to severe corrosion problems with low detection ability.

The form of corrosion can be defined according to the nature of the corrosion, the effect of the corrosion on surface morphology, or the effect on bulk properties.

2.3.1 Dissimilar Metallic Corrosion

Often referred to as 'galvanic corrosion' or 'bimetallic corrosion', dissimilar metallic corrosion can simply be defined as the corrosion that occurs as a result of one metal being in contact with another in a conducting, corrosive environment. (Oldfield, 1988) Galvanic corrosion arises from anodic activity on one of the coupled metals and is directly related to the galvanic current by Faraday's law, equation 2.4. As previously described, a particular metal will adopt a characteristic free corrosion potential, E_{corr}, in a given electrolyte. Similar to the standard electrode reduction potentials measured under extremely controlled conditions for pure metals seen in table 2.2, tabulated forms of free corrosion potentials exist which are of more practical use. These are shown in figure table 2.3, for a given range of metals in seawater that are known as 'electrochemical' or 'galvanic' series.

Values are more likely to be quoted as a range rather than a single value since different alloys interact differently with different seawater environments. Dissimilar metallic corrosion occurs when two or more metals occupying dissimilar positions in such a series are immersed in an electrolyte such as seawater. Stimulated by the potential difference

Table 2.3: The galvanic series for a range of metals in seawater.

Metal	Free Corrosion Potential (V) vs SCE
Magnesium	-1.63
Zinc	-1.05
Beryllium	-0.97
Mild Steel	-0.66
Copper	-0.34
Lead	-0.21
Silver	-0.13
Titanium	0.00
Platinum	+0.22

that exists between the two metals, the more noble material (more negative E_{corr}) acts as a cathode where some oxidizing species is reduced, the more active metal, which is the focus of corrosion and corrodes, acts as the anode.

Under a galvanic corrosion condition, the simultaneous additional corrosion taking place on the anode of the couple is called the local corrosion or the self-corrosion. The local corrosion may or may not equal the corrosion taking place when the two metals are not electrically connected, called the normal corrosion. The difference between the local corrosion and normal corrosion is called the difference effect and may be positive or negative owing to the conditions experienced.

Compared to normal corrosion, galvanic corrosion is generally more complex owing to the fact that, in addition to material and environmental factors, it involves geometric factors. The fundamental relationship in galvanic corrosion is described by Kirchhoff's second law:

$$E_c - E_a = IR_e + IR_m \tag{2.33}$$

Where R_e is the resistance of the electrolytic portion of the galvanic circuit, R_m is the resistance of the metallic portion, E_c is the effective (polarized) potential of the cathodic member of the couple, and E_a is the effective (polarized) potential of the anodic member. Generally R_m is very small and can be neglected. E_a and E_c are functions of the galvanic current I; hence the potential difference between the two metals when there is a current flow

through the electrolyte does not equal the open-circuit potential. It is important to note that E in this case is, $E = E_{eq} - \eta$. (Zhang, 1996)

In addition to the area effect associated with a small S_a/S_c, accelerated corrosion due to galvanic effects is usually greatest near the junction of the two metals, with attack decreasing with increasing distance from that point. The distance affected depends upon the conductivity of the solution.

2.3.2 Pitting Corrosion

Pitting corrosion is a form of highly localized attack that results in holes in a corroding metal, thus altering the surface morphology. It is a serious type of corrosion, though the extent of the reaction may be small, the damage may be severe. It is considered more dangerous because it is difficult to detect, predict and design against. Generally, a pit may be described as a cavity or hole whose surface diameter is about the same or less than the depth. This type of localized attack is usually instigated from a scratch or some other discontinuity on a metal surface such as emerging structural dislocations or compositional heterogeneities. This type of corrosion generally takes place in corrosion cells with clearly separated anodic and cathodic sites. The anode is situated in the pit and the cathode usually on the surrounding surface. A characteristic feature is that pitting generally occurs on passive metals and alloys when the thin surface film breaks down locally and doesn't reform. This situation usually occurs in an electrolyte that contains aggressive anions, e.g. chloride ions, which cause local breakdown of the passive surface.

Another feature of pitting is the existence of a threshold potential which represents the onset of pitting. This is graphically represented in figure 2.17 and passivity and its consequent breakdown discussed in section 2.2.9. The susceptibility of a metal or alloy to pitting can be evaluated by several methods:

- Determination of the characteristic pitting potential,
- Determination of a critical temperature of pitting,
- Measurement of pit density,
- Evaluation of the size and depth of the pits, and

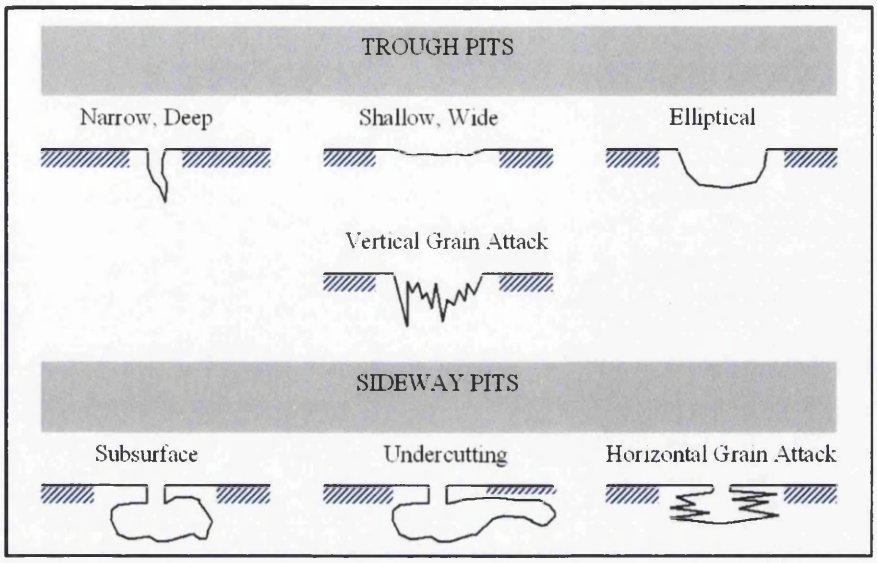

Figure 2.19: Classifications of pitting corrosion commonly encountered. (Mattsson, 1996)

- Determination of the critical concentration of aggressive ions.

Pitting provides an excellent example of the way in which crystal defects influence corrosion behaviour. Apart from loss of localized thickness, pits can be harmful by acting as stress raisers. Fatigue and stress corrosion cracking may initiate at the base of prevailing pits.

The microstructure of metals and alloys are of grains separated by grain boundaries. A specific type of surface irregularity that may lead to pitting is intergranular corrosion. This is when grain boundaries are attacked due to the presence of precipitates in these regions, since grain boundaries are often preferred sites for precipitation and segregation. The precipitates have their own distinctive thermodynamic energy and as such a corrosion cell can be set-up between these and the bulk material. This difference in nobility leads to the localized corrosion known as 'intergranular' corrosion at grain boundaries in polycrystalline materials.

Pitting corrosion is a common denominator for all types of localized attack and can take many shapes, depending on such factors as the composition of the corroding surface, orientation of grains and presence of secondary phases. Various forms of pitting can be seen in figure 2.19.

There are many similarities between pitting corrosion and crevice corrosion since they

are both cases of localized corrosion existing in restricted environments. The process of pitting consists of two main processes:

- Pit initiation → Passive film breaks down.
- Pit propagation → Activated sites propagate.

It is in the initiation stage where pitting can be distinguished from crevice corrosion. The initiation of a pit occurs when electrochemical or chemical breakdown of a passive layer exposes a small local site in a metal surface. The pit grows if the high current density involved in the repassivation process does not prevent the formation of a large local concentration of metal ions produced by dissolution at the point of initiation. If the rate of repassivation is not sufficient to suppress pit growth, two new conditions develop. Firstly, the metal ions produced by the breakdown processes are precipitated as solid corrosion products (such as oxides or more usually hydroxides), which usually cover the mouth of the pit due to the diffusion paths. This covering over of the pit restricts the entry or exit of ions in or out of the pit and allows the build up of hydrogen ions through hydrolysis of the metal cations. The concentration of H^+ increases because the H^+ ions cannot readily diffuse out from the confined volumes involved. Due to the necessity for diffusion of these H^+ ions in order to maintain charge neutrality in the pit, the solution in the pit becomes highly acidic. High concentrations of ions in addition to a low oxygen concentration contribute to a situation in which repassivation is extremely difficult, thereby the rate of pit growth accelerates.

Pitting corrosion propagates itself by the shrouding of the pit with the corrosion products. The corrosion products form a film over the pit, which assists in preventing oxygen getting to the site and stabilizing it. Consequently, many pits initiate on the surface but quickly die because they cannot cover themselves effectively. These are unstable pits. Pits that survive the nucleation process are known as metastable pits since their continued survival is dependent on their maintaining the continuity of the necessary oxide layer. If the covering over the pit ruptures then the pit will die. It is only when the pits become stable that the corrosive attack becomes potentially damaging. The various states of the pits are described graphically in figure 2.20.

Whilst some form of pitting attack is almost inevitable in inhomogeneities in the surface

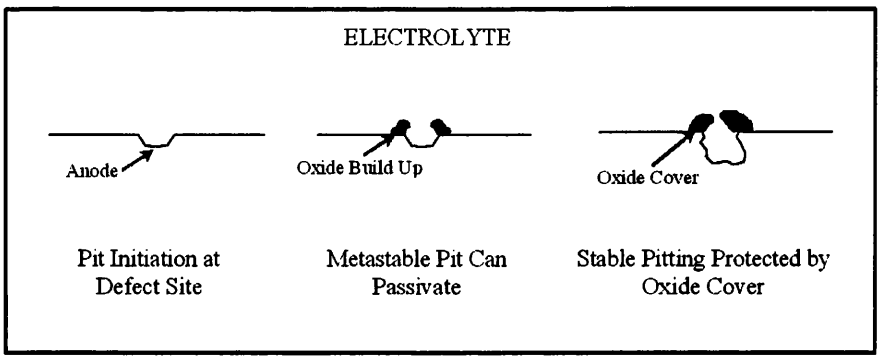

Figure 2.20: Propagation of pitting via shrouding with corrosion product. (Worsley, 2001)

of the metal, pitting corrosion can to a certain extent be prevented by the preparation of the surface to avoid highly probable initiation sites.

2.3.3 Differential Aeration and Crevice Corrosion

Crevice corrosion results when a proportion of a metal surface is shielded in such a way that it has limited access to the surrounding environment. Such surrounding environments contain damaging corrosion species, usually chloride ions. The environment that eventually forms in the crevice is similar to that precipitated corrosion product that covers a pit. Similarly, an electrochemical corrosion cell is formed from the couple between the unshielded surface, and the crevice interior that is exposed to an environment with a lower oxygen concentration compared with the surrounding environment (differential aeration). This combination of being the anode of the corrosion cell and existing in an acidic, high chloride environment where repassivation is difficult, makes the crevice interior subject to corrosive attack.

The conditions resulting from crevice corrosion are clearly similar to those from pitting corrosion. Crevice corrosion however, is initiated in a different way. The cathodic reaction in crevice corrosion is that of oxygen reduction, and occurs most frequently due to complex geometrical design including; riveted plates, welded structures, threaded components and in particular when a metal and non-metallic solid are joined in restricted areas of a design. This precise geometry set up when objects are assembled imperfectly can lead to situations where the composition of the electrolyte becomes inhomogeneous which leads to the formation of concentration cells in the structure with differing concentrations of oxygen. In this situation,

corrosion becomes localized at the region where the oxygen concentration is lower, therefore becoming the anode, whereas the surface in contact with higher levels of oxygen are the sites of oxygen reduction.

At the anodic site within the crevice, the process of metal dissolution further depletes the oxygen concentration. This means that an acidic solution is experienced within the crevice, similar to the conditions discussed in the previous section for pitting corrosion. The more tortuous diffusion paths between the bulk solution and the anodic site obviously exacerbate the situation within the crevice. This is due to the fact that where an electrolyte is in contact with metal outside the crevice, cathodic oxygen reduction is dominant and within the crevice due to poor rates of oxygen diffusion anodic activity is dominant. These two situations ensure that localized crevice corrosion persists and therefore the process can be described as autocatalytic.

Crevice sites are typically areas about 20-100μm wide, and as such they are very difficult to design against. Designing against differential aeration involves:

- Avoiding debris traps.
- Avoiding water absorbent sound proofing and insulation.
- Ensuring adequate drainage and ventilation.
- Avoiding sharp edges on structures.

A widely accepted mechanism for crevice corrosion is the Fontana Greene mechanism, which was initially proposed for crevice corrosion in stainless steels although the corrosion mechanisms operating are very similar in other metals. (Fontana, 1987) Steps involved are:

1. A uniform electrolyte is assumed. Corrosion occurs at a low rate across the whole of surfaces in contact with the electrolyte. Anodic and cathodic processes initially occur at equal rates.

2. Oxygen is consumed in the processes in stage 1, and this is replenished from the surrounding electrolyte. This is more easily achieved at the surface of the exposed metal than inside the crevice. Oxygen reduction slows within the crevice, however the anodic metal dissolution is unaffected. Effects of this are;

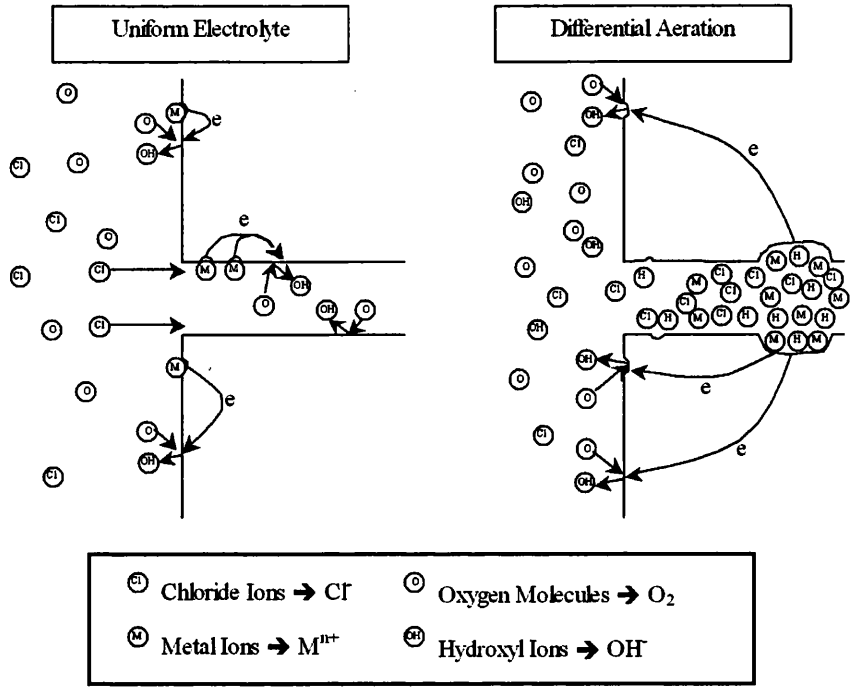

Figure 2.21: The Fontana Greene mechanism for crevice corrosion, typical of that observed in the case of stainless steels. (Fontana, 1987)

(a) The site becomes the focal point for anodic activity.

(b) The net charge in the crevice starts to become more positive than the surrounding electrolyte. Anions flow into the crevice in an attempt to reach electro-neutrality.

3. Chloride ions promote the formation of complex ions with metal cations. These react with water to produce acid and thus reducing the pH.

4. Lower pH promotes attack, combined with the increased chloride ion concentration within the crevice sets up an autocatalytic process that gets progressively more aggressive.

This process is represented graphically in figure 2.21.

2.3.4 Corrosion Control

Various methods are available to slow or negate effects, which, left untreated would be to the detriment of both integrity and performance. With respect to corrosion prevention

using coatings, there are three actions in which these perform; barrier protection, sacrificial protection, or a combination of the both. Anodic and cathodic inhibition is a route that is often taken, which alter the reactions and processes involved in the degradation of metals, and the rates and level (energy and associated current) at which the corrosion proceeds. (Gabe, 1984)

Barrier Protection

This type of corrosion protection is simplistic in nature, and yet if applied properly can be a very effective tool in preventing localized corrosion. A barrier coating can involve the application of a paint or metallic coating in order to exclude oxygen and electrolyte from the metal surface susceptible to localized attack, thus eliminating the presence of a complete electrochemical cell, meaning corrosion is halted. The absence of the electrolyte means that no ionic current flow can exist externally.

Coatings are artificial barriers to the corrosive environment on a metal surface. The most widely used organic coatings are paints. Other organic coatings include lacquers, waxes and greases. Some metallic coatings such as chrome plate and gold plating provide protective barriers because they are more corrosion resistant than the metals they protect.

Barrier or exclusion protection methods have drawbacks. The coating must be continuous, covering the entire exposed surface since if there are any discontinuities, then the site created will become anodic and extremely focused aggressive attack will result. Should the coating material be a more noble metal, this will promote galvanic corrosion of the substrate.

Sacrificial Protection

As the name suggests, sacrificial protection involves the corrosion prevention of one material by the degradation of another. This process is effectively using corrosion behaviour of dissimilar metals advantageously. By careful selection of the sacrificial material according to differences in the E_{corr} values, the size of the anode (sacrificial material) can be considerably smaller than that of the cathode. Due to the protection offered to the protected material, this is often referred to as cathodic protection.

Coating a material with a sacrificial metal has advantages that make it convenient for many applications. Cathodic protection does not require that the coating covers the entire substrate. This means that if the coating is breached, then localized attack will not necessarily ensue at this exposed site. Sacrificial coating metals used are often those elements that, in the presence of oxygen, react to produce an oxide layer. Cathodic protection begins when the barrier aspect of the coating has been breached to reveal substrate material.

Corrosion Inhibition

Corrosion inhibitors are added to the environment in which a given metal must be used, to make the environment less corrosive. Inhibitors may be organic (e.g. polyanaline) or inorganic (e.g. strontium chromate) in nature. Inhibitors are applied in coatings that are formulated is such a way that the corrosion rate is reduced by suppressing either the anodic or cathodic reactions. (Trethewey and Chamberlain, 1995) In the case of OCS production, inorganic inhibitors are applied during the pre–treatment and primer stage.

Anodic inhibitors are able to reduce the rate of corrosion by the formation of a passive film or salt layer by reactions with the metal ions present. This film is deposited on the anodic site. Cathodic inhibitors reduce the availability of oxygen for the cathodic reaction by precipitating insoluble salts on the cathodic area. The corrosion current and free corrosion potential are lowered, thus lowering the corrosion rate.

2.4 Modelling and Simulation

The words "modelling" and "simulation" are often distinguished by somewhat arbitrary arguments or they are simply used synonymously. To reduce the ambiguity created by this common language, separate definitions are necessary. From the Latin word *model*, modelling meaning copy, replica and exemplar is often used ambiguously to describe both model formulation and numerical modelling. Numerical modelling is in most cases used as a synonym to mean numerical simulation. Simulation, from the Latin *simulare*, meaning fake, duplicate, mimic, an imitation of a real situation. (Raabe, 1998) The purpose of a model is to aid better understanding of unknown physical phenomena. This is achieved by replacing a real system with a model. Models may be both mathematical and physical in essence. This,

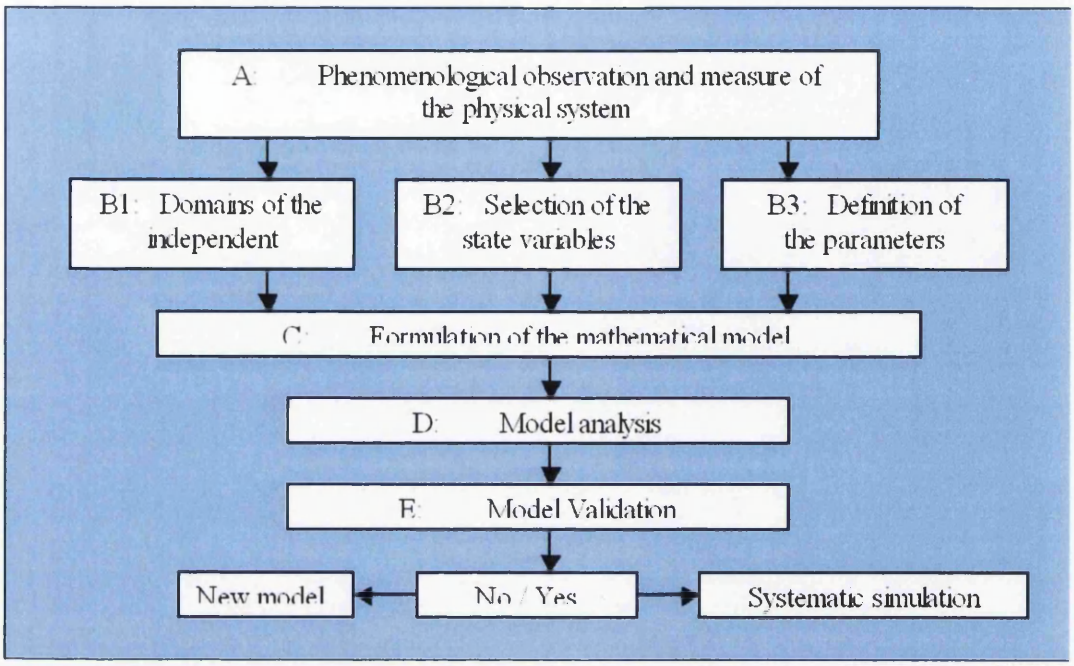

Figure 2.22: Flowchart illustrating stages in the process of modelling according to Bellomo and Preziosi (1995).

from the definition given above, describes the classical scientific method of formulating a simplified imitation of a real situation whilst preserving the essential features of the given system. In this way, a model describes a fraction of a real system by using a similar but simpler structure. As such, abstract models can thus be regarded as the basic start point of theory.

There is no such thing as a unified exact method of deriving models. In computational materials science this is certainly the case since the length scales, time scales and mechanisms encountered are often diverse. In the formulation of computer models, mathematical expressions are used to describe physical phenomena and their implementation arises through numerical methods as executable simulation codes.

The flow chart in figure 2.22 illustrates stages involved in the process of modelling (typical of those attempting to define modelling and simulation) in which overlapping between methods is not uncommon.

Table 2.4: Model Formulation Ingredients. (Raabe, 1998)

Step	Ingredient
1	*Independent variables*, e.g. time and space.
2	*State variables*, i.e. intensive and extensive or implicit and explicit dependent variables, e.g. temperature, dislocation density, displacement, or concentration.
3	*Kinematic equations*, i.e. functions that describe the coordinate changes of mass points without considering the actual forces, e.g. equations for computing strain and rotation from displacement gradients under consideration of constraints.
4	*State equations*, i.e. path–independent functions that describe the actual state of the material in terms of the values of the dependent variables.
5	*Evolution equations*, i.e. path–dependent functions that describes the evolution of microstructure in terms of the change in the values of the dependent variables.
6	*Physical parameters.*
7	*Boundary– and initial–value conditions.*
8	*Numerical algorithms or analytical methods* to solve the framework set up by steps 1– 7.

2.4.1 Model Formulation

In formulating mathematical models in materials science various ingredients are required which can be seen in table 2.4. Developing a model requires a detailed knowledge about the approach that is to be taken, in addition to the information and relationships that will be represented, albeit simplified. This includes a breakdown of the constituents that will make up a model.

If the information in table 2.4 is applied to the corrosion process, it would certainly go some way to clarifying what is required for a simplified imitation of an extremely complex process. Inevitably, the independent state variables would include time and space, since corrosion is a dynamic process that occurs across the surface of electrochemically active materials. Dependent state variables of particular interest in the case of corrosion are concentration and potential since these can be seen to influence most of the corrosion behaviour described in section 2.2. The changes in concentration and potential at a corroding surface have been shown to be very important, which places particular importance on the

Table 2.5: Characteristic times of typical simulation problems.

Time Scale	Characteristic Process
: s	Bulk diffusion
: ms – s	Interface diffusion
: μs – ms	Phase field dynamics
: ns – μs	Dislocation dynamics
: ps – ns	Molecular dynamics
: fs – ps	Debye frequency
.	

way in which the changes in these variables are represented in the model by the state equations. Known behaviour of transformations in differing conditions is required if the evolution of the corrosion process in the model and predictions are to be representative of the real world. Accurate physical parameters are needed, in addition to boundary conditions that are illustrative of observed phenomena. Finally, the model must be implemented by an algorithm that is able to capture the dominant physical and chemical processes taking place, determined by using appropriate numerical techniques.

2.4.2 Time and Length Scales

In accordance with the nature of the real world, different processes take place on different time and space scales. The large variance in temporal and spatial spread of the various potential ingredients in a computer simulation usually requires the model to exist in a particular time and/or space scale. Tables 2.5 and 2.6 display characteristic time and space scales, indicating differing types of models that are better suited for particular scales.

Since the charge carrying ions produced by anodic dissolution move around in the diffusion layer and into the bulk solution, it is obvious from table 2.5 that modelling the influence of this would require that numerical simulations are carried out that determine the state equations over time scale of seconds (s).

Having defined the time scale necessary to represent the impact of corrosion on the bulk electrolyte, this would suggest a meso–scale model would be appropriate. However, it is necessary in the case of localized corrosion to incorporate microstructure. This requires

Table 2.6: Typical space and time scales and simulation methods. (Raabe, 1998)

Time Scale (s)		Length Scale (m)	Examples
10^{7}	Macro–scale	10^{0}	Large–scale FEM, FD (large scale plasticity, heat transport etc.) Cellular automata, percolation models (scale independent) Crystal plasticity FEM
10^{0}	Meso–scale	10^{-3}	Homogenization methods Kinetic multistate Potts model Ginzburg–Landau type and kinetic phase field models, microscopic field kinetic models
10^{-7}	Micro-scale	10^{-6}	Dislocation dynamics Topological networks and vertex models Spring models
10^{-14}	Nano-scale	10^{-9}	Molecular dynamics, Metropolis Monte Carlo Local electron density functional theory

micro–scale computer simulation since the features of microstructural interest pertaining to the specific corrosion behaviour are typically in the order of 10^{-6}m in size. Due to this a micro–mesocopic approach would be needed in order to fully appreciate the influence of both microstructure and evolving state variables during the corrosion process.

2.4.3 Mathematical Representation of Physical Phenomena

Most physical phenomena, particularly in the science of materials, can be described in general by partial differential equations. In fact, it is the case that most of mathematical physics is partial differential equations. Whilst it is true that simplifications can be made that reduce the equations in question to ordinary differential equations, nevertheless, the complete description of these systems resides in the general area of partial differential equations. (Farlow, 1982)

2.4.4 Differential Equations

A partial differential equation is an equation that contains partial derivatives in contrast to ordinary differential equations, where the unknown function depends only on one variable. In partial differential equations, the unknown function depends on several variables. Most of the natural laws of physics are stated in terms of partial derivatives. These laws describe physical phenomena by relating space and time derivatives. Derivatives occur in these equations because the derivatives represent rates of change (such as concentration, flux and current).

The "order" of a differential equation is defined by the term with the highest order within the overall equation. In this respect, a second order differential equation such as,

$$\frac{d^2u(t)}{dt^2} = f(u,t) \tag{2.34}$$

Can be separated into lower order equations by substitution:

$$\frac{dv(t)}{dt} = f(u,t) \qquad v = \frac{du(t)}{dt} \tag{2.35}$$

In which, u is the state variable which is a function of the independent time variable t, v is the first time derivative of u, and f a function of u and v, respectively. Likewise the equations,

$$\begin{aligned} \frac{\partial^2 u}{\partial x^2} &= 0 \ldots 1\text{D} \\ \frac{\partial^2 u}{\partial x^2} + \frac{\partial^2 u}{\partial y^2} &= 0 \ldots 2\text{D} \\ \frac{\partial^2 u}{\partial x^2} + \frac{\partial^2 u}{\partial y^2} + \frac{\partial^2 u}{\partial z^2} &= 0 \ldots 3\text{D} \end{aligned} \tag{2.36}$$

This is known as Laplace's equation and is an equation for $u(x,y,z)$ where x, y and z are the independent space variables. Equation 2.36 can be used to calculate steady–state voltage or electrical potential fields. In this case $u = V$, where V is the voltage (V). Equations 2.34, 2.35 and 2.36 are all linear since u and its partial derivatives occur only to the first degree, and that products of u and its derivatives are absent. (Stephenson, 1996) Differential equations that only contain linear functions of the independent variables are referred to as "linear differential equations" and as such the superposition principle applies, i.e. combinations of solutions that satisfy the boundary conditions applied are also solutions to the differential

equation satisfying the aforementioned boundary conditions. For the "non–linear" cases of differential equations in two independent variables, of which the following is a typical example,

$$u\frac{\partial^2 u}{\partial x^2} + \left(\frac{\partial u}{\partial y}\right)^2 = u^2 \tag{2.37}$$

The superposition principle need not be applied.

Linear partial differential equations have a great variety of important applications in physics, chemistry and engineering. In mathematical descriptions of the phenomena of nature most physical processes or events are described by functions of two or more independent variables, e.g. one, two or three space variables, x, y and z, and a time variable t. Consequently, any relation between such a function, e.g. $u(x, y, z, t)$, and its derivatives with respect to any of the independent variables will lead to a partial differential equation. The complexity of the solution of a linear equation is strongly dependent upon the number of independent variables involved.

A linear equation is said to be *homogeneous* if each term contains either the dependent variable or one of its derivatives. For example, Laplace's equation in two–dimensions (i.e. two independent variables)

$$\nabla^2 u = 0 \tag{2.38}$$

Where ∇^2 is the two–dimensional Laplace operator (defined in rectangular Cartesian coordinates (x, y) by $\nabla^2 = \frac{\partial^2}{\partial x^2} + \frac{\partial^2}{\partial y^2}$) is homogeneous.

2.4.5 Classification of Equations

Particular solutions to partial differential equations are obtained within a certain range of the independent variables and which are in accord with certain initial–value and boundary–value conditions. This means that only particular initial and boundary conditions transform a partial differential equation into a solvable problem. Partial differential equations can be grouped according to the type of additional conditions that are required in formulating a problem. The conventional classification scheme for the important group of linear second order partial differential equations with two independent variables (x_1, x_2) is dealt with in

this instance. The general form of this equation is,

$$A\frac{\partial^2 u}{\partial^2 x_1} + B\frac{\partial^2 u}{\partial x_1 x_2} + C\frac{\partial^2 u}{\partial^2 x_2} + D\frac{\partial u}{\partial x_1} + E\frac{\partial u}{\partial x_2} + Fu + G = 0 \tag{2.39}$$

Where $A = A(x_1, x_2)$, $B = B(x_1, x_2)$, $C = C(x_1, x_2)$, $D = D(x_1, x_2)$, $E = E(x_1, x_2)$, $F = F(x_1, x_2)$, and $G = G(x_1, x_2)$ are given functions of the independent variables x_1 and x_2. It is stipulated that the functions $A(x_1, x_2)$, $B(x_1, x_2)$ and $C(x_1, x_2)$ never be equal to zero at the same point (x_1, x_2). The classification of higher–order curves in analytical geometry which are described by

$$ax_1^2 + bx_1x_2 + cx_2^2 + dx_1 + ex_2 + f = 0, \qquad a^2 + b^2 + c^2 \neq 0 \tag{2.40}$$

Equation 2.39 can for given values $\hat{x_1}$, $\hat{x_2}$, of the variables x_1 and x_2 assume hyperbolic, parabolic, or elliptic character. Roughly speaking, hyperbolic differential equations involve second order derivatives of opposite sign when all terms are grouped on one side, parabolic differential equations involve only a first order derivative in one variable, but have second order derivatives in the remaining variables, and elliptic differential equations involve second order derivatives in each of the independent variables, each of the derivatives having equal sign when grouped in the same side of the equation. Raabe (1998)

- Hyperbolic partial differentiation equation $4A(\hat{x_1}, \hat{x_2})C(\hat{x_1}, \hat{x_2}) < B^2(\hat{x_1}, \hat{x_2})$,
- Parabolic partial differentiation equation $4A(\hat{x_1}, \hat{x_2})C(\hat{x_1}, \hat{x_2}) = B^2(\hat{x_1}, \hat{x_2})$,
- Elliptic partial differentiation equation $4A(\hat{x_1}, \hat{x_2})C(\hat{x_1}, \hat{x_2}) > B^2(\hat{x_1}, \hat{x_2})$.

In this context it must be considered that, since $A(x_1, x_2)$, $B(x_1, x_2)$, and $C(x_1, x_2)$ depend on independent variables, the character of the differential equation may vary from point to point. The approach to group differential equations according to the character of their discriminant $(4AC - B^2)$ is due to its importance in substituting mixed derivatives by new independent variables.

2.4.6 Classification of Boundary Conditions

Representation mathematically of a physical phenomenon using a partial differential equation and a set of boundary conditions can be considered well formulated provided two criteria are satisfied.

1. The solution should be unique, since experience gained from nature is such that a given set of circumstances leads to just one outcome.

2. The solution obtained should be stable, i.e. a small change in the boundary conditions should bring about a correspondingly small change in the solution.

The latter criterion is vital since when the boundary conditions are arrived at by experiment, certain small observational errors in values obtained will always exist and these errors should not lead to large changes in the solution. Thus, accurate selection of boundary conditions is an essential exercise in modelling. Much work has been carried out to determine the types of boundary conditions which, when imposed on linear partial differential equations, lead to unique and stable solutions. (Stephenson, 1996) There are several types of boundary conditions which arise frequently in the description of physical phenomena, which include:

- *Dirichlet or Fixed boundary conditions*
  The value at a particular boundary is known and may not vary with time, or, even if it does, the time dependence is known.

- *Neumann or Flux boundary conditions*
  Where values of the normal derivative $\frac{du}{dn}$ of the function are prescribed at the boundary. In these cases, only a gradient term can be defined.

- *Mixed boundary conditions*
  In a great many cases there is a mixture of Dirichlet and Neumann boundary conditions used to define the boundary conditions.

- *Cauchy boundary conditions* If one of the independent variables is t (time), and the values of both u and $\frac{du}{dt}$ on a boundary $t = 0$ (the initial values of u and $\frac{\partial u}{\partial t}$) are given, then the boundary conditions are of Cauchy type with respect to the variable t.

- *Periodic boundary conditions* In cases of this type, the assumption is made that one edge of the computational grid (boundary) is connected to another. Since the boundaries are eliminated, so too is the need for boundary conditions.

2.4.7 Considerations in Numerical Techniques

Descriptions of physical processes using differential equations often involves an implicit assumption of continuum behaviour, i.e. treating something as a whole or a continuous series, with no perceptual differences between adjacent parts. The discrete nature is often of less significant interest. However, it is often the discrete nature of a system which is reflected in the overall effects attributed to a given continuum behaviour.

Equations that describe a physical system may be theoretically accurate, but are often unusable. In addition, many material constants and parameters required in the application of differential equations to physical processes can be unknown, difficult to measure with any accuracy or only measured in false environments, e.g. laboratory conditions.

2.4.8 Ionic Mass Transport

There are two aspects to the motion of ions through their environment. Firstly there is their individual dynamic behaviour as ions as individuals, the trajectories and the velocities associated with the ions moving about the electrolyte in a basically random manner. Secondly, there is the group behaviour of the ions in a solution, which is of particular importance to the situations when more ions move in a particular way to others producing a drift or flux (rate of transport – moles per unit area through a particular plane). This flux is important since an ion has an associated mass and charge. (Bockris and Reddy, 1998)

If the drift of ions were to be absent, the electrode–electrolyte interface of an electrochemical system would run out of ions to fuel the charge–transfer reactions that occur at such interfaces. The flux of ions is therefore vital for the continued function of electrochemical systems. A flux generated by the difference in concentration of ions in different regions of the electrolyte, i.e. concentration gradient producing a flow of ions is termed ordinary diffusion. Ordinary diffusion is described by Fick's first law,

$$J_i = -D_i \frac{\partial C_i}{\partial x} \tag{2.41}$$

Where J_i is the flux of a species i of concentration C_i in direction x, and is the concentration gradient in direction $-x$. D_i is the proportionality constant known as the *diffusion coefficient* (m^2s^{-1}). The variation of concentration with time due to concentration gradients, is

Table 2.7: The Laplace operator, ∇, in various coordinate systems.

Coordinates	Laplace Operator
Cartesian	$\frac{\partial}{\partial x} + \frac{\partial}{\partial y} + \frac{\partial}{\partial z}$
Cylindrical	$\frac{\partial}{\partial r} + \frac{1}{r}\frac{\partial}{\partial \phi} + \frac{\partial}{\partial \phi}$
Spherical	$\frac{\partial}{\partial r} + \frac{1}{r}\frac{\partial}{\partial \theta} + \frac{1}{r \sin\theta}\frac{\partial}{\partial \phi}$

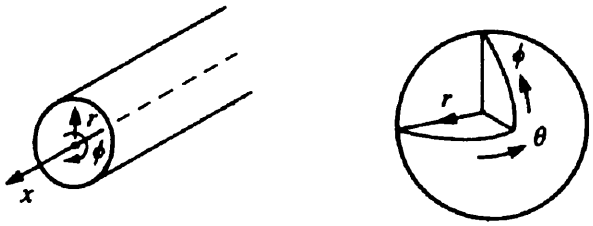

Figure 2.23: Definition of the cylindrical and spherical coordinates in table 2.7.

described by Fick's second law of diffusion,

$$\begin{aligned} \frac{\partial C}{\partial t} &= D\frac{\partial^2 C}{\partial x^2} \quad \ldots 1\text{D} \\ \frac{\partial C}{\partial t} &= D\left(\frac{\partial^2 C}{\partial x^2} + \frac{\partial^2 C}{\partial y^2}\right) \quad \ldots 2\text{D} \\ \frac{\partial C}{\partial t} &= D\left(\frac{\partial^2 C}{\partial x^2} + \frac{\partial^2 C}{\partial y^2} + \frac{\partial^2 C}{\partial z^2}\right) \quad \ldots 3\text{D} \end{aligned} \tag{2.42}$$

Introduction of a Laplace operator for a coordinate system, typically from table 2.7, for any coordinate system gives,

$$\frac{\partial C}{\partial t} = D\nabla^2 C \tag{2.43}$$

A common description of an electrochemical system is derived from the assumption that the concentrations of electro–active species are extremely small. Such an approach would mean that solute–solute interactions are ignored. Under these conditions an expression for describing the flux of a species is,

$$N_i = -z_i u_i F C_i \nabla\phi - D_i \nabla C_i + C_i v \tag{2.44}$$

Where N_i is the flux, z_i is the charge on the ion, u_i is the mobility ($m^2/(Vs)$), C_i is the species concentration, $\nabla\phi$ is the potential gradient, D_i is the diffusivity, and v is the bulk fluid velocity. Flux, potential gradient and fluid velocity are all vector quantities. The terms on the right hand side of equation 2.44 represent fluxes resulting from the migration, diffusion and convection, respectively. Strictly speaking, equation 2.44 is only valid for infinitely dilute solutions; however, this formulation is commonly extended to more concentrated solutions. The material balance in the bulk electrolyte can be expressed as,

$$\frac{\partial C_i}{\partial t} = -\nabla N_i + R_i \tag{2.45}$$

Where R_i represents a chemical reaction occurring in solution. Substitution of equation 2.44 into equation 2.45, with $R_i = 0$ for each species yields,

$$\frac{\partial C}{\partial t} + v\nabla C = z_+ u_+ F\nabla(C\nabla\phi) + D_+\nabla^2 C \tag{2.46}$$

$$\frac{\partial C}{\partial t} + v\nabla C = z_- u_- F\nabla(C\nabla\phi) + D_-\nabla^2 C \tag{2.47}$$

In the absence of convection $v = 0$, and factors involving this quantity do not appear in equations 2.46 and 2.47. Subtracting 2.47 from 2.46 gives,

$$(z_+u_+ - z_-u_-)F\nabla(C\nabla\phi) + (D_+ - D_-)\nabla^2 C = 0 \tag{2.48}$$

Combining equations 2.48 and 2.46 yields,

$$\frac{\partial C}{\partial t} + v\nabla C = D\nabla^2 C \tag{2.49}$$

Where,

$$D = \frac{z^+u^+D^- - z_-u_-D_+}{z^+u^+ - z_-u_-} \tag{2.50}$$

This is the equation of convective diffusion, which has several useful features. Because potential was eliminated, one could calculate the concentration distribution in a binary electrolyte without calculating the potential distribution. For a binary electrolyte the governing differential equation was simplified because we eliminated the potential. A similar situation arises when we have an excess of supporting electrolyte. Substituting equation 2.44 into 2.46 gives,

$$\frac{\partial C_i}{\partial t} + v\nabla C_i = z_i F\nabla(u_i C_i \nabla\phi) + \nabla(D_i\nabla C_i) \tag{2.51}$$

Which is Fick's 2nd Law (ordinary diffusion) incorporating the effects of forced diffusion brought about by potential gradients (migration) and a term corresponding to the convection in the electrolyte.

2.4.9 Numerical Differentiation

Numerical differentiation is concerned with the computation of $f'(x)$ from a given set of values of $f(x)$. This is not the same as analytical differentiation since the rules of calculus are not applied strictly and there is no rearranging of the function. Indeed, numerical differentiation computes the gradients at particular points discrete from one another.

There exist inherent problems associated with numerical differentiation, since $f'(x)$ is less accurate than $f(x)$, also, $f'(x)$ is particularly susceptible to even small errors in $f(x)$. For these reasons, numerical differentiation is referred to as a roughening process, i.e. results in increased numerical error with a corresponding degradation in data. A first order differential equation can be expressed as

$$f'(x) = \lim_{h \to 0} \frac{f(x+h) - f(x)}{h} \tag{2.52}$$

which suggests the differential or slope, $f'(x)$ at position can be calculated using the difference between two values of $f(x)$ and dividing it by the interval between the two points. Thus;

$$f'\left(x + \frac{h}{2}\right) \cong \frac{f(x+h) - f(x)}{h} \tag{2.53}$$

2.4.10 The Finite Difference Method

The basis of the finite difference method lies with the approximation of a differential term with a set of difference terms. The mathematical formulation of a variety of scientific and engineering situations, involving rates of change with respect to two or more independent variables leads to either a partial differential equation or a set of such equations. The partial differential equations need to be modified in order for a computer to understand and process them numerically. There are three standard methods of approximating differential equations by differences,

- Forward differences,

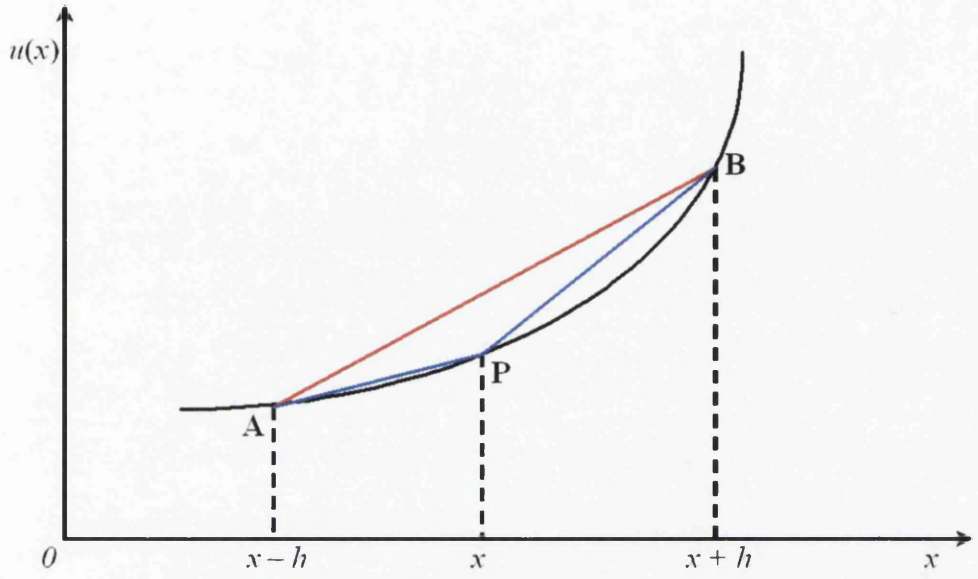

Figure 2.24: Gradient difference approximations.

- Backward differences, and,
- Central differences.

Consider a function u and its derivatives are single–valued, finite and continuous functions of x, then figure 2.24 illustrates the three difference methods.
The forward difference approximation of the gradient at point **P** is graphically represented in figure 2.24, by the chord **PB**, whose equation is,

$$u'(x) = \frac{du}{dx} \cong \frac{u_{x+h} - u_x}{h} \tag{2.54}$$

The backward difference approximation of the gradient at point P is graphically represented in figure 2.24, by the chord **AP**, whose equation is,

$$u'(x) = \frac{du}{dx} \cong \frac{u_x - u_x}{x - h} \tag{2.55}$$

The approximation chosen depends upon the direction of x is taken to make the approximation of the gradient, i.e. if the differential equation is a function of u with respect to a change in time then it would be down to the whether the calculation is stepping forward

or backward in time. For a double differential of the form $u''(x)$, one uses a central difference approximation, in figure 2.24, so that the slope of the tangent at **P**, by the slope of the chord **AB** is given by the approximation,

$$\frac{d^2u_x}{dx^2} \cong \frac{\left\{\frac{du_{x+h}}{dx} - \frac{du_x}{dx}\right\}}{\Delta x} \tag{2.56}$$

Replacing the $\frac{du}{dx}$ by backward differences gives,

$$\frac{d^2u_x}{dx^2} \cong \frac{\left\{\frac{u_{x+h}-u_x}{\Delta x} - \frac{u_x-u_{x-h}}{\Delta x}\right\}}{\Delta x} \tag{2.57}$$

Which equates to,

$$u''(x) = \left(\frac{d^2u}{dx^x}\right) \cong \frac{1}{h^2}\left(u_{x+h} - 2u_x + u_x - h\right) \tag{2.58}$$

Since $h = \Delta x$. It is referred to as central difference due to the evident symmetry. (Smith, 1978)

Numerical Errors of Finite Difference Methods

Simplifications generally made in any finite difference method, discretization of time and space, along with the replacement of the differential quotient by its difference quotient, lead to various inherent types of numerical errors being present in the solution. "Inherent errors" also arise through human error and difficulty in the measurement of data. Using insufficient significant numbers in equations and limited storage facilities in computers are another source of inherent errors.

Errors exist in the fact that, the exact solution of the continuous differential equation may differ from the approximate equation. This mismatch in the two solutions is a "truncation error" and it is calculated as the norm of the difference between the solution to the continuous differential equation and the solution to the discretized difference equation divided by the time interval used in the numerical algorithm. Due to this relationship with the time step, one would expect the error to reduce more as the time step is refined further, a property known as consistency. It is accordance with this, that, a finite difference method is said to be consistent if as the time step tends to zero, so the error approaches zero. Residual errors may be encountered if other discretization operations are performed during the approximation process, irrespective of the decrease in the time intervals.

The imprecise nature of number handling of computers leads to the introduction of "round–off errors", not to be confused with truncation errors arising from the replacement of the difference quotient. Reducing the time interval does not necessarily decrease the round–off error, as in the case of truncation errors.

An important criterion in the evaluation of the quality of a finite difference scheme is its stability, i.e. whether or not the errors discussed, accumulate and amplify without limit during the computational process.

2.4.11 Taylor Series

A Taylor series is a series expansion of a function about a point. A one-dimensional Taylor series is an expansion of a real function $f(x)$ about a point $x = a$ is given by,

$$\begin{aligned} f(x) =& f(a) + f(a)(x-a) + \frac{f''(a)}{2!}(x-a)^2 + \frac{f^{(3)}(a)}{3!}(x-a)^3 + \cdots \\ & \cdots + \frac{f^{(n)}(a)}{n!}(x-a)^n + \cdots \end{aligned} \tag{2.59}$$

If $a = 0$, the expansion is known as a Maclaurin series.

Taylor's theorem states that any function satisfying certain conditions may be represented by a Taylor series,

$$\begin{aligned} f(x) =& f(0) + xf'(0) + \frac{x^2}{2!}f''(0) + \cdots + \frac{x^{(n-1)}}{(n-1)!}f^{(n-1)}(0) + \cdots \\ & \cdots + \int_0^x \frac{(x-u)^{n-1}}{(n-1)!}f^n(u)du \end{aligned} \tag{2.60}$$

2.4.12 Gauss–Seidel Method

The Gauss–Seidel method (called Seidel's method by Jeffereys and Jeffereys (1988)) is a technique for solving a number of equations of a linear system, $Ax = b$, individually in a defined sequence using previously computed results as they become available,

$$x_i^{(k)} = \frac{b_i - \sum_{j<i} a_{i,j}x_j^{(k)} - \sum_{j>i} a_{i,j}x_j^{(k-1)}}{a_{ii}} \tag{2.61}$$

There are two important characteristics of the Gauss–Seidel method that should be noted:

1. The computations appear to be serial. Since each component of the new iterate depends upon all previously computed components, the updates cannot be done simultaneously as in the Jacobi method.

2. The new iterate $x^{(k)}$ depends upon the order in which the equations are examined. If this ordering is changed, then the components of the new iterates (and not just their order) will also change.

2.5 Modelling Methodologies

The use of numerical methods and computer models in materials science is driven by the increasing need from industry and research for quantitative predictions. This is promoted further by the ever increasing capability and speed of computer systems. Almost all areas of science and engineering is complimented by computer simulation.

The scales at which these simulations operate has been discussed previously and is determined by the requirements for the model. Microstructural phenomena at the atomic scale may be represented by ab-initio molecular dynamics, whereas mechanical properties would inevitably require a continuum method, reducing the microstructure to an averaging of constitutive laws. Most mesoscale approaches however, are formulated as continuum models that often have a discrete consideration for phenomena occurring at the microstructural level.

2.5.1 Microstructural Modelling

Investigations into microstructural phenomena at realistic time and length scales requires consideration of relatively large portions of material. This obviously means that the material to be simulated contains a huge amount of atoms, meaning that meso-scale simulations of microstructure cannot be performed by atomistic approaches. In most cases this requires the introduction of continuum models, replacing the exact solution with one approximating the movement of all atoms. By approximating the material as a continuum for obtaining meso-scale predictions makes sense, since the phenomenological state equations and structural evolution laws are often well investigated at this scale, at which experimental data can be obtained more easily than at the micro-scale and in more detail than the macro-scale. (Raabe, 1998)

Phase Field Models

Phase field models have been used to study solidification, as well as being applied to other growth processes, e.g. electrolysis in a molten salt by Dussault and Powell (2002). Phase field models tackle solid- and liquid-state phase transformation kinetics in a discretized fashion, considering both spatial and temporal changes in the chemical, crystallographic, and structural fields. These state variables appear frequently as so-called phase field variables. Among the most versatile approaches towards phase field are the Cahn–Hilliard and Allen–Hilliard kinetic phase field models, which can be regarded as metallurgical derivatives of the theories of Onsager and Ginzburg–Landau. The difference between these two approaches is that the Cahn–Hilliard model describes kinetic transformation phenomena with conserved variable fields (e.g. chemical concentration), whereas the Allen–Hilliard model deals with transformations involving non-conserved variables (e.g. crystal structure). Kinetic Phase field models have found applications in a number of areas, including ordering phenomena, solidification, dendrite growth and grain growth. (Boettinger et al., 2002; Chen and Wang, 1996)

Cellular Automata

Cellular automata are algorithms that describe the discrete spatial and/or temporal evolution of complex systems by applying local or global deterministic or probabilistic transformation rules to the sites of a lattice. Usually, although not exclusively, partitioning of the physical space takes a rectangular form. Each site must assume one of a finite number of permitted states. Transition between states is governed by a set of rules applicable to all the cells in the automaton. These rules are local in space and time and the state of the cell at discrete time depends upon the state of that cell at a previous time and the state of the neighbouring sites. Evolving in discrete time steps, a cellular automaton updates the state variables simultaneously for all nodes after time stepping.

The nature of the grid described above, results in a lattice that can be used as the basis for finite difference techniques. These cells can be regarded as the nodes in a finite difference grid, giving rise to the models known as Cellular Automaton Finite Difference (CAFD) models. (Brown, 1998) The lattice is typically regular and its dimensions can be

arbitrary. Cellular automata do not have any restrictions in the type of elementary entities or transformation rules applied. Although often used at an elementary level, cellular automaton simulations are not bound by a characteristic physical length or time scale, providing a convenient numerical bridge for various space and time scales. However, the elementary unit and transformation rules selected must adequately reflect the behaviour of the system at the level addressed.

Cellular automaton simulations have been used widely in the field of transformation; including dendrite and crystal growth. (Davies, 1997; Spittle and Brown, 1994)

Monte Carlo Simulation

Monte Carlo methods are a class of computational algorithms for simulating the behaviour of various physical and mathematical systems. They are distinguished from other simulation methods (such as molecular dynamics) by being stochastic, by using random numbers (or more often pseudo-random numbers) as opposed to deterministic algorithms.

Usually, Monte Carlo, models can be broken down into three characteristic steps. Firstly, the physical problem is translated to a probabilistic or statistical model. The next step is to solve the model by stochastic sampling including a large number of arithmetical and logical operations. Finally, the data obtained is analyzed using statistical methods. The distinguishable feature between the classes of Monte Carlo model, is the sampling technique. With regards to microstructural modelling, importance sampling is the underlying principle.

Monte Carlo simulations have found applications in nucleation, recrystallization, grain growth and solidification. (Anderson et al., 1989; Das and Mittemeijer, 2000)

2.5.2 Corrosion Modelling

As corrosion occurs over all length and time scales, the diversity of modelling approaches taken towards it is understandable. Models exist at the atomistic scale up to the macroscale. Despite this, there are relatively few that reside in the micro–mesoscopic scale and there are fewer physically based models that deal with metallic dissolution and associated concentration effects. However, a great deal of similarities exist between models that operate at different scales and in different situations.

The benefits and limitations of the modelling approaches taken for a number of corrosion models is discussed in chapter 6, along with the applicability to the micro–meso scale. Common to all the models are the fundamental relationships outlined previously, e.g. Laplace equation for potential field, ordinary diffusion and ion migration. Their application is only altered by the modelling technique used, e.g. boundary element method and kinetic Monte Carlo, and the situation in which they are used, e.g. crevice corrosion.

Turnbull (1997) uses an advanced model to predict the chemistry and potential in a stress corrosion crack in sensitized stainless steel. It considers the anodic and cathodic reactions in a trapezoidal crack, taking into account the solubility of cations in water at elevated temperatures. Additional features of the model by Turnbull (1997) of particular interest to this investigation are transport by diffusion and ion migration and the hydrolysis of metal cations. The anodic and cathodic reactions take place within the crack geometry in this instance rather than at a corroding surface, although Laplace's equation is used to model the potential drop in the environment outside the crack. Due to lack of specific data pertaining to precipitation from solution in the cathodic reaction, a rate constant was used such that supersaturation was kept to a minimum, in addition to the oxidation of hydrogen atoms in the crack not being taken into account. Convection is assumed to be negligible by Turnbull (1997) within the crack, although the contributions of the homogeneous equilibrium reaction process at a position in the crevice as well as heterogeneous processes (anodic and cathodic reactions) at the metal surfaces are included in the mass conservation rules applied in the model. An initial uniform concentration is assumed and Ohm's law is employed to calculate the initial potential distribution. This model served to conclude that the crack-tip potential is not independent of potential and reactions on crack walls cannot be ignored in predicting chemistry and potential in a crack.

A probabilistic model was given by Harlow and Wei (1998), describing the pitting corrosion of certain classes of aluminium alloys with particular emphasis on the growth process; specifically the role of clustered particles. It describes the multi-site damage and crack growth involving interactions with neighbouring particles. Harlow and Wei (1998) assumed that a pit grows at a constant voltametric rate and incorporated the effect of temperature using an Arrhenius relationship, although a constant aspect ratio (described in

section 2.3.2) is assumed, in addition to pits being spheroidal in geometry.

Laycock and White (2001) proposed a model to describe the propagation of corrosion pits in stainless steels under potentiostatic control. This model considered salt film precipitation, electrolytic migration and transport outside the pit explicitly. There is only one considered dissolution product, thereby ignoring complicated solution chemistry. The proposed model by Laycock and White (2001) described the anodic dissolution kinetics in the (near) saturated pit environment, It deals with pitting of stainless steels in two phases; nucleation and propagation. Rate terms for anodic and cathodic reactions are based on concentration differences, obeying Tafel's law. The Laplace equation is used to calculate the electrical potential in the solution away from the surfaces, which are held at the applied potential. Movement of the single species is considered using ordinary diffusion and migration terms. Laycock and White (2001) use finite element approximations to describe the potential and concentration fields, solved using a Crank–Nicholson algorithm. The 2D simulations produced by this model have shown that deposition of a porous pit covering can arise from corrosion at the pit mouth and repassivation of metastable pits does not necessarily require the collapse of this shroud. In addition, Laycock and White (2001) found that a salt film is eventually precipitated over the majority of the corroding surface leading to diffusion-controlled dissolution.

Webb and Alkire (2002) have mathematically modelled the dissolution of a single MnS inclusion within an electrochemical micro-cell. The dissolution rate was determined using an electrochemical route, which was found to be exponential in nature, The movement of the chemical species brought about by anodic dissolution was handled using diffusion and migration, using the Nernst–Einstein equation to determine the ionic mobility of the species from the diffusion coefficient; in both chloride and sulphate containing media. Once again the solution is assumed to be electrically neutral. Webb and Alkire (2002) solved the non-linear partial equations using the finite difference method. Second order forward- and backward-difference approximations were used on the boundaries. The finite difference form of the partial differential equations was obtained from partial Taylor series expansion, using unequally spaced nodes and a fully implicit scheme was implemented to step forward in time by Webb and Alkire (2002). It was felt that the model could be extended with relative

ease to consider the effect of "roughness" on pitting potential.

2.6 Conclusions and Project Aims

Zinc and its alloys are used extensively in the protection of steel, due to the barrier and cathodic protection offered to the substrate to which it is applied, either through hot–dipping or electroplating. The microstructure is known to influence the corrosion of ZnAl alloys due to compositional differences across a surface in contact with a conducting electrolyte. The physical and electrochemical processes taking place during corrosion are highly complex, involving mass transport, electrode kinetics and state transformation. Modelling a specific corrosion process must capture the dominant physical and chemical processes operating. Many models have been developed to simulate the microstructures of alloys, although relatively few corrosion models exist that operate at this length scale. In order to capture the influence of microstructure on localized corrosion effects associated with Zn and ZnAl coatings in contact with NaCl solution must operate at the micro–mesoscopic length scale.

The aims of the investigation were:

- Within a suitable modelling framework, develop a micro-scale model to describe the localized degradation experienced by pure zinc and zinc - aluminium steel coatings.
- Establish a predicted relationship between microstructure and corrosion resistance of Galfan coated steel exposed at the surface and cut–edge to 5% NaCl.
- Quantitatively predict the corrosion performance of Zn – 4.5 wt.% Al coated steel cooled at different rates.

Chapter 3

Experimental Methods

Topics addressed in this chapter include:

- Establishing a quantitative link between corrosion potential at an electrode surface and the corrosion rate, using the rotating disc electrode (RDE) technique.
- Evaluating the results of RDE testing with respect to the behaviour of passivated materials.
- Identifying the areas of a zinc – 4.5 wt.% aluminium alloy microstructure that are susceptible to corrosive attack in 5% NaCl solution.

This chapter documents the experimental procedures undertaken to aid in the development of a computer model, designed to make quantitative predictions of local degradation experienced by zinc and zinc–aluminium alloy steel coatings. Later chapters will make reference to other experimentally based investigations made by other researchers, although any quantitative predictions/comparisons made will be independent of one another.

During the course of the development of a computer model, two modes of experimentation have been used. The rotating disc electrode (RDE) technique has been used in an attempt to relate locally calculated thermodynamic behaviour to the kinetics of the corrosion process. Visual inspection using a scanning electron microscope (SEM) was conducted to validate the forms of localized corrosive attack predicted throughout the systematic simulation of different coating layers. This was performed on samples of Galfan coated steels produced during trials as part of the work conducted by Elvins (2005).

3.1 Rotating Disc Electrode (RDE) Technique

The rotating disk electrode uses a three–electrode cell comprising of; a working electrode, an auxiliary electrode and a reference electrode. Each of these serves the following purpose:

1. **Working Electrode** – This is the electrode under investigation. In the case of the conducted experiments, electrodes were taken from pure zinc and commercially pure aluminium samples. It is not called an'anode' since investigations with the RDE are not limited to anodic behaviour, rather anodic or cathodic behaviour.

2. **Auxiliary Electrode** – This is the secondary electrode, present to carry the current necessary to complete the electrochemical cell. A platinum electrode was used in the experimentation to carry this current since space was at a premium.

3. **Reference Electrode** – The reference electrode provides a stable datum against which the potential at the working electrode can be measured. This electrode is not intended to carry any current. A saturated calomel electrode (SCE) was used in this investigation.

These three electrodes, combined, are a version of the basic wet corrosion cell described in section 2.2.2.

3.1.1 Construction of the Rotating Disc Electrode

A container of capacity 2 litres was used for all experiments undertaken. At all times during the experimentation, a volume greater than 1.5 litres was maintained in this container of the chosen electrolyte; 5% NaCl solution. The working electrode is prepared from either pure zinc or commercially pure aluminium. Each electrode is a disc of diameter 5.4 mm, equating to an area 22.9 mm^2 for the working electrode. One edge of the disc was chamfered to 45^o to make assembly easier. After this, the working electrode material was polished to a 1 μm finish prior to testing with the RDE.

For each test the working electrode was embedded in a rod of insulating material (Teflon) and lowered into the container containing the electrolyte, centrally and approximately 20 mm below the surface of the 5% NaCl solution. Away from the working electrode the reference

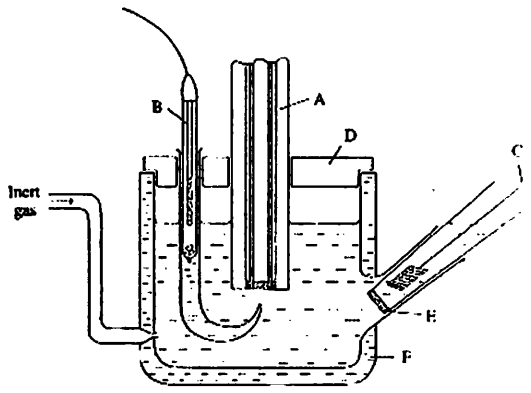

Figure 3.1: Cell for the rotating disk electrode. A – working electrode; B – reference electrode with Luggin capillary; C – auxiliary electrode; D – Teflon lid; E – porous frit; F – thermostatted water jacket (N/A). (Brett and Brett, 1993)

electrode was placed at the edge of the container such that the bottom was about 5 mm from the base of the electrolyte. Across from the reference electrode the auxiliary electrode was positioned, at a depth of 30 mm. All electrodes were held in place by use of clamps and stands.

In the case of anodic tests, an inert gas was passed through the 5% NaCl solution; both prior to, and during testing. Argon was used in order to, first, purge the solution of any dissolved oxygen, and subsequently act as a shield to any oxygen returning into the solution. This was aided by the use of a Perspex guard placed on the top of the container, with small holes at the positions occupied by the three electrodes.

The arrangement of the electrodes used, the supply of the shielding gas and the electrolyte can be seen in figure 3.1.

The rod in which the working electrode is mounted was attached directly by a chuck to a motor and was rotated at a constant velocity. In all the experiments a rotation frequency, f, of 500 rpm was used. Electrical contact was made to the working electrode by means of a brush contact.

During testing, measurements of potential (V) and current density (Acm^{-2}) were made using a Solatron 1200 analyser. Measurements were taken every second whilst the potential was increased at a rate of 1 mVs^{-1}. In the anodic testing, sweeps were made from -0.5 V to -2.0 V, whereas the cathodic sweeps were performed between -1.8 V to -0.5 V.

Units of current density were kept consistent throughout the investigation via conversion of measured values to Am^{-2}.

3.2 Preparation of Galfan Coated Steel Samples

The Galfan coated steel was received in 200 mm $\times$ 200 mm sheets. These were light gauge samples (0.47 mm steel substrate thickness) and were guillotined into samples approximately 10 mm $\times$ 10 mm in dimensions. The samples were placed in 5% NaCl solution and left in position, undisturbed for a period of 24 hours. After this period of time, the samples were removed, rinsed with distilled water, followed by alcohol and dried using heated air. This was done in an attempt to limit the degradation of the coated steels to that taking place in the NaCl solution over the 24 hours.

3.3 Experimental Results

3.3.1 RDE Results

Figure 3.2 shows the general current–potential curve produced using the rotating disc electrode. Absolute values of current density and potential versus the SCE reference electrode used (standard calomel electrode) are shown in figure 3.2, and distinctive changes are seen with respect to the current density as the potential applied to the working electrode is altered. Increasing the applied potential from the minimum 0.6 V in figure 3.2 at the working electrode can be seen to increase the current density by a factor of 4 over a small potential range of 0.05 V. After this point, further increases in potential up to 0.7 V, the current density drops consistently. After an applied potential of 0.755 V is reached, current density can be seen to be unaffected by further increases in potential until another threshold is reached at approximately 1.55 V. At this point, as can be seen in figure 3.2, the current density once again begins to increase with further increases in potential applied to the working electrode.

Figure 3.3 shows the results generated from the RDE testing performed on commercially pure aluminium. The results presented show one cathodic voltametric sweep performed and one anodic voltametric sweep performed. In figure 3.3 the potential at the working electrode (vs SCE) is plotted against the absolute value of the current density measured,

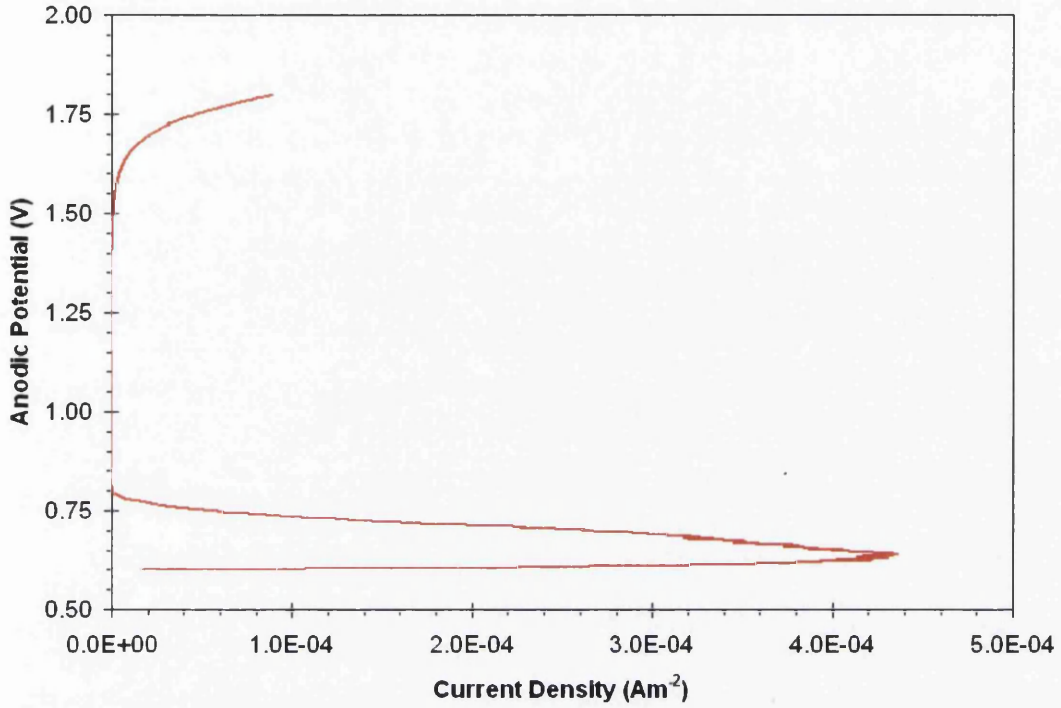

Figure 3.2: Current–potential curve generated from a RDE test on aluminium during a voltametric sweep in 5% NaCl solution.

following convention. What can be seen is that as potential is increased from the minimum, in both anodic and cathodic cases -1.8 V, the current density experienced can be seen to decrease until a certain point, thereafter this situation is reversed. The minimum current density measured during the RDE testing performed on aluminium within the potential range stipulated was 10^{-9} Am^{-2} for both measurements made in anodic and cathodic voltametric sweeps. However, this changeover occurs at a lower potential during the cathodic voltametric sweeps (-1.3 V) than during the measurements made in the anodic voltametric sweeps (-1.17 V). Further increases in applied potential from this changeover point, for both cases in figure 3.3, brought about increases in current density. These increases are different in the anodic and cathodic voltametric sweep cases, although at -0.8 V equivalent current density values is observed for both. After this current density continues to rise with increases in potential at the working electrode (vs SCE), although the gradient of this increase in current density can be seen to lower. In the anodic voltametric sweep a further switchover is seen to occur within the range of potential shown.

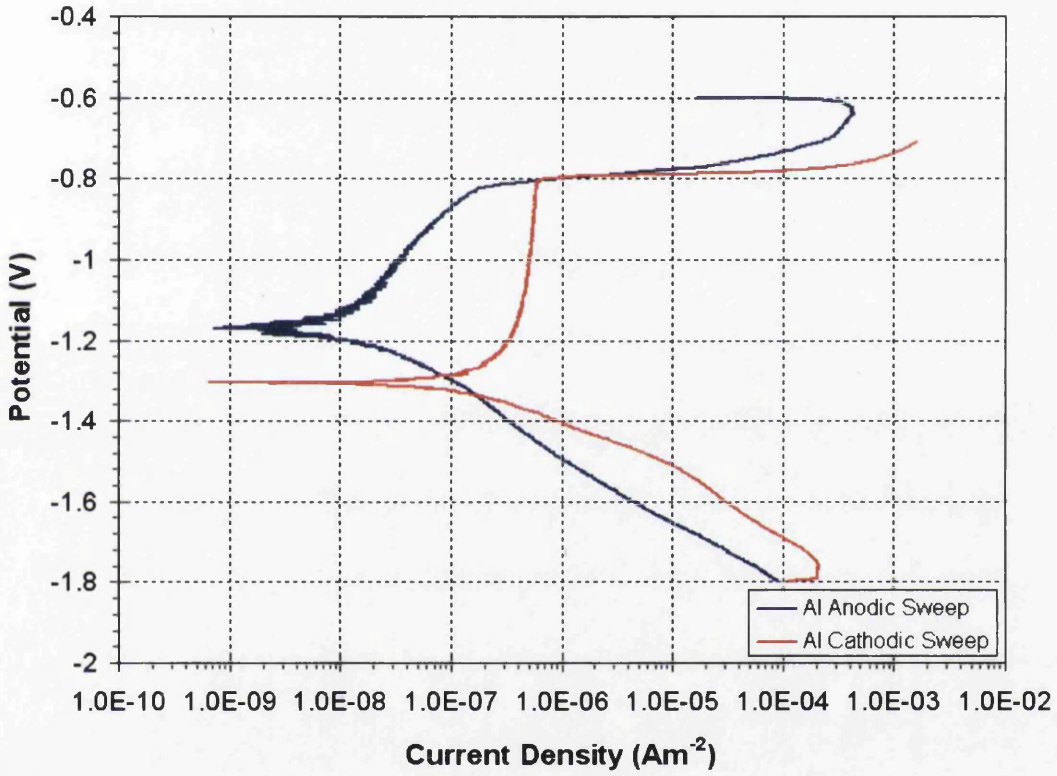

Figure 3.3: Representative results from the RDE tests performed on commercially pure aluminium; using anodic and cathodic voltametric sweep measurements in 5% NaCl solution.

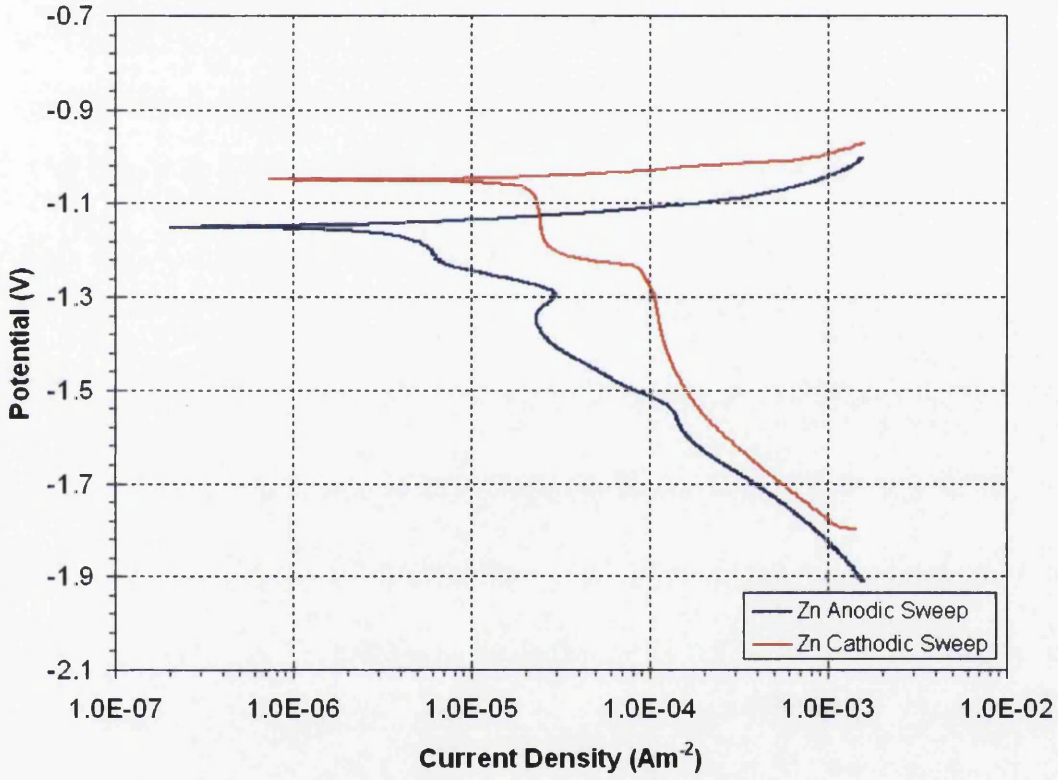

Figure 3.4: Representative results from the RDE tests performed on pure zinc; using anodic and cathodic voltametric sweep measurements in 5% NaCl solution.

Equivalent information as shown in figure 3.3 for aluminium, is shown for zinc in figure 3.4. Unlike figure 3.3 however, the form of the anodic and cathodic voltametric sweeps performed on zinc samples yield relationships linking the potential (vs SCE) at the working electrode to the current density measured that are very much alike. The major differences exhibited in figure 3.4 are where the changes in behaviour occur, in terms of potential and current produced. From minimum value sampled of -1.9 V and -1.8 V for the anodic and cathodic voltametric sweeps respectively, as the applied potential is increased a decrease in absolute current density value was observed. The point at which this trend is reversed in the case of zinc varies from -1.15 V for the anodic test, at which point the current density observed is 2×10^{-7} Am^{-2}, to -1.07 V observed for the cathodic tests, where a current density of 7×10^{7} Am^{-2} is measured. After this changeover is observed, in both cases a further increase in applied potential at the working electrode yield rises in current densities at a large, equivalent rate, which has begun to reduce as a maximum current density value of approximately 10^{-3} Am^{-2} is witnessed when sweeping in this range of potential values (vs SCE).

Figure 3.5 shows the comparison of 9 of the tests performed on the aluminium samples using a cathodic voltametric sweep of potential, i.e. from more negative to less negative potential. It can be seen from figure 3.5 that the resultant potential – current density relationship is reproducible, with only tests 4, 8 and 9 lying outside what would be reasonable tolerances. What is evident in these tests exhibiting discrepancies, is the premature termination and a smaller potential range examined, indicating errors in the measurement of these sensitive parameters during these isolated test cases.

3.3.2 SEM Results

The micrograph shown in figure 3.6 depicts the image generated by the scanning electron microscope (SEM) for a relatively large area of the Galfan coated steel immersed in the beaker containing 5% NaCl solution. Evident from figure 3.6 is that over an area of 9 mm^2 the extent of local and general degradation can vary greatly. Towards the left area of figure 3.6 there is evidence of changes in surface texture, perhaps attributed to generalized corrosion effects. In close proximity to this area there is a marked change in the surface

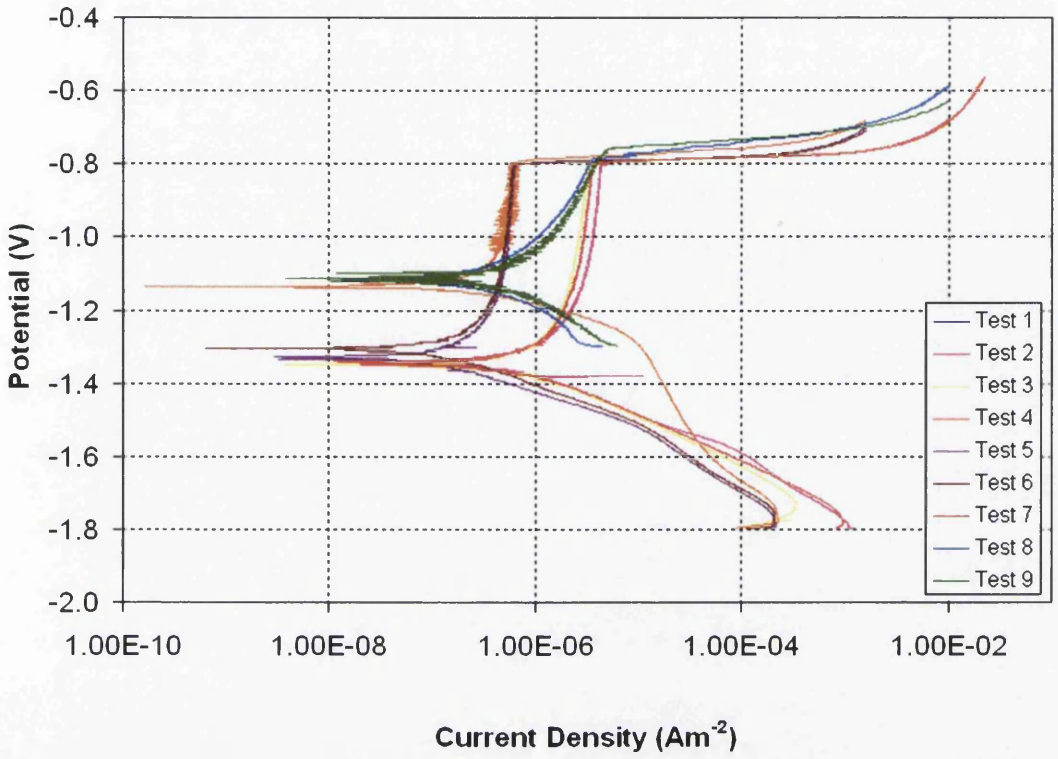

Figure 3.5: RDE results for 9 tests performed on commercially pure aluminium samples, using cathodic sweeping in 5% NaCl solution.

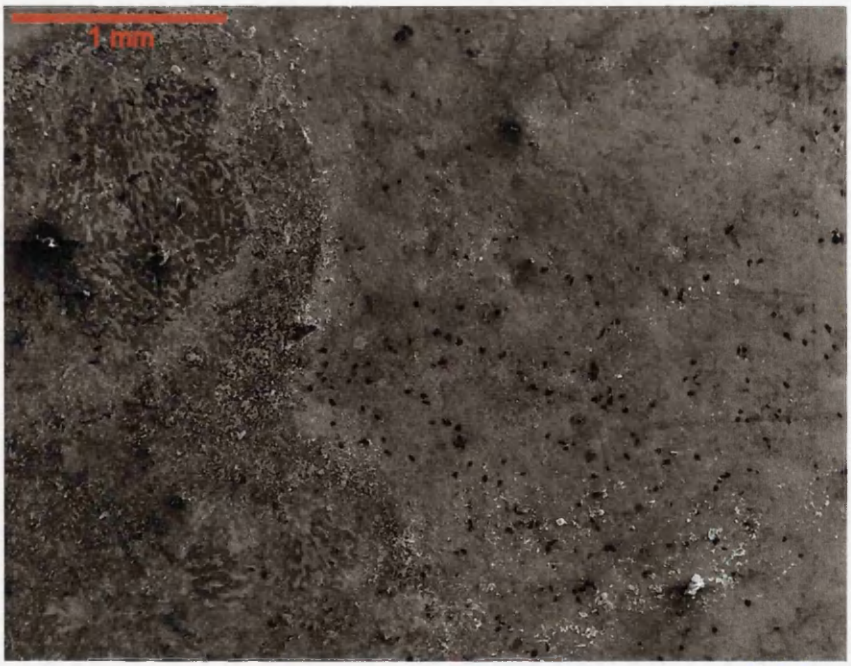

Figure 3.6: SEM image of a large area of Galfan coated steel after 24 hours immersion in 5% NaCl solution.

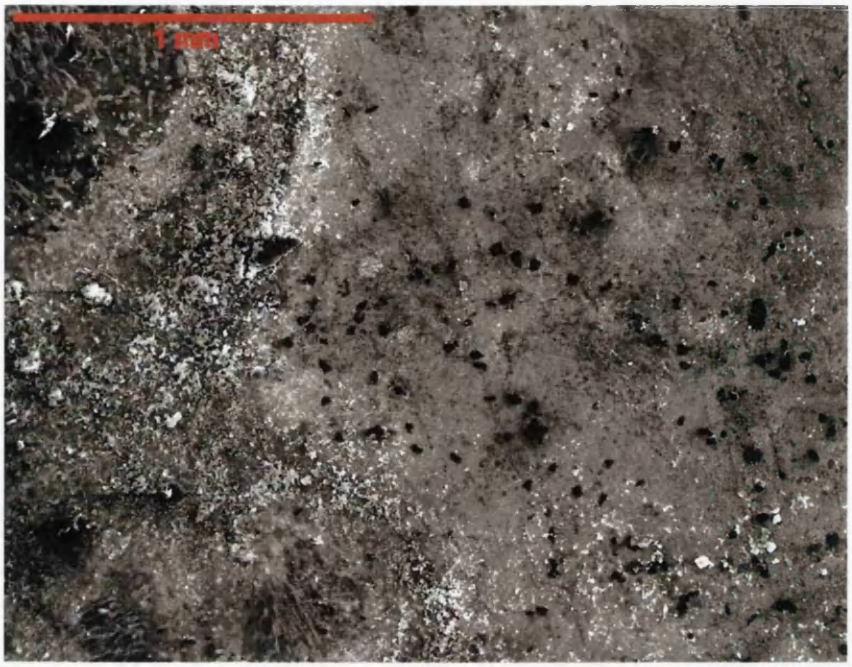

Figure 3.7: Micrograph showing differences in surface texture over an area of Galfan coated steel after 24 hours immersion in 5% NaCl solution.

texture, where 'holes', probably denoting areas subject to more localized corrosion effects, are present at a much higher level. This again can be seen in figure 3.6.

Closer examination of the same sample shown in figure 3.6 can be seen in figure 3.7 albeit at a higher contrast. This gives a clearer picture of the surface texture of the Galfan coated steel. Additional features that can be seen at this higher magnification then become apparent. The localized forms of corrosion can be seen to exist all over the exposed coating to differing degrees. Those areas that appear untouched in figure 3.6 can be seen to be the sites of minimal pitting in figure 3.7. In the areas of the coating surface where the corrosion effects are limited to very localized regions, the arrangements of these pits are not entirely randomly spread.

An area of coating layer exhibiting localized corrosion effects can be seen in figure 3.8. The arrangement of the pits at the Galfan coating surface indicates that the features associated with the localized corrosion effects exist at specific areas, often tracing paths across the surface consistent with the formation of eutectic cell formation. Within these regions bounded by the presence of pits are areas of relatively untouched coating with respect to corrosion effects. This can be seen for a smaller area in figure 3.8, although

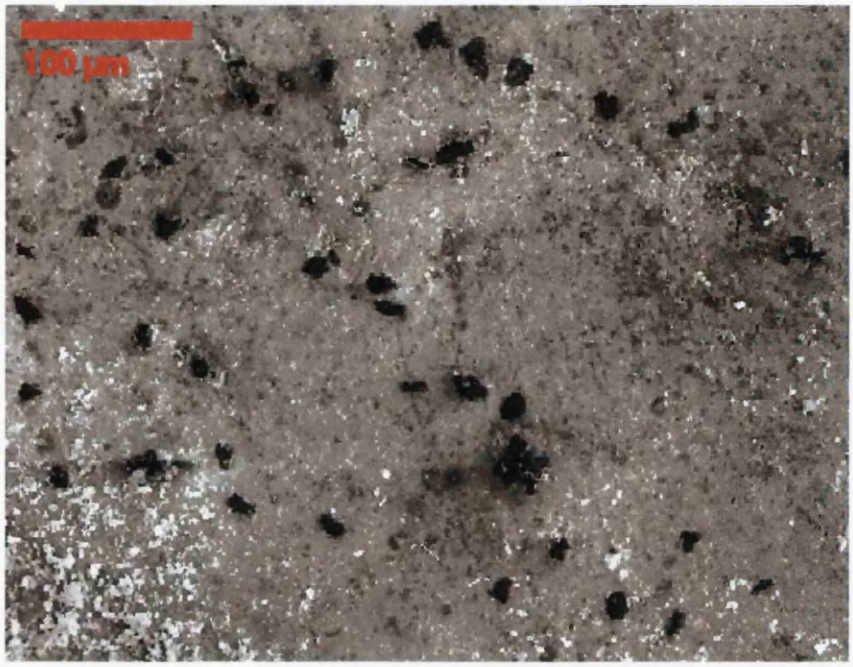

Figure 3.8: SEM image showing the localized removal of material during the exposure of Galfan coated steel to 5% NaCl solution.

on re–evaluation, figure 3.7 can also be seen to exhibit such patterns over a much greater area.

The type of pit depicted by figures 3.6, 3.7 and 3.8 is shown in figure 3.9 at a high magnification. This shows the differences in dimensions of the localized corrosion effects experienced by the Galfan coating over the 24 hour period whilst immersed in the 5% NaCl solution. Generally at the surface of the coating exposed, the pit is circular in appearance, although the 'clover' shape shown in figure 3.9 bears a certain likeness to the morphology of the primary phase observed by Elvins et al. (2005a) close to the Galfan coating surface.

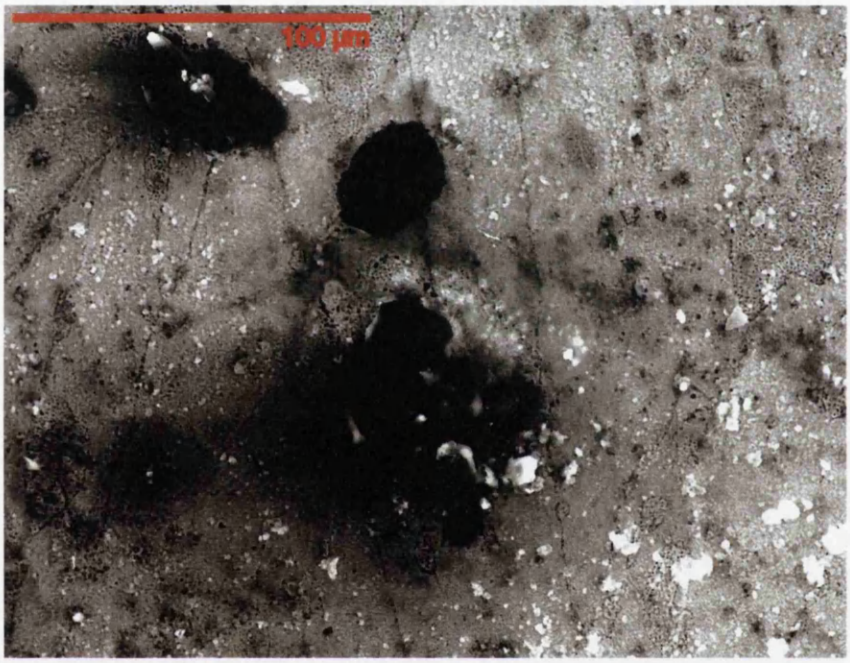

Figure 3.9: Close–up SEM image of the localized corrosion effects encountered during the exposure of Galfan coated steel during exposure to 5% NaCl solution.

Chapter 4

Modelling Procedure

Covered in this chapter:

- Description of the modelling assumptions used and mesh construction.
- Effective representation of the phases present in the simulations.
- An explanation of the algorithm used in the corrosion model.
- Numerical validation of current density fields from the corrosion model.

Described in this chapter is an attempt to predict the localized corrosion effects experienced by zinc coated steel (electroplated zinc coatings) and a zinc alloy Galfan coating (Zn – 4.5wt.% Al), in the presence of an aggressive electrolyte; 0.1% NaCl solution and 5% NaCl solution respectively.

The model described has been developed primarily from a metallurgical standpoint rather than an electrochemical one. (Brown et al., 2004) In order to reflect the influence of microstructure, the model has been developed at the micro–mesoscopic scale rather than the molecular level. (Newman et al., 1992) Simulations performed at the microscopic–mesoscopic length scales involve two– or three– dimensional field calculations performed in a finite difference computational framework.

The model comprises field–based calculations for electrical potential and diffusion / migration coupled to standard electrochemical equations. This in an effort to capture the main features of localized corrosion described previously, and relating these

effects back to their source; materials properties, defects (e.g. grain boundaries, porosity etc.), geometric effects (e.g. crevice attack) and galvanic effects (cut–edge corrosion).

All simulations are pH neutral, isothermal at 298K. Unless stated otherwise, a grid comprising $200 \times 50 \times 200$ elements in the x, y and z directions respectively is used in the simulated cases.

4.1 Modelling Assumptions

Attempting to simulate the localized corrosion of zinc and zinc alloy steel coatings with a physically–based numerical model, inevitably requires simplifying assumptions to be made. These assumptions pertaining to the characteristic behaviour of the zinc / ZnAl coatings, steel substrate and electrolyte, allow the modelling of a complex system to become feasible.

The model has been developed to predict and evaluate the zinc alloy coatings only. To this end there is no dissolution of the steel substrate, as well as to there being no grain structure in the substrate material, which may be a site of corrosion in reality.

The electrolyte is assumed to be uniform at the start of the simulation in terms of the concentration of electro–active species involved in the localized degradation of these steel coatings. In addition to this, throughout the simulation the electrical conductivity and thereby the electrical resistivity remain constant and uniform; these being used in post–processing procedures.

It should be noted that the Galfan microstructure represented in two– and three–dimensions are entirely synthetic, i.e. they have been generated to look like the actual microstructure. It has not been produced by a direct simulation of microstructural evolution of the solidification of the Zn – Al alloy. The eutectic phase depicted in the representation of the Zn – 4.5wt.% Al case is treated as a homogenous material with regard to its composition and material properties. It is therefore assumed to act uniformly in the corrosion effects experienced, although sensitive to spatial disparities in ionic concentration and electrode potentials. In reality, however, it is known that a rod structure, or more likely a lamellar structure would be adopted by the Zn/Al eutectic material.

As outlined previously, the presence of aluminium in the hot–dip bath during the production of Galfan–coated steel suppresses large–scale intermetallic formation. It is

considered a reasonable simplifying assumption, in this case, to neglect the influence of any minimal layer of intermetallics in the corrosion performance of the Galfan steel coatings.

Evans (1981) further subdivided the classification of the corrosion of metals into those which form films and those that do not. From section 2.2.2, the corrosion of zinc in a charge carrying aqueous environment can be summarized by,

$$Zn_{(s)} \longrightarrow Zn^{2+}_{(aq)} + 2e^- \tag{4.1}$$

Supported cathodically at pH neutral by oxygen reduction,

$$O_2 + 2H_2O_{(l)} + 4e^- \longrightarrow 4OH^-_{(aq)} \tag{4.2}$$

A first order model that deals with the evolution and movement of a single ionic concentration (increases of which are brought about by anodic dissolution) has been used. The model assumes that the $Zn^{2+}_{(aq)}$ produced in anodic zinc dissolution, equation 4.1, rapidly undergoes hydrolysis to produce solid zinc hydroxide via,

$$\begin{aligned} Zn^{2+}_{(aq)} + H_2O_{(l)} &\rightleftharpoons Zn(OH)^+_{aq} + H^+_{(aq)} \\ Zn(OH)^+_{(aq)} + H_2O_{(l)} &\rightleftharpoons Zn(OH)_{2(s)} + H^+_{(aq)} \end{aligned} \tag{4.3}$$

This reaction of Zn with non–dissociated molecules of water (Johnson et al., 1971) gives rise to a single representative concentration of the corrosion process, H^+; due to the film–forming behaviour of zinc. An equivalent reaction is assumed in consuming aluminium ions ($Al^{3+}_{(aq)}$) from dissolution events, although there is a greater concentration of $[H^+]$ per unit volume due to a higher valency, n. In this way the model tracks the effective free proton concentration (C, mol dm^{-3}) arising from the dissolution of the coating during the corrosion process.

Direct estimation of the overall corrosion effects experienced, considering only one electro–active species, places particular importance on the formation of corrosion products and the passivation of the system.

4.2 Discretization

To be able to numerically simulate localized corrosion, first of all a representative volume of space must be discretized. This discretized domain must be capable of demonstrating the

electrochemical phenomena taking place, in addition to the the microstructure of the material from which inherent corrosion behaviour is derived.

The model, as described, is limited to the local micro–scale variations in metallurgical structure that are deemed most important for the development of localized corrosion effects. The model uses a suitably sized irregular, orthogonal mesh to represent the microstructure of the coating, the steel substrate and liquid electrolyte. The model permits non–uniform nodal spacings in the x, y and z directions in order to represent spatially disparate features in each simulation of $nx \times ny \times nz$ elements.

The mesh provided a finite–difference–based computational framework on which field based calculations can be performed. Each element on the mesh can be assigned a combination from a finite number of states or a single state. In the model this combination can be drawn from the following:

1. Solid phase 1; Zinc.
2. Solid phase 2; Aluminium.
3. Solid Phase 3; Steel (mild steel composition).
4. Solid Phase 4; Non–active insulating material.
5. Liquid Phase; 0.1% or 5% NaCl solution.

As with modelling any situation/process, the primary criterion upon which to judge effectiveness is by direct comparison of that model with actual experimental measurement. Accelerated corrosion tests have been carried out extensively in these electrolytes for the coated steels in question, over 24 hour periods of exposure. In the interest of purposeful scientific inquiry, simulations are performed over the time scale of 24 hours.

Once again, the success of any simulations in capturing the physical processes taking place is dependent upon the effective discretization of time in the model. In order not to underestimate the localized degradation taking place at the steel coating – electrolyte interface, using a time increment, Δt (s), of 20 minutes (1200 seconds) is typical. This time scale is also suitable for capturing the movement of ionic concentration, the dynamically evolving system that is time dependent in the model.

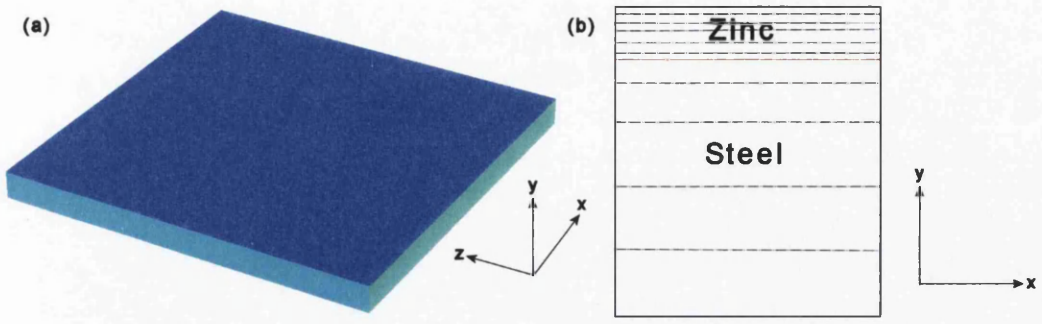

Figure 4.1: (a) Arrangement of 2μm zinc layer (dark blue) and 0.47mm steel (light blue) in the case of EZ exposed surface; and, (b) Relative differences in nodal distances in the vertical direction - not to scale.

4.3 Solid Representation

The solid metallic constituents are represented in the model by synthetically approximating the arrangements and observations of the coated steel products of interest, electroplated zinc coated steel (EZ coating) and Galfan coated steel (Zn – 4.5wt.% Al). In the accelerated corrosion testing, as with the *in situ* evaluation, there are two situations of interest for the corrosion performance of these steel coatings; surface corrosion performance and cut–edge corrosion performance.

Surface corrosion refers to the situation when the surface of the solid matter in contact with electrolyte is a continuous section of coating. Cut–edge corrosion is an arrangement where both coating layers, front and back, in addition to the steel substrate are exposed to the aggressive electrolyte. This is perpendicular in orientation to the the surface case. In all cases described a non–uniform regular mesh is used. This allows for greater resolution in regions of interest.

4.3.1 Surface Exposure of Electroplated Zinc Coated Steel

In the case of evaluating the surface corrosion performance of electroplated zinc (EZ) on a steel substrate half of the mesh (lower portion) is assigned one of two solid phases. The upper portion of the mesh is assigned as electrolyte. Directly in contact with the electrolyte is a pure zinc layer 2μm thick. Below this is occupied by a steel substrate of light gauge thickness, 0.47mm. Primary interest is the local dissolution of zinc and so nodal spacings

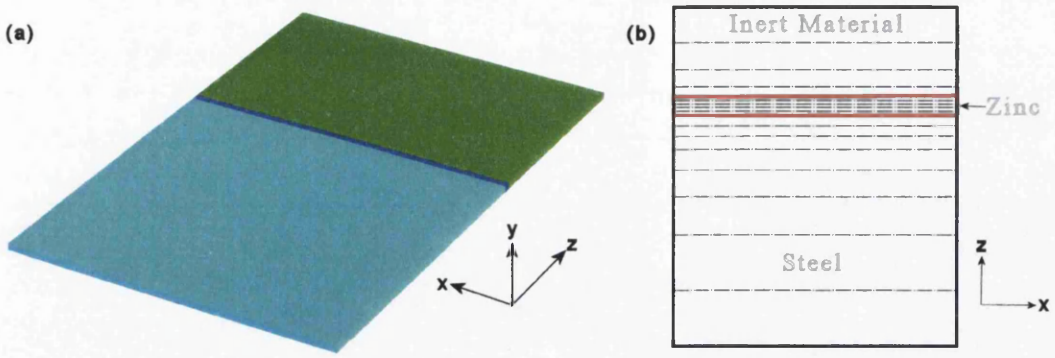

Figure 4.2: (a) Arrangement of 0.47mm steel substrate (light blue), 2μm zinc coating (dark blue) and inert material (green); and, (b) Relative differences in nodal distances in the z direction - not to scale.

for this phase in the y direction are fine (shown in figure 4.1) whereas those in the steel are significantly larger. Figure 4.1(a) shows the arrangement of this simulation, shown by dark blue, steel depicted by the light blue area.

Distribution of elements in the y direction can be seen in figure 4.1(b). Nodal spacings in the x and z directions are regular, culminating in the representation of an area of exposure of 2.5mm $\times$ 2.5mm being typical in simulating this case.

4.3.2 Cut–Edge Exposure of EZ Coated Steel

In this case, a slice of the setup described in section 4.3.1 is rotated through 90^o so that both steel and zinc coating is exposed to electrolyte at the start of the simulation. In addition to this, a region of inert material (green region) is included adjacent to the zinc coating layer (dark blue). This allows the electro–active species to be tracked above the interface away from the zinc layer where they arise. Figure 4.2(a) shows the arrangement described. Again the zinc layer is approximately 2μm in thickness in contrast with the relatively massive steel substrate, typically 0.47mm in thickness. These varying dimensions are captured in the z direction by varying the nodal spacings shown in figure 4.2(b). Nodal spacings in the x direction are regular such that a cut–edge length of 2.5mm can be represented.

4.3.3 Surface Exposure of Galfan Coated Steel

Although entirely synthetic, the microstructural representation does exhibit a good likeness to that observed in reality. This crude approximation is achieved by nucleating regular geometrical shapes in the volume of mesh assigned to solid material. The size of these shapes is randomized between an upper and lower limit. Once formed, these are assigned as solid phase 1 – zinc. These regions are an approximation to primary zinc crystals formed in the non–equilibrium solidification of Galfan coatings (section 2.1.3).

The primary phase is nucleated and grown until a volume fraction equating to 20% of the volume assigned for the coating layer is reached. This is based on direct measurement by Elvins et al. (2005a), earlier thought to be around 14%. (Elvins et al., 2003) After this limit is reached, the remaining simulated solid volume is assigned as solid phase 2 – ZnAl eutectic.

In the representation of an exposed surface of Galfan, the steel substrate is not included in the computational framework. The coating layer is typically 25μm in thickness, far greater than an EZ coating, and hot–dip methods ensure a consistent, continuous coating layer due to total submersion, pre–treatment and 'wiping'. The absence of a substrate requires only one solid structure be simulated. This means that in the solid coating layer simulated nodal spacings are regular in the x, y and z directions. The microstructural features of interest (primary zinc dendrites) limits the area exposed to 2.5mm $\times$ 2.5mm.

Figure 4.3: (a) Arrangement of zinc rich phase in ZnAl eutectic; and, (b) Presence of depressions at eutectic grain boundary simulated on Galfan coating surface.

A simulated Galfan layer can be seen in figure 4.3(a), in which the dark blue regions are primary zinc crystals and grey area denotes ZnAl eutectic. This eutectic is assumed to be homogeneous in nature and as such no attempt is made to distinguish individual lamellae or rod structures, whichever is prevalent.

Figure 4.3(b) shows the X–ray representation of the simulated solid matter described by figure 4.3(a). This demonstrates the incorporation of depressions around the eutectic cells at the final point of freezing for the Galfan coating layer. These depressions have a strong influence in the surface corrosion of Galfan coated steels, since their presence reveals additional surface area of primary zinc dendritic phase exposed to the electrolyte. The 'trenches' formed in figure 4.3(b) are generated using a grain growth routine, where eutectic material is removed from these boundary regions to a pre–determined depth. The size of these eutectic grains is linked to those observed in microstructural investigation. Eutectic cell size in the model is determined via the manipulation of the nucleation points chosen before grain growth steps.

4.3.4 Cut–Edge Exposure of Galfan Coated Steel

The simulation of corrosion at the cut–edge of a Galfan coated steel is similar to the arrangement for the cut–edge of EZ, only that, in this case, a back coat and an additional block of inert material is included. The steel substrate is situated at the centre of the z direction. At either surface perpendicular to this substrate there is a 25μm simulated Galfan layer. This is formulated in the same way as in section 4.3.3, although rotated through 90^o and 270^o about the x axis shown in figure 4.3. This means that there is a front and back metallic coating present, the thicknesses of which are controlled in reality by the process of 'wiping' by the gas knives, discussed in section 2.1.2.

No surface depressions are present in the cut–edge simulation of Galfan coated steel. The nodal spacings over the Galfan layer are regular in all directions included in the two– and three– dimensional simulations. These nodal spacings are smaller than those used for the steel in order that the primary phase structures assume the same shape / form.

Inert material is located at either side of the simulated Galfan coated steel. These blocks of solid phase 4 (section 4.2), represent a relatively large distance in the z direction. All

nodal spacings are regular in the x direction totaling a maximum cut–edge length simulated of 2.5mm using the standard mesh of $200 \times 50 \times 200$ elements.

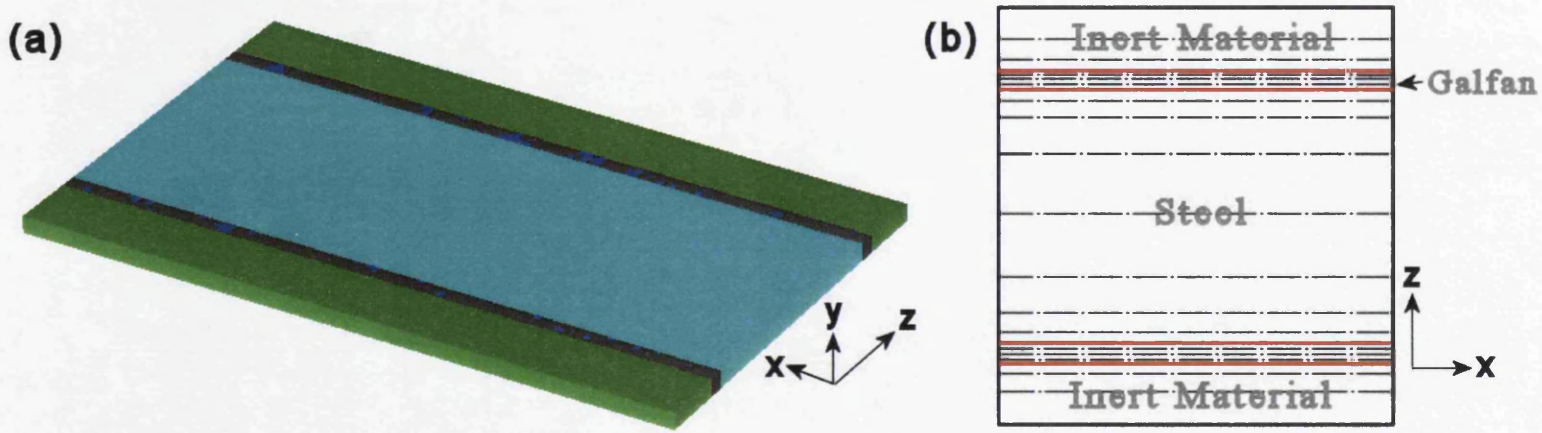

Figure 4.4: (a) Arrangement of cut–edge for Galfan coated steel – 0.47mm steel substrate (light blue), 25μm Galfan coating (dark blue indicating primary zinc and grey showing eutectic) and inert material (green); and, (b) Relative differences in nodal distances in the z direction - not to scale.

The arrangement of these constituents in the simulation of Galfan coated steel at a cut–edge can be seen in figure 4.4(a). This shows the setup for a light gauge steel substrate (light blue) and a cut–edge length of 0.5mm. The Galfan layer can be seen by the dark blue zinc crystals in grey eutectic. Inert insulating material included is represented by the green regions in figure 4.4(a).

Figure 4.4(b) shows a visualization of the system used to capture the relevant detail by variation of nodal spacings in the x and z directions.

4.4 Electrolyte Representation

As outlined in previous sections, each cell in the orthogonal grid possesses an integer value identifying the site as either solid or electrolyte. Electrolyte cells, occupying the top half of the grid, are then also defined further; in terms of concentration (C, mol dm^{-3}), electrical potential (ϕ, V), current density vector (i_x, i_y, i_z, Am^{-2}), volume fraction of the cell occupied by corrosion product (p), and the volume fraction of any cell containing a combination of any solid phase and liquid phase that has already been corroded away. These values are the basis for the field based calculations rather than the limited information contained in the solid sites; composition (wt.% Al) and solid fraction (f). The volume corroded away from a solid site (i.e. volume of electrolyte) is equivalent to, $1 - f$.

The process of modelling the localized corrosion process at hand must take into account that both anodic and cathodic sites occur on surfaces in electrical contact, albeit spatially discrete from one another. These sites, completing the corrosion cell and RedOx pairing (chapter 2.2) limit the overall movement of the ionic species used in the first order model. In addition, this balanced behaviour also thereby limits the cumulative concentration of this proton concentration in the represented electrolyte.

The nodal spacings in the x and z directions throughout the represented electrolyte are dictated by those deemed suitable for the simulated EZ or Galfan coated steel, described previously. Non–uniform grid dimensions are applied in the y direction in order to capture various features occurring during this electrochemical process; diffusion and steady–state voltages away from a corroding material. The movement of electro–active species in a solution containing an actively corroding material is driven by diffusion (natural and forced).

Imitating these will be discussed in subsequent sections. However, it is important to note that this movement is limited to a small thickness of electrolyte close to the surface, called the diffusion or double layer (δ layer).

This diffusion layer may be as small as a few microns in thickness or much greater, depending on the species evolving, from what system and the electrolyte carrying this (ionic) mass and charge. Beyond this diffusive layer exists bulk electrolyte, assumed in this instance to be of uniform composition and properties (conductivity, temperature, concentration, etc.). Despite this uniformity, detail exists in the bulk electrolyte due to the steady state voltage field containing effects brought about by perturbations in concentration in the δ–layer and the associated changes in potential gradients.

Whilst the setup of the grid spacings in the vertical direction do not attempt to determine the thickness of this diffusion layer, either in reality or in the simulation, an appropriate array of spacings is needed if the simulations are to yield the results aimed for. Close to the solid–electrolyte interface previously defined, nodal spacings are small, typically limited to 1μm–2μm. This increases the likelihood of capturing any diffusion of ionic concentration, either residing from previous time increments or emanating from the simulated corroding surface during that time step. Near to the top of the computational framework, grid spacings are increased such that electrical potentials can be calculated far removed from the surface and relative to the thickness of the diffusive layer. The total thickness of the electrolyte represented is typically about 500μm / 0.5mm, although irregular griding permits variations around this value.

4.5 Algorithm for Numerical Simulation of Localized Corrosion

The algorithm that follows performs field calculations inside a discretized volume of space at a series of discrete time increments. This process starts at the calculation of electrical potential and then proceeds through various stages to the final step of dealing with the deposition / removal of corrosion products. At this point, time is incremented again and, once again, the field calculations begin at the next time iteration with the calculation of electrical potential.

4.5.1 Electrical Potential

An important factor controlling localized galvanic corrosion will be the effective electrical potential over the surface. This will usually vary from point to point. A relationship between electrolyte concentration, C, and potential, ϕ, was defined in section 2.2.3, known as the Nernst equation (equation 2.6). This equation may be written in a different form in order to estimate the concentration overpotential (see section 2.11) from a single concentration, making it applicable to a single order model. The Nernst equation then becomes,

$$\phi_0 = E_0 - \frac{RT}{nF} \ln\left(\frac{C}{C_0}\right) \tag{4.4}$$

Where C is the local concentration of H^+ and C_0 describes the initial concentration at that point, which is also assumed to be the bulk concentration of H^+ in the model. R is the universal gas constant (J mol^{-1} K^{-1}), F is the Faraday constant (C mol^{-1}), n is the unit charge and T is the temperature, 298K.

Equation 4.4 is used by the model in order to determine the surface electrical potential for all solid metal sites in contact with electrolyte. Clearly, different solid phases will also possess different standard electrode potentials, E_0. For each metal E_0 is temperature and electrolytically dependent. This then distinguishes differing corrosion behaviour for differing areas of the microstructure, in addition to the changes in local concentrations experienced. These electrical potentials are then held fixed as Dirichlet boundary conditions (section 2.4.6) for the remainder of the time step. Having determined the surface electrical potentials the bulk electrical potential in the electrolyte can then be determined merely by solution of the Laplace equation (section 2.4.4) for all electrolyte cells

$$\nabla(-\kappa\nabla\phi) = 0 \tag{4.5}$$

Where κ is the electrical conductivity (Ω^{-1}m^{-1}) that is temperature and concentration dependent. However, the simplifying assumption is made that the electrical conductivity / resistivity is uniform throughout the electrolyte and does not change with concentration. The temperature dependence of resistivity can be ignored since all simulations are isothermal, leading to,

$$\nabla^2\phi = 0 \tag{4.6}$$

Replacing the Laplace operator (table 2.7) in equation 4.6 to describe an orthogonal grid (Cartesian coordinates) gives,

$$\left(\frac{\partial^2\phi}{\partial x^2}+\frac{\partial^2\phi}{\partial y^2}+\frac{\partial^2\phi}{\partial z^2}\right)=0 \tag{4.7}$$

Each partial term is approximated using second order central approximations and is then solved throughout the computational grid using the Gauss–Siedel iterative method. An implicit scheme is set-up and unequally spaced nodes are used. The calculations of electrical potential are performed iteratively until either, all sites in the mesh possess values for electrical potential that fall within a preset tolerance with respect to their neighbours in the constructed mesh, or, a pre–defined maximum number of iterations is reached. Typically this tolerance is 10^{-5}V and a maximum number of iterations would be 200. The calculation of the electrical potential fields is carried out in the simulation under a regime of overrelaxation. This aids in reaching an acceptable value that falls within tolerances set and decreases simulation time.

Calculations performed in the determination of the electrical potential field are carried out using a method called *successive overrelaxation* (SOR). A value for λ of 1.75 is used as there is an implicit assumption made that new values are converging to the correct value. The relationship between this SOR and the the new value, yields a final calculation of ϕ in an iteration to,

$$\begin{aligned}\phi^{itn}_{i,j,k} &= \lambda\phi^{itn}_{i,j,k}+(1-\lambda)\phi^{itn-1}_{i,j,k}\\ &= 1.75\phi^{itn}_{i,j,k}-0.75\phi^{itn-1}_{i,j,k}\end{aligned} \tag{4.8}$$

Where itn is a reference to the current iteration, i, j and k denote the relative grid positions in the x, y and z directions and λ is a weighting factor.

In determination of the electrical potentials throughout the electrolyte, zero flux boundary conditions (section 2.4.6) are used on the top and side faces of the mesh, regardless of whether diffusion/migration is taking place in those regions.

4.5.2 Metallic Dissolution

Having determined the electrical conditions at the surface as a function of local microstructure and electrolyte concentration, the next step in the algorithm is to determine

the amount of localized corrosion taking place. At this point the details of the model will become material-specific.

The rate at which dissolution occurs at interface sites will be related to the potentials experienced at those positions. In the current model the kinetics of dissolution for phases present at the metal-electrolyte interface have been approximated from experimental data obtained from the rotating disc electrode (RDE) technique, described in chapter 3. Results from the RDE provide Tafel curves for both pure zinc and commercially pure aluminium samples. Using these curves, the rate of dissolution, which is a function of local current density, is derived from the electrical potentials associated with the composition of a cell, arising from equation 4.4, thus in this model, current density, $i \propto [H^+]$.

The amount by which each corroding metal/electrolyte interface cell corrodes is calculated from the local current density and the previous time increment. The volume fraction of material dissolved in each cell is then calculated. Once a cell is completely dissolved it is re–labelled as an electrolyte cell. Therefore in any given time increment the total increase in concentration in the electrolyte is quantified via,

$$C_A = \sum_{i=1}^{ni} \sum_{j=1}^{nj} \sum_{k=1}^{nk} \delta f_{i,j,k} c_a \Delta x_i \Delta y_j \Delta z_k \tag{4.9}$$

Where ni, nj and nk define the total number of sites on the mesh, $\delta f_{i,j,k}$ is the volume fraction of a cell transforming, c_a is a constant volume concentration contribution term and $\Delta x_i \Delta y_j \Delta z_k$ is the volume of the cell.

4.5.3 Cathodic Behaviour

Left unregulated, the localized corrosion effects predicted by the model, as presented so far, would propagate unopposed. This would not be realistic since in this case it is known that the cathodic reaction is the rate determining process. To ensure electro-neutrality in the model there is a counterbalancing procedure to equation 4.9, whereby an equal and opposite concentration decrease, C_c, is forced at all metal/electrolyte interface sites (subject to satisfying the condition below),

$$C_C = \frac{C_A}{V_{SE}} \tag{4.10}$$

Where V_{SE} is the total volume of all electrolyte cells at the solid-electrolyte interface that are able to accept a further decrease in concentration as part of the cathodic reaction. Another feature of the present model is that there is also a lower limit placed on cell concentration such that sites acting cathodically that reach this limit will cease to be able to lower concentration further. This has the eventual effect of lowering the overall corrosion rate.

4.5.4 The Role of Corrosion Products

Another mechanism that significantly affects localized corrosion is the presence of corrosion products. In terms of modelling it is necessary once again to make simplifying assumptions. For the corrosion of a Zn–Al–steel system it is known that corrosion product films do form and eventually may prevent further corrosion occurring. Consequently, in the current model, each electrolyte cell may contain a certain volume fraction of corrosion product. The decision that must be made is how much corrosion product forms and where should it be deposited?

In the present model, the corrosion products are deposited at metal/electrolyte surface sites within a pre–determined concentration and potential bands. These deposits alter the movement of concentration via manipulation of the diffusion coefficient applied to the cells,

$$D_{i,j,k} = D_0(1 - p_{i,j,k})^2 \tag{4.11}$$

If $p_{i,j,k}$ reaches unity in a cell then that site acts as a complete barrier to diffusion. It has been assumed that at each time increment the volume of corrosion product deposited at the surface is 5% of the total volume of metal dissolved in that time step. The deposition of this product and its associated influence on subsequent diffusion of H^+ (described by equation 4.11) can be seen in figure 4.5.

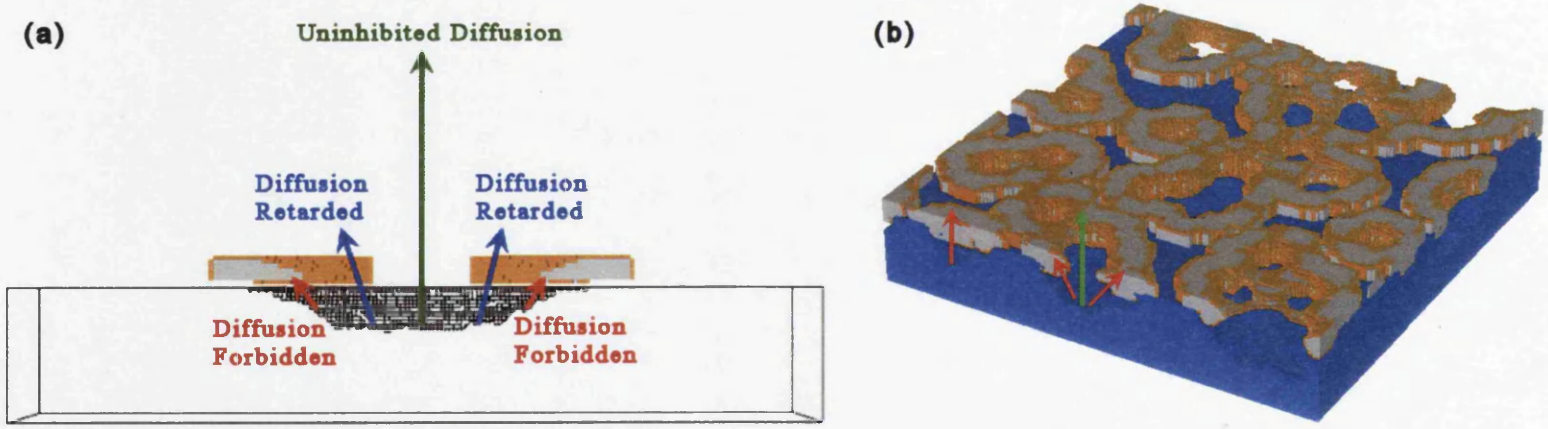

Figure 4.5: (a) The effect of deposited corrosion product on diffusion from active local corrosion sites. Grey represents $p_{i,j,k} = 1$ and brown describes $0 < p_{i,j,k} < 1$; and, (b) Corrosion product deposited on a zinc block.

Also, all sites containing corrosion product have their fraction, $p_{i,j,k}$, reduced by an arbitrary and very small amount to simulate gradual dissolution of corrosion product. Corrosion product that is not deposited at a surface is not considered to influence corrosion.

4.5.5 Diffusion, Migration and Convection

The movement of the charged particles in solution, which have been evolved during the previous dissolution step, may be modelled by laws governing convection, diffusion and the transport of ions through an electrical field. In the current model, diffusion through 0.02 mol dm^{-3} (0.1%) NaCl solution and 0.86 mol dm^{-3} (5%) NaCl solution (with negligible convection) occurs over a time increment due to ordinary diffusion and migration effects. This is modelled by the diffusion-convection equation 4.12 including the ionic migration term.

$$\frac{\partial C}{\partial t} + W\nabla C = -\nabla(D\nabla C) + nF\nabla(uC\nabla\phi) \tag{4.12}$$

Where D is the diffusion coefficient at 298K (m^2s^{-1}), n is the unit charge and u is the ionic mobility ($m^2/(Vs)$).

At this point, if the flow field is known, the effects of electrolyte convection could be included via the velocity vector, W. However, in this case all simulations are conducted under negligible convection, and so any detail of flow is removed, transforming equation 4.12 to,

$$\frac{\partial C}{\partial t} = -\nabla(D\nabla C) + nF\nabla(uC\nabla\phi) \tag{4.13}$$

It is obviously easier and less awkward to consider the terms in equation 4.13 separately. Expanding the Laplace operators then leads to two separate governing equations; ordinary (or Fickian) diffusion and migration (forced diffusion), which may be used independently or summated to approximate the movement of H^+ in the model. These are described by,

$$\frac{\partial C}{\partial t} = -D\left(\frac{\partial^2 C}{\partial x^2} + \frac{\partial^2 C}{\partial y^2} + \frac{\partial^2 C}{\partial z^2}\right) \tag{4.14}$$

And,

$$\frac{\partial C}{\partial t} = nF\frac{\partial}{\partial x}\left(uC\frac{\partial\phi}{\partial x}\right) + nF\frac{\partial}{\partial y}\left(uC\frac{\partial\phi}{\partial y}\right) + nF\frac{\partial}{\partial z}\left(uC\frac{\partial\phi}{\partial z}\right) \tag{4.15}$$

Where u is the ionic mobility of H^+ (assumed to be constant), thereby describing the forced diffusion of H^+ over a time increment Δt. The ionic mobility was estimated from the diffusion coefficient at a position by the Nernst–Einstein equation,

$$D_{i,j,k} = RTu_{i,j,k} \tag{4.16}$$

And this is affected by the volume fraction of corrosion product present, since this has been incorporated using equation 4.11.

First and second order central difference terms are introduced into equations 4.14 and 4.15, to allow implicit approximation of the ordinary and forced diffusion taking place over a time increment in the model. Zero flux boundary conditions (section 2.4.6) are applied to the side faces of the mesh. A fixed boundary condition is used at the top surface that maintained this surface at the initial concentration. This is done in order to model diffusion within a system containing excess electrolyte.

Relaxation is used in the implicit calculation of the concentration fields. Calculations are performed using the Gauss–Siedel iterative technique up to a maximum number of iterations, or until values fall within a pre–defined tolerance with respect to their neighbours within the computational grid. In calculating the simulated concentration field of H^+, using a tolerance of 10^{-6} is typical while imposing an iteration maximum of 200. In the case of the concentration fields, *underrelaxation* is used, with an empirically derived λ value, 0.75. This means that at the end of each iteration, the effective free proton concentration of each cell is determined according to,

$$\begin{aligned} C^{itn}_{i,j,k} &= \lambda C^{itn}_{i,j,k} + (1-\lambda) C^{itn-1}_{i,j,k} \\ &= 0.75 C^{itn}_{i,j,k} + 0.25 C^{itn-1}_{i,j,k} \end{aligned} \tag{4.17}$$

Where itn is a reference to the current iteration and λ is a weighting factor.

4.5.6 Summary of Algorithm

The proposed algorithm for numerical simulation of localized corrosion can be summarized as:-

1. **Discretization** – Generate a discrete solid model of a representative volume of space that differentiates between different solid phases and electrolyte and captures sufficient detail of those features deemed important for the localized corrosion process.

2. **Surface Electrical Potential** – Determine the electrical potential at all solid/electrolyte interface cells as a function of material standard electrode potentials and local electrolyte concentration.

3. **Electrolyte Electrical Potential** – Using the potentials from 2 as fixed or Dirichlet boundary conditions solve the Laplace equation for the electrical potential field throughout the electrolyte.

4. **Solid Dissolution** – Calculate the volume fraction of any interfacial cells that will dissolve and increase local electrolyte concentration accordingly. Cells that completely dissolve are relabelled as electrolyte cells.

5. **Cathodic Reaction** – To ensure electro-neutrality an equal and opposite drop in electrolyte concentration must be applied within the electrolyte.

6. **Diffusion, Migration and Convection** – Transport of charged particles through the electrolyte may be calculated via the standard convection-diffusion equation with the added migration term and taking into account the effects of corrosion products.

7. **Corrosion Products** – Deposition/dissolution of corrosion products at solid/electrolyte interfacial sites is carried out.

8. **Current Density** (Optional) – Using numerical differentiation the current density fields within the electrolyte may be calculated for comparison to experiment.

9. **Time Step** – The time step is incremented and the procedure is repeated again from step 2.

4.6 Current Density comparison to Scanning Vibrating Electrode

To provide comparisons between modelled behaviour and reality the Scanning Vibrating Electrode Technique (SVET) has been used. (Elvins et al., 2003) This calibrated device uses a thin electrode (typically $\leqslant 125\mu$m diameter) that vibrates in the vertical direction (amplitude $\sim 15\mu$m) and scans across the surface in a repeating pattern. It is used to

determine the electrical potential gradient (and hence current density) in the vertical direction at a height of about 100μm above the surface and provides graphical output of the current density distribution over the surface as corrosion proceeds.

As a post-processing step simulated current densities are calculated via numerical differentiation of the electrical field using equation 4.18. This post-processing enables comparison of the predictions made by the computer model to experimentally derived SVET data. Comparison between the form of the simulated current density fields from the model to match reported numerical/analytical solutions is the subject of discussion in section 4.7.

$$i_y = -\frac{1}{\beta}\frac{\delta\phi}{\delta y} \tag{4.18}$$

4.7 Numerical Validation

It has been described how current density can be related to the corrosion taking place in a system. Later sections will show how comparison between current density predictions can be favourable or not, depending on the simulation set up. It is also the case that differences in current density fields do not necessarily correspond to major differences in quantitative measurements. This section is intended to validate the potential fields from the computer model by comparison to rigorous numerical models and experimentation.

4.7.1 3D Current Density Fields

In the computer model the 3D current density fields calculated at each time increment are performed with respect to all 3 dimensions, giving 3 different components; u, v and w. Whilst this is important in revealing the behaviour of the model, a more important measure of current density with respect to validation is the vertical current density field, v. This is due to the measurement of current density during corrosion by means of scanning vibrating probes being the major source of comparative data in order to attempt validation of form and move toward quantitative predictions.

Figure 4.6(a) shows the current density field as it appeared from assessing the current flux in three dimensions. Taking into consideration all of the values present after this calculation, high spots can be seen to occur around any edges in geometry. These values dwarf all others

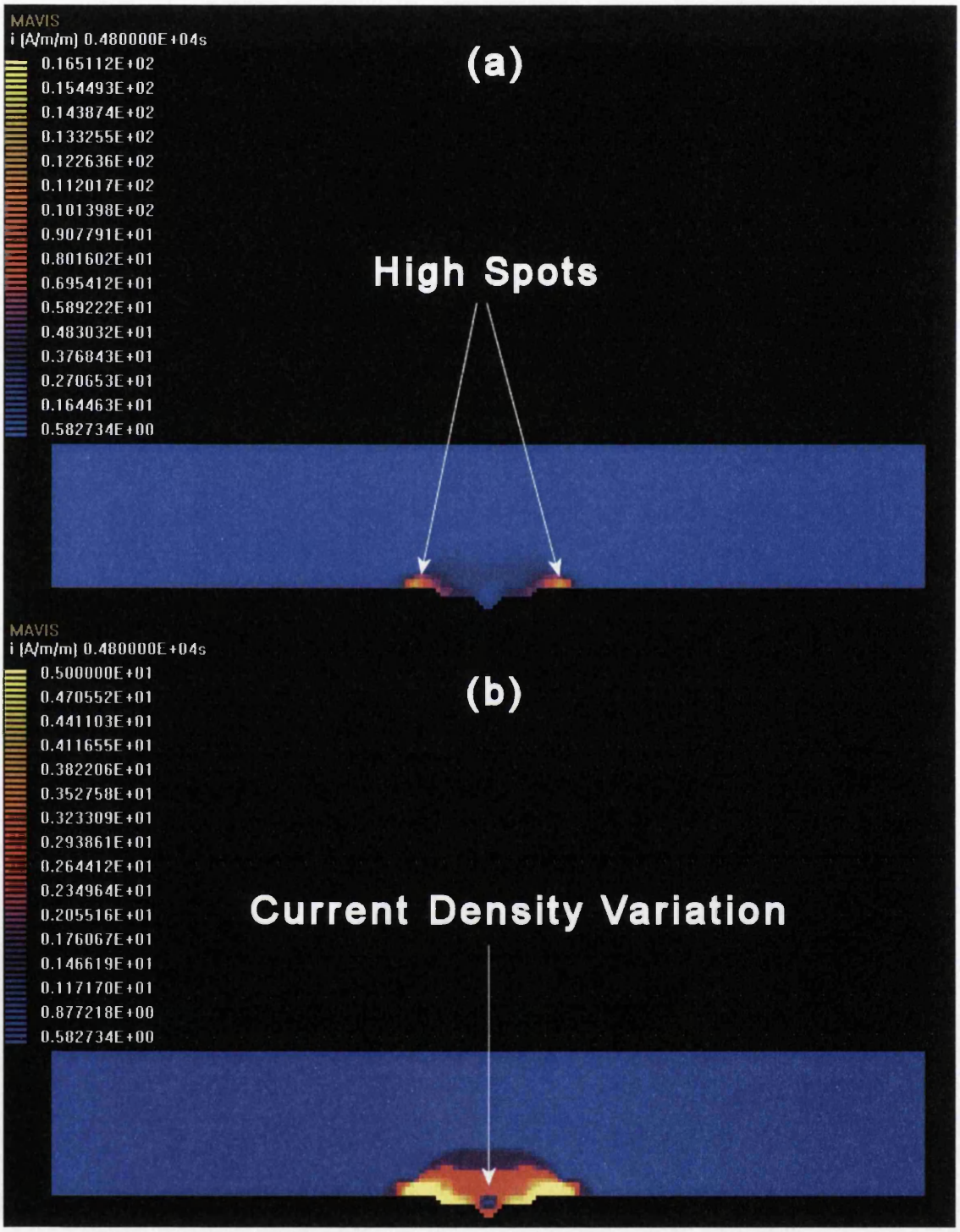

Figure 4.6: 2D slice taken from 3D simulation of a single pit; (a) All current densities present, and, (b) High current densities masked.

around them and suggest graphically that apart from these regions the current densities calculated are all virtually the same. Oldham (1997) considers the diffusion-controlled current densities close to a right-angled electrode edge, concluding that its value may be enhanced compared to current densities remote to the edge. From figure 4.6 it appears that this may be the case taking place in the computer model, since the high spots may be obscuring any lower value definition.

By limiting the current densities shown in the graphical representation of this generated transient field, shown in figure 4.6(b), more detail can be seen to exist in the generated field away from the geometric feature; a newly formed pit in figure 4.6.

In summary, the maximum values of current density fields can be seen to occur in the model at the corners of the pit, although the maximum above the centre of the anodic activity occurs at a position remote from the surface. This effect of height on the current distribution measured with respect to a vibrating electrode probe is discussed by Isaacs (1991). Relationships have also been considered for current with respect to the surface concentration (Mahon and Oldham, 1999) and concentration of electro–active solutes away from the electrode surface (Myland and Oldham, 1999), including differing electrode geometries and kinetics (Mahon and Oldham, 2001).

4.7.2 Electrochemical Processes – Current Densities

Recent work published by Livingstone-Bridge et al. (2001) and Alfred et al. (2002) is of particular relevance in terms of validating the current density fields predicted by the model. These sources describe the solution of Laplace's equation in uniform electrolyte for the geometry of a polarized disc, radius R, inlaid in a coplanar conductor and immersed in an aqueous solutions of conductivity κ. As is the case in the computer model with regards to an area of anodic activity, the geometry corresponds to a corroding inclusion on the surface of a metal sheet when the rate of corrosion is controlled by ohmic polarization.

Livingstone-Bridge et al. (2001) describes two independent, but different solutions of Laplace's equation, both based on the premise that the two metallic regions have distinct uniform electrical potentials, as is the case in the computer model where the straightforward approximation of the steady-state voltage fields is made. The results of these two numerical

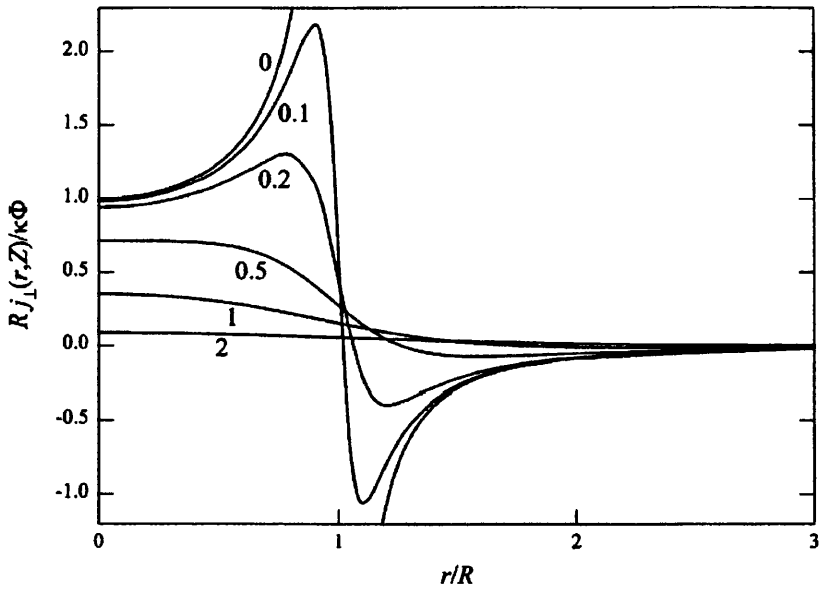

Figure 4.7: The vertical current density in the vicinity of a corroding anode of radius R, normalized by division by $\kappa\Phi/R$, where Φ is the corrosion potential and κ is the solution conductivity . The number associated with each curve is the value of Z/R where Z is the constant height above the metal sheet at which $j_\perp$ is sampled. (Livingstone-Bridge et al., 2001)

methods have been found to be qualitatively similar to reported experimental findings using the SVET.

4.7.3 Numerically Derived Current Density Predictions

$$\frac{Rj(r,Z)}{\kappa\Phi} = \frac{2NR^2}{Z^2}\sum_{n=1,3}^{N-1}(N-n)J_0\left\{\frac{(N-n)r}{nZ}\right\} \times\left\{\frac{(N-n)R}{nZ}\right\}\exp\left\{\frac{n-N}{n}\right\}\frac{1}{n^3} \tag{4.19}$$

The majority of the curves in figure 4.7 were derived from equation 4.19 by giving the Z/R ratio a variety of non-zero values. These graphs express the normalized radial distribution of the vertical component of $j_\perp$ of the corrosion current density distribution at various heights above the metal surface. A noteworthy feature of figure 4.7 is the transition, as the values of Z increases, of the radius at which $j_\perp$ peaks from the region of the rim of the anode to its centre.

For all Z values not less that $R/2$, a peak occurs above the centre of the disk-shaped

region, having height that varies with Z. When $Z < R/2$, the peak occurs away from the axis of symmetry.

Another transition that occurs as Z increases is the value of the radius r at which at which $j_{\perp}(r,Z)$ equals zero. This is not, of course, where the current density is zero, but rather where the current distribution lies parallel to the metal surface. With an increasing Z, the location of this horizontally moves steadily outwards from a position at the anode's edge. (Livingstone-Bridge et al., 2001)

For the Z/R values of the 0.2, 0.5 and 1.0, figure 4.8 uses a three-dimensional display method as is sometimes used to report experimental SVET data. In all cases a negative 'moat' surrounds a positive 'mountain'. When Z is less than $R/2$, the mountain is volcano-shaped, when $Z = R/2$, the mountain is topped by a plateau, whereas at larger Z values the mountaintop is peaked. Experimental plots published lack the resolution present in a mathematical model, but there are distinct similarities to the third type of current density profile.

In the models published by Livingstone-Bridge et al. (2001), no particular region is encouraged to be more cathodic than others, resulting in cylindrical symmetry.

4.7.4 Current Density Predictions from Corrosion Model

A validation simulation was performed, including the situation of an anodic disc of radius R=0.5mm, and at a polarization Φ, set in a material of a constant cathodic capacity 6 mm $\times$ 6 mm in dimensions. Electro–neutrality was observed and the cathodic current densities at the surface of the material were calculated using Laplace's equation to satisfy the steady–state voltage fields at this polarization in the presence of an electrolyte of constant conductivity, κ. Vertical current densities were then calculated at different raster heights, Z, and these are then presented in a similar manner to the two numerical solutions in section 4.7.3 in order to aid comparison. Results for three sampling heights are given; 100 μm, 180 μm and 300 μm. This equates to $Z/R = 0.2$, $Z/R = 0.36$ and $Z/R = 0.6$ respectively.

What can be seen in figure 4.9 is that as the sampling height, Z, is increased the peak of current density, $j_{\perp}$, moves towards the centre of the radius, away from the edge of the

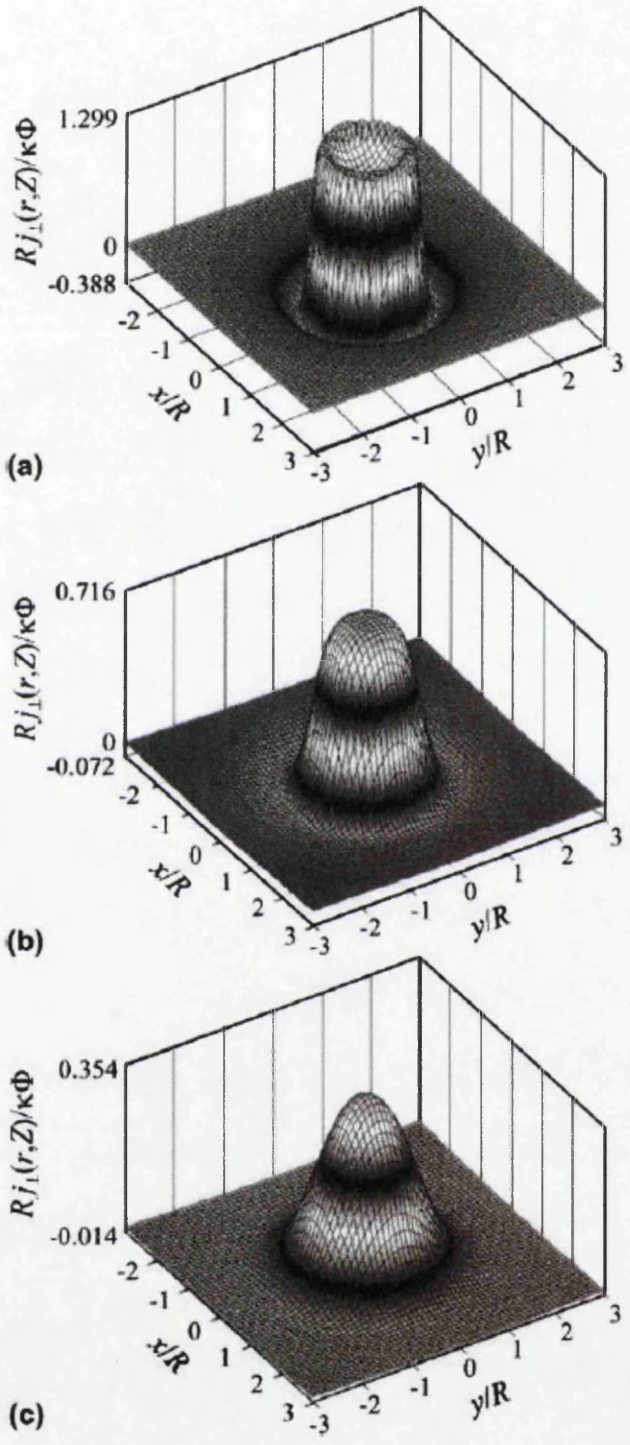

Figure 4.8: Three-dimensional maps of the normalized vertical current density, when the raster height Z equals: (a) $R/5$, (b) $R/2$ and (c) R. Each ordinate has been scaled to match the maximum and minimum current densities. (Livingstone-Bridge et al., 2001)

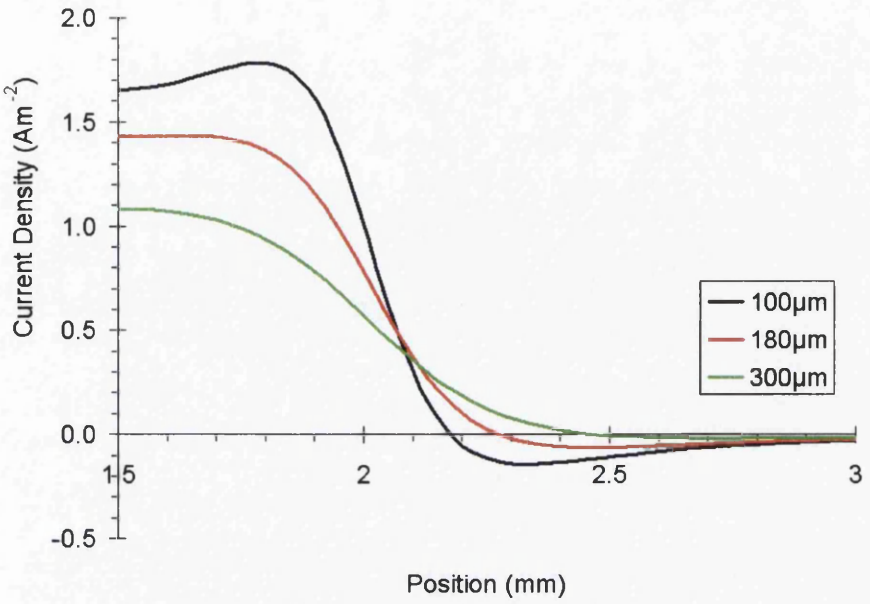

Figure 4.9: Vertical current density, $j_{\perp}$, above a simulation of a polarized disc in a semi–infinite homogenous material.

polarized inclusion. It can also be seen, consistent with the numerically calculated $j_{\perp}$ illustrated in figure 4.7, that the intensity of the current density diminishes at a greater height. Another feature shown to replicate that shown in figure 4.7 is the transition of positive $j_{\perp}$ to negative $j_{\perp}$, occurring further from the centre of the anodic material, and indeed the edge of the inclusion as the height is increased. In addition, the negative peak is also greatest at lower sampling heights.

The trends in the 3D current density profiles numerically solved in figure 4.8 can be seen to occur in the results from the solution of Laplace's equation in a solution of uniform conductivity in the simulation of a disc–shaped inclusion shown in figure 4.10. At 100 μm, $Z < R/2$, a highly concentrated negative moat surrounds a volcano–shaped mountain. A raster height of 180 μm yields a plateau–topped mountain profile, typical of the transition shown in figure4.8(b), and the negative moat can be seen to spread further from the edge of the polarized disc. This negative moat becomes even more diffuse at higher raster heights where $Z > R/2$, as seen in figure 4.10 at 300 μm. Here the peak of current density occurs at the axis of symmetry, above the centre of the disc. A prominent feature highlighted in section 4.7.3 that can be seen to be captured by the model is the increase in radius, r (position shown in figure 4.9), at which $j_{\perp}(r,Z)$ becomes zero as the raster height is increased.

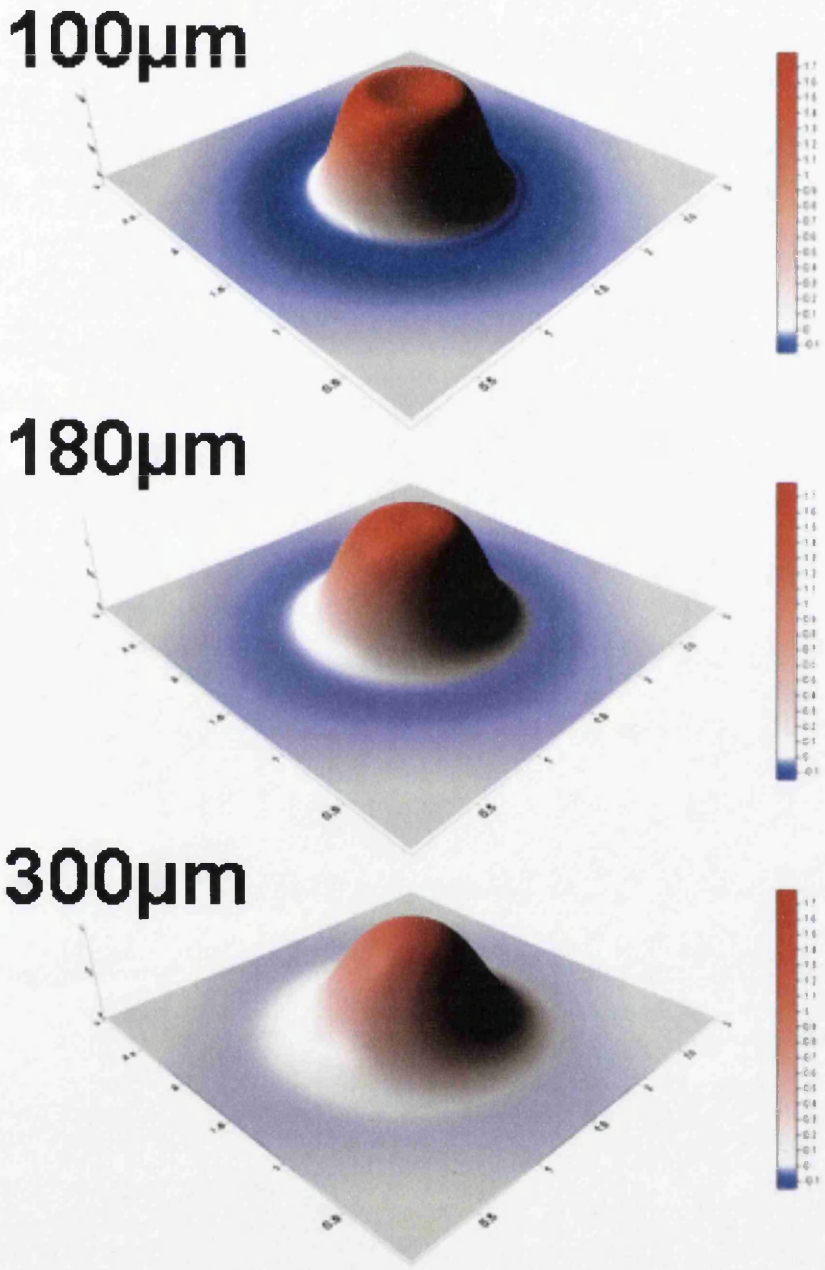

Figure 4.10: Three dimensional maps of vertical current density, $j_{\perp}$, at three different raster heights. Current density values in Am^{-2}.

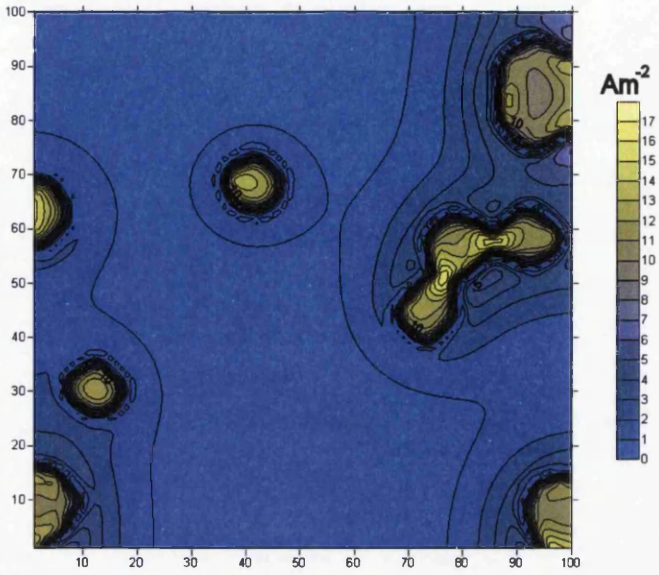

Figure 4.11: Validated vertical current density field 100 μm above corroding zinc in 0.1% NaCl solution. Distances in mm.

The form of the current density fields predicted appears to follow that expected from calculations using Laplace's equation. It can be appreciated that the discrepancies exhibited between the 3D current density vectors and the vertical current density fields measured from the SVET may arise from underlying detail, influence of geometrical effects and the changes in current density fields as a result of direction rather than simply magnitude.

In the simulation of the disc–shaped inclusion, no area outside of that material held at an anodic potential, had any restrictions on the cathodic potentials calculated. This is obviously not the case when corrosion is acting on areas of the same surface, even a pure metal in an electrolyte of constant conductivity. Figure 4.11 shows the current density map above pure zinc with several instances of pre–nucleated corrosion sites. The areas of the surface selected for cathodic current can be seen to be influenced by the proximity to anodic effects operating. This localization of cathodic in perimetric regions can be seen to deviate from the cylindrical symmetry seen in figures 4.9 and 4.10, reinforcing the links made from theory to observations.

Chapter 5

Results

Presented in the chapter are the predicted results from investigations into:

- Surface and cut–edge corrosion of Electroplated Zinc Coated Steel.
- Corrosion performance of Galfan coated steel at the exposed surface and cut–edge.
- Influence of cooling rate of Zn – 4.5 wt.% Al steel coatings on the surface and cut–edge corrosion experienced.

The reults from the corrosion model are presented in this chapter. The simulations were performed in order to quantitatively predict the localized corrosion effects experienced by electroplated zinc (EZ) and Galfan coated steels in an aggressive electrolyte; 0.1% and 5% NaCl solution respectively. The purpose of the simulations shown was to ascertain whether or not the numerical model was able to predict observed events and corrosion mechanisms from fundamental relationships and readily available data; diffusion coefficients, electrical resistivities and ionic mobilities.

All simulations were performed at pH neutral, isothermal and, unless stated otherwise, on a mesh comprising $200 \times 50 \times 200$ nodes in the x, y and z directions respectively. Details of the types of setup used in the simulations shown are outlined in chapter 4 although some features have been distorted in order to enable closer examination of the behaviour of the model in certain circumstances. Unless stated to the contrary, the simulations involve the representation of light gauge steel substrates of thickness 0.47 mm and coating thicknesses of 2 μm and 25 μm for EZ and Galfan respectively.

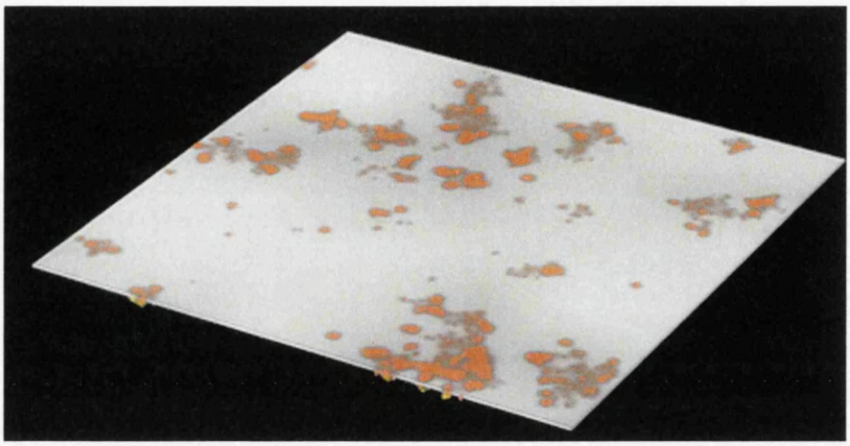

Figure 5.1: Concentration field, $[H^+]$ at the Galfan coating – electrolyte interface.

In all cases depicted for the case of EZ coated steel nucleation has been started via the dissolution of a single cell at the solid–electrolyte interface. This was done to avoid the situation of having generalized corrosion all across a perfectly planar surface in the surface corrosion case. It is assumed that these nucleation events have arisen from the presence of a defect (e.g. coating discontinuity or a dirt particle) that has brought about local elevations in ionic concentrations at that point. Deliberate nucleation is not used in the simulation of the localized degradation of the Galfan coated steel at any point, and once time marching has begun no further nucleation events are enforced, even in the EZ cases.

As described previously in chapter 4, the numerical model is driven by local fluctuations in simulated ionic concentrations. The evolution of this concentration from a corroding Galfan coated steel can be seen in figure 5.1. This shows higher values of the effective free proton concentration (orange areas) above areas of anodic dissolution at the coating – electrolyte interface. Figure 5.1 only represents the layer of electrolyte cells at the initial surface and highlights the effect dissolution events have on the H^+ concentration experienced in the local neighbourhood. The evolution of the ionic concentration field then alters the thermodynamics and kinetics of the predicted corrosion of the zinc and zinc alloy steel coatings.

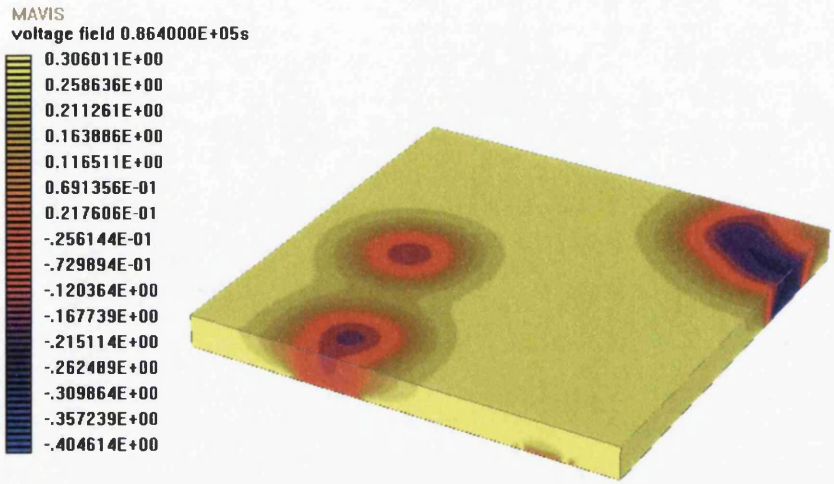

Figure 5.2: Electrical potential field throughout 0.1% NaCl solution in contact with the surface of an electroplated zinc coating after 24 hours.

5.1 Zinc Steel Coating Results

Simulations were performed in order to demonstrate the capability of modelling in this manner, the corrosion processes taking place when an electroplated zinc (EZ) coated steel is exposed to 0.1% NaCl solution; both at the surface or at a cut–edge. The evolution of ionic species emanating from the surface in the case of EZ coated steel is the same as that for Galfan coated steel shown in figure 5.1, where a concentration contribution is made to the local neighbourhood according to the volume of the cell transforming.

5.1.1 Surface exposure of Electroplated Zinc (EZ) coated steels to 0.1% NaCl solution

The electrical potential field predicted throughout 0.1% NaCl solution in contact with an exposed EZ coated steel is shown in figure 5.2. What can be seen is the result of applying the Laplace equation to solve the electrical potential field throughout the bulk electrolyte, using the electrode potentials determined at the coating – electrolyte interface using a Nernst relationship as a Dirichlet boundary condition. In the case of figure 5.2 the simulated time of exposure to the NaCl solution is 24 hours. The areas experiencing the highest value of potential, in this case indicating cathodic activity, are shown by the yellow areas and a representative predicted maximum value of +0.31 V is observed. The areas of the

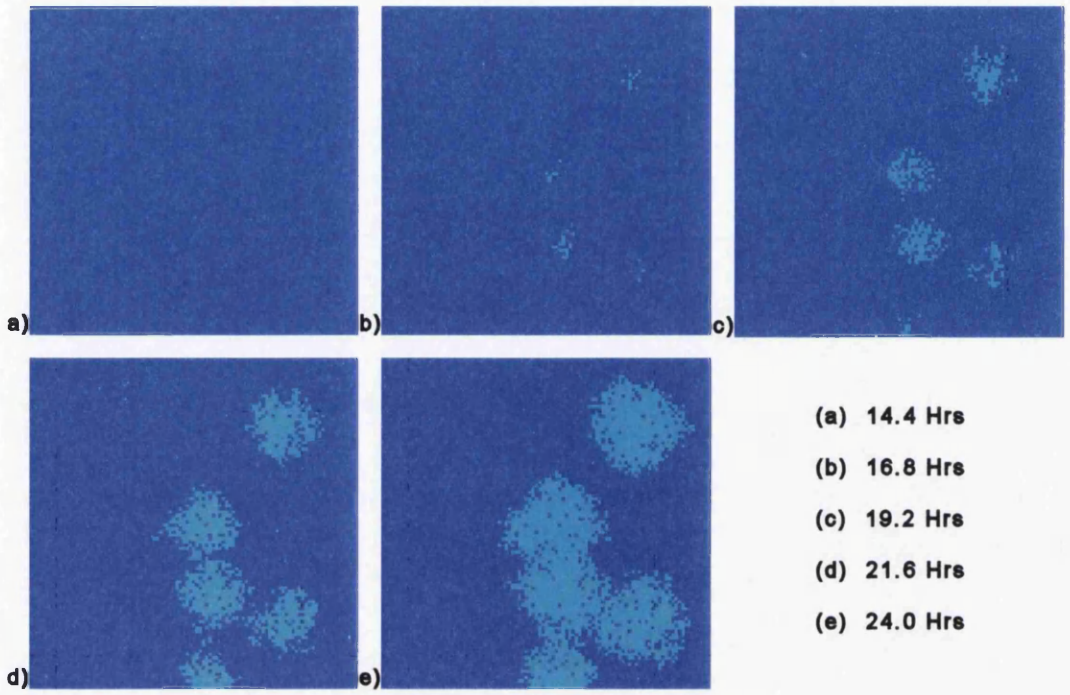

Figure 5.3: Exposed steel at the solid–electrolyte interface during 24 hours exposure of an EZ coated steel to 0.1% NaCl solution.

surface where anodic zinc dissolution is predicted are shown by the most negative areas, to a minimum potential value of -0.41 V. The most severe anodic attack predicted can be seen to occur in the portion of the electrolyte to the right of figure 5.2, where there were more nuclei sites in close proximity. The anodic dissolution predicted by the defects assumed to be situated to the left of figure 5.2 can be seen to give rise to substantial anodic attack (low, negative potentials) albeit of lower severity. Also present in figure 5.2 is a small localized corrosion effect visible at the bottom close to the coating – electrolyte interface. Whilst this has arisen from an forced nucleation point of equal magnitude as the others, this localized attack is far less severe in terms of magnitude and form.

Figure 5.3 represents a plan view of the material exposed to the 0.1% NaCl solution during simulation of surface EZ corrosion. The total area exposed to the 0.1% NaCl solution in figure 5.3 is 2.5 mm $\times$ 2.5 mm. What can be seen is that as the simulation progresses the area fraction of the coating and exposed substrate alters. It can be seen from figure 5.3(a) and (b) that between 14.4 and 16.8 hours simulated time, the steel substrate becomes exposed to the electrolyte. In figure 5.3 the dark blue areas represent the electroplated zinc coating and

the light blue the steel substrate. Once this steel is exposed the model predicts an increase in anodic activity resulting in higher rates of zinc removal, increasingly exposing greater areas of steel substrate. This can be seen in figure 5.3(c) to (e) as an increasing area fraction of steel substrate (light blue) is observed.

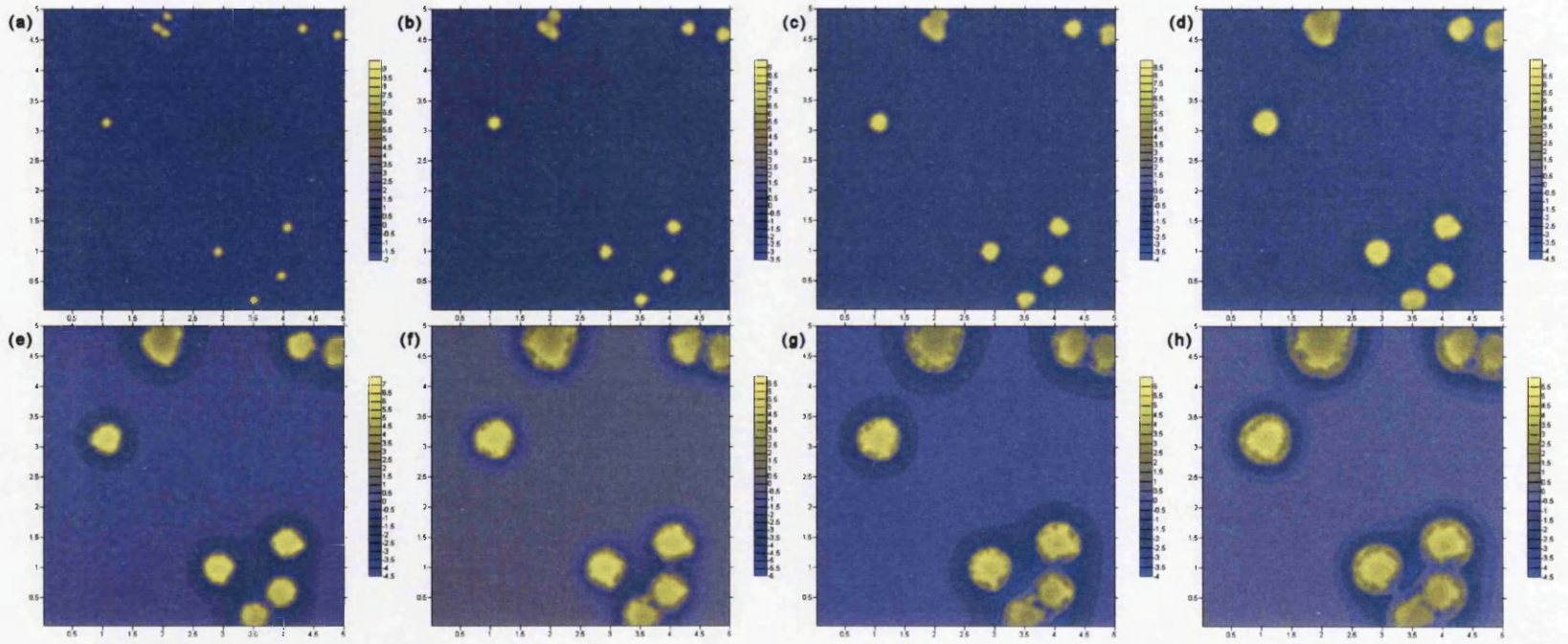

Figure 5.4: Current density (Am^{-2}) maps 100 μm above the initial solid–electrolyte interface during the surface corrosion of a EZ coated steel in contact with 0.1% NaCl solution; (a) 4.8, (b) 7.2, (c) 9.6, (d) 12.0, (e) 14.4, (f) 16.8, (g) 19.2, and, (h) 24 hours simulated time respectively. Distances in mm.

Typical normalized vertical current density fields above an exposed EZ coated steel can be seen in figure 5.4. The evolution of the vertical current density at a plane parallel to the coating surface, generated in the model using equation 4.18, can be seen throughout the 24 hours simulated exposure time in figures 5.4 (a) through (h). In figure 5.4(a) the highest positive values of current density in the y direction are represented by the yellow areas. These yellow areas denote anodic current density and occur at areas that have been subject to the initial deliberate nucleation of local defects at the EZ surface. Corresponding cathodic current densities, i.e. negative values of $\frac{\delta i}{\delta y}$, can be seen in figure 5.4 as blue areas. During the early stages of the simulation, the maximum cathodic current densities can be seen to be spread out across the sampled plane, as can be seen in figure 5.4(a), (b), and to a certain extent (c). During the latter stages of the simulation of the EZ coated steel exposed to 0.1% NaCl solution, the maximum cathodic current densities are observed in spatially discrete, perimetric regions around the areas of anodic dissolution predicted at the coating surface. The magnitude of the highest anodic current density and cathodic current density can be seen to change over the duration of the simulation. In figure 5.4 it can be seen that the upper limit of the normalised vertical current density can be seen to increase from an initial value of 3 Am^{-2} up to a maximum of 9 Am^{-2} after 7.2 hours (figure5.4(b)). After this maximum, the magnitude of the positive current densities experienced by areas of the surface subjected to anodic dissolution is reduced.

Significantly, the point at which the steel substrate is exposed to the 0.1% NaCl solution marks a change in the anodic current densities predicted 100 μm above the simulated corroding interface. After a simulated time of 16.8 hours the steel substrate becomes exposed, as shown in figure 5.3. At this point the maximum positive current densities experienced, and thereby the subject of the most intense anodic dissolution predicted, occurs at areas away from the centre of the nucleated defect. These areas then reside around the perimeter of the exposed steel region during the rest of the simulation, whilst zinc remains in electrical contact with the steel at the corroding surface. These predicted effects can be seen in figure 5.4(f) through (h).

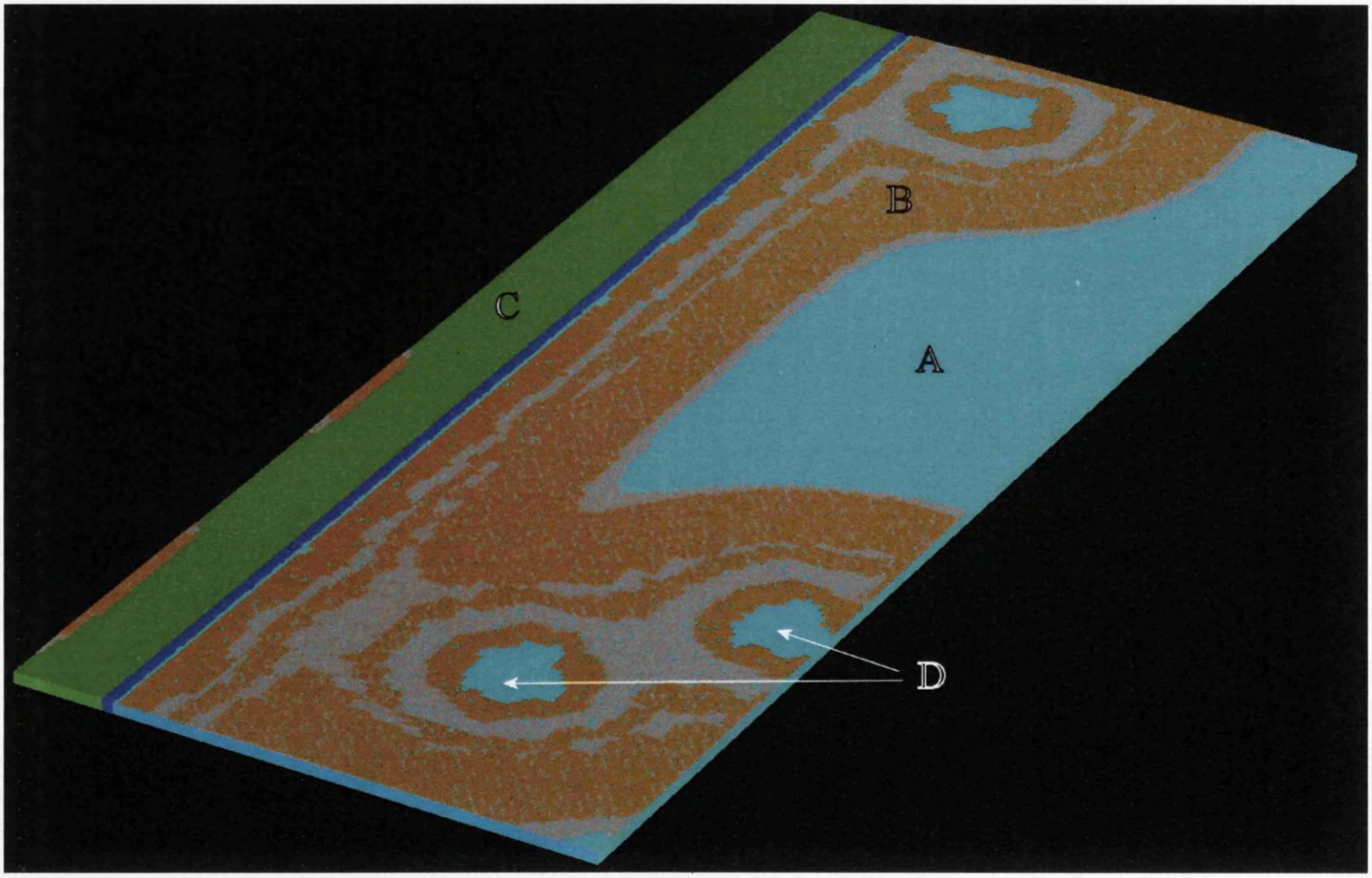

Figure 5.5: Solid model showing the resultant degradation experienced at the cut–edge of an EZ coated steel sample. A – Exposed steel; B – Sites containing $\geqslant 0.1$ volume fraction corrosion product; C – Inert resin material; D – Sites of imposed nucleation.

5.1.2 Cut–edge exposure of Electroplated Zinc (EZ) coated steels to 0.1% NaCl solution

The result of 24 hours degradation of an EZ coated steel exposed at the cut–edge to 0.1% NaCl solution can be seen in figure 5.5. As was the case for the surface exposure of the EZ coated steel, nuclei instigating the corrosion process were present, although in this case these nuclei were present over the zinc and steel exposed at the solid–liquid interface. The inert material included in the simulation in order to map the transient variable fields throughout the simulation, described in chapter 4, is indicated in figure 5.5 as the green region, C. The area of steel that remains exposed after 24 hours simulation is indicated by the light blue region, A. The dark blue region shown is the electrolytically applied pure zinc coating, the focus of much anodic dissolution. The region marked B in figure 5.5 signifies the presence of corrosion products deposited at the solid–liquid interface. These corrosion products are shown as either grey or brown regions according to the volume fraction of those cells that are occupied by the corrosion products, as discussed in section 4.5.4. The corrosion products can be seen to be spread across the area of exposed steel, leaving the zinc coating layer uncovered after 24 hours simulated corrosion. In addition to the zinc being uncovered, the positions across the steel that were also the sites of forced nucleation remain untouched; and these can be seen in figure 5.5 at the positions marked D.

The electrical potential field predicted throughout the 0.1% NaCl solution can be seen in figure 5.6, at a simulated time of 5.3 hours, corresponding to the setup shown in figure 5.5. The cathodic voltages can be seen by the blue and purple regions and the most cathodic areas can be seen to the right of figure 5.6, corresponding to the exposed steel with no forced nucleation of corrosion effects present. The most intense cathodic voltages occur at these sites and at 5.3 hours the maximum value of these is 0.4 V. This value can be seen to reduce in the electrolyte when examining positions closer to those above the zinc coating. At areas of the exposed steel where local corrosive effects are taking place, the voltages experienced in the electrolyte exhibit a different polarity, and these anodic potential areas are denoted by the yellow, orange and red regions in figure 5.6. The most intense areas of anodic dissolution can be seen to occur over the zinc coating, close to the solid-liquid interface. The maximum value of this anodic potential after 5.3 hours is -0.66 V, and anodic areas, albeit of a lower

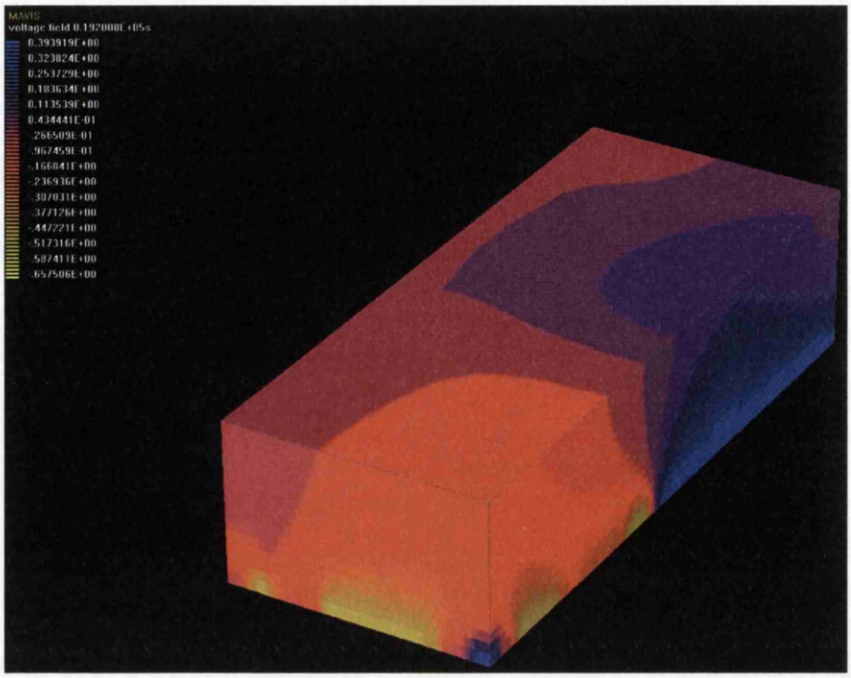

Figure 5.6: Electrical potential field throughout the 0.1% NaCl solution at 5.3 hours during the cut–edge corrosion simulation of an EZ coated steel.

intensity, can be witnessed across the exposed steel areas in figure 5.6.

5.2 Zinc–Aluminium Steel Coating Results

This section describes the attempts made to model the localized corrosion effects experienced by a two–phase, hot–dipped zinc–aluminium steel coating, namely Galfan. Firstly the effects of the exposure of a two–phase structure to 5% NaCl solution is considered in terms of surface and cut–edge corrosion. Simulated structures similar to those generated in mass production are considered. Finally, the effect of the geometric arrangement is considered in several 2D cases for the combination of exposed steel and Galfan coating.

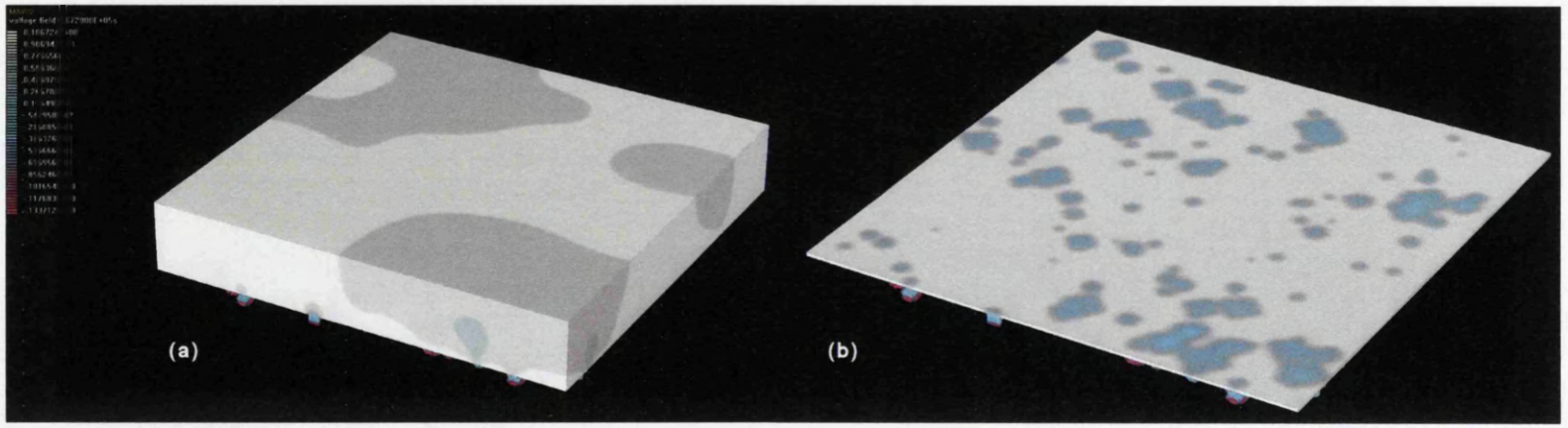

Figure 5.7: Electrical potential throughout 5% NaCl solution above a corroding Galfan coating after 18.6 hours simulated time; (a) All electrolyte included in the simulation shown, and, (b) Electrolyte elements above the initial Galfan–electrolyte interface ignored.

5.2.1 Surface exposure of Galfan (Zn – 4.5 wt.% Al) coated steels to 5% NaCl solution

The electrical potential field above a corroding Galfan coating exposed to 5% NaCl solution is shown in figure 5.7. Anodic potentials are represented as purple areas in figure 5.7, whereas cathodic potentials are described by the white regions. The maximum value for anodic voltages predicted after 18.6 hours is -0.13 V, and the corresponding maximum for cathodic potential present is 0.11 V. Figure 5.7(b) describes the electrical potential of the initial coating–electrolyte interface, and it is the case that many areas of elevated potential have arisen from the presence of multiple phases and effects brought about by simulated local corrosion effects. However, when one considers the entire electrolyte generated in the simulation, it is clear that the activity at the interface brings about few areas of change throughout the bulk electrolyte, as shown in figure 5.7(a).

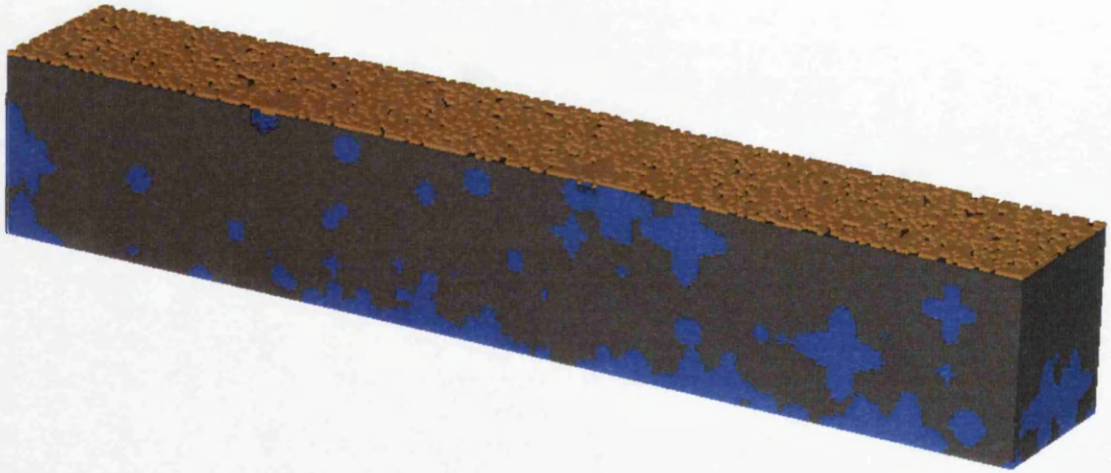

Figure 5.8: 3D representation of simulated Galfan coating exposed to 5% NaCl solution for 24 hours.

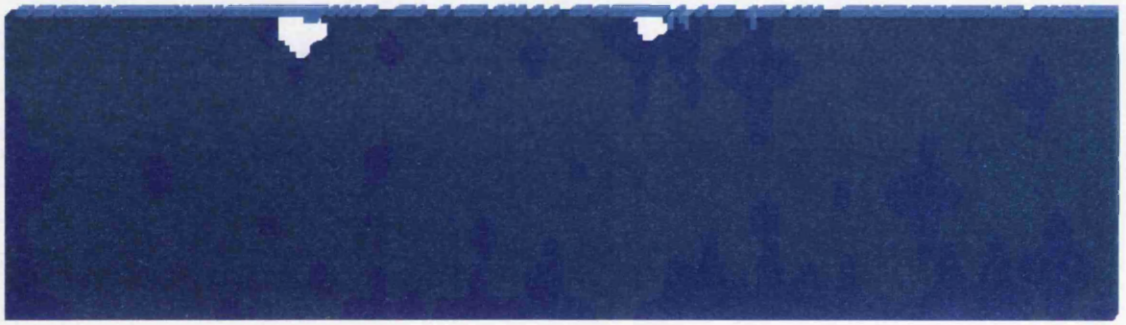

Figure 5.9: Vertical slice taken from a 3D simulation for the surface degradation predicted of an exposed Galfan coating.

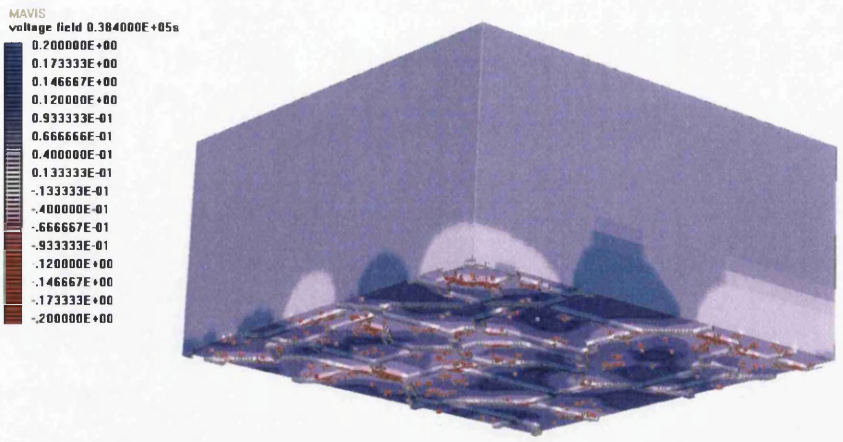

Figure 5.10: Electrical potential field in simulated 5% NaCl solution above a corroding Galfan coating after 10.67 hours exposure.

The resultant degradation at the surface of a Galfan–type coating exposed to 5% NaCl solution is shown in figure 5.8. The size and shape of the dendritic zinc rich phase, shown as dark blue regions, are somewhat exaggerated in the simulation shown in figure 5.8 in order that the behaviour of the structure may be examined. The rest of the solid material shown is the ZnAl eutectic, denoted by the grey areas. It can be seen in figure 5.8 that it is the primary zinc phase that is the subject of the majority of the localized degradation at the surface. It can also be seen for the most part that the surface of the Galfan coating is covered with a layer of corrosion product, although the brown cells present in figure 5.8 indicate that the electrolyte cells present at the solid–liquid interface contain a relatively low volume fraction of corrosion product (< 0.1).

Figure 5.9 represents a vertical slice taken from the simulation shown in figure 5.8, one cell thick. This clearly shows the greater removal of primary zinc material (dark blue) with respect to the eutectic phase (lighter blue). In this case the corrosion product deposited at the surface is represented by the lightest blue cells present at the corroding surface. Apparent from figure 5.9 is the different degree of degradation experienced by the same material at different positions at the coating–electrolyte interface.

The electrical potential experienced throughout the 5% NaCl solution above the surface of a Galfan coating can be seen in figure 5.10. The depressions (pre–placed in the grid to simulate depressions at eutectic grain boundaries) included in the Galfan microstructure are

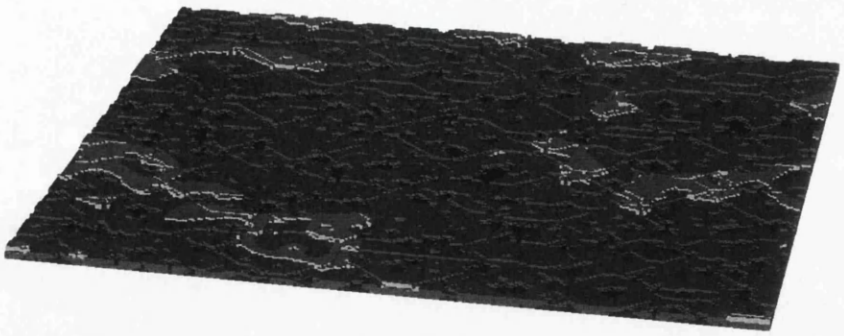

Figure 5.11: Solid model after 24 hours of simulated exposure to 5% NaCl solution. Lighter areas are regions containing $\geqslant 0.1$ volume fraction of corrosion product.

evident, as is the selective dissolution of the zinc rich phase present at the coating–electrolyte interface. These are the sites of the highest anodic potential present, which after 10.67 hours is approximately -2 V, which is equal and polar opposite to the maximum cathodic voltage of 2 V. The greatest regions of anodic activity can be seen in figure 5.10 at the points where two or more eutectic cell depressions meet, whereas the majority of the cathodic activity is present at the higher areas of the exposed surface at regions that are predominantly occupied by eutectic material.

A larger area of Galfan is represented in figure 5.11 where the degradation experienced over 24 hours exposure to 5% NaCl solution is shown. Once again the primary zinc dendites present at the coating–electrolyte interface are subjected to a greater degree of corrosion than the relatively untouched eutectic phase. The electrolyte sites whose volume fraction of corrosion product is greater than 0.1 are shown to be deposited in definite areas across the surface at sites where, with respect to material composition, very little variance is evident.

The corrosion product deposited at the surface of the Galfan coating can be seen more clearly in figure 5.12, indicated by the region labelled A. It can be seen that the corrosion products are deposited above and below the initial solid–liquid interface, throughout the depressions and across the planar interface. The partial and complete removal of a zinc dendrite at the surface of the exposed Galfan coating can be seen at points B and C respectively.

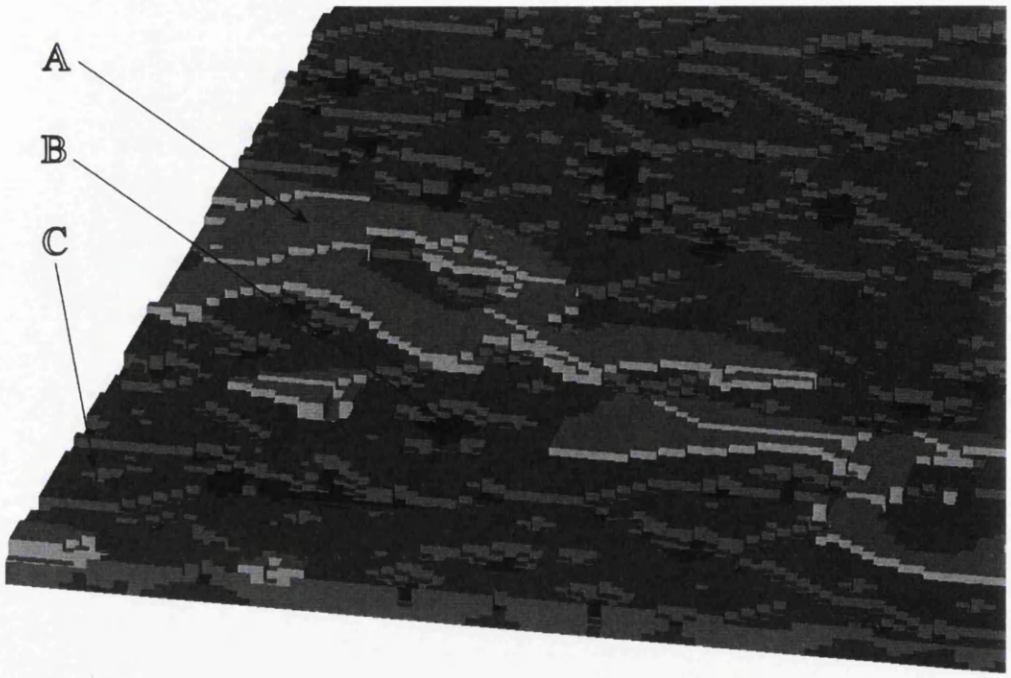

Figure 5.12: Magnified view of corroded surface showing corrosion products (A), partially dissolved primary Zn dendrites (B) and completely dissolved primary Zn dendrites (C).

5.2.2 Cut–edge exposure of Galfan (Zn – 4.5 wt.% Al) coated steels to 5% NaCl solution

A 3D simulation of the surface and cut–edge exposure of a Galfan coated steel to 5% NaCl solution can be seen in figure 5.13. The amount of steel present in figure 5.13 is not representative of the thickness of steel used in the applications described previously, nor is the dendritic structure accurately matched to those generated during mass fabrication. However, figure 5.13 does show the behaviour of the computer model in this situation. Firstly, the degradation at the surface does exhibit the same form and extent of that shown for the surface case in figure 5.8. At the cut–edge the amount of degradation experienced by the zinc rich phase present at the solid–liquid interface is greatly increased due to the presence of the steel present. Some of the dendrites have been completely consumed by the localized corrosion effects operating at the interface whereas for other areas it is predicted that only partial dissolution of the dendrite has taken place. The deposition of corrosion product can be seen to take a different form at the cut–edge than the exposed surface. Rather than a complete covering, in the case of the cut–edge the corrosion products are deposited around

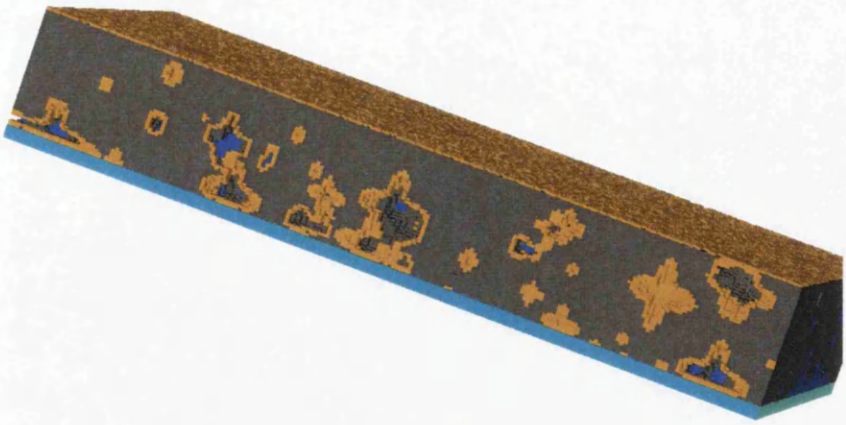

Figure 5.13: 3D representation of simulated Galfan coated steel exposed at the surface and cut–edge to 5% NaCl solution for 24 hours.

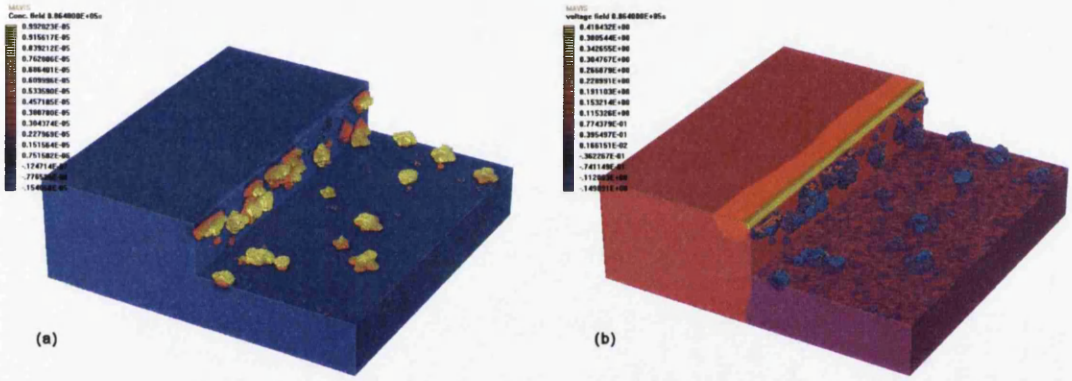

Figure 5.14: 3D variable fields around a simulated Galfan coated steel sample exposed at the surface and cut–edge, depicted in figure 5.13 (inverted); (a) Concentration Field, $[H^+]$, and, (b) Electrical potential field, (V).

active sites of anodic zinc dissolution. It is also evident in figure 5.8 that at sites further away from the steel substrate the zinc denrite regions are completely covered after 24 hours, whereas those sites close to the steel, the corrosion products can be seen to 'shroud' the local areas of zinc removal.

Figure 5.14 shows the ionic concentration field, (a), and electrical potential field, (b), around the setup shown in figure 5.13. In terms of the concentration evolving from the localized corrosion effects occurring at the surface and cut-edge of a Galfan coated steel, it is predominantly from the areas affected by the local anodic dissolution of the zinc rich dendrites. The morphology of the predicted pits mean that this concentration is retained in

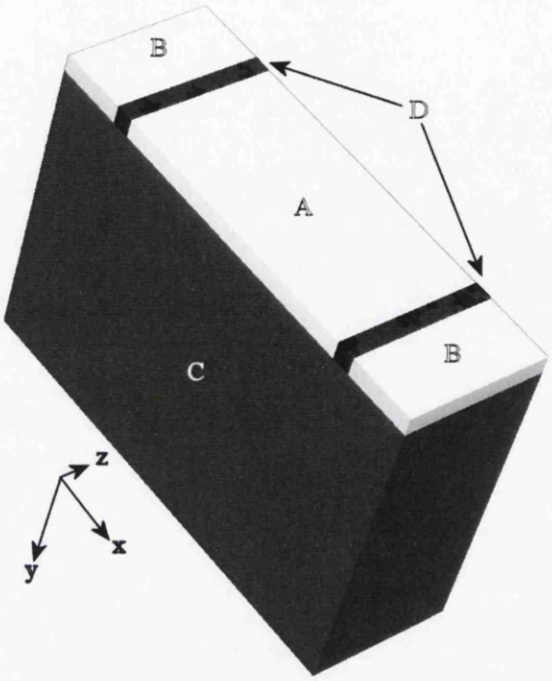

Figure 5.15: Solid model of cut–edge corrosion specimen viewed from below. A – steel, B – inert resin layer, C – electrolyte, and, D – ZnAl coating layer comprising primary zinc dendrites (darker) in a eutectic matrix (lighter). Length, x=0.77 mm, height, y= 0.5 mm and width, z=250 μm.

the pits, and also, significant perturbations in concentration are not shown to exist in the bulk electrolyte shown in figure 5.14. The maximum concentration of H^+ is observed within the pits and is 0.99×10^{-05} mol dm^{-3}. The maximum anodic voltage experienced in figure 5.14 equates to -0.15 V. Conversely, the highest cathodic electrical potential observed is greater at 0.42 V, and is highly localized along the length of the steel exposed to the NaCl solution.

The simulations performed in order to reflect the resulting microstructure observed from Galfan steel coatings produced via hot–dipping were setup as shown in figure 5.15. The steel, A, is coated on both sides by a Galfan coating layer 25 μm thick, D, which in turn is bounded at either side by an inert resin layer, B. The electrolyte simulated is shown by the volume C, which is approximately 0.5 mm in depth.

The make up of the ZnAl coating layers shown in figure 5.15 is shown more clearly in figure 5.16. The Galfan coating layers, C, can be seen to be made up of zinc dendrites, E, within a ZnAl eutectic matrix, D. In this case the electrolyte is not shown.

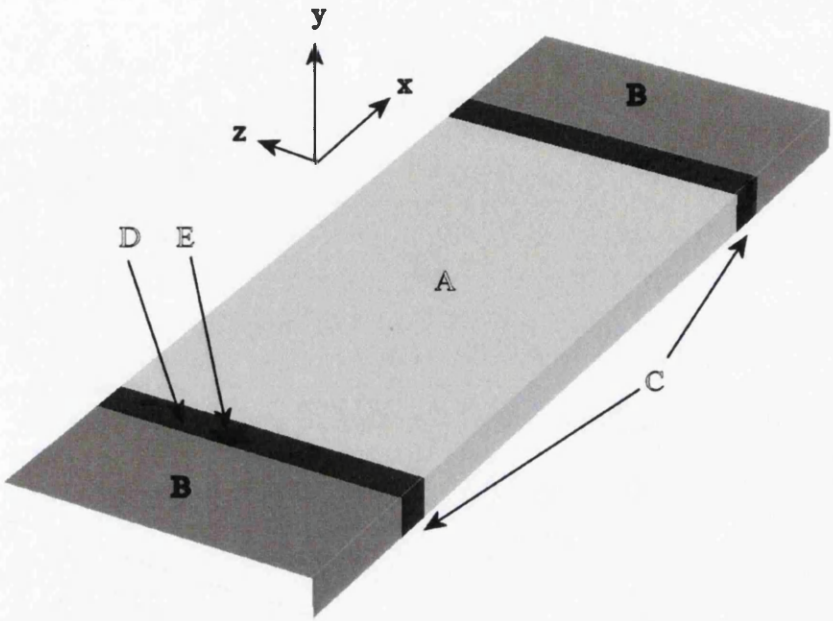

Figure 5.16: Solid model of cut–edge corrosion specimen viewed from above with electrolyte not shown. A – steel, B – inert resin layer, C – ZnAl coating layer comprising primary zinc dendrites (E) in a eutectic matrix (D). Length, x=0.77 mm and width, z=250 μm.

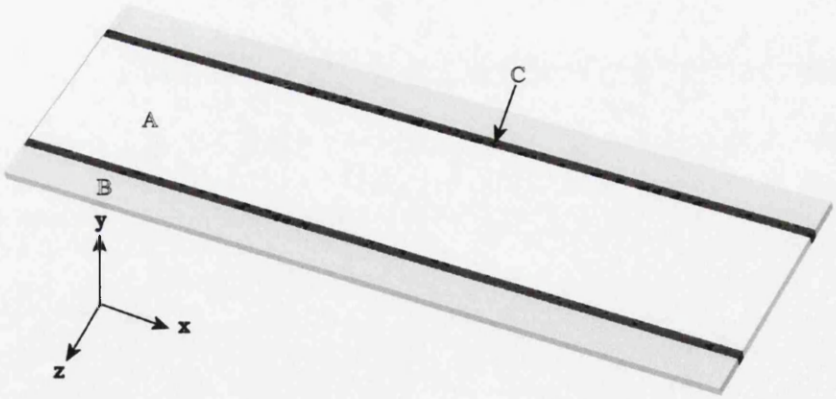

Figure 5.17: Solid model of cut–edge corrosion specimen viewed from above with electrolyte not shown. A – steel, B – inert resin layer, C – ZnAl coating layer comprising primary zinc dendrites in a eutectic matrix. Length, x=2.5 mm and width, z=0.77 mm.

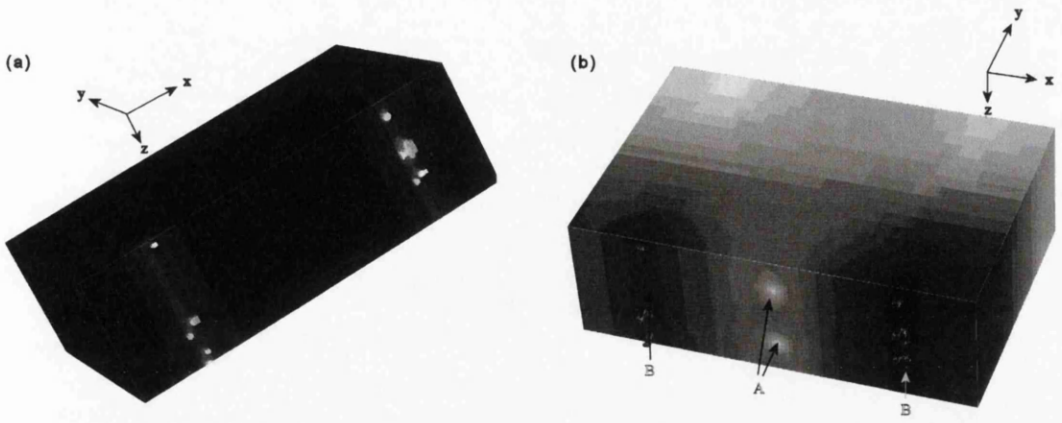

Figure 5.18: Variable fields throughout 5% NaCl around the setup shown in figure 5.16 after 24 hours simulated exposure (non-electrolyte elements not shown); (a) Concentration field, and, (b) Electrical potential field.

Figure 5.17 shows the same setup of the solid model, except that the cut–edge length exposed to the 5% NaCl solution is 2.5 mm, far greater than the 0.7 mm described by the two preceeding figures. This represents the upper limit of simulation size that is able to contain the form of the zinc dendrites present in the Galfan coating layers simulated, C. The thickness of the steel substrate, A, remains the same at 0.47 mm; a light gauge strip steel. In addition to this, the width of the inert layer, B, is also kept constant.

The variable fields experienced throughout the 5% NaCl solution above the setup shown in figure 5.16 are depicted in figure 5.18. The H^+ concentration throughout the electrolyte is shown in figure 5.18(a) and shows that the local perturbations exist exclusively above the area occupied by the Galfan coating layers, and these are denoted by the lighter areas. These localized sites are also equivalent in size and shape to the primary zinc dendrites present in the modelled ZnAl coating layer. The electrical potential field in the electrolyte is shown by figure 5.18(b). The anodic potentials are shown by the darker areas and occur at positions above, or close to, the Galfan coatings. The resultant dissolution sites after 24 hours, indicated at B, can be seen to be the sites of the maximum anodic electrical potentials. The areas of the highest cathodic potential (shown as lighter areas) can be seen to be at the the centreline of the exposed steel substrate, A.

The H^+ concentration residing in the 5% NaCl electrolyte after 24 hours simulated time is shown in figure 5.19. The light areas signify local increases in the ionic concentrations at

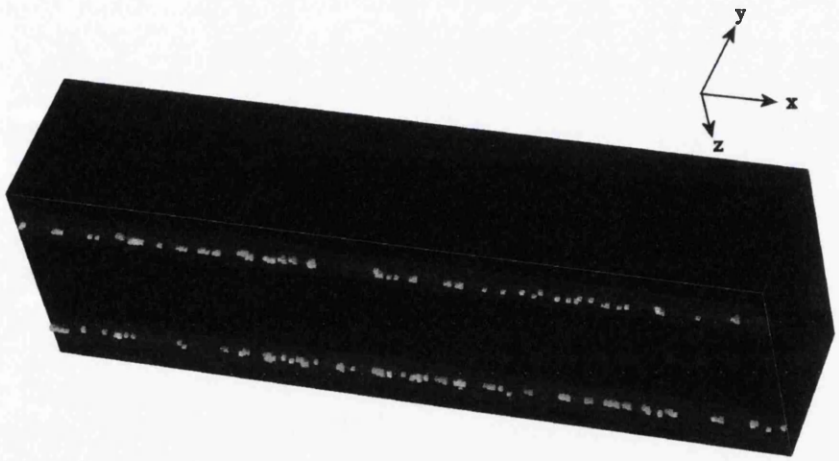

Figure 5.19: Concentration field [H^+] in 5% NaCl solution after 24 hours simulated exposure (non-electrolyte elements not shown).

those positions, and can be seen once again to occur at locations above the simulated Galfan layers, assuming the same shape and size of dendrites that may have been the subject of anodic dissolution. It can be seen from figure 5.19 that a scaling up of the cut–edge length exposed to the aggressive electrolyte to this upper limit, brings about an equivalent increase in the number of local anodic sites operating along the length. In addition, the evolving ionic concentration still remains close to the initial solid–liquid interface and is predominantly persistent within the pits formed by localized dissolution.

The electrical potential field that corresponds to the simulation set-up and time of the concentration field shown in figure 5.19, is shown in figure 5.20. Whilst the cut-edge length has been increased, it is still the case that the highest cathodic voltages are experienced at two distinct points along the centerline of the steel substrate, A and B, as was seen to be the case in figure 5.20. The maximum anodic potential can be seen to occur at the darkest region present in figure 5.20, C. Whilst this high anodic voltage is not seen to extend over the entire cut-edge length, the localized dissolution at the positions of the Galfan coating layer can be seen to bring about elevated anodic potentials, indicated by the darker regions.

A good description of the electrode potentials at the surface and electrical potentials throughout the 5% NaCl electrolyte is given by figure 5.21; representing the potentials after a simulated time of 10.6 hours and over an exposed cut–edge length of 0.5 mm. The highest value of cathodic potential is experienced at the steel–electrolyte interface, and this can be

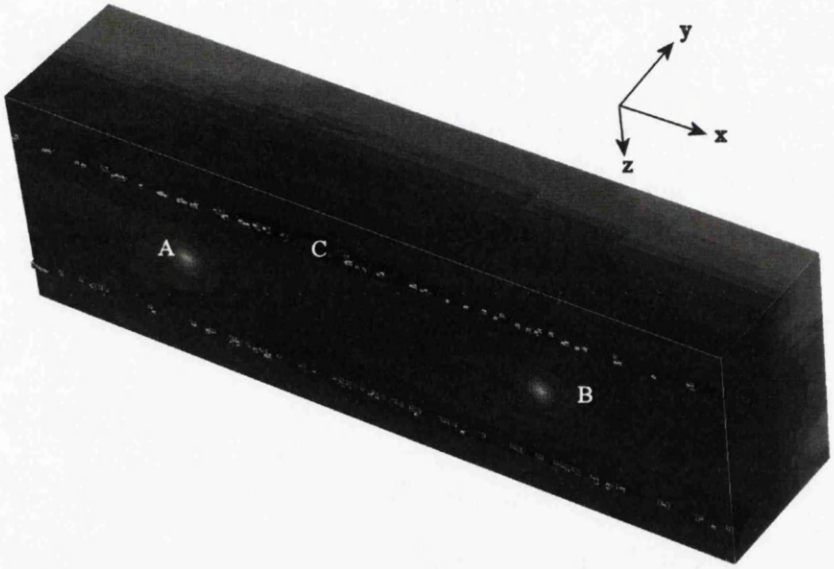

Figure 5.20: Electrical potential field in 5% NaCl solution after 24 hours simulated exposure (non–electrolyte elements not shown).

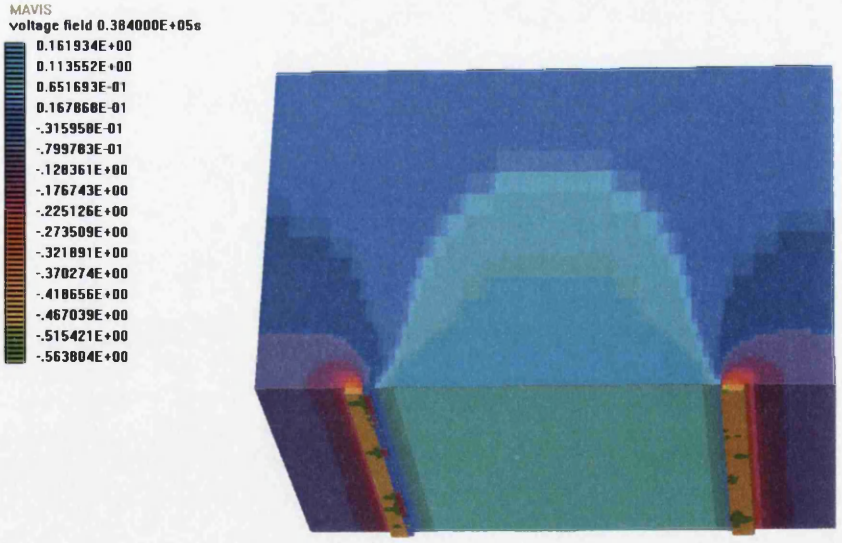

Figure 5.21: Electrical potential field throughout 5% NaCl solution over a short length of exposed cut–edge Galfan coated steel.

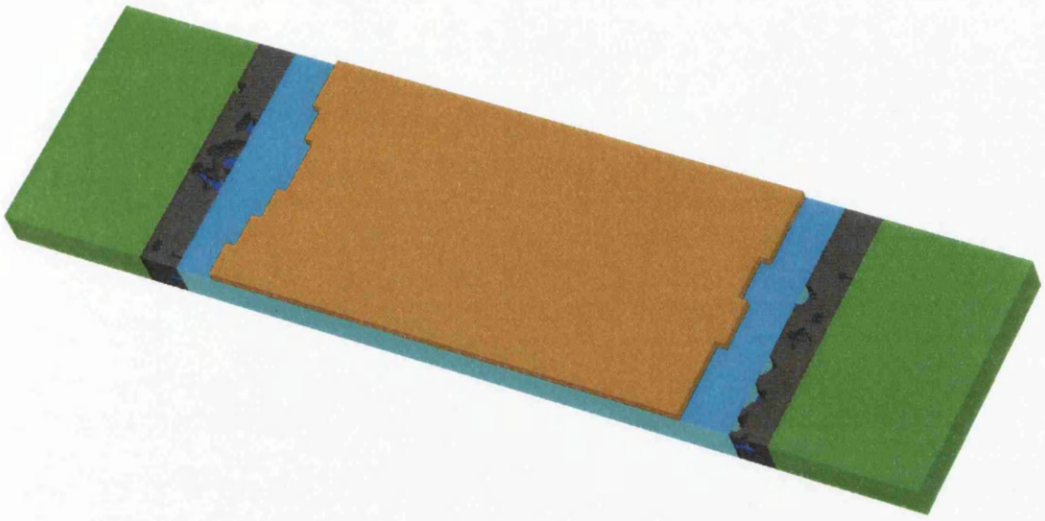

Figure 5.22: Solid model that shows the degradation of a simulated Galfan coated steel, occurring at both front and back metallic coatings.

seen to extend vertically into the liquid, tailing off towards the coating layer forming a dome of high cathodic potentials in the electrolyte (cyan). At the steel–electrolyte interface close to the coating–steel interface, the polarity of the potentials is reversed and anodic potentials are predicted. The anodic potentials present occur at the coating–electrolyte, particularly if:

1. The material in contact with the electrolyte is a phase rich in zinc. This is shown clearly by the green areas that map out the shape of the dendritic phase present at the surface.

2. The area of the coating lies directly adjacent to the steel substrate (orange areas).

An important feature in figure 5.21 is that since electro-neutrality is preserved within the simulations, the cathodic current density must be far more diffuse that the anodic current density since the maximum cathodic potential, +0.16 V, is far lower than the maximum anodic current density, -0.56 V, whilst occupying a greater area of the exposed surface.

Figure 5.22 shows the solid model reflecting the resultant degradation experienced by a short cut-edge length after 24 hours exposure to 5% NaCl solution. As expected, it is the primary zinc dendrites present at the initial solid-liquid interface that are the focus of the localized anodic dissolution events. The shape and size of the zinc regions removed can be seen to be equivalent to the size of the pits that can be seen to have formed in figure 5.22.

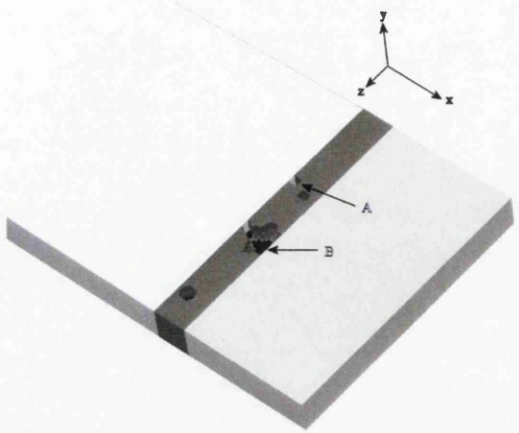

Figure 5.23: Magnified view of the cut–edge of a Galfan coated steel after 24 hours exposure. Primary zinc dendrites have completely dissolved in some positions on the coating layer (A) and are as yet only partially dissolved in other areas (B).

The steel substrate can be seen to be covered to the most part by a layer of cells containing corrosion product, albeit at low volume fraction levels. However, at the regions of the steel substrate directly adjacent to the Galfan coating layers included in the simulation, it is apparent that no corrosion product has been deposited.

A magnified view of the solid model described by figure 5.22, can be seen in figure 5.23. This highlights the degradation experienced by the Galfan coating layers, and is shown without electrolyte elements, including those containing corrosion product. It can be seen from figure 5.23 that in addition to the zinc dendrites (darkest region) being the focus of the localized corrosion effects, the degree to which the zinc dendrites have been dissolved is dependent upon their size and the position that they occupy during the simulation. Zinc dendrites in close proximity to the ZnAl-Steel interface can be seen to be completely 'eaten away', shown at position A, whereas those further away from the steel substrate (white area) experience lower levels of zinc removal. In the model dendrites that are larger in size remain the active sites of corrosion throughout the 24 hours exposed to the 5% NaCl solution. Whilst it is unclear from figure 5.23 whether or not the large dendrites lose an equivalent volume per area exposed, it is apparent that the larger dendrites have only been partially dissolved as primary zinc still remains at those positions, like that shown at B.

The predicted normalized current density calculated 100 μm above a simulated cut–edge of length 2.5 mm is given in figure 5.24. The anodic current densities are indicated by the

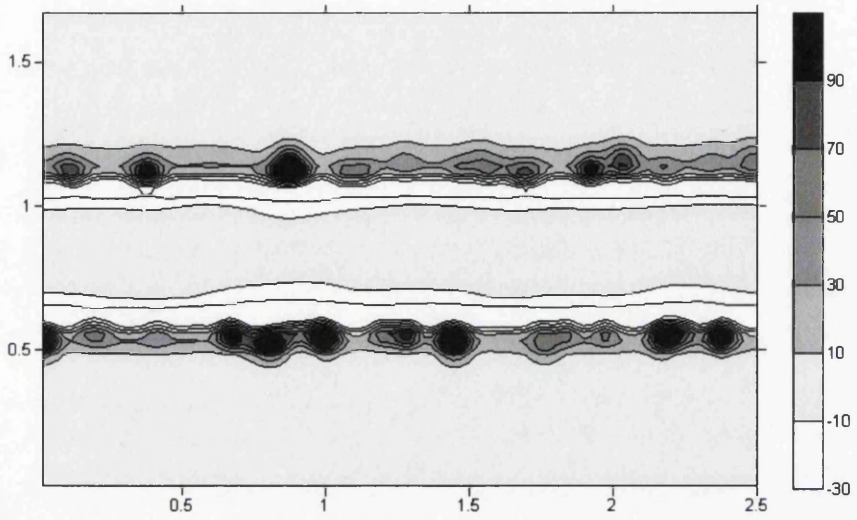

Figure 5.24: Predicted current density field (Am^{-2}) 100 μm above a corroding cut-edge after 24 hours simulated exposure. Length scales are in mm.

dark areas and the cathodic current densities are denoted by the lighter areas. Important to note from figure 5.24 is the dramatic increase in the current density values predicted, both anodic and cathodic, from those predicted in the surface case shown for the surface corrosion of EZ coated steel in figure 5.4. However, while these values are approximately a factor of 10 higher, the ratio of maximum anodic to cathodic current density remains the same, 3:1 anodic to cathodic. In this case the maximum anodic current density experienced is +90 Am^{-2} and a maximum cathodic current density value of -30 Am^{-2} is observed. The maximum anodic current density occurs at discrete positions along the length of the cut–edge, above the Galfan coating layers. The frequency of these high 'spots' is directly proportional to the distance between exposed dendrites at the solid–electrolyte interface. The maximum cathodic current density is located along the steel substrate at a definite distance from the coating layer, before the intensity drops toward the centreline of the steel substrate. The areas above the inert resin material assume a vertical current density vector equivalent to zero.

The formation of the corrosion products deposited at the solid–liquid interface during the course of a cut–edge corrosion simulation of a Galfan coated steel can be seen in figure 5.25. Firstly it can be seen that no deposition of corrosion products has taken place at any point during the simulation at the surface of the inert resin material included, marked as region A in figure 5.25. After 10 hours exposure to the electrolyte, two thin lines of corrosion

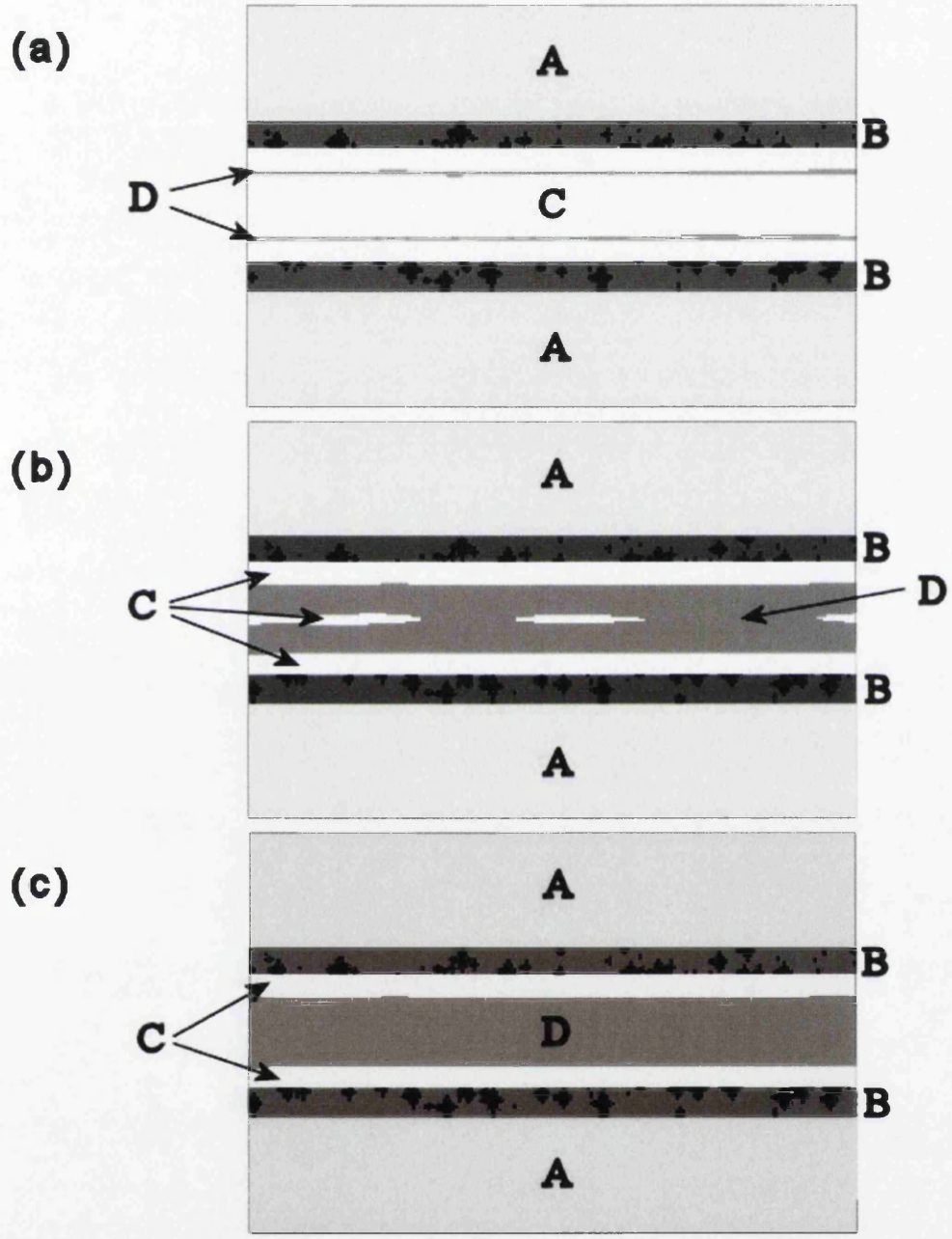

Figure 5.25: The development of a corrosion product layer on the surface of the exposed steel. Top views at times (a) 10, (b) 16, and, (c) 24 hours. The electrolyte is not shown. An inert resin layer is shown as A, the Galfan coating layer is shown as B. The exposed steel regions are C and the growing corrosion product layer is D.

product, labelled region D in figure 5.25, can be seen to have been deposited symmetrically about the centreline of the steel substrate, away from the Galfan coating layers, region B. After a further 6 hours exposure, figure 5.25(b), the corrosion product film present on the steel substrate can be seen to have spread toward the centre of the steel substrate, whilst maintaining the same region from the Galfan layers uncovered, region C. In addition, region C incorporates small areas along the centreline of the steel substrate that have not been the sites of corrosion product deposition after 16 hours corrosion, figure 5.25(b). These central C zones have been covered with corrosion product after a further 8 hours, leaving only the steel regions adjacent to the Galfan coatings and the coatings themselves uncovered, as shown in figure 5.25(c).

5.2.3 Influence of geometric arrangement on corrosion performance of Galfan coated steels

The influence of multi–metal exposure has been described up until this point as either a surface and/or cut–edge corrosion problem. This section describes the applicability of the computer model to various situations that may be encountered in the surface environment, using 2D simulations. The concentration fields that arise from these geometric set-ups and the associated voltage fields are shown after 24 hours exposure to 5% NaCl solution. Other information that could be obtained from such simple simulations are given. In all cases the gauge of the steel substrate is not representative of those used in service, although it is assumed that this is the only surface area exposed to an aggressive environment, which is more likely to be the case, leading to very localized environments.

Included in figures 5.28 and 5.27 are the cases previously described for the surface and combined surface and cut–edge exposure of a Galfan coated steel; cases used for the surface and cut–edge respectively. Figure 5.26 shows the degradation experienced in 2D over 24 hours exposure for various cases; termed surface, scratch, cut–edge, pin and bolt. Figure 5.26(a) (left hand images) shows the set-up of the simulations at $t = 0$. It is assumed that an oxide film is present at the initial horizontal surface height, i.e. that of the surface case, and this is gradually removed arbitrarily over the initial time increment as described earlier. This oxide film, along with any corrosion products deposited is represented by the

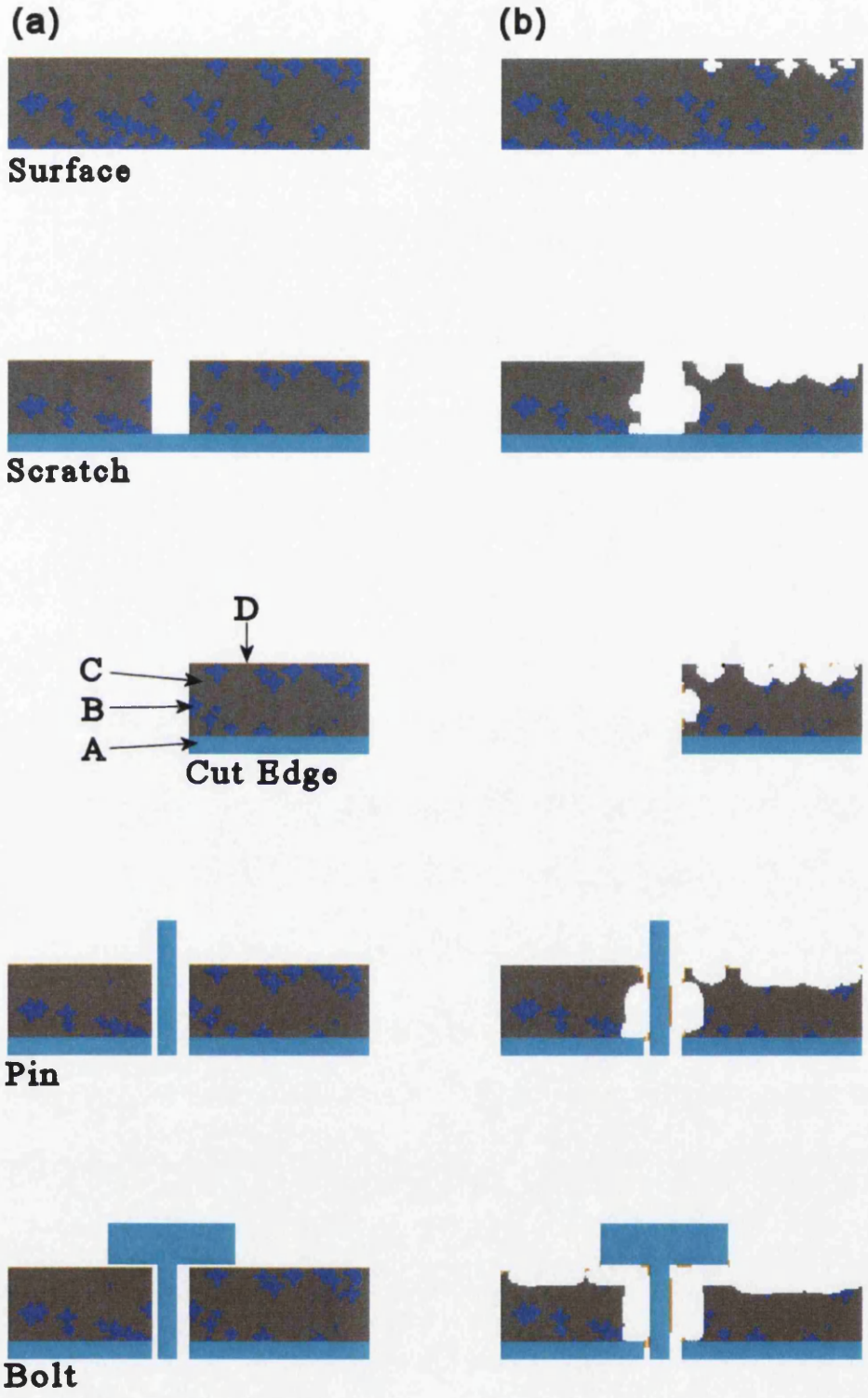

Figure 5.26: 2D representation of the solid matter in the simulation of different cases for Galfan coated steel; A – Steel; B – Primary Zinc; C – Eutectic; D – Oxide Film. (a) Prior to exposure, and, (b) After 24 hours exposure to 5% NaCl solution.

brown elements. Light blue areas denote the presence of steel, dark blue regions represents primary zinc and grey areas ZnAl eutectic. Insulation is applied to the top and sides of the simulation. The scratch case varies from the surface case, in that a portion of the coating layer is removed from the centre of the solid material represented and a steel substrate is included at the bottom of this arrangement, therefore exposing an area of steel equivalent in width to the portion of Galfan coating removed. In the case of the cut–edge all material from the edge of the right section of the Galfan coating has been reassigned in the simulation as electrolyte (5% NaCl). The setup used to simulate the fabrication of a structure using a pin differs from the scratch case, such that the steel at the base of the scratch is removed and a section assuming the properties of steel is introduced into this gap. This is done such that the pin is surrounded at all sides except the base by electrolyte, although electrical contact between the two structures is still assumed to be intact. A slight variation of the pin setup is used to simulated on–site fabrication of Galfan coated steels using a bolt. The only difference here is that the central steel structure has now been extended to include a head, once again surrounded by electrolyte whilst maintaining electrical contact. It is important to note at this point that before any alterations were made to the setup from the surface case, the structure in the Galfan coating layer was formulated using the same random numbers, in order that all coatings remained the same for comparison.

The effect of 24 hours exposure of the set-ups shown in figure 5.26(a) to 5% NaCl solution can be seen in figure 5.26(b). The surface case experienced the least degradation at the positions on the surface containing zinc rich material. The cut–edge case experienced a greater degree of degradation at the surface, in addition to a large amount of material loss at the cut–edge. A greater amount of corrosion product was also deposited at the cut–edge compared to that experienced at the surface. The introduction of the scratch further increased the severity of material degradation at the surface. A large degree of anodic dissolution can be seen to have occured within the scratch itself, including localized attack on the left hand portion of the Galfan coating. However, the Galfan surface to the left remained relatively untouched by corrosion effects, be they general or localized. Notably, however, there appears to be a reduction in the amount of corrosion product deposited across the solid–liquid interface. The inclusion of a pin at the centre of the setup has the effect of

accelerating the material lost from the 'cut' Galfan coating edges, in particular the left hand portion of the Galfan coating. The degree of anodic attack taking place on the surface of the right hand Galfan coating is also seen to exhibit a slight increase in severity. In contrast to the scratch case, the amount of corrosion product deposited during the 24 hours simulated is significantly higher, both on the exposed surfaces and on the pin itself. Finally, the extention of the model to include a 'bolt' structure has the effect of increasing the overall corrosion taking place. It is the only case where significant material removal has taken place at the surface of the Galfan coating to the left. In addition to this the edges of the 'cut' Galfan coating have visibly retreated from their original positions. An increase in corrosion product deposition is also apparent, as is the reduction in localization of these effects.

Most significantly, however, is the relationship evident in figure 5.26 that as the amount of steel is increased in the simulation, there is a marked increase in the volume/area of eutectic material that is removed. In addition to this, in terms of corrosion product deposition, with the presence of steel, zinc and aluminium, their respective structures/arrangement is significant in terms of volume/area over which it is deposited and the amount that is laid down.

The voltage and concentration fields around the material at the time step shown in figure 5.26(b) can be seen in figure 5.27(a) and (b) respectively. Areas of the highest anodic potential are denoted by the red areas in figure 5.27(a), whereas the areas of the highest cathodic potential are shown by the white areas. In figure 5.27(b), the areas of highest H^+ concentration, thereby the most considerable concentration perturbations, are indicated by yellow regions, whereas the initial concentration, thereby the bulk concentration, is given as blue areas.

The electrical potential around the surface case exhibits very little detail, suggesting that all of the corrosion that will take place in this environment has occurred, although one site indicates that a localized corrosion effect is still operating. Figure 5.27(b) suggests that there is still elevated concentrations within the pits formed with the removal of the zinc dendrites present at the surface. The electrical potential field for the scratch case, shown in figure 5.27(a), shows high anodic potentials at spatially discrete positions across the right hand surface and within the scratch. The cathodic potentials can be seen to occur exclusively

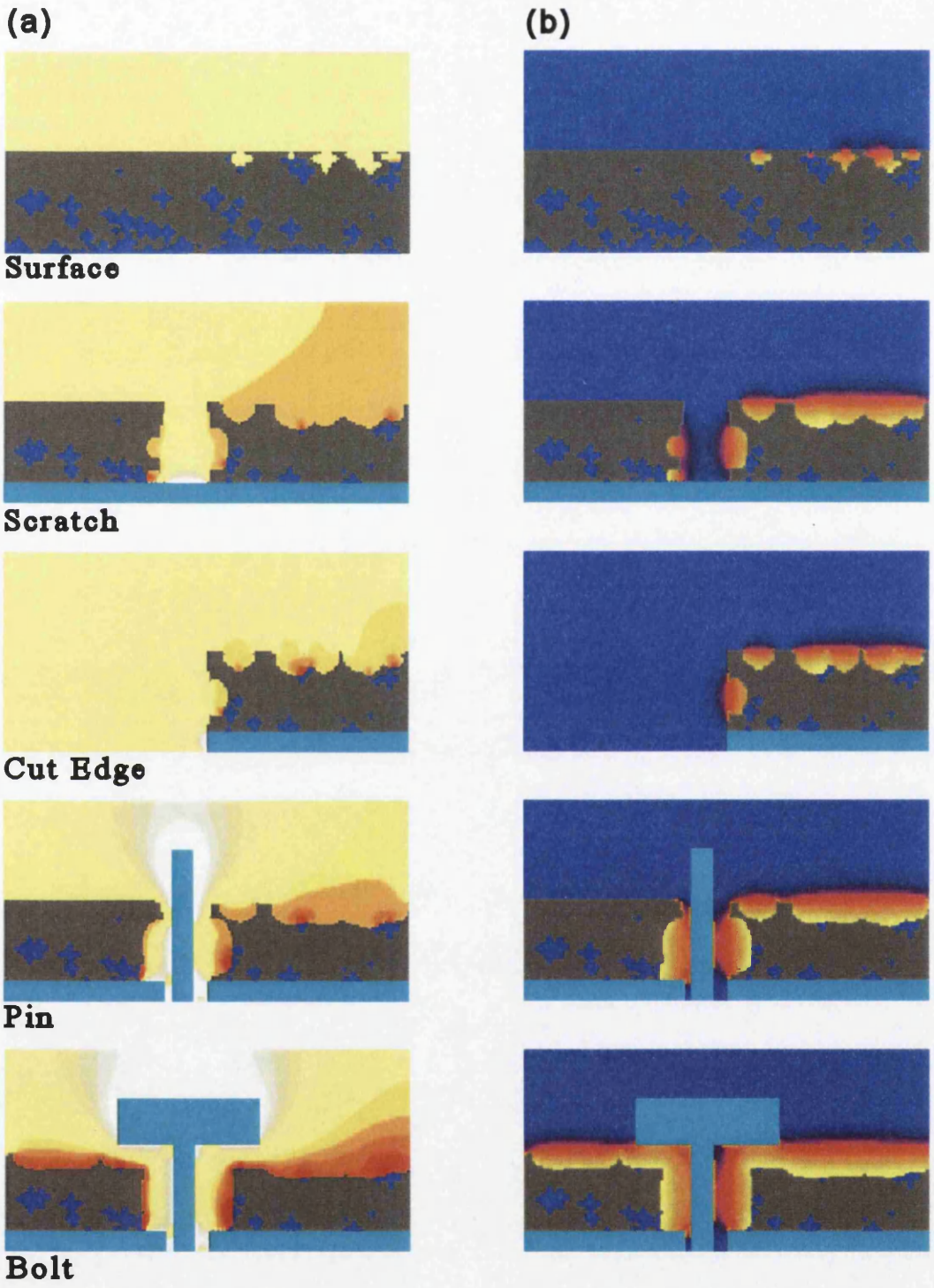

Figure 5.27: 2D representation of the electrolyte around corroding surfaces of Galfan coated steel after 24 hours simulated exposure to 5% NaCl solution. (a) Electrical potential field, and, (b) Ionic concentration field; $[H^+]$.

at the site of the exposed steel. Once again, somewhat obviously, the ionic concentration is elevated in the area of material loss, the sites of local concentration contribution. This is observed once more when considering the case of the ionic concentration field for the cut–edge case. A similar trend is observed for the electrical potential field around the cut–edge that was the case inside the scratch. Spatially discrete local anodic sites are indicated by the red regions, all supported by the relatively small white (cathodic) zone adjacent to the exposed steel.

In figure 5.27 it can be seen that in the cases of the pin and bolt a definite change has been brought about in the concentration and electrical potential fields by the inclusion of these features. With respect to the concentration fields, a higher concentration is maintained at this point in time within the scratch and can be seen to have greatly increased the electrical potential fields in those regions. The widespread occurrence of high anodic potential in the two cases has been supported by the higher surface area of exposed steel. Cathodic potentials can be seen to be occupying a greater area of the surface, as well as being a far more prominent feature throughout the electrolyte. All this appears to have the effect of transforming the predicted corrosion mechanism from one that is highly localized, to a more generalized form via the removal of higher amounts of the eutectic matrix constituent of the Galfan layer. This is dramatically seen in the case of the bolt when viewing the high anodic potentials present at the surface of the left hand portion of Galfan coating layer, previously unscathed after 24 hours simulated exposure.

Current density fields around the surface and cut–edge cases described in figure 5.26 are shown in figure 5.28. These show the contributions made by the vertical and horizontal components of the current density vectors calculated from the previously determined electrical potential field.

The 2D current density vector plot around the corroding surface case, shown in figure 5.28(a) shows the highest potential gradient are observed close to the active sites of localized corrosion, given by the green arrows. What can be seen when observing the way the magnitude and direction of these vectors away from the corroding surface is that many of these pit-like features contribute to creating 'dome' shaped paths through the electrolyte. The most dramatic of these paths of changing flux occurs to the right of figure 5.28(a), which

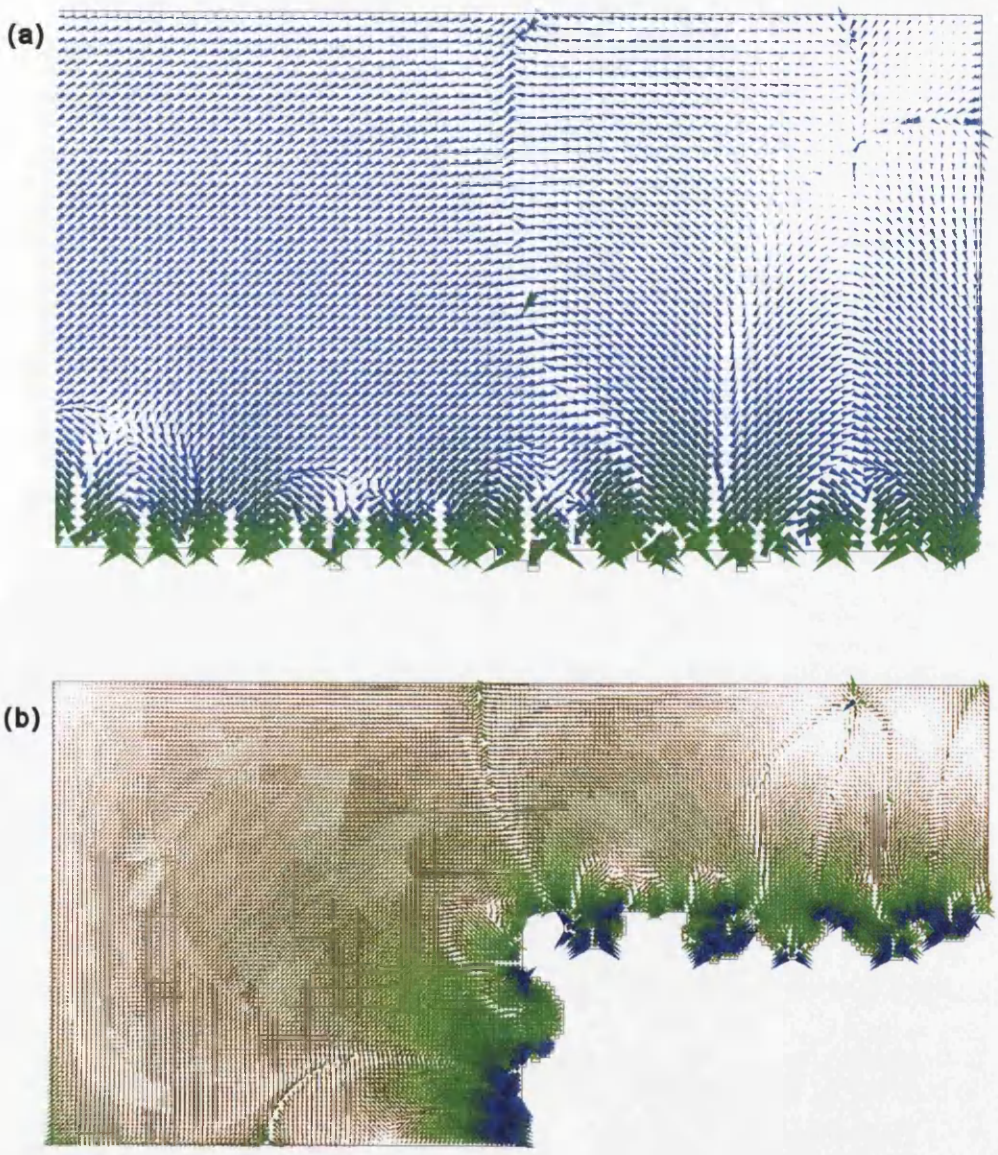

Figure 5.28: 2D current density vector plots for (a) Surface, and, (b) Cut–edge cases depicted in figure 5.26.

can be seen to interact with another of the larger changes in the bulk electrolyte. What is significant, however, is that these larger changes in flux, at this particular time step are not necessarily the result of localized degradation of a much higher magnitude occurring at the surface.

Similarly, in figure 5.28(b), the same effects can be observed in the 2D vector plot around the cut–edge case. Here, once again, the cases of the highest flux occur at positions within the voids left by the action of the localized corrosion effects operating at the cut–edge. The potential gradients in the x and y directions can be seen to be significantly perturbed further into the electrolyte than was the case for the exposed 2D surface. The 'domes' of flux can be seen to extend past the diffusion layer into the bulk electrolyte. It is visually apparent that these lines of flux are far more distinct and extend further into the electrolyte, reflecting the higher amounts of degradation taking place.

5.3 Influence of Cooling Rate on Corrosion Performance of Zn – 4.5 wt.% Al Steel Coatings

Excluding bath chemistry and applied pre–treatments, the most direct influence the manufacturers have on the microstructure of Galfan is the cooling of the coating after hot–dipping. The effect of this parameter has been investigated previously by Elvins (2005) using accelerated corrosion testing in 5% NaCl solution (SVET) and metallographic studies. This chapter documents the attempts made to simulate the same cases that were tested by Elvins et al. (2003). The same terminology for the cooling rate of the Galfan coating (the power output of the cooler) has been used since the Galfan coatings of interest are those that are used in service. Within this chapter the cooling rates considered are termed 55% (slowest cooling), 80% and 100% (fastest cooling). The thickness of the gauge used in the simulation are those that have been used previously, denoted by a letter; L for light gauge material, i.e. 0.47 mm gauge thickness, and H for the heavy gauge steel substrate, i.e. 0.67 mm gauge thickness.

The cooling rate alters the microstructure such that at high cooling rates (100L and 100H samples) a greater number of smaller primary zinc dendrites are observed, whereas the number of dendrites decreases and are larger in the slower cooled Galfan coatings (55L

and 55H samples). Elvins et al. (2003) deduced from metallographic studies that the volume fraction within the Galfan coating is independent of cooling rate at 14%. This estimate was later revised at a level observed in coatings being manufactured at that time of 20% (Elvins et al., 2005a), and this is the value employed in the model when formulating the Galfan coating in the simulations. The corrosion performance of these Zn – 4.5 wt.% Al coatings at the cut–edge is assessed with respect to the cooling rate and gauge thickness, whereas the formation of localized corrosion at the surface of the Galfan coatings is only considered as a function of cooling. This is because variation of the quantity and size of dendrites at the surface of the Galfan coating is, for the purposes of simulation, not a function of gauge.

5.3.1 Effect of Cooling Rate on the Surface Corrosion of Performance of Galfan–Type Coatings

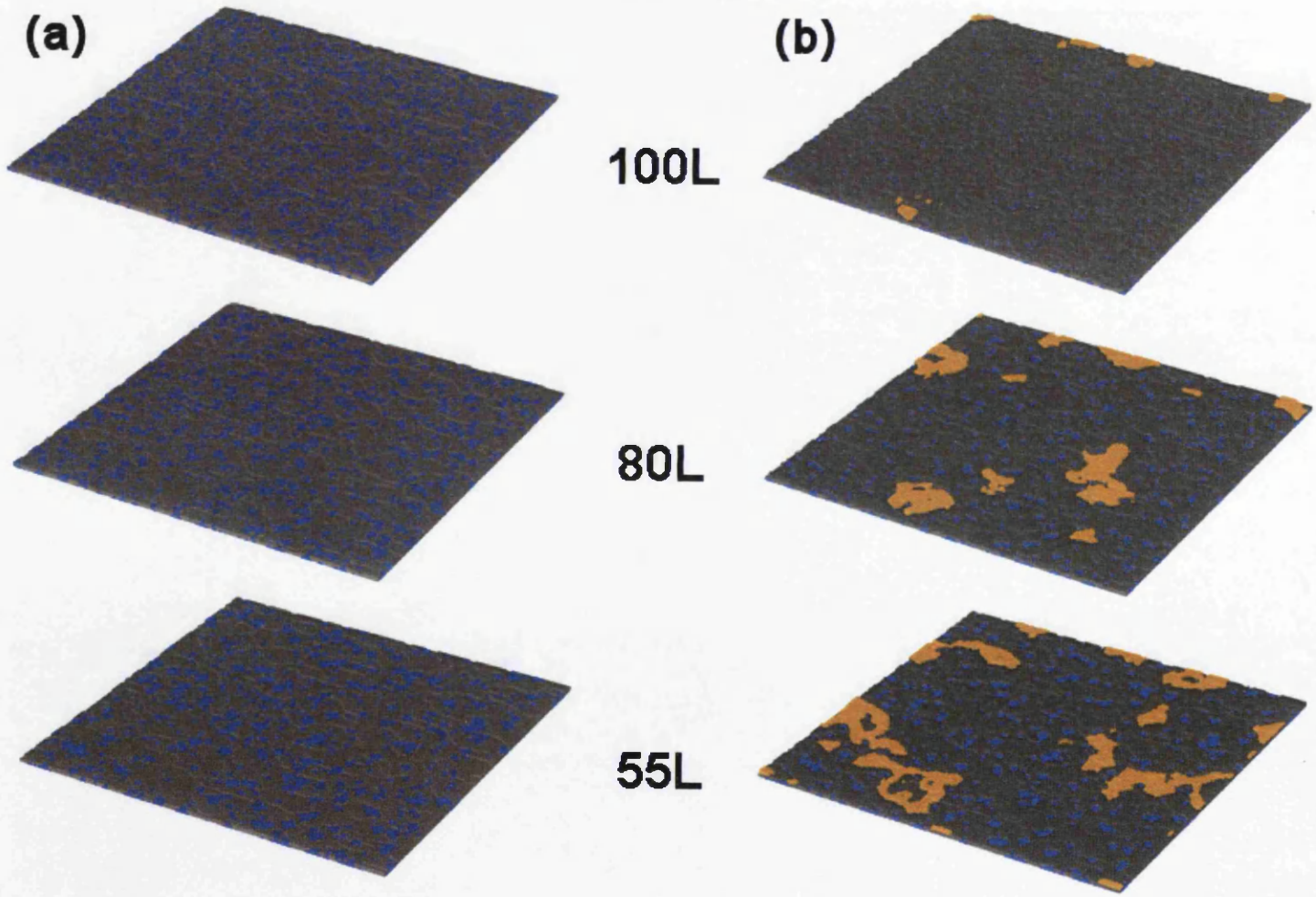

Figure 5.29: Solid model of the surface exposure of the Galfan surface to 5% NaCl for different cooling rates; (a) At the start of the simulation, and, (b) After 24 hours exposure

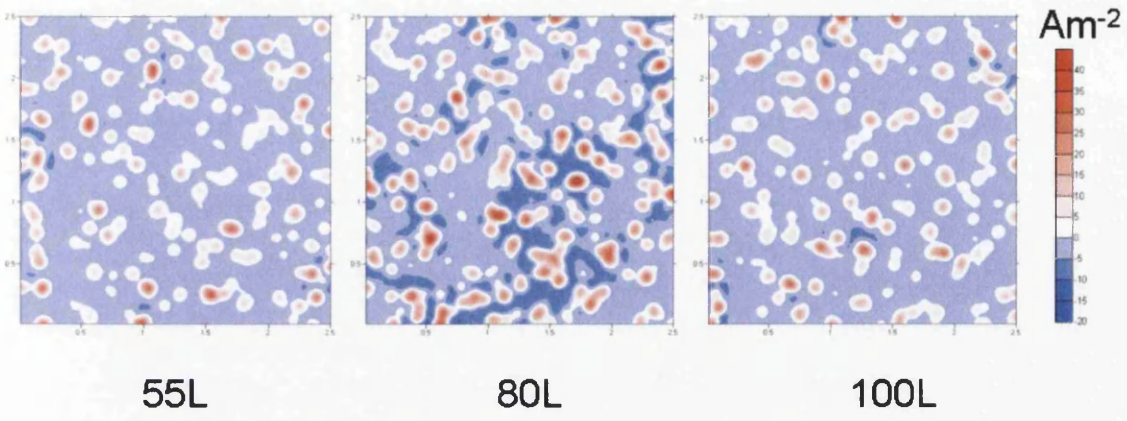

Figure 5.30: Vertical current density fields after 5 hours simulation shown as a function of cooling rate 100 μm above the surface of the solid material shown in figure 5.29. (Dimensions in mm).

Figure 5.29 shows the solid model for the surface corrosion of Zn – 4.5 wt.% Al , Galfan type coatings at 3 different cooling rates; 55%, 80% and 100% of the cooler power output. The 3 coatings are labelled 'L' for light gauge steel because primary zinc dendrite sizes are estimated from those observed in coatings on this gauge of steel. (Elvins et al., 2003) Visibly, the area of exposed primary zinc phase appears to be relatively constant at the start of the respective simulations shown in figure 5.29(a), reflecting the nucleation and size tolerances of these features. However, the distribution of this primary phase varies with primary phase at the higher cooling rate simulations exhibiting more agglomeration of these features in agreement with experimental observation. After the 24 hours simulated time in contact with 5% NaCl solutions, figure 5.29(b), differences in the corrosion performance of these coatings can be seen. Most prominent is the changes in the volume of corrosion product deposited at the surface of the solid model, shown by the brown matter in figure 5.29. The volume/mass of corrosion product deposited can be seen to increase with a decrease in cooling rate, both in terms of number of locations and the amount formed at these sites. In addition, the amount of zinc visibly present at the surface of the solid model also increases as the cooling rate decreases. This suggests that pitting occurring at the surface of faster cooled coatings may have a higher depth to width ratio.

The influence of the starting solid model (figure 5.29) on subsequent degradation, brought about by contact with 5% NaCl solution, can be seen after 5 hours in figure 5.30.

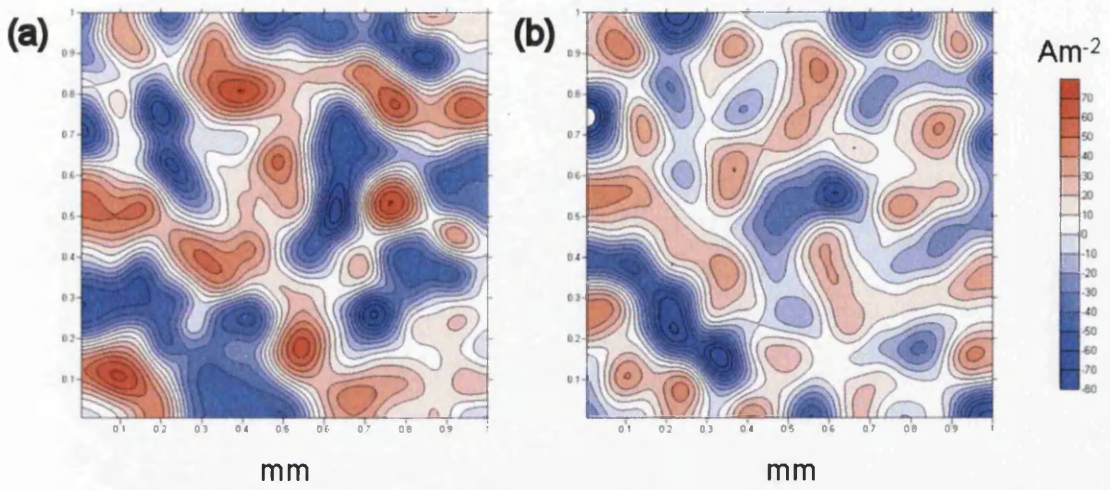

Figure 5.31: Vertical current density fields 100 μm above corroding Galfan surfaces 1 mm $\times$ 1 mm, after 12 hours contact with 5% NaCl solution; (a) Cooled at 55% power output, and, (b) Cooled at 100% power output.

This shows how the vertical component of the current density fields vary according to the material exposed at the surface of Galfan coatings cooled at various rates. The results predicted by the model present somewhat of an anomaly, since the magnitude of anodic and cathodic current densities appear to increase as the cooling rate is increased from 55% to 80% power output of the cooler, whereas they reduce on further increases in cooling rate; 80% to 100%.

The number of active anodic sites predicted from the current density maps in figure 5.30, generated 100 μm into the electrolyte, suggests that there is little difference between the number of sites in the fast (100%) and slow (55%) cooled samples acting anodically at the respective surfaces. However, as with the intensity of localized effects predicted, the number of anodic sites is seen to be highest in the moderately cooled case (80%). Highlighted for the moderately cooled Galfan surface corrosion is the localization of the cathodic current density at perimmetric regions around the anodic sites acting at the surface.

Figure 5.31 shows the current density fields for the simulations performed in the same conditions as those in figure 5.29, for the slow and fast cooled microstructures over a small (1 mm $\times$ 1 mm) area; thus neglecting the anomalous case (80% cooler power output). A difference in microstructure can be seen to change the corrosion performance of a Galfan

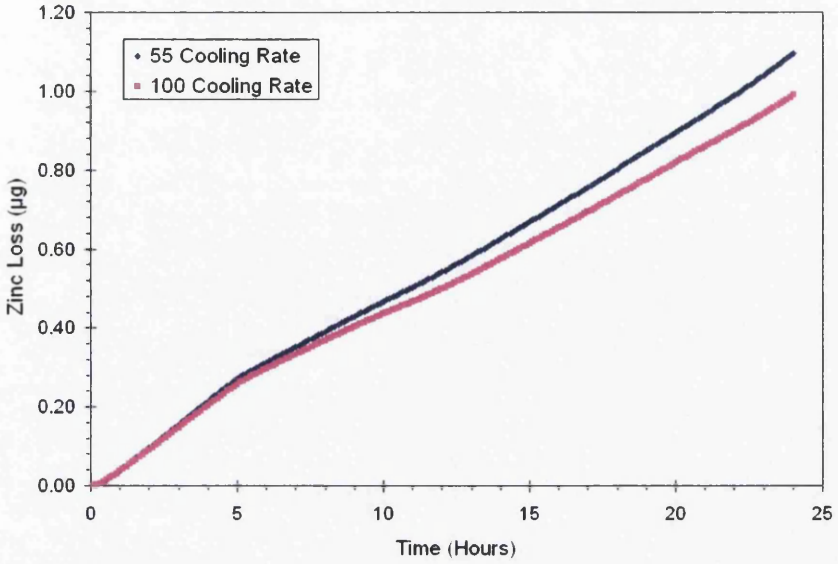

Figure 5.32: Variation of zinc loss from a Galfan surface 1 mm $\times$ 1 mm over time in contact with 5% NaCl solution comparing the cooling rates.

coating in terms of vertical current density fields produced. The anodic current density can be seen to occur within the predefined eutectic cell depressions (as discussed in section 6.2). The magnitude of the maximum current density, both anodic ($+ve$) and cathodic ($-ve$), are greater for the slow cooled Galfan coating. Also, a larger cathodic area is covered by these maximum values for the slower cooled sample (figure 5.31(a)). However, by considering the contours applied to the current density maps in figure 5.31, one could say that in contrast to figure 5.30, there are a greater number of anodic sites acting on the surface of the fastest cooled (100%) Galfan surface.

The graph shown in figure 5.32 represents the material lost from 2 of the simulations shown in figure 5.29; 55% and 100% cooler power output applied to the hot–dip Galfan coating. Initially, the degradation rates of the two simulated coatings are comparable, thus the graphs are superimposed onto one another. By the time that 5 hours simulated time is reached (time increment reached in figure 5.30) differences in the corrosion performance become apparent. Prior to this point a different corrosion rate, $\frac{dM}{dt}$, is experienced to that exhibited subsequently. Figure 5.32 suggests that the corrosion rate for the Galfan surface prior to this point is independent of cooling rate. This 'rate change' suggests that the microstructure of the Galfan affects the surface corrosion performance exhibited in

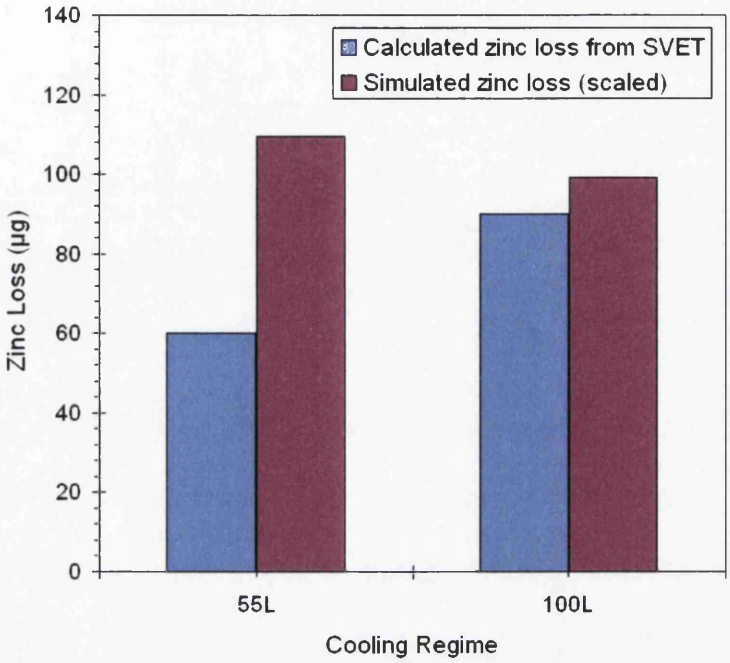

Figure 5.33: Comparison of simulated and observed (Elvins et al., 2005a) total zinc loss over 24 hours from the surface of differently cooled Galfan coating surfaces 10 mm $\times$ 10 mm.

accelerated corrosion testing.

The overall extent of corrosion, in terms of material loss at the surface of a Galfan coating in contact with 5% NaCl solution is shown in figure 5.33. This shows that the deviation in corrosion rate leads to a difference in zinc dissolution. Scaled in figure 5.33, the amount of zinc lost from the surface of a coating is predicted to decrease with an increased cooling rate applied to the hot–dip Zn – 4.5 wt.% Al steel coating. This contradicts those published experimentally estimated zinc losses from equivalent coatings by Elvins et al. (2005a), where increased zinc loss is observed at higher cooling rates.

5.3.2 Cut–Edge Corrosion of Zn – 4.5 wt.% Al Galfan Coated Steel

Figure 5.34 shows the vertical current density fields above the cut–edge of those coatings shown in figure 5.29 applied via hot–dip methods to light gauge steel. The maximum values of anodic and cathodic current densities are found in the case of the slowest cooled coated steel (55%); and are +55 Am^{-2} and –75 Am^{-2} respectively. These values get progressively lower as the cooling rate is increases; 80% and 100% cooler power output used. At 100 μm,

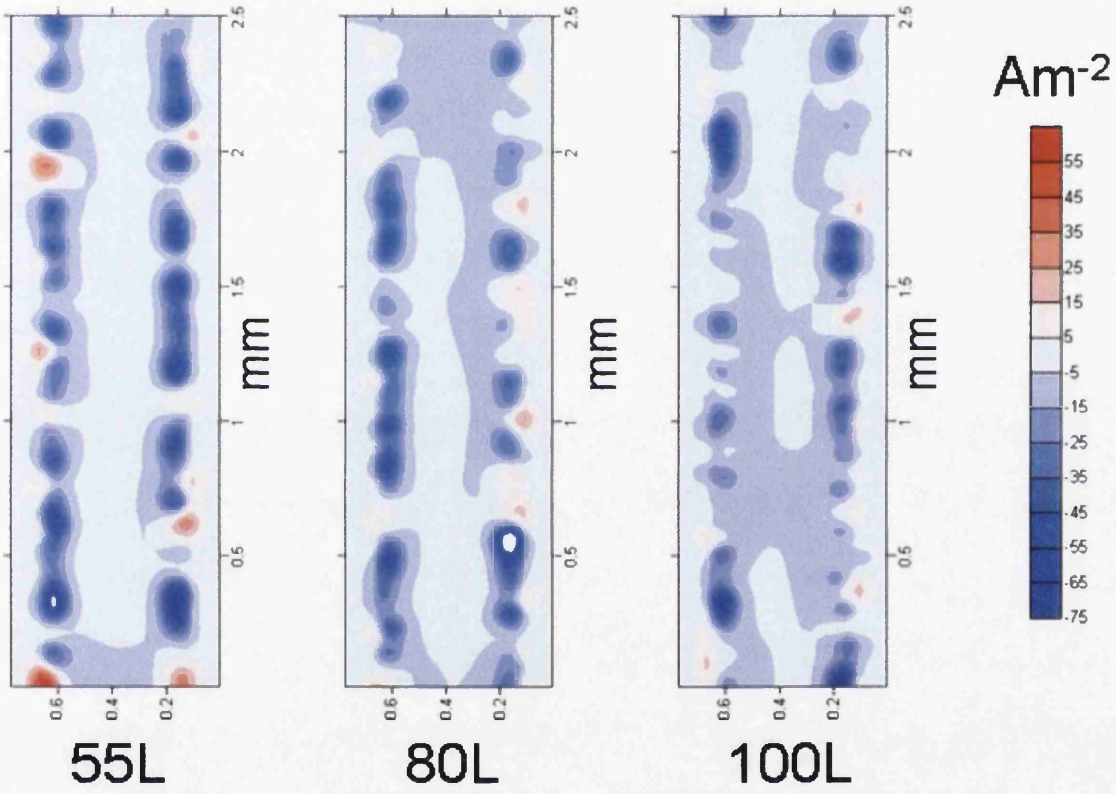

Figure 5.34: Vertical current density fields 100 μm above the cut–edges of Galfan coated light gauge steel after 5 hours simulation, solidified at different cooling rates.

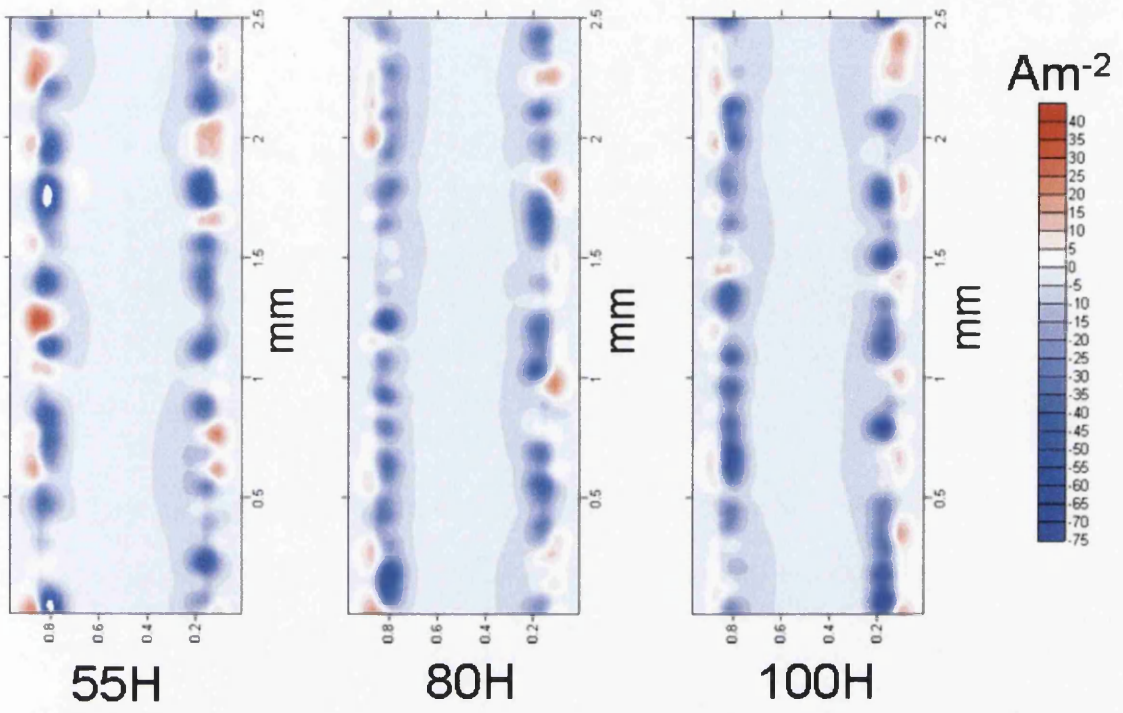

Figure 5.35: Vertical current density fields 100 μm above the cut–edges of Galfan coated heavy gauge steel after 5 hours simulation, solidified at different cooling rates.

the vertical current density fields indicate the presence of more anodic sites acting in the 55L case than the 80L and 100L cases. However, the more intense areas of cathodic activity (discounting the maximum values) can be seen to extend further across the exposed steel substrate at higher cooling rates.

The same trends with respect to the vertical current density fields above light gauge steel samples exposed at the cut–edge can be attributed to equivalent heavy gauge Zn – 4.5 wt.% Al coated steels, as shown in figure 5.35. There exist some differences between the two gauges however. The number of active anodic sites along the 'H' samples in figure 5.35 can be seen to be greater than the 'L' samples. These anodic sites, on the whole, exhibit a lower intensity of anodic current density, the maximum of which is approximately +40 Am^{-2}, compared to +55 Am^{-2} for the 'L' cases. The cathodic zones do not appear to extend towards the centre of the exposed steel, both in relative and absolute terms, as is the case for the 'L' gauge steels; although the maximum cathodic current density remains the same at approximately –75 Am^{-2}.

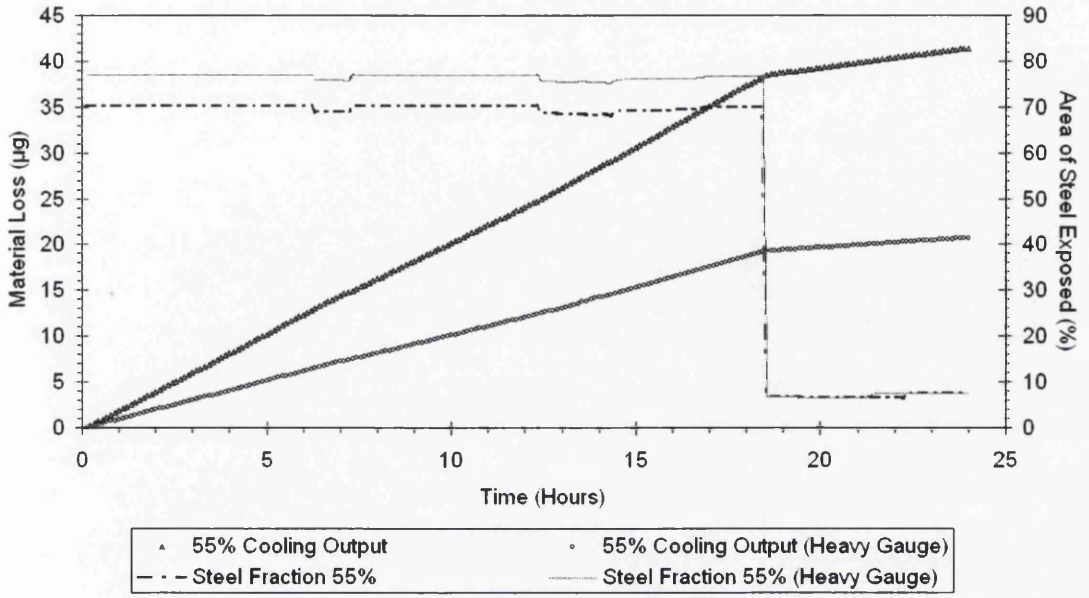

Figure 5.36: Graph showing the predicted zinc loss and exposed steel substrate (%) over time for a cut–edge length of 2.5 mm; shown for 55% output cooled light and heavy gauge samples.

The material loss from the 55L and 55 H simulations is shown in figure 5.36, in addition to the area fraction of the steel exposed to the 5% NaCl solution. Again, as with the surface corrosion case, a 'two rate' situation is revealed. However, the change in material loss, $\frac{dM}{dt}$, i.e. corrosion rate, can be seen to coincide with a dramatic reduction in exposed steel at the cut–edge. After this reduction in exposed steel the corrosion rate falls. The heavy gauge sample 55H exhibits lower corrosion rates prior to, and after the change in exposed steel is brought about. Obviously, the discrepancy between the area fraction of exposed steel between the two cases is due to differing gauge thicknesses in the steel phase whilst ZnAl material is kept at a constant, circa 25 μm.

The differences between material loss from a Galfan coated steel cut–edge with respect to the cooling rate is shown in figure 5.37, showing the degradation of the light gauge case over 24 hours. Contrary to the cases in figure 5.36, during these simulations a oxide/hydroxide film is included at the solid–liquid interface of the model. This was removed at a constant rate, giving rise to very similar degradation rates at the early stages of the simulations. Over a time period of $4\frac{1}{2}$ to 5 hours, all 3 cooling rate cases experience an acceleration in corrosion rate. This accelerative effect is experienced most in the slow cooled case. The difference in

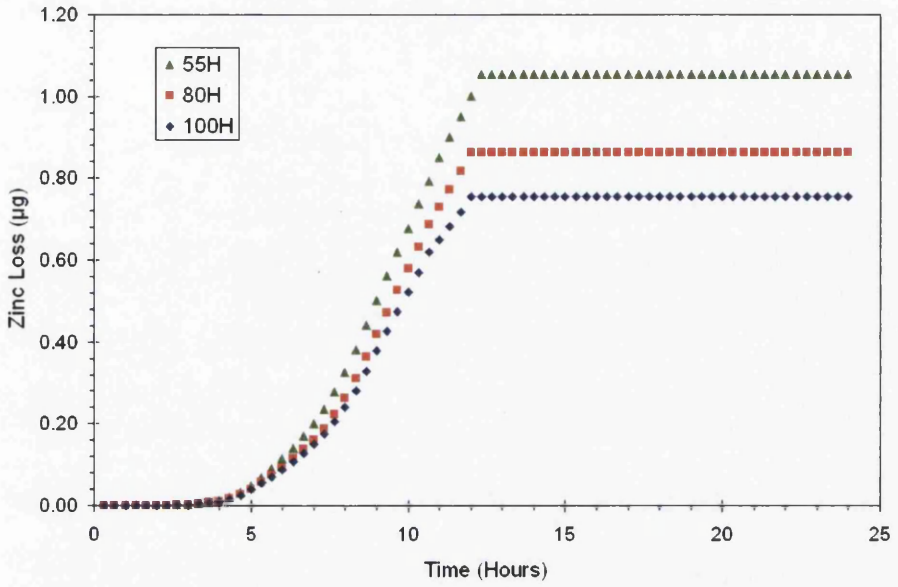

Figure 5.37: Variation of zinc loss from the cut–edge of Galfan coated heavy gauge steel over time in contact with 5% NaCl solution, comparing the cooling rates of the coatings. Passive film present at the start of the simulations.

change of rate with respect to time between 55H and 80H samples is greater than an increase in cooling rate from 80H to 100H. The corrosion rate for all 3 cases then remains constant for a period of approximately $4\frac{1}{2}$ hours, where the respective rates are 55H $>$ 80H $>$ 100H. The corrosion ceases at a distinct point for all simulated microstructures *ca* 12 hours, after which no further degradation occurs. This reduction in corrosion rate to zero takes place more abruptly as the cooling rate is reduced and slightly later in the 55H case.

Figure 5.38 shows the resultant degradation experienced by 55H, 80H and 100H, of cut–edge length 2.5 mm after 24 hours simulated exposure to 5% NaCl solution. The data used in figure 5.38 has been scaled to match those experimental results published by Elvins et al. (2005a). The simulated results match the trends observed, in that an increase in cooling rate brings about a reduction in zinc loss experienced. Evident in figure 5.38 is a disparity between simulated and observed material loss, although the order of magnitude of dissolution predicted is relatively accurate. Interestingly, the amount to which these predicted values deviate from observed estimations increases as the cooling rate decreases.

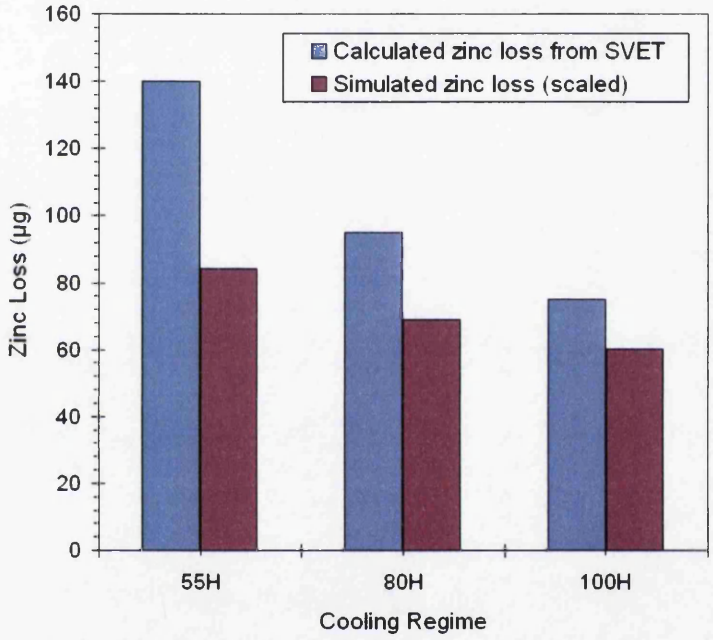

Figure 5.38: Comparison of simulated and observed (Elvins et al., 2005a) total zinc losses over 24 hours from the cut–edge; shown for differently cooled Galfan coated heavy gauge steel.

Chapter 6

Discussion

This chapter focusses on the following:

- What can be drawn from the experimental methods and the effectiveness of the computer model in capturing these relationships.
- The benefits and limitations of the modelling framework adopted, including possible extensions from alternative methods available.
- Microstructural influence on corrosion behaviour of Zn – 4.5 wt.% Al with respect to cooling rate.
- Quantitative validation of the results from the computer model with independent experimental data.

6.1 Experimental Methods

The Rotating Disc Electrode (RDE) is a hydrodynamic method involving forced convection. The electrode moves with respect to the solution. The RDE is used to provide i–E curves, thereby giving data pertaining to hydrodynamic voltammetry. This method involves the convective mass transport of reactants and products, described in section 2.2.3. This technique is used due to the steady–state being achieved quickly, offering rapid precise measurement, which is also unaffected by double–layer charging. The movement of a species was described in terms of diffusion, migration and convection in section 2.4.8.

The purpose of testing in this way is to introduce quantitative data from which predictions are made to the localized degradation of zinc–aluminium steel coatings. The results gained

from testing the zinc and aluminium samples are used in the numerical model to relate the influence of potential at the coating–electrolyte interface to the corrosion rate, which has been shown to be directly related to the current density.

The established relationship between the current and the potential shown in figure 2.17 when discussing the passivation of a metal in section 2.2.9, can be seen to have been captured by the RDE testing by figure 3.2. The transition from the active state to the passive state, and subsequently to the trans–passive state can be seen as the magnitude of the applied potential is increased. During the cathodic sweep performed on the commercially pure aluminium sample, certain distinctive points can be seen to be present in figure 3.2. The passivation potential (E_p) and current (i_p) can be seen in the lower portion of the graph by the rapid changes in gradient. Also of significance, especially in the case of aluminium, is the breakdown potential (E_b) which can be clearly seen to the upper extreme of figure 3.2. This occurs at the point when the curve moves away from the y axis (passive region), and often denotes the breakdown of passivity, in addition to the onset of pitting.

The polarization curves shown in figures 3.3 and 3.4 are the result of the anodic and cathodic current densities at each potential measured. Trethewey and Chamberlain (1995) show a comparison between the sum of modelled reactions to observed measurement, which shows that the experimental curve can be seen to almost superimpose itself upon the combination of all reactions incorporated.

In figure 3.3, the dominant reactions present that are the component most likely to influence the form of the $E/\log i$ plot are those for hydrogen evolution, dissolution of aluminium and that for the reduction of oxygen. Similarly the components of the system that are dominant in the case of the polarization curve for zinc (figure 3.4) are zinc dissolution, oxygen reduction and the evolution of hydrogen. In both cases the extent to which these influence the overall current density is dependent upon the potential. It is the case that the effect of zinc/aluminium ion reduction, hydrogen oxidation and and hydroxyl ion oxidation can be ignored since the contribution of these is assumed to be negligible.

In all $E/\log i$ plots shown in figures 3.3 and 3.4 the free corrosion potential (E_{corr}) occurs at the mixed potential point of zinc/aluminium dissolution and oxygen reduction. The potential regimes shown in these polarization curves are not governed by a Tafel relationship,

discussed in section 2.11, since the oxygen process is under diffusion control. That is, the current density is determined by the rate at which the oxygen can diffuse through the solution (all tests performed in 5% NaCl solution) to the electrode surface. The E_{corr} values shown can be seen to be different for the anodic and cathodic sweeps in both the zinc and aluminium case. In the case of zinc the anodic sweep can be seen to yield a more negative value of E_{corr}, whereas the same test performed on aluminium gives rise to a less negative value of E_{corr} with relation to a cathodic sweep.

An important feature when comparing zinc and aluminium is the differences between the tests performed using anodic and cathodic sweeping. Figure 3.4 shows that when testing zinc, the form of the $E/\log i$ is comparable for both, only that the polarization curve has been transformed such that higher current densities are experienced at less negative potentials during the cathodic sweeps. This is most probably due to the higher oxygen content in the 5% NaCl solution during cathodic sweeps than those performed using anodic sweeping whereby the solution had been purged. This is clearly shown not to be the case for aluminium, shown in figure 3.3 where the form of the $E/\log i$ plot can be seen to alter significantly between polarization curves generated by anodic and cathodic sweeps. No firm trend can be identified with respect to the relative current densities experienced during the potential range examined since the curves do not maintain a constant relationship. This indicates that the polarization and passivation behaviour of aluminium is more complex than that for zinc, which is widely accepted.

The main advantage of hydrodynamic methods, as stated above, is that steady state is achieved very quickly. The benefit of steady state being achieved quickly is that the charging of the double layer is limited, removing this from the system allowing rapid measurement with a high degree of precision. The reproducibility of RDE testing can be seen in figure 3.5 whereby all but a few $E/\log i$ plots fall within a reasonable tolerance. This, combined with the ease and minimal time required for testing, lends itself to increased validity and adaptability to any model incorporating experimentally derived current density/corrosion rate data. An important aspect of using RDE data within a numerical model is that it permits a high degree of control over predictions made since it is one of the few convective electrode systems for which the hydrodynamic equations of the convective–diffusion equation have

been solved rigorously for the steady state. (Bard and Faulkner, 1980)

Whilst predictions of degradation can be made using fundamental thermodynamic relationships and experimentally derived electrochemical reaction rates, validation must always be made to the underlying mechanisms occurring and processes that are observed in practice. Figure 3.6, showing a relatively large area of a Galfan coating, indicates clearly that although the degree of corrosion varies across the surface, most incidents of this anodic attack are highly localized in the form of pits. This form of corrosion, visually apparent in figure 3.6, signifies the presence of defects at the Galfan surface more susceptible to anodic attack than the surrounding areas.

Figure 3.7 shows clearly that the majority of the localized corrosion effects experienced during the exposure of the Galfan coated steel over the 24 hours to 5% NaCl solution are all of a similar size and shape. This indicates that the defects present across the surface are most probably of the same form. Elvins (2005) proposed that the incidents of localized corrosion events at the surface were due to the presence of the primary zinc phase at the Galfan coating surface, which would seem plausible in the case shown in figure 3.7. A feature which would further support the observations made by Elvins et al. (2005b) is the location of these anodic dissolution events at the grain boundary depressions formed in the final stages of freezing of the ZnAl eutectic phase. This would go a long way in explaining the formation of the pits observed during the examination of the corroded Galfan samples using the scanning electron microscope, shown in figure 3.8.

Figure 3.9 reinforces the assumption that the local anodic attack is limited to the primary zinc phase. The local removal of material can be seen in figure 3.9 to reveal areas similar in dimension to those shown in figure 2.5. The relative attack between these voids/pits and the surrounding areas denotes the action of dissimilar metallic corrosion during the initiation of the corrosion process and goes some way to describe the differences observed in the RDE tests on zinc and aluminium.

It is widely known that aluminium forms a highly–protective, tenacious oxide layer which prevents further attack of the surface. Whilst in reality the zinc dendrites will contain very small amounts of aluminium due to coring effects, this will be far lower than that present in the solidified eutectic phase. This higher content of aluminium in the eutectic inevitably

offers greater protection to the eutectic phase via the formation of the aforementioned films being more likely at these areas of the Galfan coating surface.

Whilst incorporation of kinetical data pertaining to the behaviour of elemental materials at imposed potentials increases accuracy of predictions made, and removes the requirement for probabilistic or arbitrary functions for metallic removal, limitations still exist. The data is included in the model via direct input of the values obtained, albeit converted to more suitable units. The specific rate at which material is removed is equated from the potential to which the area simulated is subjected. As described in chapter 4, the cells within the modelling framework contain information that relates to the composition of the coating at that position. The rate is then calculated at that position under those conditions according to the composition allocated. This is done using quadratic interpolation between the data determined experimentally for commercially pure aluminium and pure zinc. During the generation of the simulated (synthetically approximated) coating layer, it is assumed that the composition of the entity remains at 4.5 wt.% Al. During the nucleation and growth of the primary phase it is assumed that the material removed from the system is entirely pure zinc, meaning that no cell of that primary phase contains any aluminium, thereby no interpolation is necessary. However, the cells within the model that are allocated the state corresponding to eutectic are assumed to possess aluminium levels around 5 wt.% Al.

The quadratic interpolation between the data for zinc and aluminium is made for those eutectic sites that are in contact with 5% NaCl solution (in the simulation of Galfan coated steels only), according to composition, which remains predominantly zinc. Unfortunately no measurements of corrosion rates fo ZnAl alloys are available, nor does this type of interpolation of data represent the influence of the oxide layers which would be produced during the exposure of eutectic material to the NaCl solution. The approximation is made in the model that an amount of material is removed using a weighted average of pure Zn and Al results for any ZnAl alloy sites. In addition, treating the primary zinc phase as pure zinc crystals neglects the influence of small levels of aluminium that may be, or become, exposed to the NaCl solution.

Including the data from the RDE means information relating to the passivation and polarization of the two metals tested is intrinsically contained within the model. It does

not however, mean that the performance of these specific metals or alloys under different conditions, e.g. pH regimes, is included. Consequently, should it be necessary that these pH relationships contained in the Pourbaix diagrams described in section 2.2.7 be included, then a series of conditions and restrictions must be explicitly outlined in the computer code.

The electrolyte used in both RDE testing and SEM evaluation was selected as this was most relevant for assessing the performance of a model depicting the localized corrosion effects of zinc alloy steel coatings with respect to readily available accelerated corrosion tests. It must be appreciated that changing the electrolyte used would have a substantial effect on the corrosion effects experienced and the extent to which these progress over time. This is due in the most part to the considerable influence the environment has on the corrosion process. It is extremely important to consider the conductivity of the electrolyte, since this carries the ionic current thereby playing an important role in corrosion reactions. (Trethewey and Chamberlain, 1995) The concentration of the NaCl solution is critical since the conductivity, and therefore the electrical resistivity, is greatly affected by the salinity of the solution. The actual solution in contact with the zinc alloy coatings is of great significance as different chemicals and reagents present during the corrosion process will alter the effects experienced over the duration of exposure or alternatively change the corrosion mechanisms/reactions taking place.

The above means that if predictions are to be made for the degradation of the zinc alloy steel coatings under investigation in different environments (and under different conditions due to temperature dependencies, including resistivity) then further RDE experimentation would be required to suitably adapt the model. As discussed previously, this would be a straight–forward procedure incurring minimal time consumption due to the ease of measurement and reproducibility of results. The benefits of interpolating the results obtained for pure metals rather than testing each coating layer are that the model retains the simplistic fundamental features and does not become alloy specific.

6.2 Modelling Approach

A general modelling approach has been outlined for the numerical simulation of localized corrosion phenomena in the previous sections. The model is used to produce two– or three–

dimensional transient field based simulations, operating at the microscopic–mesoscopic level.

As a well-known example of a macroscopic numerical approach, consider a cathodic protection system used to protect sea–going vessels from corrosion. Typically, this system will comprise several anodes that provide a sufficiently strong electrical field over the surface of the vessel to reduce or eliminate the possibility of corrosion occurring. The problem facing the designers of such systems is to determine the optimum number, location and power of anodes with which to provide efficient and effective cathodic protection. A numerical solution to this problem requires generating a 2D or 3D mesh of the physical system and then solving the well-known Laplace equation for all surfaces. This calculation provides a graphical representation of the predicted electrical field that can then be analysed and/or modified at will. It is common in such cases to largely ignore the electrolyte and merely solve, using a boundary element method, for the surfaces of interest.

Such a macroscopic approach has proved to be of value and yet it is also limited. The accuracy of such a method relies almost entirely on the polarization curves that are inputted into the model. The use of such curves envisages that all those areas of an object that are of the same material will behave in the same way. After time, with differing amounts of corrosion occurring at different locations, regions that are nominally the same material may well behave very differently, depending on their recent history of corrosion. If a model exists only at the macroscopic length scale then it will be extremely difficult for it to capture what are often the most important corrosion controlling events that occur at much smaller length scales.

The model used here does consider the local forms of corrosion to be of paramount importance to the performance of steel coatings. As such, particular attention is given to the local conditions of the electrolyte, in addition to the compositional differences across the surfaces of interest. It is still the case that the corrosion of the material is approximated directly from polarization data, in this instance from the RDE (chapter 3). However, this relationship is explored further since the simulated dissolution of the coating material brings about perturbations in local concentration which can be seen to alter local surface electrical potentials, and thereafter current density.

This data relating the surface electrical potential to the corrosion rate, shown to be proportional to current density in section 2.2, is incorporated by the model by the linear/quadratic interpolation between the data obtained for pure zinc and commercially pure aluminium. This is obviously the source of another assumption in the modelling of the localized corrosion effects associated with Galfan coatings, since the model treats eutectic cells as two separate entities according to the composition of the cell. Firstly, the amount of zinc contained in the cell that is permitted to transform is calculated. After which, the amount of aluminium in the cell is assessed with regards to the potential experienced in its local neighbourhood in order to determine the amount permitted to corrode over a time increment. This does not take into account the exact behaviour of these two metals combined as an alloy, especially the influence of structures produced during the solidification of these alloys onto a steel substrate.

As the corrosion of metals and alloys can be controlled by processes occurring over wide ranges of length and time scales, there are clear benefits in considering the corrosion process as a multi–scale phenomenon. A complete description of the process must necessarily entail an understanding of those key events that take place from the molecular level all the way up to the macroscopic level. Macroscopically, much work has already been done in the numerical modelling field. At the molecular level (while there is sometimes electrochemical understanding of important reactions and mechanisms) there is still a significant challenge to numerical models. Molecular level simulation, e.g. molecular dynamics modelling, is usually very expensive computationally and is generally carried out for much shorter time scales than those appropriate to corrosion problems.

At intervening length scales several models for corrosion have been developed in the past. Nagatini (1992) developed a purely diffusion controlled model. Meakin et al. (1993) developed a model that could simulate simplistic passivation and depassivation phenomena and was able to recreate distinctive morphological features of stable and unstable pitting corrosion. Electrochemical models have been proposed based on birth and death processes but these are concerned more with the stochastic nature of initiation processes rather than microstructural and morphological effects. (Shibata, 1990; Williams et al., 1985) Mola et al. (1990) considered the random aspects both of nucleation as well as early stages of pit growth.

Monte Carlo (Malki and Baroux, 2005; Newman et al., 1992), and more recently cellular automaton techniques, have been used to simulate localized corrosion. (Taleb et al., 2005) However, while these methods often produce very interesting behaviour, it is notoriously difficult to make these techniques quantitative and thus applicable to real systems.

Many of the simulations operating at sub macroscopic length scales have been developed by invoking random movements of particles or random dissolution events. However, relatively little numerical simulation has been performed to date that links field based simulation to well–known electrochemical equations. This is surprising when one considers the advances already made in multi–scale computational materials science in other fields (Raabe, 1998) that often use this approach.

The algorithm presented here is one that has been used with some success at the microscopic/mesoscopic length scale. (Barnard et al., 2005; Brown et al., 2004) Essentially it uses a combination of standard continuum differential equations coupled to basic electrochemical equations. (Prentice, 1991)

At the stage of discretization, the model must rely upon adequate electrochemical understanding of the localized corrosion phenomenon of interest and thus determine exactly what a representative volume is. This volume should therefore capture the important physical features sufficiently well. In this model it is the local micro–scale variations in metallurgical structure that are deemed most important for the development of localized corrosion behaviour and a suitably sized irregular, orthogonal mesh has been used to represent this microstructure.

Although in reality ZnAl eutectic is a two–phase structure, it is treated in the model as a single phase, albeit with a different standard electrode potential to other phases. Similarly, primary zinc dendrites have been assumed to be pure zinc, ignoring any small Al content that may be present due to coring effects during solidification. Surface depressions around eutectic grains have been observed in practice and this feature of the microstructure has been included, these can be seen as slight depressions in the surface in figure 4.3.

As always, there exists a variety of computational frameworks on which such a simulation can be performed; including finite element, finite volume, cellular automaton and Monte Carlo. Each method has advantages and disadvantages providing opportunity for

zealous arguments between modellers advocating their own particular system. However, the primary criterion on which to judge the effectiveness of any model is by direct comparison of that model to actual experimental measurement. Secondary considerations could then include speed of calculation, meshing facilities, graphics etc.

As stated previously, the microstructures used in simulations are entirely synthetic, generated to look like those observed in microstructural investigations, with a degree of success. Exciting work currently being done using phase field methodology to simulate microstructural evolution also tends to work in a finite-difference computational framework. Thus the ability to 'import' a simulated microstructure into the current algorithm is straightforward.

Clearly, in different systems different modelling assumptions may be necessary. Specifically, information concerning multi–stage reactions with multiple chemical species may well be required from electrochemical theory for certain systems.

The types of procedure described in previous sections represent an attempt to include important rate–controlling steps into the algorithm. At this point, the procedures described appear to be good enough to recreate observed corrosion phenomena. However, in any creative process such as modelling, alternative or improved methods are bound to be developed in the future.

Determination of the surface electrical potential is a critical step for the success of the modelling approach described. Equation 4.4 is used to determine the surface electrical potential, estimating the effect of changing concentration for all species via the perturbations in concentration of H^+ only. Direct estimation of the overall corrosion effects experienced considering only one electroactive species distinguishes the model from those that deal with individual species. (Cordoba-Torres et al., 2001; Johnsen et al., 1997) This is deemed appropriate for a first order model since perturbations in H^+ are brought about during the anodic dissolution of both zinc and aluminium. Clearly, different solid phases will also possess different standard electrode potentials, E_0. If the data was available, temperature or other dependencies of E_0 could be included here, highlighting the flexibility of this approach. Distribution of Zn^{2+} and pH across a galvanic couple can be seen to support this approach due to the pivotal role corrosion products in the model. (Tada et al., 2004a,b)

The algorithm does not deal with convection, as the electrolyte is assumed to be stationary above the discretized solid material in any simulation. At the point of determining the effects of diffusion/migrations, if the flow field is known, the effects of electrolyte convection could be included via the velocity vector, W, into equation 4.12. This would be pertinent for zinc and zinc alloy coated steels since great interest exists in the cut–edge degradation in the use of inclined roofing, as well as zinc run–off from rainwater in different environments. (Elvins et al., 2005b) Similarly, at this stage, temperature and concentration dependency for diffusion and migration could be implemented, assuming the relevant data is available. For some systems it may be necessary to model multi–species diffusion and this will depend on the complexity of the corrosion process model. In such cases data for individual diffusivities including any interaction terms would be required. The modelling framework would allow for multi–species simulation, provided the electrochemical processes taking place are understood explicitly.

Unfortunately, accurate quantitative data concerning deposition/dissolution rates of corrosion product films is not generally available. Furthermore, the quantitative effect of corrosion product films on surfaces with respect to diffusion and electrochemical behaviour does not seem to be available in any great depth. Experimentation in this area would provide information necessary for accurate representation in a model. In terms of modelling it is necessary again to make simplifying assumptions.

It is recognized that a very simple model of corrosion product formation is used and thus is an area where significant improvements could be made. A particular issue is that in the absence of a multi–species simulations, the corrosion products are assumed to be of the same material/composition. This obviously does not take into account the relative activity and adherence of the differing corrosion products, i.e. zinc or aluminium salts, with regard to their deposition or breakdown. This behaviour is of great interest since it would distinguish the onset of localized corrosion effects across the simulated surface, as well as specific sites preferentially protected by any films deposited. The definite breakdown of passivity under specific conditions for an alloy system whose pH–potential relationship is well–known could be included at this stage. (Isaacs, 1989; Punckt et al., 2004; Schmuki, 2002)

From the preceding discussions, it is clear that some limitations and approximations are

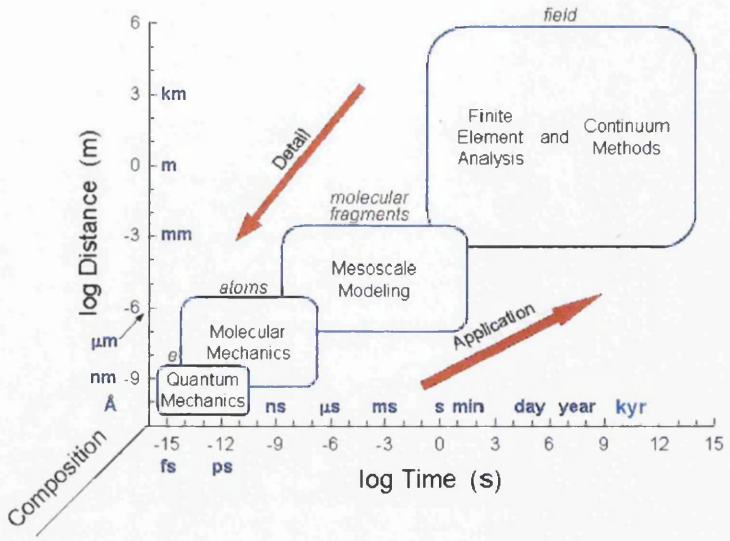

Figure 6.1: Multi–scale modelling: time and length scales.

necessary at various steps in the algorithm. However, within the framework of the algorithm, there is scope for increased sophistication in terms of numerical procedures as well as improved accuracy with the availability of better quantitative data. The computational framework used is based on a finite-difference approach. Finite element methods, the phase field method, front tracking techniques and even meshless methods may well provide advantages over this. Comparison to real data is the critical test. Such comparison is discussed for the model in the following chapters. Also, the role of stress has not been considered here. Work on stress-corrosion modelling is already being attempted, (Jivkov et al., 2005) the above algorithm embedded within a finite element stress model would appear to be a promising avenue for such research.

An algorithm has been presented that is capable of capturing certain important localized corrosion effects at the micro/mesoscale, by approximating the effects of submicron processes on concentration perturbations experienced. The approach taken is quite general and could be framed equally well within different computational schemes. The key requirements for the successful development of such models are the ability to capture the important aspects of material structure adequately and to sensibly couple this to a mechanistic model of the localized corrosion process.

It is felt that such models can provide useful illumination for certain localized corrosion

problems in that they can potentially deal both with microstructure and geometric effects. It is accepted that such an approach will not necessarily work for all systems and that the proposed algorithm contains much scope for improvement. It is tempting to draw a flow chart linking together boxes for atomistic, micro scale, meso scale and macro scale simulations as the way forward. However, while figure 6.1 is seductive, it is the overlapping of the boxes in the flow chart that pose the greatest problems. It is still the case that true multi–scale simulations are very difficult to achieve for real, complex systems. Multi–scale modelling of localized corrosion, let alone many other topics in the field of computational materials, is a problem still waiting for a final solution.

6.3 Discussion of Results

The results presented in the in chapter 5 had been selected as illustrative examples of the mechanisms captured by the computer model; including galvanic effects, the degree of localization, pitting and selective dissolution as well as the influence of nucleation on the progress of anodic dissolution. Discussion is also given to the influence of microstructure on the ZnAl coating simulations.

6.3.1 Influence of Nucleation on Predicted Localized Corrosion Effects

In the case of the electroplated zinc (EZ) coated steel it was necessary to nucleate defects at the surface since it was assumed that the coating was in essence a pure zinc layer. The result of this assumption was that there existed no sites exposed that were more prone to degradation with respect to others. Should these nucleation sites not be present, then a generalized corrosion regime would be predicted, exhibiting gradual dissolution of the entire coating layer in a uniform manner via movement of anodic and cathodic zones over the exposed surface.

The act of removing a cell within the represented zinc layer, as if the transformation took place instantaneously at the start of the simulation, means that a local corrosion cell is established since the particular sites are distinguished as sites of anodic activity, effectively forcing the material directly adjacent to act in a cathodic manner. The situation then experienced is one where the area of anodic activity is far less than the area operating

cathodic mechanisms, describing a localized form of corrosive attack. The nucleation of the defects in this manner with respect to EZ steel coating can be seen to limit the number of active anodic sites throughout the simulation to those predetermined at the initial solid–liquid interface. This can be seen in the voltage field in the 0.1% NaCl solution after 24 hours in figure 5.2, throughout the simulation in the form of vertical current density in figure 5.4, and, ultimately lead to the exposure of the steel substrate directly below these nuclei as can be seen in figure 5.3.

Whilst the solid–liquid interface in all cases was assumed planar, with the exception of the eutectic depressions in the Galfan surface case, nucleation of localized corrosion effects was not necessary in the case of simulations involving the zinc–aluminum alloys simulated. This was due to the microstructural changes across the surface arising from compositional differences. These had the effect of naturally setting up local corrosion cells arising from galvanic effects. These galvanic effects are present because of the differing zinc content between the primary zinc phase to the eutectic matrix. It was assumed in the simulations that the primary zinc dendrites were pure zinc crystals and that the composition of the eutectic was homogeneous, calculated from the amount of zinc left in the system once the dendritic phase had been represented. The aluminium levels in the eutectic phase are at a relatively low levels compared to the weight fraction of zinc present, although it is clear from figure 5.7 that even small compositional changes can cause large local potential differences across the coating–electrolyte interface due to the presence of dissimilar metals/metallic phases present.

The result of the surface exposure of the Galfan steel coating is that the electrical potentials arising from compositional changes at the exposed surface are setup such that the anodic potentials, and thereby current occurs at the sites occupied by the primary zinc phase. The more rapid removal of this material leads to pitting occurring at these positions, thereby promoting further dissolution of this phase due to the pivotal role effective free proton concentration plays in the model. The resultant degradation is highly localized since predicted pitting at these discrete positions occupies a much smaller area of the exposed surface than the supporting cathodic activity.

It is a recognized fact that one of the most challenging aspects facing the field of computational materials science is describing the nucleation of natural phenomena. In

the case of predicting the occurrence of localized corrosion effects this is a critical step and requires a detailed knowledge of the corrosion mechanisms operating, which are a consequence of the specific materials properties; physical and chemical. Validation is necessary therefore to validate the nucleation of such local defects. It is known from the work of Elvins et al. (2005a) that the unaided nucleation exhibited by the model in the case of the Galfan layer is typical of that which is experienced in the accelerated corrosion testing of these coating layers using 5% NaCl solution at pH neutral.

Initiation of corrosion has been considered by other workers during the course of the investigation, both with respect to zinc systems (Amin, 2005; Neufeld et al., 2002), and other cases (Isaacs, 1989) including stainless steels (Punckt et al., 2004; Sourisseau et al., 2005) in order to gain a greater understanding of the initiation of the localized effects. This was seen to fall outside the scope of the current investigation, although it is recognized that this is an important area pertaining to the corrosion performance of all materials.

6.3.2 Evolution of Electro–Active Concentration

The evolution of the effective free proton concentration, H^+, for both EZ and Galfan coated steel is assumed to be attributed to the rapid hydrolysis of the zinc or aluminium cations produced during the anodic dissolution of Zn or ZnAl cells. As has been established, even in the Galfan case this is almost exclusively the anodic dissolution of zinc. Figure 5.1 shows the evolution of this concentration from a Galfan coating, originating from positions occupied by the primary zinc phases present. Figure 5.27(b) shows how perturbations in this ionic concentration remains close to the corroding surfaces, reflecting the anodic and cathodic balance occurring.

The use of the H^+ concentration in this first order model of the localized corrosion effects experienced by zinc and zinc–aluminium steel coatings simplifies the scenario somewhat, since the interactions of the individual species in solution is not considered, only the effects estimated from the migration term in equation 2.44. No distinction therefore has to be made with regard to the cathodic reaction, whether it be oxygen reduction at the surface or hydrogen evolution within a pit (Volkov et al., 2004), allowing a cathodic routine to be applied to the entire exposed surface.

However, as the simulations are performed at pH neutral and it has been discussed that the rate–determining step involved in the localized corrosion process is the cathodic reaction, it is apparent that the concentration of oxygen is an important factor. An approach used in order to represent this effectively whilst keeping a first order model was to use the diffusion coefficient of oxygen rather than hydrogen. Rather than estimating the rate at which the oxygen can diffuse to the surface after a time step where an amount has been consumed, consistent with the degradation predicted, the diffusion of the effective free proton concentration is reduced away from the surface; increasing dependence on any 'available' oxygen present.

6.3.3 Zinc Steel Coatings

During the simulation of the surface exposure of the EZ coated steel, the predetermined nucleation of a corrosion defect immediately sets up a concentration cell, creating a situation whereby any subsequent corrosion is most favourable at such positions. In addition to this, the most likely cell to corrode during the subsequent time increments is the cell directly below this defect. Once this cell has dissolved, over one or many time steps, the next cell likely to corrode is the one directly below this one and so on. This means that the tendency for corrosion during the surface exposure of these EZ is mostly in the vertical direction. This leads to the case experienced in figures 5.2 and 5.3 where the localized corrosion effects are limited to the cases nucleated, where concentration perturbations are forced and the same position where further concentration contributions are made to the Neumann or Moore neighbourhood.

The tendency for corrosion to form pits at the surface is due, for the most part, to the representation of the corroding surface and the initial potentials predicted across the solid–liquid interface. The dominant concentration at the predetermined nuclei at the start of the simulation sets up spatially distinct anode and cathode sites. The area ratio of the anodic sites to the cathodic sites is very small, i.e. $S_A << S_C$, therefore the corrosion mechanism is highly localized. This method of predicting the degradation of a steel coating from nucleated defects is a valid case should the relationship between defects arising during the fabrication of these products and the corrosion experienced in certain environments be

known. It is probable that this would have been the case should investigations have been made to correlate imperfections identified by automated systems and the typical corrosion performance.

Once the concentration cells have been setup across the EZ coating exposed to the 0.1% NaCl solution, it is the calculation of the rate of zinc loss to the RDE data for pure zinc that is responsible for the greater tendency to predict pitting type behaviour. The high tendency for localized effects to progress vertically, therefore creating trough pits (figure 2.19 on page 36), is due to the calculation of rate from the exchange current density at the surface. Since the corrosion rate is proportional to the rate of current passing through a plane at the surface, the surface area of an exposed cell at the solid–liquid interface is a major influence. This means that the position of that plane/cell within the orthogonal grid is critical. As an irregular mesh is used the nodal spacings, described in chapter 4, vastly differ between the y direction and the x and z directions. This means that where the nucleation site has been removed, the largest area exposed to the elevated concentration left behind is that below it, $y - 1$. This is then the calculated as the largest potential from the Nernst equation, which in turn yields the highest current density. Since $\frac{dM}{dt} \propto i$, the largest material lost from a site over a time increment occurs at these positions.

The type of localized corrosion phenomena occurring at the surface changes once the 2 μm EZ steel coating has been penetrated, exposing the steel substrate, over a typical simulated time–scale shown in figure 5.3. The pitting experienced during the early stages of surface corrosion simulation is replaced by a regime of galvanic corrosion taking place. What is apparent from figure 5.3 is that once the steel substrate has been exposed at a particular point, the focus of the corrosion is to remove the coating layer around these points, eating the protective barrier layer back laterally.

The mechanism of the galvanic corrosion taking place in the case of the EZ coated steel exposed to 0.1% NaCl after 14.4 hours simulated time can be seen in figure 6.2. The effects of this process is considered in figure 5.4. During the early stages of the simulated corrosion processes, before 14.4 hours in figure 5.4, the vertical current density is at a maximum directly above the pits described previously. After this time, whilst there is steel substrate exposed to the electrolyte, the maximum current density is experienced around the perimeter

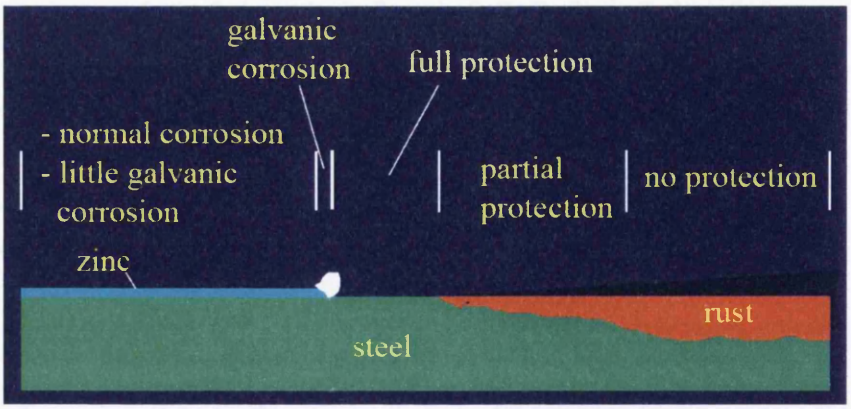

Figure 6.2: Protection offered by the zinc coating to the steel substrate as a function of distance. (Zhang, 1996)

of the exposed steel substrate. This is due to the cathodic protection offered by the zinc present near these sites to the exposed steel. Due to the increases in intensity of this anodic region, there exists a more focussed area of cathodic activity in perimetric areas around the exposed steel substrate, more visible in figures 5.4(e) to (h).

The increased lateral corrosion is due to the galvanic corrosion taking place in those areas highlighted in figure 6.2. This is brought about because of the relative positions in the galvanic series (table 2.3), whereby the zinc corrodes in preference to the steel. The steel in the simulation resides in the position marked 'full protection' in figure 6.2, whilst other areas of the zinc coating away from the nuclei sites are the subject of little galvanic corrosion. This is an important aspect of the model since the influence of a strong cathode on a less noble metal at the same surface is related to the distance of separation, in addition to the relative area each material exposes to the electrolyte, which poses challenges in terms of modelling. (Schifler, 2005) Figures 5.3 and 5.4 show that the model captures the galvanic effects occurring when a small amount of steel is cathodically protected by a zinc coating, especially the effect of increasing the corrosion rate of the anodic metal and suppressing the corrosion rate of the cathodic alloy.

In the case of the surface corrosion of EZ coated steel, the greater the area of exposed steel, the more degradation is predicted to the zinc phase present. During the early stages of the localized corrosion effects, the majority of the corrosion products are deposited onto the zinc coating at the initial surface level around those areas of degradation nucleated. After

the steel has become exposed during the simulation the corrosion products formed during this period are done so at the sites next to steel cells, due to this being a more cathodic phase, rather than a local cathodic area on a homogeneous surface falling within arbitrary concentration and potential bands.

Contrast this to the cut–edge EZ coated steel case where a large area of steel is protected by a small area of material offering cathodic protection, zinc. The case is reversed here where, from the outset, both materials are exposed to the electrolyte and the relative areas are such that the prospective cathode is large compared to the anodic material. The influence of separation length is still in evidence in figure 5.5, where a region experiencing full galvanic protection is present along the length of the cut–edge and has not been the subject of any corrosion product deposition. This is due to the elevated H^+ concentrations predicted at these positions due to the sacrificial degradation of the zinc coating. Further from the EZ coating layer, the steel is under partial protection from the coating layer since the distance has been increased and at these positions there has been substantial corrosion product deposition, denoted by the grey material shown in figure 5.5. At regions further still from the coating layer are areas of the steel substrate that are unprotected from that offered cathodically by the zinc coating layer. This is unsurprising as the zinc coating layer represents a thickness of 2 μm, much smaller than the 470 μm gauge thickness of the steel.

There is a greater amount of coverage given by the corrosion products in the cut–edge case when compared with the surface case. The larger area of steel offers a more diffuse cathode, coupled with lower H^+ concentrations over the steel that promotes lower volume fractions of corrosion product to be deposited. The corrosion of the zinc coating layer itself is far more uniform than in the surface case, mainly due to the relative thicknesses of the coating and substrate and the reduced influence of the initial nucleation on corrosion. There is very little pitting occurring in the predicted cut–edge corrosion of EZ coated steel since the galvanic corrosion is the most prominent process taking place. However, the nucleation of defects is not limited to the zinc coating in this case, but is also present across the homogeneously represented steel. This can be seen to change the pattern of the electrical potentials produced, shown in figure 5.6, and the corrosion products deposited in those positions.

There can be seen to exist areas of anodic potential above the steel layer at the sites of the nuclei, arising from the dissolution of the steel material at those positions. This consequently prevents the deposition and 'healing' of this site due to the concentration and potential tolerances imposed during this particular routine in the simulation.

6.3.4 Zinc – Aluminium Steel Coatings

The exposed surface of the Galfan coated steel can be seen to create a more complex potential field in the electrolyte, shown in figure 5.7, even in the absence of nucleating any surface imperfections/defects. The reason no defects were imposed in the case of the surface exposure of Galfan type alloys to the 5% NaCl solution is due to the dissimilar metallic phases present at the surface. Each phase is susceptible to anodic dissolution to a different degree and the presence of the other phase influences the tendency towards dissolution as a function of area and distance of separation in the model.

All cells of each phase present in the surface corrosion simulation of Galfan are assumed to be of the same composition. Whilst this is the case, the corrosion of these phases can be seen to be influenced by their position on the exposed surface, as can be seen in figure 5.7(b). Some areas can be seen to be untouched, at an electrical potential indicating cathodic activity, whilst other areas can be seen to be the subject of highly localized effects, at an electrical potential of a highly anodic site. Interestingly, it is only when a group of local 'anodes' are operating at areas of the simulated Galfan layer that there is a substantial effect predicted in the bulk electrolyte, shown when all electrolyte elements are considered in figure 5.7(a). This indicates that the position and circumstances from which the localized corrosion arise is critical to the detail being present in the voltage fields predicted. Whilst the standard electrode potential, E_0, contributes toward the fixed boundary condition at the coating–electrolyte, it is clearly the effect of the concentration perturbations that result in the shift in the Nernst relationship used. These perturbations exist at multiple sites close to one another, ultimately leading to a voltage field being present in the electrolyte beyond the diffusion layer.

The corrosion mechanism predicted for the surface corrosion of a Galfan coated steel can be seen to be a galvanic type attack, yielding results like those shown in figures 5.8

and 5.9. The corrosion effects are setup because of the different phases exhibiting differing potentials when exposed to the 5% NaCl solution and the relative material loss is related to the galvanic effects brought about by the neighbouring material. It is predicted by the model that the zinc rich primary phase corrodes in preference to the ZnAl eutectic phase due to the relative positions zinc and aluminium occupy in the galvanic series and the composition of each phase with respect to aluminium content. The dissolution of zinc preferentially to the eutectic can be seen in figure 5.8. Here the zinc is locally attacked due to the higher potentials at the interface determined using the first order Nernst relationship previously described. Clearly seen in figure 5.8 is that the small aluminium content of the eutectic phase (*ca.* 5%) is enough to suppress degradation of this phase by reducing the potential predicted, thereby the rate based on direct reference to the current density from the RDE. This form of selective dissolution is very similar in nature to that of dealloying. (Erlebacher, 2004; Erlebacher et al., 2001)

The distance effect associated with galvanic corrosion is also evident at the corroding surface of a Galfan coating. This is highlighted in figure 5.9 since dendrites of similar dimensions present at the surface for an equivalent time are degraded to different extents. A dendrite whose surrounding sites over a short distance are eutectic cells, experiences a higher degree of localized attack during the cathodic protection of the eutectic phase, than one whose neighbouring elements is a mixture of primary and eutectic in which case the corrosion experienced is far more generalized. It can also be seen that the selective removal of the dendritic phase leaves pits. The concentration build–up in these features obviously leads to a higher degree of degradation predicted. The passivation behaviour of the aluminium can be seen in the surface case of Galfan to lead to the eutectic material present at the surface being relatively untouched, a result of the data used in the model that was derived from experimental measurement using the RDE.

Electrode potentials across the surface can be seen to have been directly affected by the material present at the surface and the relative degradation of these phases due to the concentration contributions made during the transformation of cells undergoing anodic dissolution. It can be seen from the electrical potential field shown in figure 5.10 that the areas of highest anodic potential (with the highest likelihood of dissolution) occur at

positions of greatest primary zinc exposure. These can be seen to occur at positions where the zinc dendrites are prominent at the interface within the simulated eutectic cell depressions. Due to the galvanic effects included in the model this forces the cathodic areas to be on the surface of the eutectic cells near to the edges, although less protection is offered directly adjacent to the depressions; since this is close to the anodic activity taking place and therefore higher H^+ concentrations are experienced. The cathodic protection offered reduces further toward the centre of the eutectic grain in a similar manner to the surface EZ coated steel simulation due to the increase in anode and cathode separation. It is the case however, that this pattern is interrupted when zinc dendrites are present at the centre of the eutectic cells at the surface.

Due to the structure and complexity of the corrosion taking place at the surface of the Galfan coating, it is extremely difficult to deposit the corrosion product on the surface. It was assumed that the corrosion product was to be a volume equivalent of 5% of that dissolved and, once again, be deposited as a function of ionic concentration and voltages in the electrolyte cells at the solid–liquid interface. However, it can be seen in figure 5.11, that wherever possible, the model deposits this product at those cathodic sites highlighted in figure 5.10. This demostrates that the model, with its limited capability to reflect this complex elctrochemical process, is able to reflect to some degree, the overall effect that corrosion products have on subsequent corrosion. This is shown in figure 5.12 where the product, A, is deposited a short distance away from an active anodic site, B, at a position where after 24 hours little or no anodic dissolution is taking place.

Again, it is recognized that this is a rather simplistic approach taken towards the formation of corrosion products and obviously a significant area upon which to improve the present model. Considerable interest exists in the formation of corrosion products and passive films in zinc and zinc alloys, both in atmospheric (Alimenti et al., 2004; Friel, 1986; Rodríguez et al., 2002) and wet corrosion. (Amin, 2005; Li, 2001; Muster and Cole, 2004; Pieraggi et al., 2005)

Galvanic effects taking place at the surface of a simulated Galfan surface can be seen to be exacerbated at the solid–electrolyte interface by the presence of the steel substrate, as shown in figure 5.13. Here the steel substrate can be seen to vastly accelerate the localized

corrosion of the dendritic phase due to the dissimilar metals in electrical contact. The distance effect can be seen once again, as the dendrites close to the steel are the subject of a greater amount of anodic dissolution. Zinc dendrites further from the steel substrate can be seen in figure 5.13 to exhibit less degradation since only a fraction of cathodic protection is offered to the steel when compared to those in close proximity. The steel substrate can be seen to have an impact on both of the Zn containing phases present close to the substrate since the eutectic phase can be seen to have been somewhat 'eaten away' at the sites of the most substantial degradation. This is due to the predicted passivating effect of the low aluminium levels in the eutectic phase being suppressed due to the high anodic potentials at these sites, thus increasing the current density and therefore the corrosion rate.

The corrosion product at the Galfan cut–edge can be seen to occur at the localized anodic sites (i.e. zinc dendrites) close to the steel substrate around the area adjacent to the localized corrosion. The corrosion products present in figure 5.13 can be seen to have been deposited across the surface of the active zinc dendrites further away from the steel substrate. This reflects the lower potentials and concentration at these sites and represents self 'healing' of these zinc anodes. The thickness of the steel substrate present in figure 5.13 is a fraction of those used in practice. In addition, all of the steel shown in figure 5.13 is predicted to be in the regime of full protection from the Zn–Al coating layer, similar to the situation outlined in figure 6.2. However, it is not suggested here that should a realistic substrate thickness be included, the rest of the steel would be protected.

With the accelerated corrosion of the zinc dendrites during the exposure of the steel substrate in addition to the Galfan coating layer, there is a change in the morphology of the pits formed. A transition from 'trough' to 'sideways' pits is observed. This is due to the increased removal of material from the zinc dendrites present at all the exposed surfaces, such that anodic attack is occurring not only to the primary dendrite arms, but also at the secondary dendrite arms. This has the effect of making diffusion of ionic concentration from the pits more difficult. Consequently, H^+ concentration is retained in the pits, reflecting the elevated concentration of electro–active species and subsequently, the electrode potentials at the fixed boundary conditions are at a maximum in these geometric traps. This is conducive to further dissolution, thereby driving the localized corrosive effects and is responsible for

the form of the concentration and potential field shown in figure 5.14.

Behaviour with regard to pitting occurring via the removal of zinc from the dendritic phase in the cut–edge exposure is maintained when a gauge thickness of steel that is more realistically used in the service environment is included. The problems that the inclusion of such a structure poses has been discussed in chapter 4. Figures 5.15 and 5.16 show that the Galfan layers are much smaller than the steel substrate, in addition to their thicknesses being much smaller than the depth of the electrolyte. However the fine elements placed at the surface of the material and in the diffusion layer can be seen to minimize the effects of these disparate length scales. Another problem identified was the limit of cut–edge length represented, whilst maintaining definition of the primary zinc dendrites. It can be seen from figure 5.17 that a cut–edge length of 2.5 mm is adequately represented by a $200 \times 50 \times 200$ mesh, although any increased cut–edge length would require a greater amount of nodes in the x direction.

Over a short distance of cut–edge exposure of a Galfan coated steel, pits are seen to develop over 24 hours exposure to the 5% NaCl solution at sites occupied by primary zinc dendrites. This is replicated over a longer cut–edge length as shown in figure 5.19. In both cases the size and morphology of the pits, shown as volumes of electrolyte, are similar and the concentration building up within these pits can be seen to be equivalent, shown by the lighter areas. The electrical potential determined throughout the electrolyte is one of a cathodic area over the steel and anodic potentials occurring over the Galfan layer. Figure 5.21 even shows that the model will distinguish between the zinc rich phase, the eutectic phase and the steel with respect to the surface electrode potentials in contact with electrolyte.

A predicted phenomenon that appears to be independent of the cut–edge length is the occurrence of two focii of cathodic potentials that occur at the centre of the steel substrate at $\frac{1}{4}$ and $\frac{3}{4}$ length of the cut–edge. These focused cathodic zones are present at a cut–edge length of 0.77 mm (figure 5.18(b)) and 2.5 mm (figure 5.20). The only difference is that the influence of these sites is less in the longer cut–edge case since they effect smaller proportions of the cut–edge length due to the distances between the focii and the cathodic protection they require from the Galfan coating.

Resultant degradation experienced by the cut–edge corrosion of the Galfan coated steel

Figure 6.3: Micrograph showing the selective dissolution of the primary zinc phase at the cut-edge of a Galfan coated steel. (Elvins, 2005)

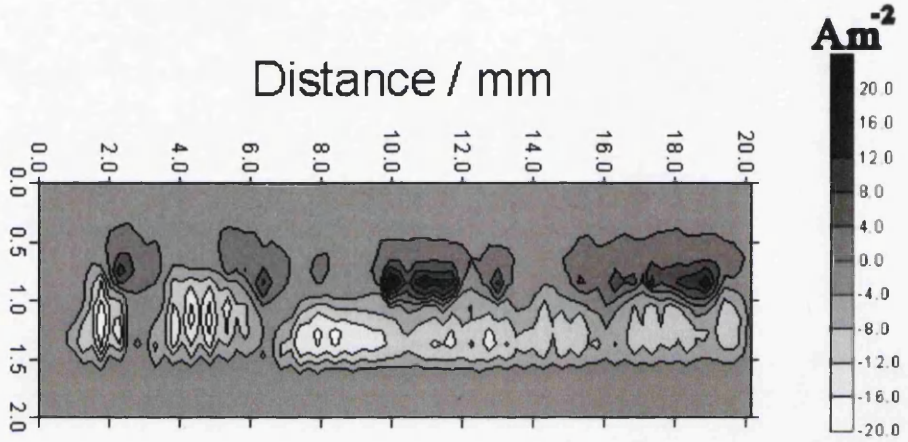

Figure 6.4: SVET measurement of the current density 100μm above the cut–edge of a Galfan coated steel after 12 hours immersion in 5% NaCl solution. (Elvins et al., 2003) Distortion in scale exists between the x and y axes.

is very similar to that previously described. The zinc dendrites are the focus of most of the material removal via anodic processes acting. This is reduced at greater distances of separation form the steel, i.e. anode and cathode separation. This can be seen to be predicted by the model in figure 5.23, which has reproduced what is experienced in practice, figure 6.3, using thermodynamic relationships and kinetical data. The formation of corrosion product over the steel substrate is widespread in figure 5.22, albeit at relatively low levels. Again, there is a region close to the steel substrate along the length of the cut–edge that is fully protected, although corrosion product has not formed. Once again, this is due to the tolerances imposed during the corrosion product routine.

The removal of zinc from the coating layer creates concentration perturbations in $[H^+]$,

and spatially distinct anodic and cathodic sites along the length of the cut–edge. The flow of electrons and ionic mass transport is captured in the current density field within the electrolyte. The form of the vertical current density fields, shown in figure 5.24, can be seen to be consistent with those produced via SVET (scanning vibrating electrode technique) testing, shown in figure 6.4. Discrepancies arise due to the determination of current density being critical to the distance over which the calculation is performed, a situation that is often encountered in modelling natural phenomena.

The formation of corrosion product, predominantly at the surface of the steel substrate, goes some way to explaining the cathodic focii described previously. From figure 5.25 it is apparent that the corrosion product spreads from the region close to the Galfan coating toward the centre of the substrate, whilst the area directly adjacent is left untouched. The corrosion product moves toward the centre as the cathodic zones on the steel substrate alter due to product formation and reducing cathodic capability of the areas at shorter distances from the steel. Obviously, due to the potential tolerances imposed the amount and position of corrosion product will be dependent upon the dissolution taking place and supporting cathodic activity. Later in the simulation, corrosion product hinders the cathodic activity over the majority of the substrate, although small areas in the centre remain uncovered. These sites then have the maximum capability in the simulation to balance the anodic activity taking place leading to the cathodic focii shown in figure 5.18(b). This is independent of the cut–edge length since the corrosion product will always have the tendency to grow toward the centre in the same manner. This is obviously an area where the current model could be strengthened.

6.3.5 Influence of Setup and Exposed steel on Galfan steel coatings

The influence of the setup of simulations involving steel, zinc and aluminium has been seen to alter the corrosion experienced when the Galfan coating formulated using the same parameters to 5% NaCl solution. Obviously, the surface and cut–edge cases in 2D simulations exhibit the same behaviour as those performed in 3D.

In addition to capturing the pitting and galvanic type behaviour, the model is able to capture the diffusional aspects of 'crevice' corrosion in the scratch case. This differs from

the Fontana–Greene mechanism described in section 2.3.3 since at the base of the scratch is the steel which is overwhelmingly cathodic in behaviour. In this case an increased amount of corrosion takes place within the scratch due to, initially, galvanic effects between the steel and the Galfan coating, but this is exacerbated by the slower diffusion of the evolving H^+ not consumed in the cathodic processes occurring at the steel substrate to the bulk electrolyte.

The pin case not only presents a much greater cathode to anode area ratio, due to the increased amount of steel, but also represents smaller channels through which mass transport can take place. The electrical contact means that the area for cathodic potential is much greater around the pin and can be seen to exhibit very high areas of cathodic activity at the base of the pit, but in addition a large area at the position of the pin protruding out from the coating discontinuity seen in figure 5.26(a). This results in the higher degradation of the surface due to the greater amount of protection that is needed by the steel and this is offered by the combination of the increased degradation within the scratch, in addition to the surface in electrical contact with the pin.

A further increase in the degradation is experienced by the coating material both within the coating discontinuity and also across the surface of the coating when the bolt head is included in the simulation. The increased degradation can be attributed to the increased steel exposed, the position of this steel and the diffusion altered diffusion of the free proton concentration. The bolt head is away from the areas of elevated H^+ concentration, allowing it to act in a strong cathodic manner. This requires a greater amount of cathodic protection, which results in higher amounts of material lost from the coating layer. The diffusion of the proton concentration from the coating discontinuity is impeded in the y direction, forcing any free proton concentration not consumed in the cathodic activity at the bottom of the scratch across the surface of the adjacent coating layers. A concentration is then built up above the surface resulting in a higher degree of degradation, visible in figure 5.27(b).

With regards to the use of Galfan coated steel as the substrate for an OCS (organically coated steel) product, it is of most interest for the cut–edge, scratch, pin and bolt situations; since most corrosion protection problems occur at areas of coating discontinuity brought about by cutting or fabrication. In efforts to hide the exposed cut-edge, folds and arrangements are made as to remove the electrolyte from the electrochemical cell although,

should electrolyte be present, aggressive local environments would ensue.

Current density vectors show the detail that exists in the bulk electrolyte from complex current paths close to the surface. The current density around the surface case and the cut–edge cases show this in 2D in figure 5.28. These offer far more detail at areas of localized corrosion close to the surface than would be able to be measured experimentally using a scanning vibrating method. Some of this information is lost when calculating only the vertical component of current density, although the vertical current density does identify the position and intensity of the localized corrosion processes taking place at the surface.

6.4 Influence of Cooling Rate on Corrosion Performance

In terms of the surface corrosion of Galfan coated steel, there is obviously a discrepancy between the simulated and predicted corrosion performance. There are several features that may contribute toward these contradictory results. From these, indications of possible improvements to a computer model for the prediction of these specific coating alloys at different production conditions may be gained. The correlation between the results for predicted degradation behaviour for Galfan coated steels exposed at the cut–edge, is encouraging in terms of validating the computer model.

6.4.1 Microstructural Dependence of Surface Corrosion Performance

The degradation shown visually in figure 5.29 highlights the influence of the starting microstructure on the amount of degradation predicted throughout the simulation. What is unclear however, is the influence the eutectic has on the corrosion performance since the microstructural feature that has been varied is the zinc dendrites. Including estimated surface depressions around the boundary of the eutectic cells present at the surface can be seen to have an influence in terms of anodic activity (current density, $i_a \propto \frac{dM}{dt}$) in figure 5.31. However, these eutectic cell sizes can be seen to change under differing processing conditions as in table 6.1.

Previous results suggest that the surface texture of the Galfan coating formed on the steel substrate is critical to the amount of zinc lost during local corrosion effects acting on the surface. A major feature of this texture is the eutectic cell depressions, distributed arbitrarily

Table 6.1: Summary of the microstructural evaluation of the zinc – 4.5 wt.% Al galvanizing coatings obtained using different cooling rates. (Elvins et al., 2005a)

Sample ID	Volume fraction of primary zinc phase %	Eutectic cell size mm	Inter–lamellar spacing μm
55H	20 (±1)	1.87 (±0.18)	1.37 (±0.05)
80H	22 (±1)	1.19 (±0.11)	0.70 (±0.05)
100H	19 (±1)	0.89 (±0.09)	0.33 (±0.05)
55L	21 (±1)	2.09 (±0.21)	0.93 (±0.05)
80L	21 (±1)	1.29 (±0.13)	0.88 (±0.05)
100L	23 (±1)	1.07 (±0.11)	0.65 (±0.05)

across the surface of the coating layer in the model. Table 6.1 shows from observation that these eutectic cells vary in size, and therefore the positions where the highest primary zinc surface area is exposed will also vary, i.e. the intersection of these depressions. This indicates one possible area where the model can be strengthened. In addition, table 6.1 indicates the observed inter–lamellar eutectic spacings, which also haven't been included in the model since the ZnAl eutectic has been considered a homogeneous material. Modifications made to the existing model would have to take into account the disparity in these distances with respect to the simulation length scales, making appropriate changes to the computational grid and in generating the solid model. Alternatively, a multi–scale modelling approach may be deemed necessary or even an entirely different model for the localized corrosion model, e.g. taking a phase field approach toward the microstructure.

A feature identified in previous chapters as a weak approximation, although one whose consequences are easily controlled and manipulated, is that of the corrosion product deposition. Whilst this simplified approach has inherent limitations, it does give an indication of the conditions at the surface and relative spread of localized corrosion effects acting at the exposed surface. Although knowing the details of this routine and estimated tolerances imposed, one would be reluctant to extract any quantitative measurement for comparison. (This demonstrates a clear advantage of developing a unique code, rather than the use of a commercial package. That is, clear knowledge of the procedures operating during the simulation and a detailed appreciation of their influence on the predictions made.)

The corrosion products present in figure 5.29(d) also give a clear indication as to whether the corrosion taking place is indeed localized or general. The degree of localization predicted by the model with regard to the surface corrosion of the Galfan type coatings is higher at lower cooling rates. This is due to the presence of fewer anodic sites with uninterrupted supporting cathodic areas around them. The relative surface area ratio of anodic material to cathodic material is constant at the start, meaning that any changes in corrosion performance predicted can be directly attributed to alterations in the dendrite size/configuration.

The increased levels of corrosion products present at the surface of the moderate and slower cooled Galfan coatings indicates from the model that the localized corrosion effects occurring are in effect operating in a more 'stable' regime than the more generalized, faster cooled samples. This would suggest that the faster cooled samples would be a better hot–dip coating for the purpose of protecting a steel substrate, as the 'eating' away of large–bodied dendritic features could be far more detrimental; both in terms of pitting and the build up of concentration around larger areas of material susceptible for metallic dissolution.

6.4.2 Influence of Microstructure on Current Density Predictions

As can be seen from figures 5.30 and 5.31, there are differences between the relative current densities predicted at equivalent cooling rates at different simulation sizes using the same mesh size. In addition to this, there is a counterintuitive result for the moderately cooled Galfan coating in figure 5.30.

With regard to the slight differences between figures 5.30 and 5.31 in the case of the fastest and slowest cooled simulated Galfan coatings, this may be attributed to the effects of the simulation area and the mesh used. The mesh is constant between the two simulations performed, although the nodal spacings in the x and z directions are $2\frac{1}{2}$ times greater in figure 5.31. This has implications since the vertical current densities are calculated between two much larger planes of current flux, thereby encompassing the effects of more microstructural features from the corroding surface below. This may also have the effect of aggregating the effects of the areas of exposed primary zinc into fewer anodic current density zones than would be the case in figure 5.30. It would then be the situation that the current density would be equivalent, as exhibited in figure 5.30. This indicates that the simulations

performed in figure 5.30 were performed on a mesh and computational grid setup that is close to the limit of resolution in the model.

The beneficial eutectic cell depressions features in the current density fields shown in figure 5.31 may not also be present close to the limit of resolution since these features are included in terms of the removal of 'trenches' 2 cells wide, not as a definite measure. However, as stated, the dimensions of these features, even at the more suitable simulation sizes need to be improved in terms of quantifying the eutectic grain effect.

The counterintuitive result shown for the moderately cooled case in figure 5.30 may be due in part to the limit of being close to the resolution of the model, but also the representation of the primary zinc features. It may be the case that the size and distribution of the primary phase, up to the 20% volume fraction permitted, is such that the zinc dendrites overlap one another, a situation one would not expect in practice. This then would build up the potential, concentrations and therefore current density at those points exposing high exposed surface areas of primary phase present. This may be further exacerbated by zinc loss, due to a more complex pit morphology acting as a concentration trap in the simulations. A possible solution to this would be a separate modelling procedure for the representation of the microstructures, including the thermal effects during solidification. Two possibilities would be phase–field, mentioned in brief previously, and cellular automata on a fine mesh, translated onto a finite difference computational grid, CAFD.

6.4.3 Predicted Surface Corrosion Rates

In simulating the localized corrosion effects experienced by Galfan coating layers cooled at different corrosion rates, the nucleation of such effects are allowed to be determined naturally by the model. This means that the localized corrosion effects develop due to the establishment of the local corrosion cell at the surface of the coating layer; anode – primary zinc, cathode – eutectic and electrolyte – 5% NaCl solution.

Initially, the relative area fraction of the solid model components present at the surface is equivalent and the concentration of the electrolyte is of a constant concentration. The surface electrode potentials are influenced by neighbouring material,although at this point the corrosion of susceptible sites is not influenced by concentration overpotential. It is logical

then that the Galfan coatings cooled at all rates exhibit comparable degradation rates, as shown in figure 5.32.

Once the localized corrosion effects have become established, i.e. when the graphs deviate in figure 5.32, the influence of the microstructure becomes apparent. The deviation in zinc loss comes about once the susceptible areas of the microstructure have undergone a certain degree of degradation. At this point, evolving concentration not consumed in the cathodic reactions, remains in the electrolyte having the effect of charging the δ–layer. Differences between the cooling rates in terms of zinc loss therefore is linked to the size of the primary zinc dendrites and their distribution throughout the eutectic. The interaction of large dendrites, creating concentrated cathodic zones yields higher zinc losses compared to those coatings containing fewer smaller dendrites, supported cathodically by larger, more diffuse cathodes across the surface. This situation is clearly defined by correlating the vertical current density at 5 hours in figure 5.30 to the initial rate in figure 5.32, and the current density after 12 hours in figure 5.31 to the secondary rate.

Appreciating that the corrosion rate is the same at the start of the simulation, the overall effect of the cooling rate on the corrosion performance can be seen to contradict those observed via SVET testing in figure 5.33. There are several issues that may contribute to this discrepancy. Outlined previously, there are issues in calculating the current density within the model. The measurement of current offers method for the monitoring and locating where corrosion develops, although the SVET also requires calibration and the potential measurements also require conversion. (Isaacs and Davenport, 1990) In terms of relating zinc loss to current density, this is a straightforward procedure in the model since all volume changes and densities are known at any point in time. In order to determine the experimental zinc losses from the current densities, Faraday's law is employed. Consequently this is a data processing procedure where, as is the case in modelling, assumptions are made and error may arise.

6.4.4 Influence of Steel Substrate

Differences in the corrosion performance of the Galfan coatings with electrical contact to a steel substrate are demonstrated in terms of vertical current density in figures 5.34

and 5.35. The slower cooled coatings exhibit a greater degree of localization and an associated concentrated zone along the length of the exposed edge close to the coating–steel interface. The faster cooled samples exhibit a greater amount of cathodic protection across a larger fraction of the steel substrate, albeit more diffuse than is the case for the slower cooled. Evident from figure 5.34 is that this greater apparent cathodic protection is not necessarily accompanied by a greater intensity of anodic dissolution. That is, the throwing power of the anodes operating on the slower cooled samples is greater than the slower cooled ones, such that the anodic current density is more intense 100 μm above the simulated exposed cut–edge.

6.4.5 Effect of Steel Gauge

The model behaves the way one would expect in terms of gauge thickness, i.e. less cathodic protection offered with larger steel gauges for a equivalent thickness of coating applied. Also, the cathodic zones, previously across the thickness of the steel in the faster cooled, is now confined to areas adjacent to the steel substrate. This is further evidence of the dependence on length of the galvanic effects used in the simulations.

The larger cathode area promotes a higher number of anodes to operate along the length of the cut–edge (figure 5.35), although at a lower intensity. This is reflected in the zinc loss rates shown in figure 5.36. It is important to note that the information regarding differences in microstructural features from table 6.1 is not included in the simulation results shown. As such, any small changes brought about by gauge alteration cannot be quantified in terms of alterations in corrosion performance.

The effect of the steel substrate in terms of corrosion rate can be clearly seen in figure 5.36. The effect of the steel substrate as a powerful cathode early in the simulation means that the establishment of the localized corrosion effects is immediately set up meaning that the rate is fairly constant. The exposed steel substrate is fairly constant throughout the simulation, until a sudden onset of passivation. The corrosion of the Galfan layer is reduced beyond this point, reflecting the much smaller area of steel acting as the most strongly cathodic material. The reduction in corrosion rate in the heavier gauge steel is more greatly reduced, since a greater reduction in the exposed steel fraction is experienced.

This highlights once again that the passivation of the corrosion process would be a natural model improvement to attempt, since on visual inspection of the simulation results show the corrosion product is deposited in cells only at small volume fractions.

6.4.6 Predicted Zinc Loses from the Cut–Edge

In a similar manner to that observed in the case of the surface corrosion of these Galfan type coating alloys, the degradation rates of the simulated cut–edge exposure of these coatings change with time. The graphs for the three different cooling rates are shown in figure 5.37, which differs from those illustrated for the 55L and 55H cases in figure 5.36 since a passive film is present at the start of the simulation, dissolved as function of time. It can be seen that during the establishment of localized corrosion, all three cooling rates exhibit an equivalent, increasing corrosion rate. This takes place once anodic and cathodic sites become available at spatially discrete sites across the solid–electrolyte interface. During this dissolution of the passive state, the localized corrosion cells begin to operate as a function of the microstructure and conditions are set up that demonstrate differences that can only be attributed in the model to the solid phases present and their subsequent behaviour to the concentration perturbations brought about. At this point the corrosion rate of the slower cooled Galfan coating (55%) is the fastest accelerating and the pick–up of the 100% cooled Galfan coating is lowest. After this point, a regime of stable localized corrosion processes is reached, and this continues until a very distinct point predicted by the model, at which point the majority of the solid material is covered in a corrosion product / passive film (section 6.3). The model can then be seen to predict a passivated state for the solid material included.

Whilst the model has described the breakdown in passivity, the establishment of localized corrosion, stable pitting and ultimately passivation, inherent limitations remain. This is once again due to the arbitrary way in which passive layers and corrosion product are deposited in the model. If improvements are needed to be made to the way in which these are carried out, distinction must be made between those features that occur discretely, e.g. potentials; polarization and passivation, onset of pitting in stainless steels, and those that occur continuously, e.g. concentrations; anodic dissolution, corrosion product deposition. (Kruger, 1990; Prentice and Chang, 1987)

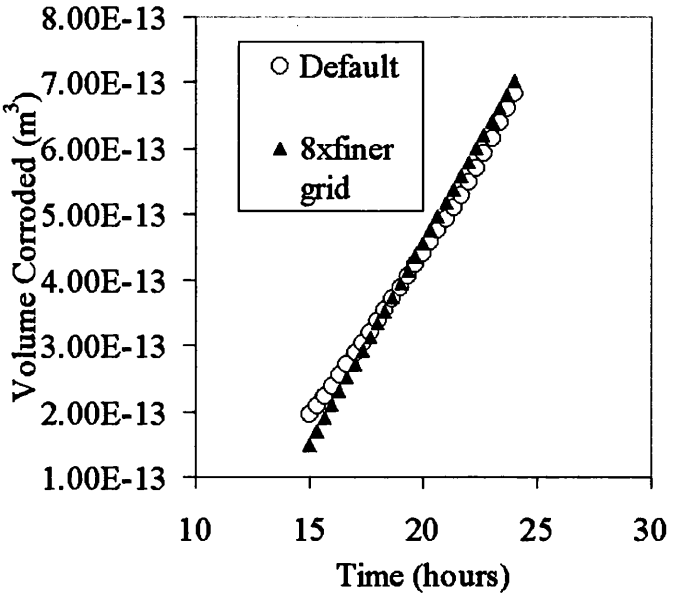

Figure 6.5: Graph showing the volume of material corroded for simulations performed on different mesh sizes for the same exposed EZ coated steel.

Despite these limitations, palpable and indistinct, the overall zinc lost over 24 hours simulated time can be seen to correlate with those zinc losses observed via SVET experimentation in figure 5.38. That is, at a higher cooling rate, a lower amount of degradation to the coating layer is experienced. Considering that the current density predictions reveal a greater amount of cathodic protection given to the steel substrates, the model supports the use of high cooling rates in practice. All these factors demonstrate that the model is capable of making predictions for this scenario, and that other microstructural variations might be assessed with a relative degree of confidence.

6.5 Further Validation and Sensitivity

6.5.1 Electroplated Zinc (EZ) Steel Coatings

The current density fields produced during the simulations of EZ coated steel over a 24 hour period of exposure to 0.1% NaCl solution are presented here with reference to those published by Worsley et al. (2004). The sensitivity of the model with respect to grid size is also considered.

The resultant volume loss from a simulated EZ coated steel exposed to 0.1% NaCl

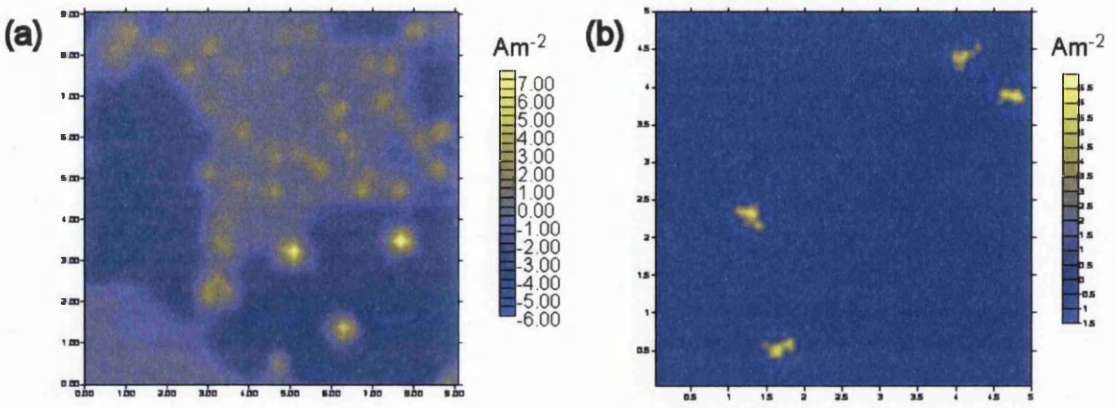

Figure 6.6: Current density fields 100 μm above the surface of an EZ coated steel after 8 hours exposure to 0.1% NaCl solution; (a) SVET generated, and, (b) Simulated. Distances in mm.

solution is shown in figure 6.5, for two different mesh sizes during a period of stable pitting. In this case the default simulation is a gridsize of $100 \times 50 \times 100$, compared to a mesh representing the same area/volume of exposed material and electrolyte present that is 8 times finer; $200 \times 100 \times 200$ cells. The differences between the two meshings can be seen not to significantly effect the volume of the material predicted to undergo anodic dissolution/transformation. This lends further support to the view that the model is grid independent, provided that the mesh is sufficiently fine to capture the processes taking place. Problems would be encountered by the corrosion model should the simulation be scaled up from the intended micro–mesoscopic scale intended, since the volume needed to be transformed during a single instance of anodic dissolution would be large and not representative of the distribution of potential across the active surface; since any cell may only assume one value of ϕ. In contrast, should the mesh be too fine a situation whereby an estimated volume of material greater than that of an exposed cell would be required to transform could undermine the model or require prohibitively small time increments. So, constraints must be placed on the computer model limiting it to the micro–meso scale, ignoring submicron phenomena and macroscopic effects, discussed in section 4.

Simulated and SVET measured current density fields in the 0.1% NaCl solution above an area of EZ coated steel can be seen in figure 6.6. The simulated area is $\frac{1}{4}$ of that shown for the SVET map. As can be seen, the SVET varies across the surface, so correlation between

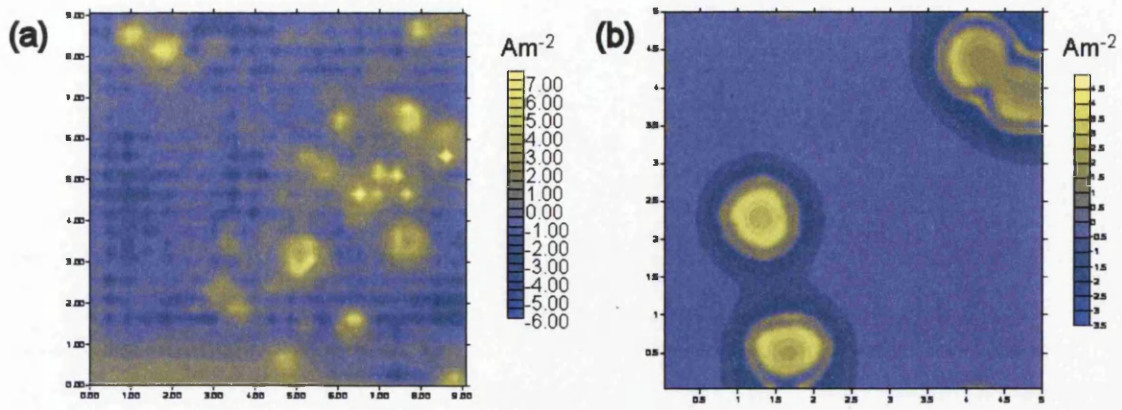

Figure 6.7: Current density fields 100 μm above the surface of an EZ coated steel after 24 hours exposure to 0.1% NaCl solution; (a) SVET generated, and, (b) Simulated. Distances in mm.

figure 6.6(a) and (b) is dependent upon the area selected. Since in the EZ case the corrosion effects are nucleated, one can say that the predicted current density map matches closely that observed after 8 hours exposure in terms of form and at the correct order of magnitude since frequency of local anodic current density is arbitrarily determined.

The predicted current density fields 100 μm above the surface of an EZ coated steel can be seen to match closely to those observed even at later stages of the simulation, shown after 24 hours in figure 6.7. In this instance the features typical of exposed steel producing a ring of maximum anodic current density around the circumference due to those processes discussed in section 6.3 can be seen to be present in figures 6.3(a) and (b). This has the effect of adding validity to the predictions made for the degradation of these materials, even with the dependence of the simulations on knowing the typical state of the coatings. The only significant difference in figure 6.7 is the respective resolution of the maps shown, a possible reason for the absence of the concentrated zones of cathodic current densities predicted in close proximity of the localized corrosion effects in figure 6.7(a).

6.5.2 Galfan (Zn – 4.5 wt.% Al) Steel Coatings

The current density fields produced during the simulations of Galfan coated steel over a 24 hour period of exposure to 5% NaCl solution are presented here with reference to those published by Elvins (2005). Consideration is given here to the accuracy of the coating layer

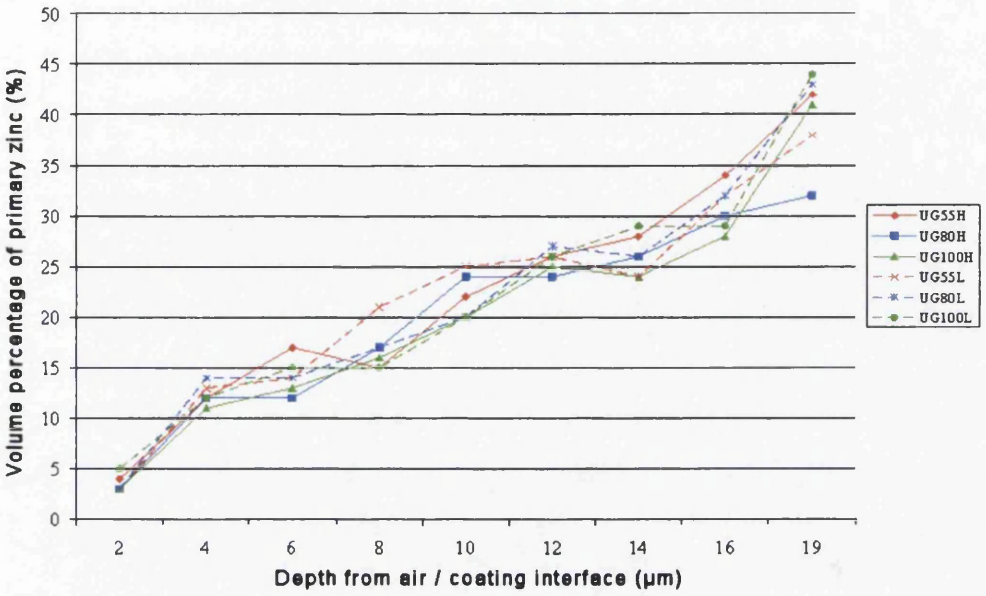

Figure 6.8: Area fraction of primary zinc in Galfan coatings observed by Elvins (2005) as a function of through coating thickness. Different cooling rates and steel substrate thicknesses are shown.

as represented in the solid model used for simulations.

As stated previously, Elvins (2005) carried out a microstructural investigation into the microstructures of the Galfan coatings as a result of different cooling rates. A product of this research was the measurement of the area fraction of the primary phase present at different levels of the coating thickness. This through thickness relates to the solid model represented, from the coating–electrolyte interface to the steel–coating interface.

Elvins (2005) found that the area/volume fraction of primary zinc present in Galfan coatings cooled at varying rates (55%, 80% and 100% power output of the cooler) varies according to figure 6.8. This shows how the primary zinc phase increases linearly as the distance to the steel–coating interface decreases. Oscillations around this linearity are present due to the vertical postion with respect to the dendrite grown from the steel–coating interface and the dendrite arm spacings present.

The area fraction of the primary phase in the solid model as a function of through thickness is given for the light gauge steel samples in figure 6.9. Only the light gauge is given since the same dendrite dimensions are used in all simulations with respect to cooling

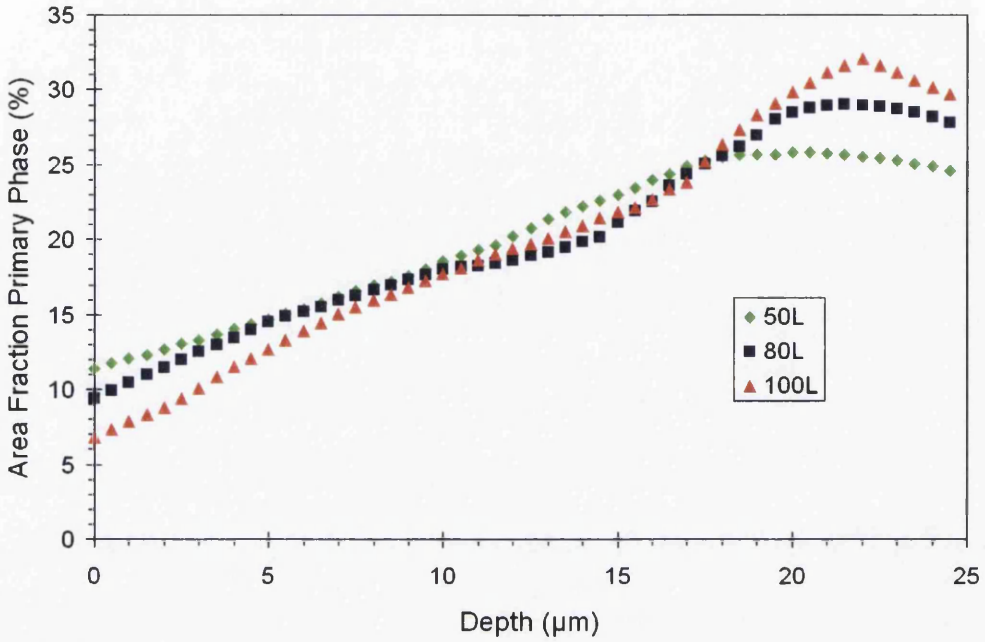

Figure 6.9: Simulated area fraction of primary phase in Galfan coatings as a function of through coating thickness. Cooling rates and steel gauge thicknesses refer to those observed in figure 6.8

rate. In practice, the gauge of the steel substrate has an influence on the dendrite size, although this does not alter the trend observed (figure 6.8), nor does it alter significantly the overall volume fraction of primary phase present; approximately 20%. Figure 6.9 shows that when the solid model is formed, adhering to the global limit of 20%, the trend regarding levels of the primary zinc phase with respect to the through coating thickness can be seen to match that observed. At the steel–coating interface the area fraction of the primary phase is approximately 30%, decreasing linearly to levels of 10% ($\pm$ 2%) at the coating–electrolyte interface.

6.5.3 Current Density Maps

The use of the current density fields at a fixed height, 100 μm above a simulated Galfan coating allows comparison with experimental findings, in addition to enabling interrogation of the computational framework.

Figure 6.10 shows the current density fields from two simulations performed on the same mesh of 200 $\times$ 50 $\times$ 200 cells but with varying nodal spacings in the x and z directions such

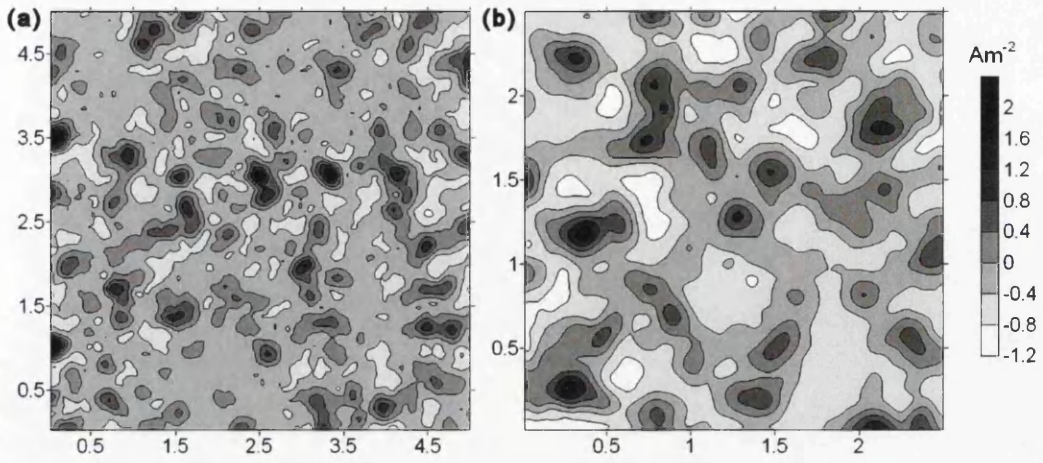

Figure 6.10: Current density field above a simulated corroding Galfan surface; (a) 5 mm × 5 mm, and, (b) 2.5 mm × 2.5 mm after 18 hours immersion. Distances in mm.

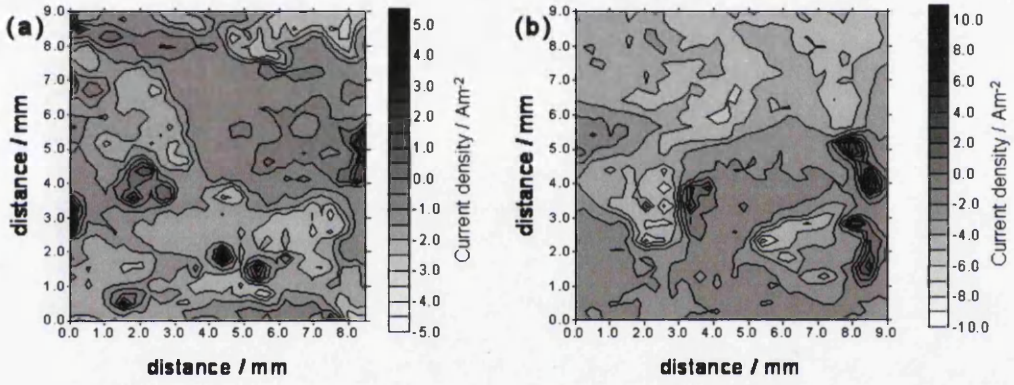

Figure 6.11: Current density fields measured using the SVET for surface corrosion of Galfan–coated heavy gauge steels after 12 hours immersion for different cooling rates (Elvins et al., 2005a); (a) 55%, and, (b) 100% cooler power output.

that figure 6.10(a) represents an area 4 times that represented in figure 6.10(b). The current density field shown for the smaller area can be seen to replicate an equivalent area generated in the coarser simulation, and the intensity and frequency of the localized anodic sites are equivalent between the two scenarios. This suggests that the computer model is independent of grid size, should the mesh be suitably fine in the case of simulating the localized corrosion effects experienced by Galfan coated steels. The simulation performed in figure 6.10(a) is close to the upper resolution of the model in terms of permissible inter–nodal spacing, which is determined by the smallest feature present in the microstructure known to influence the corrosion performance.

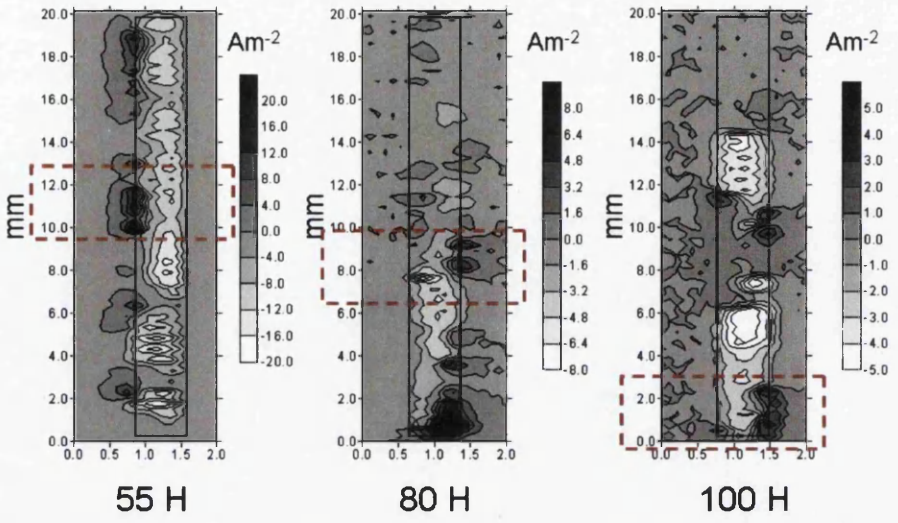

Figure 6.12: Current density fields measured using the SVET for cut–edge Galfan–coated heavy gauge steels for different cooling rates. (Elvins et al., 2005a) Maps are shown for scan performed after 12 hours. Dashed boxes show the area simulated by figure 5.35 in chapter 5.3

The current density fields generated from the SVET shown in figure 6.11 for the surface corrosion performance of differently cooled Galfan coatings, can be seen to offer an opposite relationship to predictions made by the model. Firstly, the magnitude of the most anodic current density is highest for the faster cooled sample, in fact double that of the slower cooled sample. The simulated result for the effect of cooling rate predicted a doubling down from the slowest to the fastest cooling rate (see figure 5.31). In addition to this, the number of zones of anodic current density is observed to be lower than is expected from predictions made, for all cooling rates included.

For the cut–edge case the predicted current density fields can be seen to be comparable to sections denoted by the dashed boxes of the SVET measured current density maps shown in figure 6.12. This suggests that the dominant processes taking place have been captured to a reasonable degree. Differences exist, which have been discussed in chapter 5.3, although the most prominent occurring here is the dominance of one side being the location of most of the anodic corrosion events taking. This is due to the front and back being of different thicknesses in reality, obviously affecting the microstructure making this side more likely to act sacrificially to protect the steel cathodically.

Chapter 7

Conclusions

A physically based computer model has been developed in order to predict the localized corrosion effects experienced during aqueous corrosion of pure zinc and zinc – 4.5 wt.% aluminium steel coatings. The localized effects are obtained using fundamental thermodynamic relationships and experimentally derived kinetic data. The first order model created is based on the perturbations brought about by the evolution of a single ionic species, which is emanating from an active surface. Using an irregular orthogonal computational grid, calculations of concentration and potential are performed using the finite difference numerical method.

Simulations of the localized effects experienced by pure zinc and ZnAl alloy coatings from defects present at the surface have shown the model capable of predicting the effects of pitting. The simulations of the exposure of a steel substrate, from coating discontinuities and preceding localized degradation, reflect favourably on the models capacity to capture the effects of dissimilar metallic corrosion. Galvanic effects in multiple scenarios have shown the model to be sensitive of distance, area and concentration under which the corrosion effects are operating. The model has performed beyond its original aims for novel situations without major adjustment; crevice, droplet and scratch. Limitations have been identified and discussed throughout. The modelling approach and framework appear to hold many opportunities for simulation of electrochemical processes.

Validation of the model has been performed with regard to current density fields, comparing predicted vertical current density to those produced via experimentation and to rigorous mathematical solutions. The absolute corrosion rate has been evaluated from those estimated

from the scanning vibrating electrode technique (SVET). To this end, the form of the vertical current density fields generated numerically has been successfully validated using independently derived mathematical relationships.

The conditions in the electrolyte have been replicated to a high degree compared to those measured during accelerated corrosion testing of electroplated zinc (EZ) and Galfan steel coatings. In the case of the EZ coatings, the current densities predicted match closely those values measured via the SVET, and are only one order of magnitude out when predictions are made in the case of Galfan coatings. During validation, factors affecting the calculation and measurement of current density can explain the subtle differences encountered.

Corrosion rates determined for the surface and cut–edge corrosion of Galfan (zinc – 4.5 wt.% aluminium) coated steels correlate closely with those calculated from SVET measurements. The predicted corrosion rate at the surfaces of Galfan coatings cooled at different rates is of the same order in terms of zinc loss measurements made, although they predict an opposite trend to that observed. Several reasons for this have been proposed. In contrast, the cut–edge corrosion performance (with respect to the cooling rate) yielded very similar results as those observed. In addition, the trend that is observed is replicated by the quantitatively assessed simulations adding further confidence to predictions made. The effect of gauge thickness has also been included.

During the course of the investigation the suitability of the modelling framework has been interrogated, and where necessary modified and improved. The effect of the microstructure on the localized anodic effects experienced during aqueous corrosion have been captured by the model. The model appears to be independent of grid size should the mesh be sufficiently fine, such as to capture the smallest influential microstructural feature operating in the corrosion process.

Chapter 8

Further Considerations

The existing computer model, having been validated with respect to the Zn – 4.5 wt.% Al coating alloy, could be used to investigate other coating systems in this and other similar binary alloy systems. The obvious coatings for which this may be applied are the 55 wt.% Al coating layer called Zalutite and the <1% Al galvanized and annealed coating layer, Galvanneal. A note of caution exists, the dominant features pertaining to the corrosion performance of the coating layer should be understood and the extent of intermetallic formation known.

The suitability of the modelling framework has been scrutinized with regard to capturing the dominant physical and chemical processes taking place during pitting. A possible avenue for further investigation would be those materials that are susceptible to pitting; including stainless steels, copper and Al – Cu aerospace alloys. The model may also be adapted to represent a basic crevice situation, focused on the concentration effects on local dissolution rather than the traditional crevice geometry models.

A major advancement of the model would be to remove the excess or bulk electrolyte from the simulations. In its simplest form this would require alterations to the boundary conditions, as demonstrated in appendix A. Obviously, removal of the bulk solution involves alterations in the electrochemical processes taking place, requiring a much more detailed investigation.

As stated, the model presented here is a simplified first order model, based on the concentration perturbations of a single ionic species. An obvious area of improvement would

be the expansion of the current model to include multiple species. A first step would be the inclusion of a field to include the oxygen field as demonstrated in appendix B. This extra concentration field would help in determining the cathodic reaction in all simulations and the establishment of differential aeration. The diffusion of oxygen would be of particular importance when estimating the corrosion effects experienced by organically coated steels (OCS). These organic coatings have been known to undergo photo–active degradation, thus altering the diffusion of oxygen through the organic layer. (Böhm et al., 2000; Robinson et al., 2004) Further concentration fields may be added, of which, another concentration of great importance would be Cl^-_{aq}, shown to determine the pitting behaviour of materials.

Throughout this document, particular emphasis has been placed on the influence of the microstructure and its influence on the specific corrosion performance of a metal/alloy. Knowing that any predictive simulation of the corrosion performance is dependent upon the relevant microstructural features being captured, more advanced microstructures may need to be simulated. This may involve generating the microstrucures from thermodynamic relationships or replicating those observed. A new modelling procedure may be required and finer, more computationally expensive meshes may be required. Application of a stress field, in order to satisfy the case of stress corrosion cracking (SCC) would obviously suit a finite–element (FE) approach, although the movement of an interface due to anodic dissolution would support a 'meshless' method.

Appendix A

Limited Electrolyte

Particular emphasis was placed on the cut–edge corrosion performance of the ZnAl coated steels within this document since it is this failure mechanism that is most troublesome in the applications organically coated steels (OCS) find in the service environment. This is in part due to the unsightly problem of organic coating delamination, brought about by anodic undermining of the metallic coating layer between the pigmented organic material and the steel substrate. Efforts are made, when deemed feasible, to hide the cut–edge from aqueous environment by sealing the this away from the elements, e.g. using a series of folds. Whilst one might expect that this would remedy the situation, consideration must be given to the case when this protection is penetrated. The removal of the bulk electrolyte would then lead to a different environment that would have to be treated differently in terms of modelling any corrosion effects that would ensue.

A brief description is given here of preliminary tests performed in order to ascertain the suitability of the framework used in the model to describe situations in the absence of a bulk electrolyte. Two simple cases are given; droplets on a metal/alloy surface and a scratch through a Galfan type coating alloy.

A.1 Electrolyte Droplet

In order to represent a droplet, obviously not all of the cells used in the simple mesh constructs described previously are required. Therefore, a simple geometry of a hemisphere is assigned electrolyte, situated above a solid model comparable to that of the surface corrosion case. The other material (i.e. air) is assumed to be inert and take no part in

transformations, diffusion and calculation of potentials. In previous simulations, a Dirichlet (fixed) boundary condition is placed on the concentration value for the top elements of the electrolyte, mimicking the presence of the bulk electrolyte, assumed to remain at the initial concentration. This is no longer sufficient in terms of the concentration field, since small local perturbations in concentration will impact the global concentrations throughout the electrolyte. To this end, a Neumann (flux) boundary condition is applied to the 'dome' of elements in contact with the inert material, assumed in this instance to be air, into which no H^+ may diffuse/migrate.

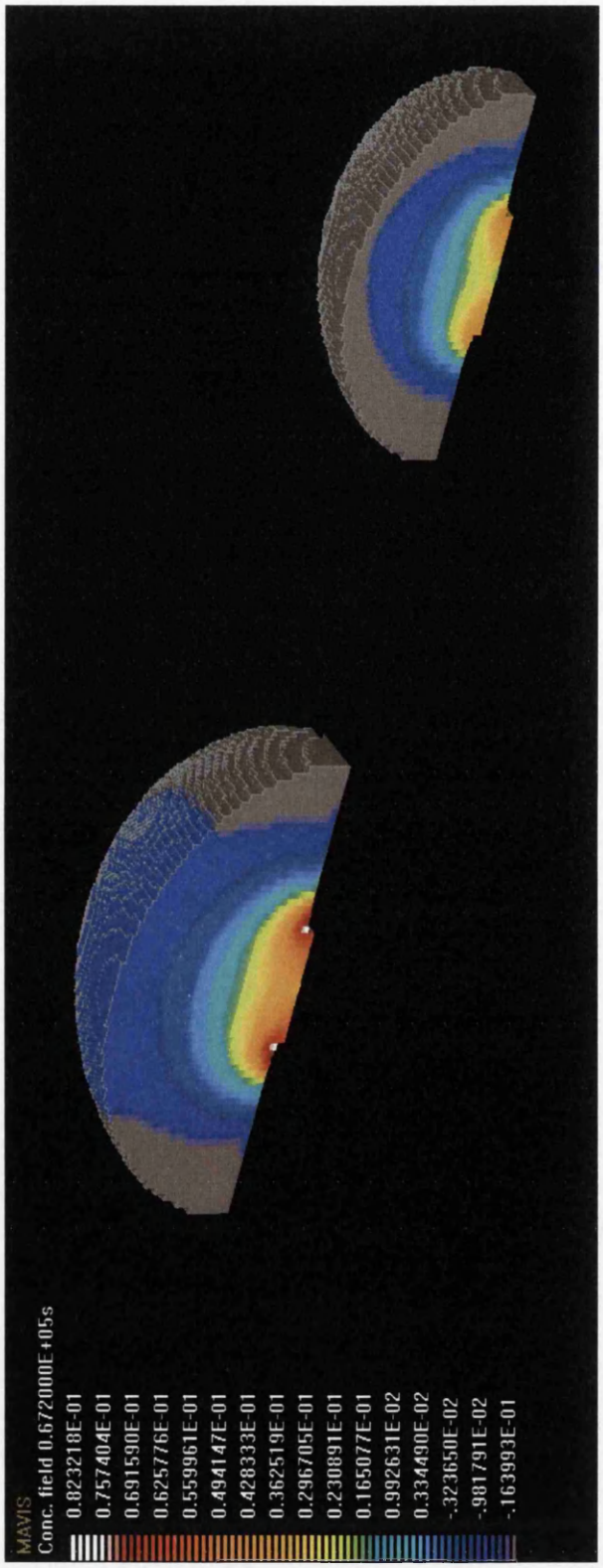

Figure A.1: Concentration of H^+ in two 5% NaCl droplet after 18.6 hours contact with pure zinc.

Figure A.1 illustrates the typical concentration build up associated with corrosion occurring within two droplets in contact with pure zinc, using the different boundary conditions. What can be seen is that over 18.6 hours, in the absence of the bulk electrolyte, the build up of concentration is far more extreme from the two nucleated corrosion effects on the centre of the droplets, than would be the case in a similar situation with an excess of electrolyte. Interestingly, the greatest concentration is experienced at the corners where the corrosion steps down from the initial surface. This may be attributed to the corrosion current density being highest at these geometries on a pure surface, ultimately encouraging the resultant degradation to have a high lateral tendency in the simulation.

Figure A.2: Electrical potential in two 5% NaCl droplets, in addition to a section of pure zinc after 74 hours contact.

The electrical potential within the two droplets previously described, can be seen in figure A.2. The electrical potential throughout the pure zinc layer is also included and is representative of the electron movement through the metal. The familiar dome shaped voltage profile is still evident in the large droplet in figure A.2, although larger effects are present throughout the electrolyte due to the greater influence of the concentration perturbations. A cautionary note can be drawn from the smaller droplet in figure A.2 however, since a numerical anomaly is clearly present. This is symptomatic of trying to model a complex process using such a fine mesh over relatively large time scales. Alternatively, this may be attributed to round–off error.

Figure A.3: 2D vector plot showing the current density in the x and y directions at a 2D plane through the centre of two droplets in 5% NaCl solution after 12 hours contact with pure zinc.

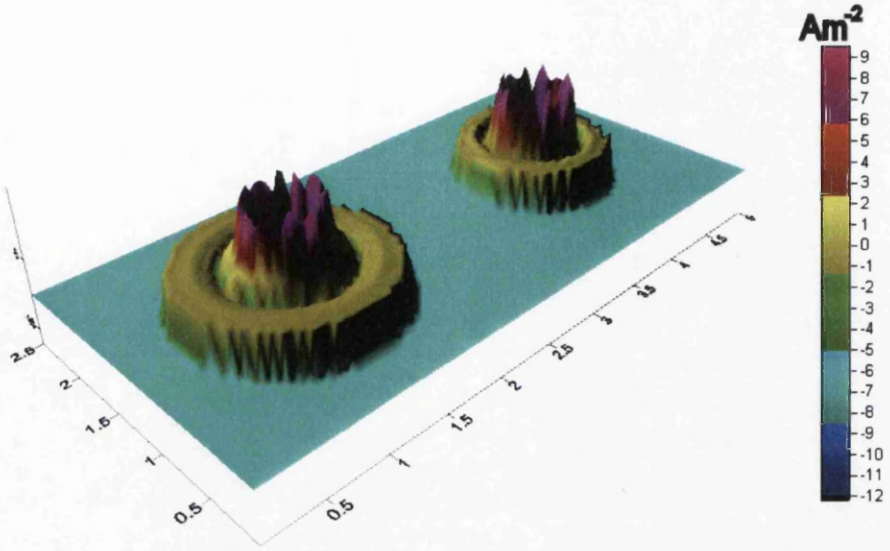

Figure A.4: Surface plot of the vertical current density in the droplet 100 μm above the initial surface after 18.6 hours exposure to 5% NaCl solution.

Prior to the numerical anomaly developing in the smaller droplet, at 12.6 hours, the current density vectors can be seen in figure A.3. In both droplets the greatest vertical current density can be seen to occur at the centre of the droplets, in addition to there being a high horizontal component of the current density at the edges of where the material has been removed. Definite lines of current flux can be seen throughout the droplets, whereby from the 2 directions chosen, the slopes with repect to both are changing constantly and equal to zero at numerous points.

The vertical current density 100 μm above the zinc material can be seen in figure A.4. Some of the the features of the vertical current density described in section 4.7.2 are present, cathodic zones exist almost symmetrically around anodic sites, whereby the maximum anodic current density is located above the geometric changes, diminishing towards the centre of the anodic effect. Careful consideration must be made with respect to the model of corrosion current densities however, with the withdrawal of the supporting electrolyte. (Oldham, 2000) An interesting feature here is the transition from the centre, anodic to cathodic, as one would expect, in addition to reverting to cathodic current density near the edge of the droplets.

Figure A.5 shows a single droplet using the same condition above, only in contact with a

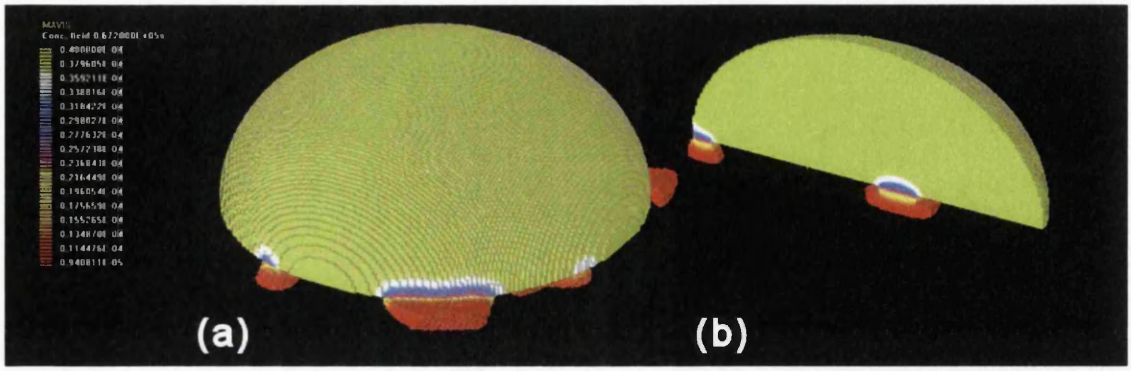

Figure A.5: Concentration of H^+ in 5% NaCl droplet after 18.6 hours contact with a section of Galfan coating; (a) entire droplet, and, (b) Section through droplet.

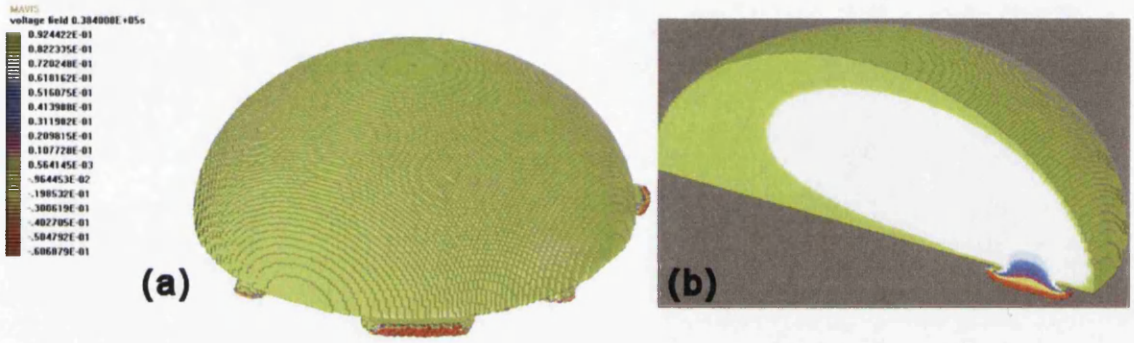

Figure A.6: Electrical potential in 5% NaCl droplet after 10.6 hours contact with a section of Galfan coating; (a) Entire droplet, and, (b) Section through droplet.

Galfan–type coating rather than pure zinc. In this case concentration can be seen to increase above the zinc removal taking place to the dendritic phase. The presence of the eutectic, acting more efficiently as a site of oxygen reduction results in the concentration not making such an impact on a greater volume of the droplet as was the case when in contact with a homogeneous surface. The removal of the zinc dendrites also acts as a concentration trap, exacerbating this situation.

The presence of dissimilar metals in contact with this limited electrolyte does have an effect on where the maximum potentials are experienced across the local anodic effect, i.e. the centre, shown in figure A.6. In figure A.6(b) the high electrical potentials can be seen to occur within the pit created from anodic dissolution, reflecting the high concentrations in these regions.

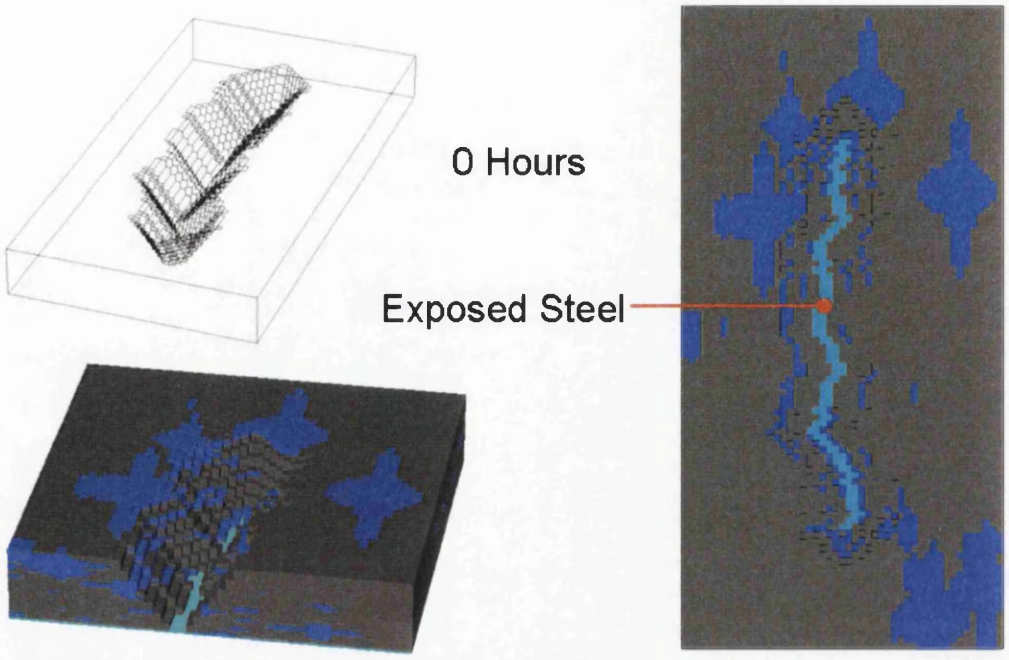

Figure A.7: Setup used in the simulation of a scratch through a Galfan coating including; X–ray representation of volume of electrolyte and section showing 'trench' created. Light blue – steel, dark blue – primary zinc and grey – eutectic.

A.2 Scratch

An extension to the droplet case was attempted whereby a scratch was made through a multi–phase coating layer and replacing the solid material removed by electrolyte. This invokes a situation whereby metallic phases of three distinct standard electrode potentials are present, and very few cells adjacent to one another are at the same level, exposing a large surface area within the scratch. Neumann boundary conditions are used on all faces of the concentration fields. Flux boundary conditions are used for solving the electrical potential for the surface in contact with air, whereas those in contact with metallic constituents remain fixed.

The setup of the simulation can be seen from the X–ray construct shown in figure A.7. The electrolyte occupies the volume missing from this trench. Whilst the Galfan layer used is crude, it does allow different phases in contact with the electrolyte at different levels along the length of the scratch. The exposed steel along the length of the scratch can also be seen in figure A.7. The random distribution of the primary phase has led, in this instance, to having

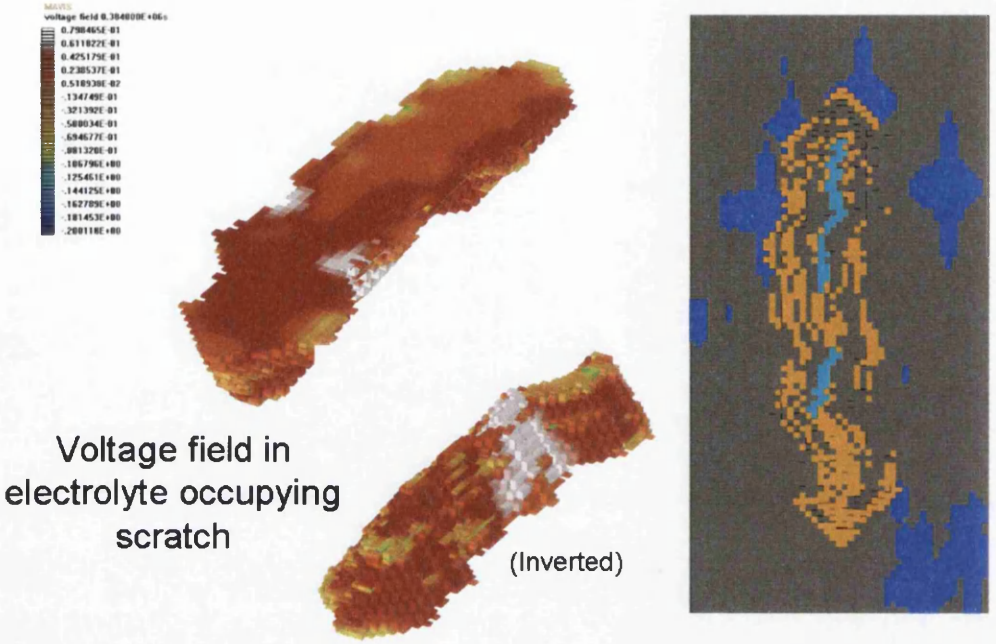

Figure A.8: Electrical potential field in 5% NaCl solution occupying a scratch through a Galfan coating after 105 hours and the resultant degradation on the solid material; where the corrosion product is shown as brown.

more dendrites close to the base of the scratch at either of the ends compared to that in the middle.

The limited electrolyte in contact with multiple metallic phases appears to have generated a complicated electrical potential field in figure A.8. After the 105 hours, only very small amounts of anodic dissolution is taking place, if any at all. The corrosion products present in the cells next to primary zinc limit the potentials in the electrolyte adjacent to them. Also, most of the remaining uncovered eutectic material is passive at these potentials, leaving only small areas offering the amount of cathodic protection needed to protect the steel substrate. The evidence that the coating has stopped the anodic attack means that the coating exposed has 'self–healed', in addition to depositing a retarding layer of corrosion products on the a large section of the powerful steel cathode exposed by the scratch.

Appendix B

Simulation of Multiple Species

The influence of concentration has been treated throughout as the major influence in the propagation of the corrosion process. The first order model presented up until this point dealt with the concentration of a single species, H^+, considered to be representative of the overall balance of species present; brought about as a result of evolution, consumption, solution strength and hydrolysis. From appendix A, indications are that the effects of concentration perturbations is even more influential in the case of limited electrolytes.

As discussed, a natural progression of the physically–based corrosion model would be expansion of the concentration field to include more electro–active species. Possible benefits would include more accurate selection of anodic and cathodic sites, capability of the model to capture corrosion effects brought about by differential aeration and improvements in the formation of corrosion products during the cathodic routines performed; in addition to improving estimations of the cathodic capacities of each phase.

The most obvious concentration to include would be oxygen, as the most likely cathodic reaction to take place at moderate pH values is cathodic oxygen reduction. However, including both concentration fields may allow the model to select the simple corrosion reactions taking place. Including oxygen also has an impact on the corrosion current densities and also the conductivity of the solution. Aerated NaCl solution has a natural concentration of dissolved oxygen in it, which is dependent on the temperature and the salinity of the charge carrying solution. The conductivity, directly related to the resistivity is related to the temperature and salinity according to figure B.1.

The concentration of oxygen in the droplets described in appendix A is described

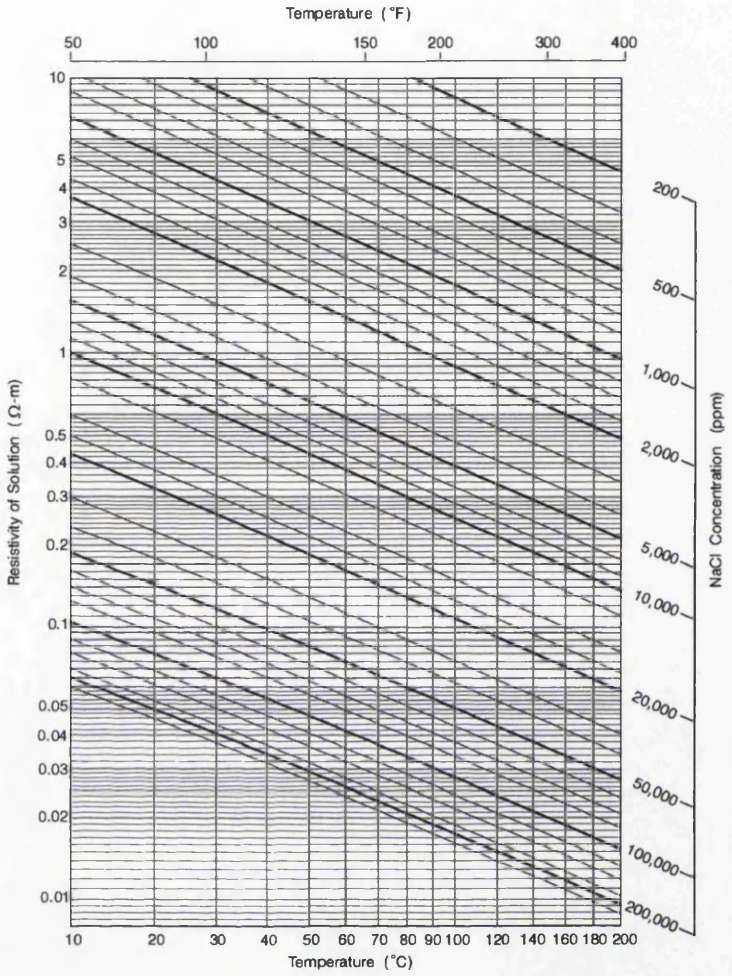

Figure B.1: Temperature and salinity dependence of water resistivity.

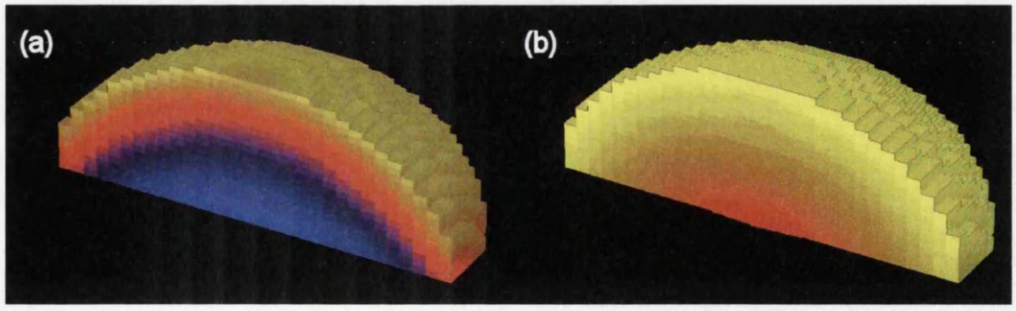

Figure B.2: Concentration of O_2 in 5% NaCl droplet; after (a) 0.6 hours, and, (b) 12 hours.

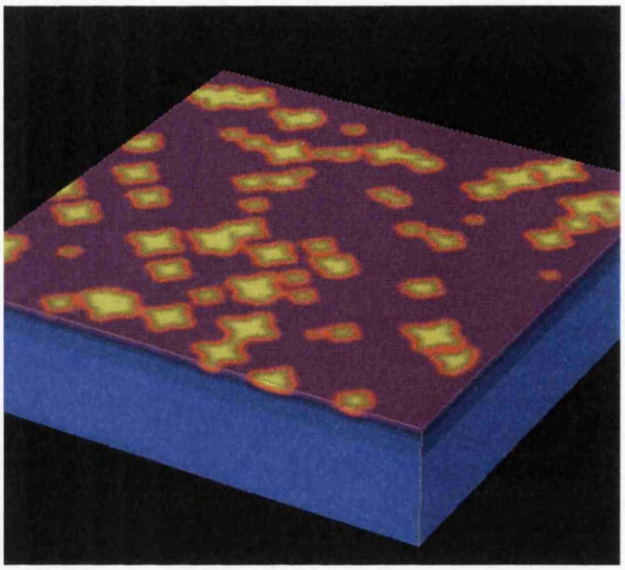

Figure B.3: Concentration of H^+ in 5% NaCl solution (inverted) after 12 hours contact with a section of Galfan coating.

over 12 hours in figure B.2 for a Galfan coating corroding in the presence of 5% NaCl solution, at 298 K / pH 7. An initial concentration of oxygen, determined from established reference data, was assigned to the whole of the droplet at the start of the simulation. This concentration was then used as a fixed boundary condition at the outside of the droplet, representing the natural diffusion into the droplet as the consumption of oxygen takes place during the cathodic reaction. Obviously, the diffusion coefficient of oxygen in 5% NaCl prevents instantaneous balancing this concentration, in addition to a maximum value of concentration a cell may have to reflect the natural limit of dissolved oxygen. What can be seen in figure B.2 is that at the start, the supporting cathodic routine in the model predicts a depletion of oxygen at the start of the simulation (0.6 hours) due to the extensive cathodic reation occuring over the majority of the exposed surface. After 12 hours, shown in figure B.2(b), localization has become established in the model, giving rise to only a locally depleted area close to the site of anodic activity (centre). In contrast, oxygen is being replaced at the sites, cathodically polarized or not, at short diffusional distances, i.e. at the edges of the droplet.

The form of the effective free proton and oxygen concentration fields alters somewhat when the bulk electrolyte is included. The concentration of H^+ can be seen in figure B.3.

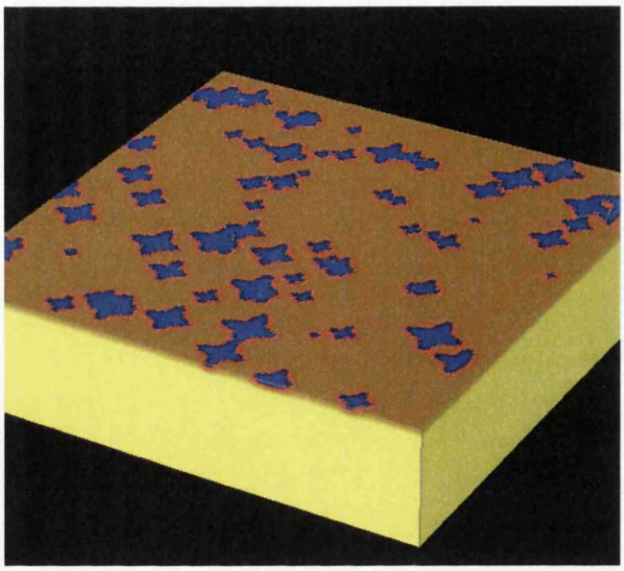

Figure B.4: Concentration of O_2 in 5% NaCl solution (inverted) after 12 hours contact with a section of Galfan coating.

This is a familiar case whereby the elevated concentration stays very close to the surface, but in particular, in close proximity to the anodic sites; the place where this concentration evolved. Very little reaches into the bulk concentration due to the hydrolysis taking place, and this is exaggerated from previous cases due to the effects of oxygen diffusing from the bulk solution being included.

The corresponding oxygen concentration field in figure B.4 shows the oxygen is depleted most around the areas of anodic activity, where the consumption is greatest. At anodically unaffected areas across the Galfan surface the oxygen concentration has been lowered to a lesser extent, reflecting not only the lower contribution of these areas to the overall cathodic reactions taking place, but also the relative ease for oxygen to diffuse/migrate to these areas from the bulk. The effect of the diffusion can be seen as a lowering of oxygen over a short length scale across the electrolyte directly adjacent to the Galfan coating (top in figure B.4)

Other species of interest when modelling the effects in NaCl solution would obviously be Na^+ and Cl^-. Partly due to their influence on migration and ionic mass transport, but also the breakdown in passivity in chloride solutions and the initiation of mechanism of corrosion of zinc by sodium chloride particle deposition. (Neufeld et al., 2002)

References

Y De Abreu, A Da Silva, A Ruiz, R Requiz, N Angulo, and R Alanis. *Surface and Coatings Technology*, 120-121:682, 1999.

L C R Alfred, J C Myland, and K B Oldham. Corrosion current densities at a disk-shaped inclusion. *Journal of Solid State Electrochemistry*, 6(3):172–182, 2002.

G A Alimenti, M E Gschaider, J C Bazán, and M L Fereira. Theoretical and experimental study of the interaction of O_2 and H_2O with metallic zinc–discussion of the initial step of oxide formation. *Journal of Colloid and Interface Science*, 276:24–38, 2004.

M A Amin. Passivity and passivity breakdown of a zinc electrode in aerated neutral sodium nitrate solutions. *Electrochimica Acta*, 50(6):1265–1274, 2005.

M P Anderson, G S Grest, R D Doherty, K Li, and D J Srolovitz. Inhibition of grain-growth by 2nd phase particles - 3 dimensional monte-carlo computer-simulations. *Scripta Metallurgica*, 23(5):753–758, 1989.

A J Bard and L R Faulkner. *Electrochemical Methods : Fundamentals and Application.* WILEY, 1980. ISBN 0-471-08753-X.

N C Barnard, S G R Brown, and H N McMurray. Modelling the localized corrosion effects experienced by zinc–4.5wt.% aluminium steel coatings in 5% nacl solution. In C A Brebbia, V G DeGiorgi, and R A Adey, editors, *Simulation of Electrochemical Processes*, pages 99–108. WIT Press, 2005. ISBN 1-84564-012-8.

N Bellomo and L Preziosi. *Modeling Mathematical Methods and Scientific Computation.* CRC Press, 1995.

J O Bockris and A K N Reddy. *Electrochemistry 1 : Ionics.* Plenum Press, 2nd edition, 1998. ISBN 0-306-45555-2.

W J Boettinger, J A Warren, C Beckermann, and A Karma. Phase-field simulation of solidification. *Annual Review of Materials Research*, 32():163–194, 2002.

S Böhm, H N McMurray, S M Powell, and D A Worsley. Photoelectrochemical investigation of corrosion using scanning electrochemical techniques. *Electrochimica Acta*, 45(14): 2165–2174, 2000.

C M A Brett and A M O Brett. *Electrochemistry Principles, Methods, and Applications.* Oxford University Press, 1993. ISBN 0-19-855388-9.

S G R Brown. Simulation of diffusional composite growth using the cellular automaton finite difference (CAFD) method. *Journal of Materials Science*, 33(19):4769–4773, 1998.

S G R Brown, N C Barnard, and H N McMurray. 3-dimensional modelling of localized corrosion effects in zinc and zinc alloy steel coatings. In P Vincenzini, editor, *Proc. 3rd Int. Conf. on Computational Modelling and Simulation of Materials III*, (CIMTEC 2004), pages 393–403, Acireale (CT), Italy, 2004.

J A V Butler. *Trans. Faraday Soc.*, 19:729, 1924.

S C Chapra and R P Canale. *Numerical Methods for Engineers: with software and programming applications.* McGraw Hill, 4th edition, 2002.

L Q Chen and Y Z Wang. The continuum field approach to modeling microstructural evolution. *Journal of Materials*, 48(12):13–18, 1996.

D Christian. Performance of prepainted and unpainted galfan test panels in corrosive environments. In *Proc. Of Eighth Galfan Licencees Meeting.* ILZRO, 1986.

P Cordoba-Torres, R P Nogueira, L de Miranda, L Brenig, J Wallenborn, and V Fairen. Cellular automaton simulation of a simple corrosion mechanism: mesoscopic heterogeneity versus macroscopic homogeneity. *Electrochemica Acta*, 46:2975–2989, 2001.

A Das and E J Mittemeijer. Simulation of eutectic solidification structures of binary alloys: A multiparticle diffusion limited aggregation model. *Metallurgical and Materials Transactions A*, 31(8):2049–2057, 2000.

C H J Davies. Growth of nuclei in a cellular automaton simulation of recrystallisation. *Scripta Materia*, 36(1):35–40, 1997.

D Dussault and A Powell. Phase field modelling of electrolyis in a slag or molten salt. Mills Symposium August 22-23, 2002.

J Elvins. *The relationship between microstructure and corrosion resistance of Galfan coated steels.* EngD thesis, University of Wales, Swansea,UK, 2005.

J Elvins, J A Spittle, and D A Worsley. Relationship between microstructure and corrsoion resistance in Zn – Al alloy coated galvanised steels. *Corrosion Engineering, Science and Technology*, 38(3):197–204, 2003.

J Elvins, J A Spittle, and D A Worsley. Microstructural changes in zinc aluminium alloy galvanising as a function of processing parameters and their influence on corrosion. *Corrosion Science*, 47(11):2740–2759, 2005a.

J Elvins, J H Sullivan, J A Spittle, and D A Worsley. Short term predictive testing for cut edge corrosion resistance in zinc-aluminium alloy galvanised steels. *Corrosion Engineering, Science and Technology*, 40(1):43–50, 2005b.

J Erlebacher. An atomistic description of dealloying. *Journal of The Electrochemical Society*, 151(10):C614–C626, 2004.

J Erlebacher, M J Aziz, A Karma, N Dimitrov, and K Sierradski. Evolution of nanoporosity in dealloying. *Nature*, 410:450–453, March 2001.

U R Evans. *An Inroduction to Metallic Corrosion.* Arnold, 3rd edition, 1981. ISBN 0-7131-2758-9.

S J Farlow. *Partial Differential Equations for Scientists and Engineers.* WILEY-VCH, 1982. ISBN 0-471-89180-0.

M G Fontana. *Corrosion Engineering.* McGraw Hill, 3rd edition, 1987. ISBN 0-07-100360-6.

J J Friel. Atmospheric corrosion products on Al, Zn, and AlZn metallic coatings. *CORROSION–NACE*, 42(7):422–426, 1986.

D R Gabe. *Coatings and Surface Treatment for Corrosion and Wear Resisitance*, chapter 4, pages 62–93. Applied Science and Industrial Technology. Ellis Horwood, 1984.

F Goodwin, A F Skerazi, and R Lynch. *25th Annual Conference of Metallurgists.* The Canadian Institute of Mining and Metallurgy, 1986.

B M Gray, C Belleau, M A D D'Amico, R L Pyle, and J F Butler. Development of hot-dip zn-fe alloy coated steel for automotive applications. In *1989 Mechanical Working and Steel Processing Proceedings*, pages 3–15, Warrendale,PA, 1989. ISS.

Gruz and Volmer. *Z. Physik Chem.*, 150A:203, 1930.

T Hada. Production technologies of hot-dip zinc-aluminium alloy coated steel sheet. In *Proceedings of the 4th International Conference on Zinc and Zinc Alloy Coated Steel Sheet*, (Galvatech'98), pages 108–114, Chiba, Japan, 1998. The Iron and Steel Institute of Japan.

D G Harlow and R P Wei. A probability model for the growth of corrosion pits in aluminium alloys induced by constituent particles. *Engineering Fracture Mechanics*, 59(3):305–325, 1998.

ILZRO. *Galfan Galvanizing.* International Lead Zinc Research Organization, Inc., Galfan Technical Resource Center, USA, January 1988.

ILZRO. *Galfan - Improved Galvanizing (Specifier's Manual).* International Lead Zinc Research Organization, Inc., Galfan Technical Resource Center, USA, June 1993.

H S Isaacs. The effect of height on the current distribution measured with a vibrating electrode probe. *Journal of Electrochemical Society*, 138(3):722–728, 1991.

H S Isaacs. The localized breakdown and repair of passive surfaces during pitting. *Corrosion Science*, 29(2/3):313–323, 1989.

H S Isaacs and A J Davenport. Measurement of localized corrosion using current density mapping. In G Prentice and W H Smyrl, editors, *Perspectives on Corrosion*, volume 86 of *AIChE*, pages 47–53, 1990.

H Jeffereys and B S Jeffereys. *Methods of Mathematical Physics*. Cambridge University Press, Cambridge, 3rd edition, 1988.

A P Jivkov, N P C Stevens, and T J Marrow. The roles of microstructure and mechanics in intergranular stress corrosion cracking. In C A Brebbia, V G DeGiorgi, and R A Adey, editors, *Simulation of Electrochemical Processes*, pages 217–226. WIT Press, 2005. ISBN 1-84564-012-8.

T Johnsen, A Jøssang, and P Meakin. An experimental study of the quasi-two-dimensional corrosion of aluminum foils and a comparison with two-dimensional computer simulations. *Physica A*, 242:356376, 1997.

J W Johnson, Y C sun, and W J James. Anodic dissolution of Zn in aqueous salt solutions. *Corrosion Science*, 11:153–159, 1971.

A M Karlson. Coated steel sheets in north america - an automotive perspective. In *Proceedings of the International Conference on Zinc and Zinc Alloy Coated Steel Sheet*, (Galvatech'89), pages 271–277, Tokyo,Japan, 1989. The Iron and Steel Institute of Japan.

J Kruger. Breakdown of protective films. In G Prentice and W H Smyrl, editors, *Perspectives on Corrosion*, volume 86 of *AIChE*, pages 14–21, 1990.

M Lamberights, V Leroy, and F Goodwin. In *Proceedings of the Third International Zinc Coated Sheet Steel Conference*, (INTERGALVA), pages SID/7–13, Barcelona, 1991.

N J Laycock and S P White. Computer simulation of single pit propagation in stainless steel under potentiostatic control. *Journal of The Electrochemical Society*, 148(7):B264–B275, 2001.

Y Li. Formation of nano-crystalline corrosion products on Zn–Al alloy coating exposed to seawater. *Corrosion Science*, 43:1793–1800, 2001.

D Livingstone-Bridge, J C Myland, and K B oldham. A model of ionic current densities in the vicinity of a corroding disk-shaped region. *Electrochemistry Communications*, 3(8): 384–389, 2001.

P J Mahon and K B Oldham. Convolutive modelling of electrochemical processes based on the relationship between the current and the surface concentration. *Journal of Electroanalytical Chemistry*, 464(1):1–13, 1999.

P J Mahon and K B Oldham. Incorporating electrode kinetics into the convolutive modelling of reactions at planar, cylindrical and shperical electrodes. *Electrochimica Acta*, 46(7): 953–965, 2001.

B Malki and B Baroux. Computer simulation of the corrosion pit growth. *Corrosion Science*, 47(1):171–182, 2005.

E Mattsson. *Basic Corrosion Technology for Scientists and Engineers.* The Institute of Materials, London, 2nd edition, 1996.

P Meakin, T Jøssang, and J Feder. *Physical Review*, E48:2906, 1993.

E E Mola, B Mellein, E M R Deschiapparelli, J L Vincente, R C Salvarezza, and A J Arvia. Stochastic approach for pitting corrosion modeling .1. the case of quasi-hemispherical pits. *Journal of the Electrochemical Society*, 137(5):1384–1390, 1990.

T H Muster and I S Cole. The protective nature of passivation films: surface charge. *Corrosion Science*, 46(9):2319–2335, 2004.

J C Myland and K B Oldham. Concentrations of electroactive solutes, during cyclic and other voltammetries, at points away from the electrode surface. 1. fundamental relationships and their validation. *Analytical Chemistry*, 71(1):183–195, 1999.

T Nagatini. *Physical Review*, A45:2480, 1992.

A K Neufeld, I S Cole, A M Bond, and S A Furman. The initiation mechanism of corrosion of zinc by sodium chloride particle deposition. *Corrosion Science*, 44:555–572, 2002.

R C Newman, Q Song, R A Cottis, and K Sieradski. *Atomistic computer simulation of alloy corrosion*, chapter 1, pages 17–26. ASTM, 1992.

J W Oldfield. *Galvanic Corrosion*, chapter 2, pages 5–22. ASTM, 1988.

K B Oldham. Diffusion-controlled current densities close to a right-angled electrode edge. *Journal of Electroanalytical Chemistry*, 420(1-2):53–61, 1997.

K B Oldham. Steady-state voltammetry at a rotating disk electrode in the absence of supporting electrolyte. *Journal of Physical Chemistry B*, 104(19):4703–4706, 2000.

B Pieraggi, B MacDougall, and R A Rapp. The role of the metal/oxide interface in the growth of passive films in aqueous environments. *Corrosion Science*, 47:247–256, 2005.

M Pourbaix. *Lectures on Electrochemistry.* NACE, 3rd edition, 1995.

G Prentice. *Electrochemical Engineering Principles.* Prentice-Hall Inc., New Jersey, 1991. ISBN 0-13-249038-2.

G Prentice and Y-C Chang. Breakdown of protective films. In R E White, R F Savinelli, and A Schneider, editors, *Electrochemical Engineering Applications*, volume 83 of *AIChE*, pages 9–14, 1987.

C Punckt, M Bölscher, H H Rotermund, A S Mikhailov, L Organ, N Budiansky, J R Scully, and J L Hudson. Sudden onset of pitting corrosion on stainless steel as a critical phenomenon. *Science*, 305:1133–1136, 2004.

D Raabe. *Computational Materials Science : The Simulation of Materials and Properties.* WILEY-VCH, 1998. ISBN 3-527-29541-0.

A J Robinson, D A Worsley, and J R Searle. Novel flat panel reactor for monitoring photodegradation. *Material Science and Technology*, 20(8):1041–1048, 2004.

J J Santana Rodríguez, F J Satana Hernández, and J E González González. Mathematical and electro-chemical characterisation of the layer of corrosion products on carbon steels in various environments. *Corrosion Science*, 44:2597–2610, 2002.

D Schifler. Galvanic corrosion modeling in flowing systems. In C A Brebbia, V G DeGiorgi, and R A Adey, editors, *Simulation of Electrochemical Processes*, pages 99–108. WIT Press, 2005. ISBN 1-84564-012-8.

P Schmuki. From bacon to barriers: a review on the passivity of metals and alloys. *Journal of Solid State Electrochemistry*, 6:145–164, 2002.

M Schuze. *Corrosion and Environmental Degradation.* Number 19 in Materials Science and Technology. WILEY-VCH, Weinham, Germany, 1st edition, 2000.

T Shibata. Stochastic studies of passivity breakdown. *Corrrosion Science*, 31:413–423, 1990.

G D Smith. *Numerical Solution of Partial Differential Equations for Scientists and Engineers.* Oxford applied mathematics and computing series. Universities Press(Belfast), 2nd edition, 1978. ISBN 0-19-859625-1.

T Sourisseau, E Chauveau, and B Baroux. Mechanism of copper action on pitting phenomena observed on stainless steels in chloride media. *Corrosion Science*, 47: 1097–1117, 2005.

J A Spittle and S G R Brown. A 3D cellular automaton model of coupled growth in two component systems. *Acta Metallurgica Et Materia*, 42(6):1811–1815, 1994.

G Stephenson. *Partial Differential Equations for Scientists and Engineers.* Imperial College Press (London), 1996. ISBN 1-86094-024-2.

E Tada, S Satoh, and H Kaneko. The spatial distribution of Zn^{2+} during galvanic corrosion of a Zn/steel couple. *Electrochimica Acta*, 49(14):2279–2285, 2004a.

E Tada, K Sugawara, and H Kaneko. Distribution of pH during galvanic corrosion of a Zn/steel couple. *Electrochimica Acta*, 49(7):1019–1026, 2004b.

A Taleb, J. Stafiej, and J. P. Badiali. Numerical simulation of metal corrosion with cluster formation. In C A Brebbia, V G DeGiorgi, and R A Adey, editors, *Simulation of Electrochemical Processes*, pages 109–117. WIT Press, 2005. ISBN 1-84564-012-8.

K R Trethewey and J Chamberlain. *Corrosion for Science and Engineering.* Longman, Singapore, 2nd edition, 1995.

A Turnbull. Modelling of crack chemistry in sensitized stainless steel in boiling water reactor environments. *Corrosion Science*, 39(4):789–805, 1997.

A O Volkov, P K Datta, J S Burnell-Gray, and R Couper. Hydrodynamic measurement of a single corrosion pit. *Corrosion Science*, 46:2613–2619, 2004.

E G Webb and R C Alkire. Pit initiation at single sulfide inclusions in stainless steel. *Journal of The Electrochemical Society*, 149(6):B286–B295, 2002.

D E Williams, C Westcott, and M Fleischamnn. Stochastic-models of pitting corrosion of stainless-steels .1. modeling of the initiation and growth of pits at constant potential. *Journal of the Electrochemical Society*, 132(8):1796–1804, 1985.

D A Worsley. Design Against Corrosion. Course Notes, 2001.

D A Worsley, H N McMurray, J H Sullivan, and I P Williams. Quantitative assessment of localized corrosion occurring on galvanized steel samples using the scanning vibrating electrode technique. *Corrosion*, 60(5):437–447, 2004.

X G Zhang. *Corrosion and Electrochemistry of Zinc*. Plenum Press, New York, 1996.